TECHNISCHE UNIVERSITÄT MÜNCHEN
Max-Planck-Institut für Extraterrestrische Physik

Hard X-ray Studies of GRB precursors and AGN

Davide Burlon

Vollständiger Abdruck der von der Fakultät für Physik der Technischen Universität München zur Erlangung des akademischen Grades eines

Doktors der Naturwissenschaften (Dr. rer. nat.)

genehmigten Dissertation.

Vorsitzender:		Univ.-Prof. Dr. A. J. Buras
Prüfer der Dissertation:	1.	Priv.-Doz. Dr. J. Greiner
	2.	Univ.-Prof. Dr. St. Schönert

Die Dissertation wurde am 04.10.2011 bei der Technischen Universität München eingereicht und durch die Fakultät für Physik am 15.12.2011 angenommen.

Contents

Summary

In this thesis I discuss the analysis of two classes of emitting black holes, namely $\gamma-$ray bursts (GRBs) and Active Galactic Nuclei (AGN). Consequently, I developed this thesis dividing it into two relevant parts, and only the first Chapter is common, since it describes the high energy instruments on which my analysis relies: two *Swift* instruments (BAT and XRT), the BATSE instrument, and the *XMM–Newton* EPIC X-ray camera.

I have studied the high energy emission of GRBs, the most luminous transient stellar-mass black holes, with respect to a particular phase of the GRB high energy emission, called *"precursor"*. Some $\sim 15\,\%$ of GRBs show activity prior to the standard main emission, whose nature is still a puzzle. In the second Chapter, after discussing the global properties of the so-called prompt emission, and the models that have been proposed in the literature to account for precursor emission specifically, I outline the open issues in the GRB fields as a whole. I investigated whether there is a distinctive characteristic of precursors with respect to the main emission, by comparing the evolution of the spectral parameters in a selected sample of bright GRBs. I found that precursors and main emission episode have very similar spectral properties, albeit a statistically significant difference emerges in the distribution of the energy at which the spectrum peaks ($E_{\rm peak}$). The spectral evolution of $E_{\rm peak}$ within precursors, i.e. the correlation with the flux, shows a similar behavior to the evolution within the main emission episode. My findings favor the models in which the precursor is due to the same fireball physics of the rest of GRB emission. This result is presented in Chapter 3, along with an outlook on this subject.

My work proceeded with the analysis of a subclass of AGN, which are the most luminous persistent emitting black holes. In Chapter 4 I summarize our understanding of AGN, with a focus on the emission (and absorption) mechanisms. The work I present in Chapter 5 is the result of the exploration of a three-year-long survey of the sky with the BAT instrument. I derived and analyzed the X-ray absorption distribution in the local universe, with a focus on the most obscured ones, i.e. Compton-thick objects, which represent just a small ($\sim 5\,\%$) fraction of the whole population. However, I show that once corrected for the bias against the detection of these sources, the real intrinsic fraction is $\sim 20\,\%$. In addition, I proved -for the first time in the BAT energy range- that a well known anti-correlation between the fraction of absorbed AGN and luminosity is tightly connected to the different form of the X-ray luminosity functions of absorbed and unabsorbed AGN. Since this points towards a difference between the intrinsic properties of the subsamples in which we split our parent population, I tried to test in Chapter 6 if indeed the less obscured sources are accreting more efficiently the gas from their environment, expressing their luminosities in terms of the so-called Eddington luminosity. To this aim, I adopted a method for estimating the black hole masses. The results indicate that the anti-correlation with respect to luminosity is in turn related to the efficiency of accretion, and we discuss some consistency tests. I propose a development of our study of AGN at the end of the final Chapter.

Zusammenfassung

In dieser Arbeit beschreibe ich die Analyse zweier Klassen schwarzer Löcher, die Strahlung abgeben: Gammastrahlenausbrüche (gamma ray bursts, GRBs) und aktive Galaxienkerne (Active Galactic Nuclei, AGN). Aus diesem Grund besteht sie aus zwei Teilen, wobei das erste Kapitel fr beide Teile relevant ist. Es beschreibt die Hochenergieinstrumente, auf die sich meine Analyse stützt: zwei Instrumente von *Swift* (BAT und XRT), das Instrument BATSE und die Röntgenkamera EPIC vom *XMM–Newton*.

Ich habe die Hochenergieemission von GRBs, den leuchtkräftigsten vorübergehend strahlenden stellaren schwarzen Löchern, in Bezug auf eine bestimmte Phase der GRB-Hochenergieemission hin untersucht, dem sogenannten “precursor”. Etwa 15 % aller GRBs zeigen schon vor der Hauptemissionsphase Aktivitt deren Natur noch ungeklrt ist. Im zweiten Kapitel diskutiere ich die allgemeinen Eigenschaften der sogenannten prompten Emission und insbesondere die in der Literatur als Erklärung für die prompte Emission vorgeschlagenen Modelle. Anschließend umreiße ich die offenen Fragen im Feld der GRBs insgesamt. Ich habe untersucht, ob sie die Precursor-Emission markant von der Hauptemission unterscheidet, indem ich die Zeitverläufe und Verteilungen der spektralen Parameter einer Auswahl heller GRBs verglichen habe. Ich fand, daß sich die spektralen Eigenschaften von Precursor und Hauptemission stark ähneln, aber ein statistisch signifikanter Unterschied in der Verteilung der Energie der strksten Emission ($E_{\rm peak}$) besteht. Die spektrale Entwicklung von $E_{\rm peak}$ innerhalb der Precursor, d.h. die Korrelation mit den Fluß, zeigt ein ähnliches Verhalten wie die innerhalb der Hauptemissionsphase. Meine Resultate bevorzugen Modelle bei denen der Precursor der selben Feuerballphysik wie die restliche GRB-Emission entstammt. Diese Ergebnisse sowie ein Ausblick auf dieses Thema werden in Kapitel 3 vorgestellt.

Meine Arbeit setzte sich fort mit der Analyse einer Unterklasse von AGNs, den leuchtkräftigsten dauerhaft strahlenden schwarzen Löchern. In Kapitel 4 fasse ich unser Verständnis von AGNs mit besonderem Augenmerk auf die Emissions- und Absorptionsvorgänge zusammen. Die Arbeit, die ich in Kapitel 5 vorstelle ist das Ergebnis der Untersuchung einer dreijährigen Durchmusterung des Himmels mit dem BAT-Instrument.

Ich habe die Verteilung der Röntgenabsorption im lokalen Universum bestimmt und analysiert. Dabei lag der Schwerpunkt auf den am stärksten verdeckten, den Compton-dichten Objekten, die nur einen kleinen ($\sim 5\,\%$) Anteil der gemessenen Objekte stellen. Ich zeige allerdings, daß unter Einbeziehung der Nachweiswahrscheinlichkeit dieser Objekte ihr Anteil an der Gesamtpopulation $\sim 20\,\%$ beträgt.

Außerdem zeigte ich – erstmals im BAT-Energiebereich – daß eine wohlbekannte Antikorrelation zwischen dem Anteil absorbierter AGNs und der Leuchtkraft eng mit den unterschiedlichen Formen der Röntgen-Leuchtkraftfunktionen absorbierter und nichtabsorbierter AGNs zusammenhängt. Da dies auf einen Unterschied in den intrinsischen Eigenschaften der beiden Teilpopulationen hindeutet, habe ich in Kapitel 6 versucht zu überprüfen, ob die weniger verdeckten Quellen tatsächlich effizienter Gas aus ihrer Umgebung akkretieren. Zu diesem Zweck wandte ich ein Verfahren zur Abschätzung der Massen der schwarzen Löcher an, womit ihre Leuchtkraft im Verhältnis zur sogenannten Eddington-Leuchtkraft ausgedrückt werden kann. Die Ergebnisse zeigen, daß die Antikorrelation in Bezug zum Akkretionswirkungsgrad steht, was ich zusammen mit einigen Konsistenzkontrollen diskutiere. Am Schluß des abschließenden Kapitels schlage ich eine Weiterentwicklung unserer AGN-Studie vor.

Chapter 1

Observing the sky at high energies

In this chapter we give a brief overview of the satellites/instruments which were relevant to this thesis. The focus is mainly on the *Swift* mission, followed by two sections dedicated to the high energy instruments on board the satellite. A substantial fraction of the chapter is dedicated to the BAT instrument, followed by the BATSE instrument onboard the *Compton Gamma Ray Observatory*, and the *XMM–Newton* X-ray satellite.

1.1 The *Swift* observatory

The *Swift* satellite is a multi-wavelength observatory dedicated to the study of γ-ray bursts (Gehrels et al., 2004), built by Spectrum Astro. It is equipped with 3 instruments to detect and study GRBs and their afterglows. Swift employs a large *Field Of View* (FOV), coded mask burst alert telescope named BAT. The scope of BAT is to detect and localize GRBs with a precision of 1-3 arcmin. After the burst detection, the spacecraft autonomously re-points itself (in approximately 25–75 seconds) to bring the burst location within the FOV of the narrow-field X-ray and UV/optical telescopes (XRT and UVOT respectively). The observation with XRT and UVOT allows to detect the afterglow (if any) and to refine its position with better accuracy.

The *Swift* mission was built by an international team from the US, UK and Italy (mirrors calibrated in MPE - Munich). After 5 years of development, the spacecraft was launched from the Kennedy Space Center on 20 November 2004. After eight weeks required for the in-flight calibration, all the three instruments were operative. The normal operations could start on 5 April 2005. *Swift* started detecting GRBs in December 2004 (GRB 041217), but the slew was not yet automatic. The first X-ray afterglow was detected as a target of opportunity 4.5 hours after GRB 041223. Once the burst has been detected and localized by BAT, its position (together with some preliminary information like duration and the burst peak count rate) is distributed to the scientific

Figure 1.1 The *Swift* satellite.

community via the *Gamma-ray burst Coordinate Network*[1] (GCN).

Optical/Infrared follow-up typically starts once the X-ray afterglow has been detected by XRT and its position is known with arcsec accuracy. The coordination among different institutions allows rapid response, radio observations, observations by very high energy, neutrinos, and gravitational waves telescopes.

The mission policy is devoted to GRBs (*Swift* spends more than half of its orbital life observing Gamma-ray Bursts). The remaining time is shared between non-GRB planned targets, *Target of Opportunity* (ToO) observations of non-GRB transients, and calibration. ToO are open to the scientific community that can ask for specific observations. The proposals are reviewed and potentially accepted by the Principal Investigator according to scientific merit and observational constraints. In fact in recent years the fraction of time dedicated to ToO observations has been steadily increased.

Mission profile The orbital radius and the inclination angle of the *Swift* satellite were chosen to meet three requirements: the protection of the instruments, by Van Allen belts, from charged particles coming from outer space or the Sun, the suppression of the background, and the orbital lifetime. The worst case scenarios predicted a 5 years lifetime. The position of the spacecraft with respect to the Earth affects the level of background contribution of all the components (cosmic rays, solar activity, magnetosphere trapped particles, X-ray background, Earth's albedo). The Earth shadows the detector from cosmic rays and its magnetic field can shield the instrument. Nevertheless the cosmic rays interact with Earth's atmosphere, providing a highly time dependent background. The low inclination with respect to the Earth equator minimizes the amount of time spent by the satellite in the *South Atlantic Anomaly* and increases the BAT's average lifetime. We summarize in Tab. 1.1 the launch and orbital characteristics.

---

[1] http://gcn.gsfc.nasa.gov/

Swift has a 584×601 km orbit with an inclination of 20.6 degrees and an orbital period of approximately 95 minutes. The orbit is expected to remain stable possibly beyond 2020.

Table 1.1 *Swift* mission launch and orbital characteristics

Mission parameter	Value
Launch date	20 November 2004
Launch vehicle	Delta 7320
Orbital radius	$\sim$ 600 km
Inclination	$< 22^\circ$
Total mass	1270 kg
Total power	1650 W
Orbital lifetime	> 5 yr

The slew The spacecraft is a 3-axis stabilized platform. One of the innovative characteristics of *Swift* is its ability to rapidly slew to repoint, with its narrow field instruments, the position of the GRB detected by BAT. The *Swift* satellite can slew from 0° to 50° in 25-75 s. The slew procedure is handled by the Attitude Control System, that grants on board autonomy: the on board system checks all the orientation constrains (zones of avoidance: 45° of the Sun, 21° of the Moon, 94° of Earth's limb) and no function control is needed to do the calculations or the maneuver. Once that the ACS has confirmed the feasibility of the repointing, the slew is performed and the pointing stability is reached in few seconds.

1.1.1 BAT

The Burst Alert Telescope (BAT, Barthelmy et al. 2005) is a highly sensitive, large field of view coded-aperture telescope designed to monitor a large fraction of the sky for the occurrences of gamma-ray bursts (GRBs). BAT provides the burst trigger time and the 1-3 arcmin accurate position that is then used to slew the spacecraft to point the two narrow-FOV instruments (XRT, and UVOT) for follow-up observations. The BAT positions and light curves are transmitted through TDRSS to the ground in 20 and 130 sec respectively, and openly distributed to the scientific community through GCN. While observing bursts, BAT simultaneously and automatically accumulates an all-sky hard X-ray survey.

Technical overview The BAT instrument was designed and built at Goddard Space Flight Center. The technical characteristics of BAT are listed in Tab. 1.2. The BAT consists of a 5200 cm^2 array of 44 mm^2 CdZnTe (CZT) elements located 1 meter behind a 2.7 m^2 coded-aperture mask of 5×5 mm^2 lead elements, with a point spread function (PSF) of 22 arcmin. The BAT coded-aperture mask was limited by the Delta rocket faring. A graded-Z fringe shield reduces the instrumental background event rate and cosmic diffuse background, and a thermal radiator and control system keep the detector plane at a constant temperature. The control of the BAT instrument is done through the Image Processor which also provides the on-board event processing (burst trigger detection, burst location calculations, and burst figure-of-merit calculation). In Fig. 1.2 we report an image of BAT together with the portion of the sky which represents BAT's field of view.

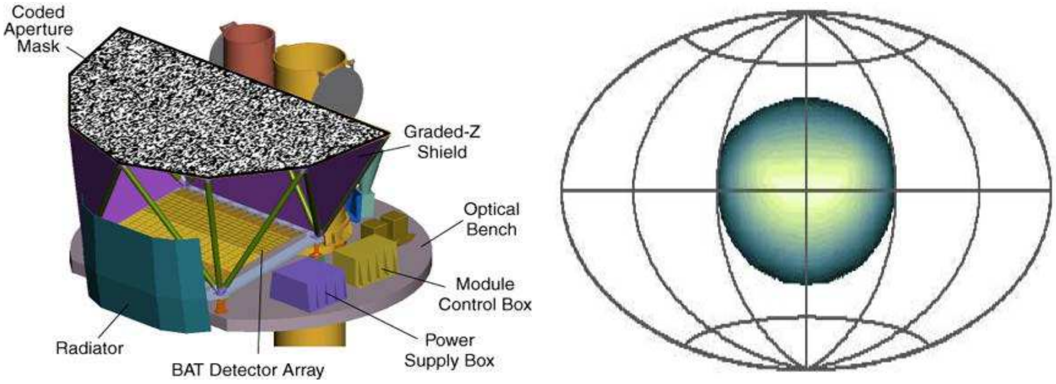

Figure 1.2 *Left:* Cut away view of the Burst Alert Telescope (BAT). The coded mask is the randomly filled gray grid. The 32k detectors lie at the bottom. Behind BAT, also the two narrow field instruments are partly visible. *Right:* Field of view of the BAT superimposed onto the projection of the sky (arbitrary coordinate system). Color scale indicates full coding (white) and progressively partial coding (blue).

Table 1.2 *Swift*-BAT characteristics

Parameter	Value
Energy Range	15-350 keV (approx.)
Energy Resolution	5 keV@60 keV
Aperture	Coded mask, random pattern, 50% open
Detecting Area	5240 cm^2
Imaging Effective Area	1400 cm^2 (max.; on-axis)
Detector Material	CdZnTe (CZT)
>50% Coded Field of View	1.4 sr
>10% Coded Field of View	2.2 sr
Detector Elements	256 Modules of 128 elements/Module
Detector Element Size	$4.00 \times 4.00\times 2.00$ mm^3
Coded Mask Cell Size	$5.00 \times 5.00 \times 1.00$ mm^3 (Pb Tiles)
Instrument Dimensions	2.4 m × 1.2 m× 1.2 m
Telescope PSF	22 arcmin (FWHM)
Position Centroid Accuracy	1-3 arcmin
Sensitivity (for exposure T)	2×10^{-10} erg s^{-1} cm^{-2} $(\mathrm{T} / 20\ \mathrm{ks})^{-0.5}$ (15-150 keV; 5 sigma)

Effective area The energy range of 15-150 keV describes the energy range over which the effective area is more than 50% of the peak value. The simplest definition of effective area, is the following: given a point-source of intensity S, the number of photons received by the detector in a time δt, in direction (θ,ϕ) is equal to $S \cdot A_{eff}(\theta, \phi) \cdot \delta t$. The effective area is thus the instrument's response to the incoming radiation and it is a direct measurement of the goodness of the instrument. The sensitivity improves with the increase of the effective area. In general, each type of instrument has its own definition of effective area. A general way to define the effective area is: $A_{eff}(\theta, \phi) = A_{geom}(\theta, \phi) \cdot \epsilon_q \cdot \epsilon_{image} \cdot \epsilon_{trans}$ where A_{geom} is the geometrical area of the detector, ϵ_q is the quantum efficiency of the detecting device, ϵ_{image} is the efficiency of the imaging reconstruction algorithm employed (if any) and ϵ_{trans} is the transmission through support structures.

In Fig. 1.3 we show the variation of the effective area (left) and the estimated systematic errors (right). The effective area is shown for a source on axis and 45° off axis. It contains the mask transmission and the 56% efficiency factor due to the cross-correlation technique used for imaging and mask-weighed flux determination (see the following paragraphs). Edge features are due to Ag (25.5 keV), Cd (26.7 keV), and Pb (88 keV). The right image shows the systematic error as a function of the energy, as provided by the BAT team for spectral analysis and recently updated (see Sakamoto et al., 2011). The effective area peaks in the 30-80 keV range. The range is governed at the lower end by the electronic discriminator threshold, and at the upper end by the increasing transparency of the lead tiles in the mask. Moreover for high energy photons (>200 keV), charge collection in the detectors becomes less reliable. For a thorough description on the choice of the energy range in our specific analysis we refer to chapter 5 and references therein.

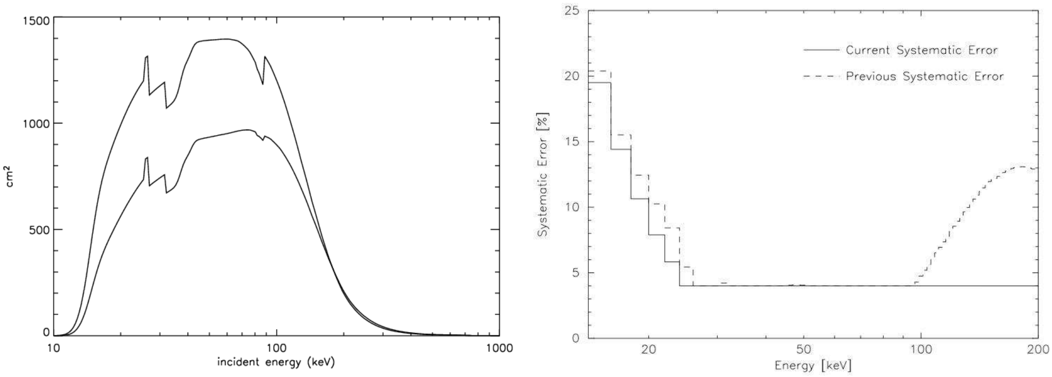

Figure 1.3 *Left:* BAT's effective area on axis and 45° off axis. *Right:* Systematic errors as a function of energy.

Coded mask apertures Focusing of high-energy radiation is so far (and also for the planned missions in the next decade) technically feasible only for photon energies up to a few tens of keV through grazing incidence reflection. It is not technologically possible to produce an image in the gamma-ray band using traditional focusing optics; especially over a large field of view. Hence, the only way to obtain an image is through the coded-aperture method.

The BAT instrument has a coded aperture (i.e. a plate with areas that are transparent or opaque to photons in a certain energy range, see Tab. 1.2) which is used to modulate (coding phase) the incoming celestial radiation, as shown in Fig. 1.4 (left image). A position sensitive detector, whose spatial resolution matches roughly the mask pattern grid size (see Θ in the right image of Fig. 1.4), is used to record the modulated signal.

The BAT coded aperture is composed of ~52,000 lead tiles located 1 meter above the CZT detector plane. The lead tiles are 5.00 mm square and 1.0 mm thick. The tiles are mounted on a low-mass, 5-cm thick composite honeycomb panel. The pattern is completely random with a 50% open filling factor. The mask is 2.4 m by 1.2 m (with the corners cut off, it is 2.7 m^2), which yields a 100° by 60° FOV (half-coded).

Ideally, the mask pattern is designed in such a way that each source at different positions in the FOV casts a unique shadow onto the detector plane. Thus, the incident directions can later be reconstructed from the count rates recorded in the detector. All the "optical" elements of a coded aperture are passive, involving the shadows casting from the aperture (mask) onto an imaging sensor (see Fig. 1.4).

Random mask A natural extension of the pinhole mask (a shield with one single aperture) is the random pinhole aperture. Independently proposed by Dicke (1968) and Ables (1968), this aperture consists of a large number of randomly spaced pinholes having an overall transmission ~50%. Invented as a natural consequence of the pinhole camera which has ideal imaging capabilities , but suffers greatly from a conflict between resolution and sensitivity, a random pattern allows to increase the sensitivity maintaining the original angular resolution.

Coding/decoding phase The encoded information of the incoming photons has to be reconstructed by decoding the observation, afterwards. It is apparent that this method of producing sky images is a two-step procedure, in contrast to the direct (one-step) imaging procedure of focusing techniques.

An important concept is partial coding. When a source is on-axis, its aperture shadow fully illuminates the detector array, and so it is fully coded. BAT has a small region near the center of its field of view which is 100% coded (see Fig 1.2). However, for a source off axis, only a portion of the aperture shadow will illuminate the detector array, and the rest is blocked by the shield which surrounds the BAT instrument. The partial coding effect is analogous to the off-axis vignetting effect for classical telescopes. The fractional illumination is called the partial coding fraction. The BAT field of view which contains at least 10% partial coding is about 2.2 steradians (>50%, 1.5 steradians; >90%, 0.5 steradians). As shown in Fig. 1.4 (right panel), typically two FOVs can be distinguished in:

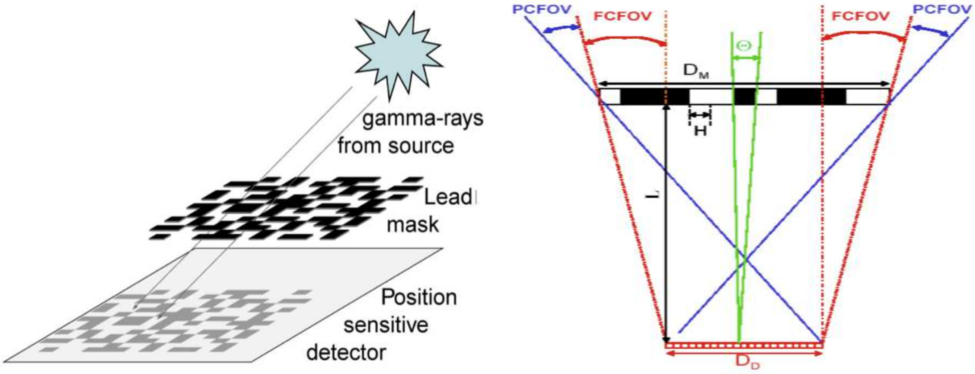

Figure 1.4 *Left:* basic BAT imaging scheme. A γ.ray source illuminates the coded aperture (mask) and casts a shadow onto a position sensitive detector. *Right:* schematic drawing of a coded mask telescope. D_D and D_M are the dimensions of the detector plane and the mask, respectively. H is the typical dimension of the mask element and Θ is the angular resolution.

- the fully coded field of view (FCFOV) where all the source radiation arriving at the detector plane is modulated by the mask (the radiation is 100% coded)
- the partially coded field of view (PCFOV) where only part of the source radiation is modulated by the mask and the rest is uncoded (0%< coding fraction <100%); in this part of the FOV the instrument's sensitivity scales with the coding fraction.

Of course, as the partial coding decreases, the instrument sensitivity also decreases. This is why gamma-ray burst light curves are typically noisier at their start, when the source is detected off-axis; and less noisy by the end, when the spacecraft has slewed to put the source in the fully coded region.

The encoding/decoding procedure, in mathematical terms, translates into:

$$C = M * S + B \tag{1.1}$$

where $*$ denotes the convolution operator [2], C is the information recorded in the detector plane, S is the distribution of sources in the sky to be imaged, M the mask transmission function and B the (signal-independent) detector background. The mask transmission function is, ideally, made up of zeros (opaque elements) and ones (transparent elements). In order to derive the original signal S, one needs to deconvolve the recorded information

---

[2] The convolution operator provides a way to apply an array to another of the same dimension but generally of different size. The output array has the same dimensionality of the input ones. The convolution operator is in the form:

$$(A * B)_{i,j} = \sum_{k=1}^{m} \sum_{l=1}^{n} B(i + k - 1, j + l - 1) A(k, l)$$

where i=1,..., M-m+1 and j= 1,..., N-n+1. M and N are rows and columns of the image (e.g. the sky), m and n are rows and columns of the "kernel" (e.g. the mask).

using a suitable function D such that:

$$\hat{S} = D * C = D * (M * S) + D * B \tag{1.2}$$

The best choice of aperture design and decoding function D is the one that produces D$*$M $=\delta$ and with D$*$B as small and uniform as possible. If we consider eq. 1.2 using matrices instead of employing the convolution operator, we get that the deconvolution problem can be solved if we find the matrix D = M^{-1}. This obviously requires that the mask pattern originates a non-singular matrix (i.e., the rows of the M are linearly independent) and is know as the "inversion problem".

Instrument operations The BAT instrument has two basic modes of operation:

1. scan-survey mode,
2. burst mode.

These two modes reflect the two major types of data that BAT produces: hard X-ray survey data and burst positions. Most of BAT's time is spent waiting for a burst to occur in its FOV. It accumulates events in the detector plane looking for increases in the count rate over a range of time scales. When the trigger algorithm is satisfied, it switches to the burst mode and a buffer saves ∼ 300 s pre-burst information. The spectra are accumulated in 80 energy channels.

When not in burst mode, the instrument is accumulating spectra in each of its 32K detector elements every 5 minutes. These 32K spectra (granted in 18 energy intervals) are recorded and become part of the survey data. During the scan-survey mode each block periodically goes into calibration mode.

The Figure Of Merit (see the last paragraph of this section) calculation is within the BAT flight software. It decides if the current burst trigger is worth performing a spacecraft slew maneuver.

Burst trigger The production of a GRB alert and of the burst position by BAT is a two step process: 1) the detection of the onset of a burst by looking for increases in the event rate across the detector plane, and 2) the formation of an image of the sky using the events detected during the time interval at the beginning of the burst.

The burst trigger algorithm looks for excesses in the detector count rate, above background and constant sources. In Low Earth Orbit, detector background rates can vary by more than a factor of two during a 90-minute orbit. The durations of GRBs range from milliseconds to minutes, during which they may have anywhere from one to several dozen peaks in the emission. Therefore, the triggering system must be able to extrapolate the background and compare it to the measured detector count rate over a variety of timescales and in several energy bands.

The trigger algorithm continuously applies a large number of criteria that test the count rate from the detector plane (and subsections of the plane) on timescales ranging from 4 ms to 32 s using a variety of background estimates (constant, linear, and parabolic with time). The burst trigger threshold is manageable, ranging from 4 to 11 sigma above background noise with a typical value of 6.5 sigma. Once a rate trigger occurs, an image is formed through the coded mask system. To maximize the signal-to-noise ratio of the counts used for imaging, the software varies the energy band (typically four different energy bands are used) and the foreground time period over which the counts are accumulated. The BAT processor continuously tracks hundreds of these criteria (which can be adjusted) sets simultaneously.

A key feature of the BAT instrument for burst detection is its imaging capability. Following the burst trigger, the on-board software checks for and requires that the trigger corresponds to an uncatalogued point source, thereby eliminating many false triggers such as magnetosphere particle events and flickering in known (cataloged) bright galactic sources. Every 64 s the detector array count rate map is processed through the imaging algorithm and scanned for point sources. All sources found are compared against an on-board catalog. Any new source or any known source with an intensity above a manageable level will constitute a "new source" and initiate the burst response procedure. Because a burst detection requires the imaging, the threshold for the rate trigger is set to permit many "false positives" that are subsequently rejected by the imaging step. Consequently the imaging step is usually the most restrictive step and therefore determines BAT's burst sensitivity.

For example, one trigger criterion may specify that the count rate of the detectors on the left side of the detector plane in the 100-150 keV band over a 128 ms interval should be compared to the linear extrapolation of the background rate over a baseline interval from 5 to 3 seconds earlier. This searches for short, hard GRBs near the right edge of the FOV, even in the presence of a rising or falling background, but it is relatively insensitive to long, soft bursts.

Due to the limited memory buffer, the BAT data products that are available after processing include generally 300 s before and after the trigger time. Hence it may happen that if *Swift*-BAT triggers on a precursor several hundreds of seconds before the main event (e.g. GRB 060124), only the first pulse is included in the burst mode data. Time-stamping of events within the BAT has a relative accuracy of 0.1 ms and an absolute accuracy from the spacecraft clock of ∼0.2 ms.

Figure of Merit algorithm The Figure of Merit (FOM) algorithm is part of the spacecraft's autonomy that decides if the burst just detected by BAT is worth requesting a slew maneuver by the spacecraft. With each new burst detected and localized by BAT, the FOM determines through a series of criteria if this new burst is worth interrupting the current follow-up observation by the XRT and UVOT. If the new burst has more "merit", a slew request is sent to the spacecraft, which then checks the constraints (see §1.1) and informs the FOM if the slew will be done. Also the targets of opportunity (ToOs) undergo the same process.

Survey mode While searching for bursts the BAT performs an all-sky hard X-ray survey and monitors for hard X-ray transients. The BAT accumulates detector-plane maps every five minutes (5 minutes is the nominal exposure; in some cases the exposure may be greater or less) in 80 energy bandpasses. Sources found in these images are compared against an on-board catalog of sources. Those sources either not listed in the catalog or showing large variability are deemed to be transients. A subclass of long smooth GRBs that are not detected by the burst trigger algorithm may be detected with this process.

On the ground, sky images are produced by convolution with the mask pattern from the survey data using an iterative clean algorithm. An algorithm tries to find and localize sources in these sky images. For each detected source, another algorithm produces a background-subtracted counts spectrum and a refined position. Fits are performed to the counts spectrum using a detailed instrument response matrix including the off-diagonal response to determine the source photon spectrum.

1.1.2 XRT

Swift X-Ray Telescope (XRT, Burrows et al. 2000) is designed to measure the fluxes, spectra, and light curves of GRBs and afterglows over a wide dynamic range covering more than 7 orders of magnitude in flux. The XRT can pinpoint GRBs to 5-arcsec accuracy within 10 seconds of target acquisition for a typical GRB and can study the X-ray counterparts of GRBs beginning 20-70 seconds from burst discovery and continuing for days to weeks. The XRT is a focusing X-ray telescope with a 110 cm^2 effective area, 23 arcmin FOV, and 0.3-10 keV energy range. The mirror point spread function is 18 arcsec, and given sufficient photons, the centroid of a point source image can be determined to sub-arcsec accuracy in detector coordinates. The typical GRB afterglow

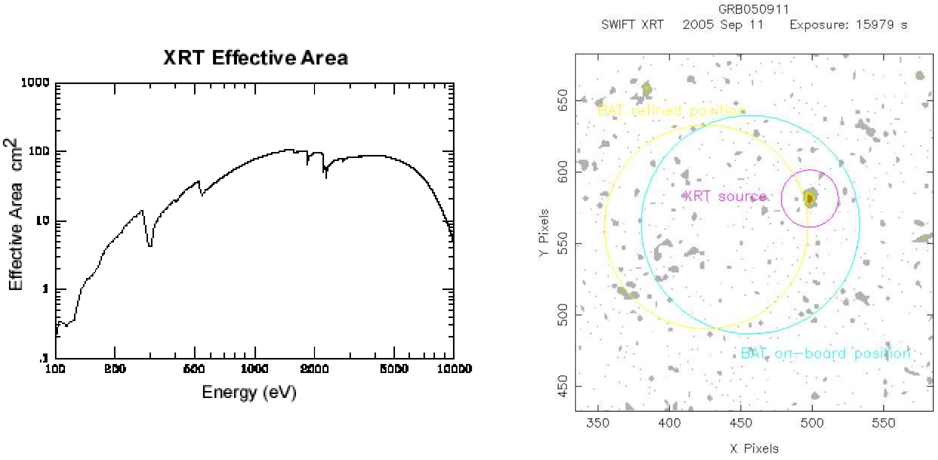

Figure 1.5 *Left panel:* XRT effective area. *Right panel:* position accuracy of the XRT compared to the BAT for the realistic case of GRB 050911. The pictures are taken from the mission website http://swift.gsfc.nasa.gov/docs/swift/about_swift/xrt_desc.html

flux allows the XRT to obtain source positions to better than 1 arcsec in detector coordinates, which will increase to ~ 5 arcsec when projected back into the sky due to alignment uncertainty between the star tracker and the XRT.

The XRT uses a grazing incidence Wolter 1 telescope to focus X-rays onto a CCD. The X-ray mirrors are the units built, qualified and calibrated as flight spares for the JET-X instrument on the Spectrum-X mission while the CCD is a copy of the EPIC-MOS instruments on the XMM-Newton mission. To prevent on orbit degradation of the mirror module's performance, it is maintained at $20°\mathrm{C} \pm 5°\mathrm{C}$.

The detectors were planned to operate at approximately $100°$ K to ensure low dark current and to reduce the CCD's sensitivity to irradiation by protons (which can create electron traps that ultimately affect the detector's spectroscopy). Due to failure of cooling system, they are passively cooled to temperatures in the range [-65,-50]° K.

The XRT supports three readout modes to enable it to cover the dynamic range and rapid variability expected from GRB afterglows, and autonomously determines which readout mode to use. The order that is normally used to follow a bright GRB is as follows:

- Imaging Mode produces an integrated image measuring the total energy deposited per pixel and does not permit spectroscopy, so will only be used to position bright sources up to 7×10^{-7} ergs cm^{-2} s^{-1} (37 Crab);

- Timing Mode sacrifices position information to achieve high time resolution (2.2 ms) and bright source spectroscopy through rapid CCD readouts. It is most useful for sources with flux below $\sim 10^{-7}$ ergs cm^{-2} s^{-1} (5 Crab);

- Photon-counting Mode uses sub-array windows to permit full spectral and spatial information to be obtained for source fluxes ranging from the XRT sensitivity limit of 2×10^{-14} to 2×10^{-11} erg cm^{-2} s^{-1} (1μCrab-1mCrab). The upper limit is set when pulse pileup becomes important (>5%).

Tab. 1.3 summarizes the instrument's properties. The XRT is also used to follow-up on BAT survey sources to determine their soft X-ray counterpart; given the 5 arcsec accuracy, XRT observations are successful in identifying the X-ray counterpart of the BAT sources.

1.2 The BATSE instrument onboard the *Compton Gamma Ray Observatory*[3]

The Burst And Transient Source Experiment (BATSE, Fishman et al. 1982) was designed for the detection, location, spectral and temporal analysis of Gamma Ray Bursts. During the 9 year of activity of the CGRO (21/04/1991 - 4/06/2000) its main results in the GRB field were:

---

[3] For a more detailed discussion than the present one I refer the reader to e.g. Ghirlanda (2002)

Table 1.3 XRT instrument properties.

Property	Description
Telescope	JET-X Wolter 1
Focal Length	3.5 m
Effective Area	110 cm^2 @ 1.5 keV
Telescope PSF	18 arcsec HPD @ 1.5 keV
Detector	EEV CCD-22, 600x600 pixels
Detector Operation	Imaging, Timing and Photon-counting
Pixel Scale	2.36 arcsec/pixel
Energy Range	0.2 - 10 keV
Sensitivity	2×10^{-14} erg/cm^2/s in 10 ks

- isotropic angular distribution of gamma ray bursts;
- non-uniform flux distribution of GRBs;
- statistical diversity of Gamma Ray Bursts temporal and spectral properties;
- discovery of gamma-ray flashes produced by atmospheric thunderstorms.

Among the other results BATSE produced the -so far- greatest catalog of gamma ray bursts, with more than 2700 events.

Technical characteristics BATSE was an all–sky viewing instrument composed by eight modules arranged on the corners of the CGRO. Each module (fig.1.6) contained 2 scintillation detectors: the Large Area Detector (LAD) optimized for sensitivity and directional response, and the Spectroscopic Detector (SD) optimized for broad band energy coverage and high resolution spectral analysis.

The LAD consisted of a thin (1.27 cm of thickness) circular ($\emptyset$=50.8 cm of diameter) layer of scintillation material (NaI) which converts the incident photon flux in optical light, afterwords collimated onto three photomultiplyers and processed through a PHA analyzer. The system was provided with a front anti-coincidence plastic layer, to reduce the charged particle background, and with an inside lead coated collector, to prevent contamination from back and side scattering. The sensitive area of the LAD is 2025 cm^2 and it has a good sensitivity from 30 keV to 1.9 MeV; the location error is on average of 2 degrees with a systematic error (to be added in quadrature) of 1.6 deg, and the fluence sensitivity is 3×10^8erg/cm^2 for a 1 sec burst. The energy resolution of the LAD was 27% at 88 keV and 20% at 511 keV and it remained quite stable in orbit (Horack, 1991). Due to their large effective area, the LAD data are suited for time resolved spectral analysis of bright and dim bursts and for variability studies.

The Spectroscopic Detector (SD) provided high energy resolution spectra (due to its large thickness=7.62 cm) for the brightest bursts (small collecting area, 127 cm^2). It consisted of a circular ($\emptyset$ = 12.7 cm) uncollimated NaI(Tl) scintillation detector viewed by a single PMT, placed in a passive lead/tin shield coated housing. The crystal has a front beryllium window to provide high sensitivity down to 10 keV, for quite normal incident photons. The SD nominal energy range was between 10 keV and 100 MeV, depending on the operational ground control settings. The data products of the SD are suited for spectral evolution studies of bright bursts with an unprecedented energy resolution and variability studies.

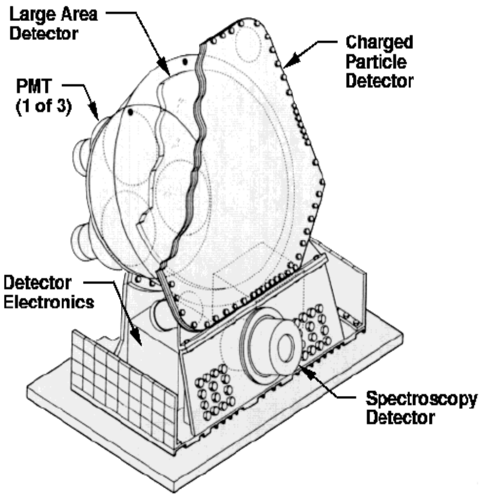

Figure 1.6 One of the eight modules composing BATSE. The LAD and SD detectors are indicated.

The trigger method High time resolution GRB data were accumulated only in response to a burst trigger. In the usual configuration the count rates in at least 2 detectors integrated from 50 to 300 keV were required to increase, above a running background average, by an amount that is specified in terms of the standard deviation of the expected background counts (σ) in each detector. The count rates were tested, independently, on three integration time intervals: 64 ms, 256 ms and 1024 ms. The background was estimated over a fixed time interval (actually set at 17.4 sec) and, if the discriminator rates in channels 2 and 3 ($\sim 50 - 300\ keV$) were 5.5σ above the averaged background count rate, a trigger signal was produced. There was an additional condition for the burst to pass the trigger control sequence: the detector with the highest signal should have a charged particle count rate less than a fraction of the neutral rate, in order to discard any event caused by charged particle showers interacting with the crystal.

When the on–board trigger criteria were satisfied, the Central Electronic Unit (CEU) started data storage with high temporal and spectral resolution for the "accumulation period", which typically lasted from 180 to 573 seconds. Following the accumulation period there was a read–out interval of the burst memory which was transmitted to the ground, lasting from 28 minutes to 90 minutes.

The monitored count rates, the energy thresholds and detector combinations, which define the trigger criterion, were programmable so that the available burst catalogs have not uniform detection conditions. The number of triggers present in the final BATSE burst catalog is more than 2700 but this number can be increased if the non triggered bursts are included (Kommers et al., 2001): the scanning of the continuous data accumulated by the instruments revealed 873 non–triggered GRBs which increase of 48% the BATSE sample, and 50 low energy bursts (25–50 keV) (possibly the equivalent of the population of X Ray Flashes discovered in the SAX data (Kippen et al., 2001).

Data Products After the failure of the onboard page recorder the BATSE daily data products were stored and transmitted every orbit to the Marshall Space Flight Center (MSFC). These data are grouped in 3 classes:

- *Burst Data*: contains the data relative to any trigger generated by a Gamma Ray Burst, solar flare or any other transient event satisfying the trigger condition.
- *Scheduled Data*: pulsar observations. It was performed if no trigger occurred during the observation, because the burst accumulation mode has the highest priority.
- *Background Data*: consist of continuously collected discriminator rates and medium resolution spectra of the background.

The **burst data** are used for temporal and spectral analysis of GRBs:

- **DISCSC** *Discriminator Science Data* - count rates, on 64 ms timescale, binned in 4 broad energy channels, summed from the LADs that were triggered by the GRB. These data cover the entire burst duration with a maximum time delay, with respect to the trigger time, of 64 ms. The energy ranges are approximately: ch1=25–50 keV, ch2=50–110 keV, ch3=110–320 keV and ch4>320 keV.
- **PREB** - *Pre-Burst data* - the eight LADs store continuously their data (4 energy channels, with 64 ms resolution) in a cyclic ring buffer. When a burst trigger occurs the buffer is read out and the data stored as PREB starting 2.048 s before the burst.
- **DISCLB** - *Discriminator Data* - these are collected to compensate the possible data gaps in DISCSC or DISCLA These data have 2.048 s time resolution for 16.384 s before the burst trigger, and 1.024 s time resolution for 49.154 s after the trigger time.
- **TTE** - *Time Tagged Events* - are obtained assigning to each photon event (for a total of 32768) the time of detection, the energy channel and the detector number. Combining this information the light curve in counts/sec with a time resolution of 2 ms in the usual 4 energy bands can be obtained. These data can be used

to perform temporal and time resolved spectral analysis with a very high time resolution but are limited to short bursts, due to the maximum number of events they can detect. In fact, one fourth of the total memory capacity is filled with the signal from all the eight LADs, for a variable time prior the burst trigger, and in the remaining three fourth are stored the counts, during the trigger, until the buffer is full.

- **STTE** - *Spectroscopy Time Tagged Event* - these are equivalent to the TTE data, but refer to the Spectroscopic Detectors (SDs) and have a higher spectral resolution (256 channels). They have a maximum memory capacity of 16384 counts and a limited time resolution of $128ms$. These data can be used jointly with SHERB to accumulate the spectra on a portion of the burst (typically the rise phase) with a user-defined time integration scheme.

- **TTS** - *Time To Spill* - These data are used to set the times for the accumulation of a certain number of events from a LAD discriminator. Their temporal resolution is variable, also within the same data set, and they have 4 broad energy channels.

- **MER** - *Medium Energy Resolution* - 4096 spectra from the LADs (summed over the triggered detectors), accumulated in 16 energy channels with a time resolution of 16 ms, for the first 2048 spectra, and 64 ms for the remaining ones.

- **HERB** - *High Energy Resolution Burst* - burst data from the LADs, on 128 energy channels, with an accumulation time that is rate dependent (so that brighter bursts have higher time resolution than faint ones). The maximum time resolution is 64 ms. The data are gathered from the four most illuminated detectors.

- **SHERB** - *Spectroscopic High Energy Resolution Burst* - The same of HERB but these are collected form the SDs and consists of 256 channels energy spectra with maximum time resolution of 128 ms for a maximum of 192 spectra.

These data are first quickly analyzed by the BATSE mission team, and then stored in *Individual Burst Data Base* (IBDB). For the temporal and spectral analysis they are converted into FITS format.

Burst Data Files

The data files used for the spectral evolution analysis of GRBs can be downloaded from the Goddard Space Flight Center (GSFC) ftp site[4] ; each trigger directory contains all the relevant data and calibration files for spectral and temporal analysis.

The burst location algorithm sometimes did not produce the best location at first run: there are cases for which the position determination has been refined during extensive data processing and the correct position for all the bursts are now available. The use of a precise position measure is required by the data reduction procedure because of

---

[4] ftp://cossc.gsfc.nasa.gov/compton/data/batse/trigger

the dependence of the detector response matrix on the angle of incidence of the photons with respect to the detector normal (Pendleton et al., 1995; Preece et al., 1996; Band et al., 1992).

The triggered events are classified according to the event type: Gamma Ray Bursts, Solar Flare, Soft Gamma Ray Repeater (SGR), Terrestrial Gamma Flash (TGF).

1.3 The *XMM–Newton* Observatory

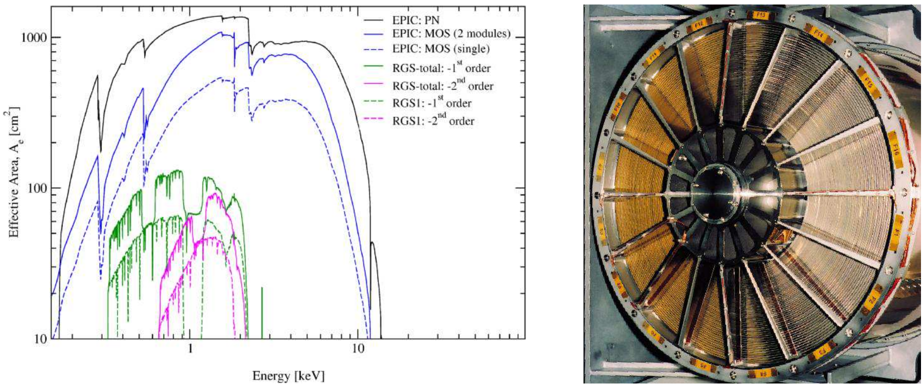

Figure 1.7 *Left panel: XMM–Newton* effective area. The relevant one for our work is the PN (black line). *Right panel:* the 58 nested mirror module of XMM. The pictures are taken from the mission website.

The 4 tons, 10 m long *XMM–Newton* spacecraft (namely X-ray Multi Mirror, Jansen 1999) is the largest scientific satellite ever launched by the European Space Agency. Its modular configuration[5] consists of the following four elements:

- The Focal Plane Assembly, consisting of the Focal Plane Platform carrying the focal-plane instruments: two Reflection Grating Spectrometer (RGS) readout cameras, an EPIC PN and two EPIC MOS imaging detectors, and the data handling and power distribution units for the cameras. The EPIC and RGS instruments are fitted with radiators, which cool the CCD detectors via cold fingers.

- The Telescope Tube (a long carbon fibre tube), maintaining the relative position between the focal plane assembly and the mirror support platform. Due to its length of 6.80 m, the Telescope Tube is physically composed of two halves: the upper and lower tubes.

- The Mirror Support Platform, consisting of the platform itself and carrying the three mirrors assemblies (Mirror Modules + entrance and exit baffles + doors + two RGS grating boxes), the Optical Monitor (OM) and the two star-trackers.

---

[5] http://xmm.esac.esa.int/external/xmm_user_support/documentation/technical/Spacecraft/index.shtml

- The Service Module, which carries the spacecraft subsystems and associated units providing the necessary resources to the satellite. Also attached to the SVM are the two solar-array wings, the Telescope Sun Shield and the two antennas.

As far as the X-ray optics are concerned, we refer the reader to Jansen et al. (2001) for a more detailed description.

Table 1.4 *XMM–Newton* instrument properties.

Property	Description
Telescope	Wolter 1
Focal Length	7.5 m
Effective Area	$\sim 1500\,\mathrm{cm}^2$ @ 2 keV
Telescope PSF	6 arcsec FWHM
Detector (PN)	12× pn-CCD, 200x64 pixels
Detector Operation	Imaging, and Photon-counting
Pixel Scale	4.1 arcsec/pixel
Energy Range	0.1 - 10 keV
Sensitivity	see fig.1.8

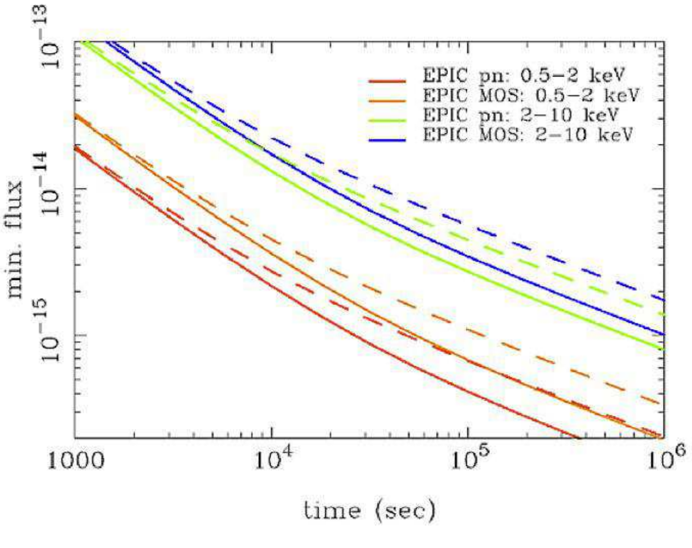

Figure 1.8 EPIC sensitivity (5σ minimum detectable flux in cgs units in respective bands) as a function of exposure time. Sensitivity is computed for an assumed power-law spectrum with photon index 1.7. Solid curves are for the nominal background rates. Dashed curves are for background levels enhanced by a factor 3.

The design of the optics was driven by the requirement of obtaining the highest possible effective area over a wide range of energies, with particular emphasis in the region around 7 keV. Thus, the mirror system (realized nesting 58 mirror shells) had to utilize a very shallow grazing angle of 30' in order to provide sufficient reflectivity at high energies (see fig. 1.7). The telescopes focal length is 7.5 meters and the diameter of the largest mirrors is 70 cm, to be compatible with the shroud of the launcher. XMM mirrors are most efficient in the energy range from 0.1 to 10 keV, with a maximum around 1.5 keV and a pronounced edge near 2 keV (the Au M edge). The design goal was to achieve a collecting area of 1900 cm^2 for energies up to 150 eV, 1500 cm^2 at 2 keV, 900 cm^2 at 7 keV, and 350 cm^2 at 10 keV, for each of the telescopes. We summarize the satellite properties in table 1.4.

Chapter 2

Precursor emission in GRBs

Gamma-ray Bursts display a huge variety of properties in both phases which seem to describe their evolution. In the first phase known as “prompt emission”, the variability time scales vary on six orders of magnitude, the spectra can still be described with ad hoc empirical models rather then physical ones, and spectral-energy correlations complicate the puzzle even further. In the second phase known as “afterglow emission” the situation seems simpler just at first sight. In fact, even if the emission mechanism is more securely associated to synchrotron emission, the temporal profiles once thought to be a simple smooth decay have recently shown multiple breaks and rebrightenings, which testify the complexity of GRBs also at late times.

In this chapter we will focus on the properties of the prompt emission, which are described in the following section, in order to discuss our contribution to the phenomenon known as “precursor emission”. We will argue that this is nothing different than a part of the whole first phase. We won’t ever deal with afterglow emission because it goes beyond the goals of this thesis. Nonetheless we chose to leave some discussion open on afterglows in the last section of the chapter, where some of the open issues are summarized.

2.1 Global properties of the prompt emission

Spectrum Gamma ray bursts are characterized by non-thermal emission in the few hundred keV range. X-ray emission is weak (in “standard” GRBs) as only a few percent of the energy is emitted below 10 keV. On the other hand, most bursts have a high energy tail which contains a significant amount of energy. GRB 940217, for example, had a high energy tail up to 18 GeV (Hurley et al., 1994). In fact EGRET and COMPTEL observations are consistent with the possibility that all bursts have high energy tail. The *Fermi*–LAT instrument has started to scratch the surface of this topic, showing that only a small fraction of GRBs show emission in the GeV range. Currently there are less than 4% of GBM bursts, that show a significant emission in the LAT, and it is not clear whether these handful of photons are of internal, rather then external origin (for a discussion see Ghisellini et al., 2010b). The delayed onset of the GeV emission, together

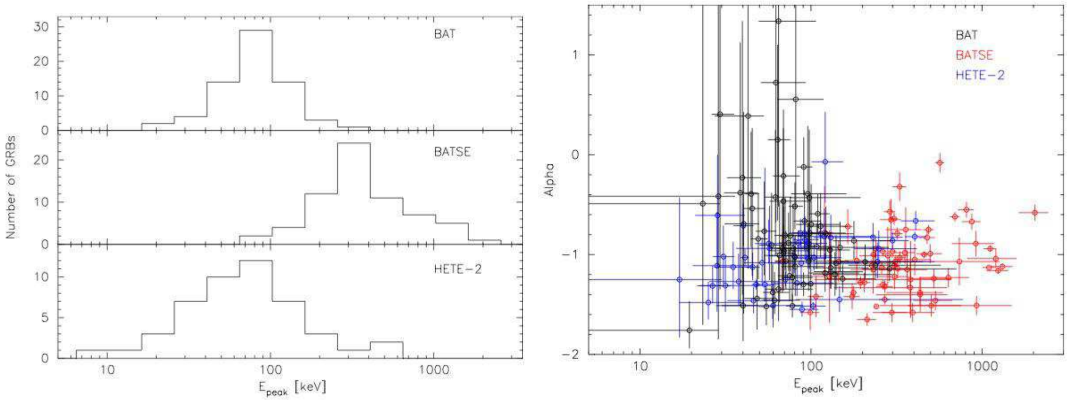

Figure 2.1 *Left:* distribution of $E_{\rm peak}$ for the *Swift*-BAT, *Hete-II*, and BATSE samples. The fit has been done with a cut-off power law model. *Right:* distribution of the low energy photon index and the observed $E_{\rm peak}$ assuming a CPL model. Pictures taken from Sakamoto et al. (2011).

with the temporal profile of the decay, seem to point into the direction of afterglows in the radiative regime, but some exceptions due to variability issues still exist (Abdo et al., 2009).

The time-integrated prompt emission is typically fitted by a Band model (Band et al., 1993), which is a smooth combination of two power laws. The smooth transition takes place at an energy $\tilde{E} = (\alpha - \beta)E_0$. The fitting formula, developed for the photon number spectrum $N(\nu)$ is defined through:

$$N(\nu) = N_0 \begin{cases} (h\nu)^{\alpha} \; e^{-\frac{h\nu}{E_0}} & h\nu < (\alpha-\beta)E_0 \\ e^{\beta-\alpha}[(\alpha-\beta)E_0]^{\alpha-\beta}(h\nu)^{\beta} & h\nu > (\alpha-\beta)E_0 \end{cases} \tag{2.1}$$

where α and β represent the spectral indices at low and high energies, respectively. There is no particular theoretical model that predicts this spectral shape. Still, this function provides an excellent fit to most of the observed spectra. For most observed values of α and β, $\nu F_\nu \propto \nu^2 N(\nu)$ peaks at $E_{\rm peak} = (\alpha+2)E_0 = [(\alpha+2)/(\alpha-\beta)]\tilde{E}$ (Piran, 2004). Typical values found in the observed spectra are $\alpha \approx -1$, $\beta \approx -2.3$ and $E_0 \approx 250\ keV$. The "typical" energy of the observed radiation is $E_{\rm peak}$. Fig. 2.1 (left) shows the comparison between the typical $E_{\rm peak}$ as observed by different satellites, derived by using the same fitting function. The different position of the peak of the distributions reflect the different detector responses.

Short events are on average harder than long bursts. "X-Ray Rich GRBs" and "X-Ray Flashes" (XRFs i.e. long duration GRBs with a soft spectrum) have been widely discussed as forming an apparently new type of transient events with respect to conventional GRBs. Since the discovery of XRF several suggestions for their interpretation have been done. They can be roughly divided into two categories: XRF differ from GRBs extrinsically (different distances or viewing angles) or intrinsically (different physical parameters, different radiation mechanisms, or even different progenitors and central engines). Fig. 2.1 (right) shows the typical peak energy, assuming a cut-off power law model, as observed by the three different instruments.

The low energy cut off in the distributions shown in Fig. 2.1 is probably real as softer bursts would have been detected by past detectors. On the other hand, before the launch of *Fermi* it was unclear whether the paucity of harder burst was real or it is an instrumental effect due to the sensitivity range of the detectors. This is also due to the fact that it is intrinsically more difficult to detect a harder burst since the number of emitted photons is lower, for equal total energy. In fact, there is a growing consensus that the high energy drop-off of the $E_{\rm peak}^{\rm obs}$ distribution is physical, since the GBM instrument would have otherwise detected those bursts (Gruber et al., 2011a).

Spectral-energy correlations It has always been clear that some form of evolution between $E_{\rm peak}$ and other quantities (flux, fluence, energy, luminosity) existed, in most cases it was quoted harder at the beginning of the burst (with typical $\sim$MeV photon energy) and softer (tens of keV) at the end of the burst. Other cases showed less clear behaviors than this simple hard-to-soft trend, some clearly showed quantities "tracking" each other, other seemed to be not correlated. As time passed by it became clear that the best comparisons have to take into account selection effects, both spectral and instrumental.

It is now widely accepted that the prompt emission spectral properties of GRBs with measured redshifts are highly correlated. In particular there exists a positive correlation between the characteristic spectral peak energy (of the νF_ν spectrum) and the isotropic equivalent energy of the prompt phase (Amati et al., 2002). However, both on the observational (Frail et al., 2001) and theoretical (Rhoads, 1997) ground, there are evidences that GRBs are all but isotropic sources. The correct proxy of the GRB energetics should, therefore, account for the collimated nature of these sources. Indeed, by estimating the GRB opening angle from the measurements of the jet break observed in the late optical light curves, the dispersion of the isotropic energy is reduced and a stronger/tighter correlation between the peak energy and the true GRB energy is found (Ghirlanda et al., 2004, 2007). Several other correlations have been found between spectral and temporal properties of the prompt emission (Reichart and Stephens, 2000; Norris et al., 2000; Liang et al., 2004; Yonetoku et al., 2004; Firmani et al., 2006). Through these correlation it has been hoped that GRB energetics could be standardized to constrain the cosmological parameters (e.g Ghirlanda et al., 2006).

Recently it has been shown that the spectral-energy correlations hold in the time-resolved analysis of single bursts down to the lowest resolution available for long (Ghirlanda et al., 2010) and short GRBs (Ghirlanda et al., 2011a), and that these are consistent with the time integrated ones. This strongly favors a physical interpretation of the correlations, and is even more challenging if seen in the scenario of GRBs as "thermostats", when the *comoving* properties are analyzed (Ghirlanda et al., 2011b).

Temporal properties: duration A "typical" GRB lasts for about 20 s. However, observed durations vary by six orders of magnitude, from few milliseconds to thousands of seconds. A non-negligible fraction of GRB (10-20%) is preceded or followed by emission with a lower flux and separated by the main emission episode by quiescent intervals which can last hundreds of seconds. The definition of duration is not unique. This is due to the fact that the start and end time of a burst strongly depend on its flux and on the value of the background. Burst duration is usually characterized through the T_{90} (T_{50}) quantity, i.e. the time needed to accumulate from 5% to 95% (from 25% to 75%) of the counts in the energy band of the instrument which is being used.

The distribution of bursts is roughly bimodal. Burst T_{90} durations can be divided into two sub-groups: long bursts with $T_{90} > 2$ s and short bursts with $T_{90} < 2$ s (Meegan et al., 1996). The short bursts are $\sim 25\%$ of the total. This does not necessarily mean that there are fewer short bursts, as there can be a selection effect of the instruments. For instance BATSE, having an harder trigger than BAT, privileged short bursts with respect to BAT (short bursts tend to be harder than long-soft ones). In fact BAT detected proportionally more long burst than BATSE. The GBM (on board the *Fermi* satellite) didn't change dramatically the picture of population studies, so far. The GRB and BATSE long burst were shown (Nava et al., 2011) to have similar distributions of fluence, and peak flux but GBM bursts have a slightly harder lowenergy spectral index with respect to BATSE GRBs. The short bursts have similar distributions of fluence, spectral index and peak flux, with GBM bursts having slightly larger $E^{\rm obs}_{\rm peak}$.

Temporal properties: lightcurves and variability The bursts have complicated and irregular time profiles which vary drastically from one burst to another. In most bursts, the typical variation takes place on a time-scale δT significantly smaller than the total duration of the burst, T. In a minority of the bursts there is only one peak with no substructure: in this case $\delta T \sim T$. A sub-class of this type of GRBs are the so called "FRED" bursts with a fast rise and exponential decay. Nonetheless, if the variability time-scales would be of the order of a few gravitational radii ($R_g = GM_{BH}/c^2$, the unit in which distances close to the black hole can be measured) crossing times, with the current instruments we would not yet be able to decompose a broad pulse into its inner components.

The smallest timescale of variation is usually in the millisecond range (both in count and flux light curves) (see e.g. Bhat et al., 1992; Ghirlanda et al., 2011a) and does not vary from the beginning to the end of the burst (Fenimore, 1999). This latter observations have been historically deemed to imply that the γ-ray radiation cannot come from shocks occurring at distances of $\sim 10^{16}$ cm from the engine. Indeed in this case the slowing of the fireball should produce pulses lasting longer than the first ones. Moreover, in this case the later the spike the broader should be all other time-scales, e.g. quiescence. Such correlation have not been observed and thus variability is thought to be due to internal shocks occurring at much smaller distances $\sim 10^{13}$ cm. A detailed description of internal shocks will be presented in the following pages.

2.2 The standard scenario

2.2.1 The compactness problem

The key to unveil γ-ray burst physics lies in the understanding of how they bypass the compactness problem. This problem was realized very early on, in one form by Rudermann (1975) and in another way by Schmidt (1978). Both used it to argue that GRBs could not originate from cosmological distances. Now, we understand that GRB are cosmological and special relativistic effects enable us to overcome this constraint.

The simplest way to the compactness problem is to estimate the average opacity of the high energy gamma–rays to pair production. Consider a typical burst with an observed fluence f. For a source emitting isotropically at a distance D this fluence corresponds to a total energy release of:

$$E = 4\pi D^2 f \approx 10^{50} \left(\frac{D}{3000\ \mathrm{Mpc}}\right)^2 \left(\frac{f}{10^{-7}\ \mathrm{ergcm}^{-2}}\right) \mathrm{erg} \tag{2.2}$$

Cosmological effects change this equality by numerical factors of order unity that are not important in this discussion. The rapid temporal variability on a time scale $\delta t \approx 10$ ms implies that the source is compact with a size $R < c\delta t \approx 3000$ km. The observed spectrum contains a large fraction of high energy γ-ray photons. These photons (with energy E_1) could interact with lower energy photons (with energy E_2) and produce electron-positron pairs via $\gamma\gamma \to e^+e^-$ if $\sqrt{E_1 E_2} > m_e c^2$ (up to an angular factor). We denote by g_p the fraction of photon pairs that satisfy this condition. The average optical depth for this process is:

$$\tau_{\gamma\gamma} = g_p \frac{\sigma_T f D^2}{R^2 m_e c^2} \tag{2.3}$$

or:

$$\tau_{\gamma\gamma} = 10^{13}\ g_p \left(\frac{D}{3000\ \mathrm{Mpc}}\right)^2 \left(\frac{f}{10^{-7}\ \mathrm{ergcm}^{-2}}\right) \left(\frac{\delta t}{10\ \mathrm{ms}}\right)^{-2} \tag{2.4}$$

where σ_T is the Thomson cross section. This optical depth is huge. Even if there are no pairs at the very beginning, they will form rapidly and then these pairs will Compton scatter lower energy photons, resulting in a huge optical depth for all photons. However, the observed non-thermal spectrum indicates with certainty that the sources must be optically thin.

The compactness problem is a consequence of the assumption that the size of a source emitting radiation cannot be larger than the smallest observed time scale of variability times the light speed (*causality* constraint). This equation holds only if the emitting source and the observer are at rest with respect to each other.

Relativistic motion The constraint on the compactness for pair production of GRBs comes from the measurement of (i) the variability time-scale and (ii) the energy of photons. However, both these quantities are modified if the source and the observer are not at rest. Consider a source of radiation that is moving towards an observer with relativistic velocity characterized by a Lorentz factor $\Gamma = 1/\sqrt{1 - v^2/c^2}) \gg 1$. Photons with an observed energy $h\nu_{obs}$ have been blue-shifted and their energy at the source was $\approx h\nu_{obs}/\Gamma$. Since the energy at the source is lower, fewer photons have sufficient energy to produce pairs. Now the observed fraction g_p of photons that could produce pairs is not equal to the fraction of photons that could produce pairs at the source. The latter is smaller by a factor $\sim \Gamma^{2\alpha}$ (where α is the spectral index) than the observed fraction. At the same time, relativistic effects allow the radius from which the radiation is emitted, $R < \Gamma^2 c\delta T$ to be larger than the original estimate, $R < c\delta T$, by a factor of Γ^2. We have then:

$$\tau_{\gamma\gamma} = \frac{g_p}{\Gamma^{2\alpha}} \frac{\sigma_T f D^2}{R^2 m_e c^2}$$

or:

$$\tau_{\gamma\gamma} = 10^{13} \frac{g_p}{\Gamma^{4+2\alpha}} \left(\frac{D}{3000 \text{ Mpc}}\right)^2 \left(\frac{f}{10^{-7} \text{ ergcm}^{-2}}\right) \left(\frac{\delta t}{10 \text{ ms}}\right)^{-2}$$

where the relativistic limit on R was included in the second line. The compactness problem can be resolved if the source is moving relativistically towards us with a Lorentz factor $\Gamma > 10^{13/4+2\alpha} \approx 10^2$. Such extreme relativistic motion is larger than the relativistic motion observed in any other celestial source. Extragalactic super-luminal jets have, for instance, Lorentz factors of $\Gamma \sim 10$, while the known galactic relativistic jets have $\Gamma \sim 2$ or less.

Two possible scenarios can be drawn: (1) a relativistic motion in the dynamical context of fireballs (see next session) and (2) a kinematic solution in which the source moves relativistically and this motion is not necessarily related to the mechanism that produces the burst, i.e. the source as a whole moves toward the observer. However, the latter solution is energetically more demanding since for a solar mass progenitor, moving at $\Gamma = 100$ the total energy required would be $E = \Gamma M_\odot c^2 \sim 2 \times 10^{56}$ erg. Moreover, in the first solution the kinetic energy is comparable to the observed energy of the GRBs: in this case the γ-ray emission and the relativistic motion are related and are not two separate phenomena. This is the case if GRBs result from the slowing down of ultra-relativistic matter. This idea was suggested by Meszaros and Rees (1992,1993) in the context of slowing down of the fireball by material of the ISM.

2.2.2 Fireballs

The evolution of a homogeneous fireball can be understood by analogy with the early universe. Consider the rapid release of a huge amount of energy in a small volume. If the temperature is high enough, photons are highly energetic and pairs are formed. The opacity is large, and radiation cannot escape. The initial temperature, at equilibrium is $T_0 = (L/4\pi r_0^2 \sigma)^{1/4} \sim 10^{10}\ L_{51}^{1/4} r_{0,7}^{-1/2}$ °K, where r_0 is the initial length scale, i.e. some Schwarzschild radii[1].

---

[1] Hereafter the convention $Q = 10^n Q_n$ is adopted.

Pure fireball This huge energy content forms a sphere of hot plasma (photons and pairs), i.e. the fireball, which expands and accelerates under its own internal energy pressure, reaching relativistic speed ($\Gamma \gg 1$). If the expansion is adiabatic (i.e. no heat is transferred during the process, so that the internal energy E of the fireball remains constant), the comoving temperature T' and the volume V satisfy $T'V^{1/3} =$ const. Moreover, conservation of energy (as viewed from the observer's frame) requires $E \propto \Gamma T' =$ const (photons are blueshifted), and by simple algebra we get:

$$\Gamma \propto V^{-1/3} \propto R, \tag{2.5}$$

$$T' \propto \Gamma^{-1} \propto R^{-1}. \tag{2.6}$$

The bigger the expansion, the lower the temperature. When T' reaches 20 keV pairs annihilate and are not replaced by newly created ones[2]. As the scattering optical depth τ scales with the inverse of the distance R, i.e. $\tau \propto R^{-1}$ the opacity, which scales linearly with the optical depth, drops consequently:

$$\tau \propto T', \tag{2.7}$$

and the energy is released in thermal photons. The resulting thermal spectrum has $k_b T \approx 1/3 \times \Gamma T_p$. Note that the observed temperature is approximately equal to the initial temperature.

In this case, the "pure fireball" evaporates, a strong single thermal signal is expected, but **no** afterglow can be produced.

"Dirty" fireball The situation is somewhat different if in addition to e^+e^- pairs, the fireball includes also some baryons (either injected with the original radiation, or present in the atmosphere surrounding the initial explosion, or both). This "baryonic loading" can influence the fireball evolution in two ways. First, when the fireball is baryon-loaded the energy distribution among matter and radiation is different. In the radiation-dominated regime, the Lorentz factor, matter density, radiation density, and their ratio scale as:

$$\Gamma \propto R, \quad \rho_{mat} \propto R^{-3}, \quad \rho_{rad} \propto R^{-4}, \quad \rho_{mat}/\rho_{rad} \propto R$$

If, at the point where $T' = T_p \approx 20$ keV, $\rho_{mat} > \rho_{rad}$ (the transition from the radiation dominated phase to the matter dominated one occurs at $\rho_{mat} = 4\rho_{rad}/3$), then a considerable fraction of the energy is not released through photons: it remains to the protons. The baryons are accelerated with the rest of the fireball and convert part of the radiation energy into bulk kinetic energy. The relativistic shell expands with constant thickness (in the observer's frame) $\Delta R \sim R_{in}$ equal to the initial radius of the fireball

---

[2] If radiation had a step distribution, the boundary between pair creation and annihilation would be $T_p = m_e c^2 = 511$ keV. However assuming a Planck distribution, the photons of the high energy tail can produce pairs also for lower temperatures.

R_{in}. In the observer frame the shell appears contracted (with respect to the comoving frame) due to its high Lorentz factor.

The radiation-dominated regime extends out to a radius where the asymptotic value of the Lorentz factor of the shell reaches, in the matter-dominated regime, the value:

$$\Gamma_{coast} = (4\rho_{rad,0}/3\rho_{mat,0} + 1)\Gamma_0, \tag{2.8}$$

where we label with the subscript 0 the radiation density and the matter density at the time the shell first becomes ultra-relativistic. The acceleration ends and the fireball enters the "coasting" phase. In this regime the dependencies become:

$$\Gamma \rightarrow \text{const}, \quad \rho_{mat} \propto R^{-2}, \quad \rho_{rad} \propto R^{-8/3}$$

At this stage, usually the fireball is still opaque to Thomson scattering and the shell must expand before producing the spectrum that is subsequently observed. The coasting radius is:

$$R_c = \Gamma R_{in} \simeq 10^{11}\ \Gamma_2 R_{in,9}\ \text{cm}. \tag{2.9}$$

Secondly, the electrons associated with this matter increase the opacity, delaying the escape of radiation. Initially, when the local temperature T' is large, the opacity τ_p is dominated by e^+e^- pairs. This opacity τ_p, decreases *exponentially* with decreasing temperature, and falls to unity when $T' = T_p \approx 20$ keV. On the other hand, the opacity due to matter, τ_b, decreases as R^{-2}, where R is the radius of the fireball. If at the radius where $\tau_p = 1$, τ_b is still > 1, then the final transition to $\tau = 1$ is delayed and occurs at a lower temperature, and a bigger radius. Independently on the considerations of the above paragraph, at some point the fireball becomes optically thin. The transparency radius is obtained by setting the Thomson scattering optical depth equal to unity:

$$R_\tau = \left(\frac{M\sigma_T}{4\pi m_p}\right)^{1/2} \simeq 2.4 \times 10^{13}\ E_{51}^{1/2}\Gamma_2^{-1/2}\ \text{cm}, \tag{2.10}$$

where m_p is the proton mass, σ_T is Thomson cross section, and M is the mass transported by the fireball. $M = E/(\eta c^2) \sim 10^{-5} E_{52}\eta_2^{-1} M_\odot$ (η is a factor of proportionality of the initial energy to mass ratio). This transition radius has a crucial role in the fireball evolution.

2.2.3 Shocks

We discussed that the observational evidences result in a need to require the source to be expanding at ultra-relativistic velocity. We showed the general properties of the resulting fireball, either in the case of a "pure fireball" made of radiation and leptons, or in the more realistic case of a "dirty fireball" that carries an amount of baryons. In the following we review the mechanism which transforms the kinetic energy of the baryons, which have been accelerated by the internal pressure of the fireball, into radiation. This shock mechanism has become the most convincing way to fulfill the observational requirements, both for the prompt phase and the afterglow phase. In Fig. 2.2 there is a graphical representation of the different phases of expansion of a fireball, from the energy release in a compact region, through shocks, as far as the interaction with the ISM.

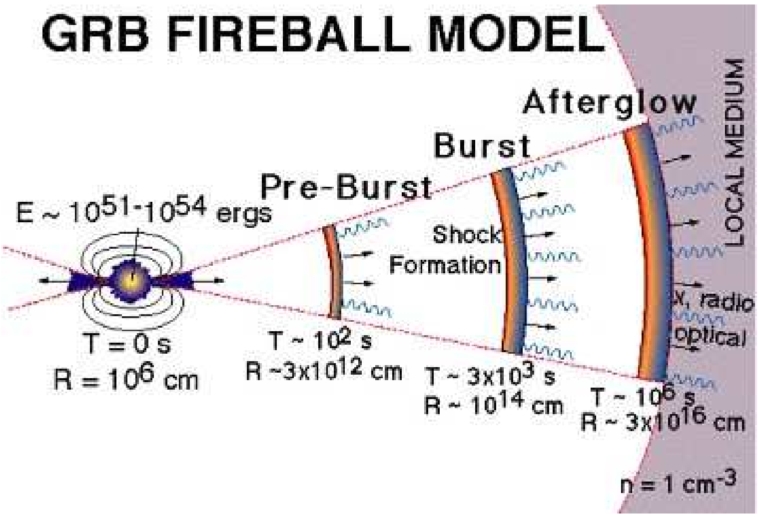

Figure 2.2 Graphic representation of the fireball relativistic expansion. Typical time-scales and radii are also shown. Picture taken from the *Swift* website http://www.swift.ac.uk/grb.shtml

Internal shocks The prompt phase can be explained through the *internal shock* mechanism. Imagine shells emitted by the central engine at different velocities and thus expanding at different velocities. At some radii the shells will catch up.

To describe the dynamics of this collision we should imagine a source expelling shells of mass m with a bulk Lorentz factor γ, followed by a second shell with mass M, expanding in the same direction with a different Lorentz factor Γ.

Assume that $\Gamma > \gamma$: the two shells will eventually catch up and mix in a single shell with mass $M + m$, expanding at a velocity given by the final Lorentz factor Γ_F. Consider that only a fraction of the initial energy is transformed into kinetic energy. We define ε' the energy release in the rest frame of the expanding material.

By applying the laws of conservation of momentum and energy we get to a system of two equations with two unknowns. By some algebra it is possible to retrieve Γ_F and ε'.

$$\begin{cases} M\Gamma + m\gamma = \Gamma_F[M + m + \frac{\varepsilon'}{c^2}] \\ \\ M\sqrt{\Gamma_F^2 - 1} + m\sqrt{\gamma^2 - 1} = [M + m + \frac{\varepsilon'}{c^2}]\sqrt{\Gamma_F^2 - 1}. \end{cases} \tag{2.11}$$

from the first equation in 2.11 we can derive an explicit expression for the energy release

ε' as a function of known parameters and of Γ_F.

$$\frac{\varepsilon'}{c^2}\Gamma_F = M\Gamma + m\gamma - m\Gamma_F - M\Gamma_F \tag{2.12}$$

The energy released in the observer frame is the following:

$$\varepsilon^p = \varepsilon'\Gamma_F = Mc^2(\Gamma - \Gamma_F) + mc^2(\gamma - \Gamma_F) \tag{2.13}$$

We now explicit Γ_F as a function of the known variables. We divide the second equation of 2.11 by the first one:

$$\frac{M\sqrt{\Gamma^2 - 1} + m\sqrt{\gamma^2 - 1}}{M\Gamma + m\gamma} = \frac{\sqrt{\Gamma_F^2 - 1}}{\Gamma_F} \tag{2.14}$$

which, squared gives the following:

$$\begin{gathered} \frac{M^2(\Gamma^2-1)+m^2(\gamma^2-1)+2mM\sqrt{(\Gamma^2-1)(\gamma^2-1)}}{(M\Gamma+m\gamma)^2} = \frac{\Gamma_F^2-1}{\Gamma_F^2} \\ \frac{1}{\Gamma_F^2} = \frac{M^2\Gamma^2+m^2\gamma^2+2mM\Gamma\gamma-M^2\Gamma^2+M^2-m^2\gamma^2+m^2-2mM\sqrt{(\gamma^2-1)(\Gamma^2-1)}}{(M\Gamma+m\gamma)^2} \end{gathered} \tag{2.15}$$

By simple algebra, from the second equation above we get:

$$\frac{1}{\Gamma_F^2} = \frac{m^2 + M^2 + 2Mm\Gamma\gamma - 2mM\sqrt{(\gamma^2 - 1)(\Gamma^2 - 1)}}{(M\Gamma + m\gamma)^2} \tag{2.16}$$

and eventually:

$$\Gamma_F = \frac{(M\Gamma + m\gamma)}{\sqrt{m^2 + M^2 + 2Mm\Gamma\gamma - 2mM\sqrt{(\gamma^2 - 1)(\Gamma^2 - 1)}}} \tag{2.17}$$

The assumption $\Gamma > \gamma \gg 1$ reads a simplification of the square root:

$$\Gamma_F \approx \frac{M\Gamma + m\gamma}{\sqrt{M^2 + m^2}} \tag{2.18}$$

$$\varepsilon^p = \varepsilon'\Gamma_F = Mc^2(\Gamma - \Gamma_F) + mc^2(\gamma - \Gamma_F) \tag{2.19}$$

These two equations can be found in a different form in literature. Consider for instance the β parameter instead of Γ where

$$\Gamma = \frac{1}{\sqrt{1 - \beta^2}}$$

By re-writing the former equations we get:

$$\beta_f = \frac{m\gamma\beta_1 + M\Gamma\beta_2}{m\gamma + m\Gamma} \tag{2.20}$$

By defining the two new parameters:

$$\alpha_\Gamma \equiv \frac{\Gamma}{\gamma}; \qquad \alpha_m \equiv \frac{M}{m} \tag{2.21}$$

and using them in equation 2.20 we get (see Lazzati et al., 1999):

$$\beta_f = \frac{\beta_1 + \alpha_m \alpha_\Gamma \beta_2}{1 + \alpha_m \alpha_\Gamma} \tag{2.22}$$

The emission mechanism during the prompt phase is still debated. According to the standard model there are a number of ultrarelativistic particles moving in intense magnetic fields. The emission is thought to be due to synchrotron emission. Open issues remain, as (i) the low efficiency cannot account properly for the observed radiation, or (ii) the spectral shape during the prompt phase. In the past ten years plenty of new ideas have been proposed, e.g. quasi-thermal comptonization (Ghisellini and Celotti, 1999) or Compton drag (Lazzati et al., 2000).

One of the open problems inside the standard model is that, even if the internal-shock model properly accounts for the light curves of the prompt phase of GRBs, it is not enough efficient to account for the observed luminosity. In the collision between two shells the energy released in photons cannot be much higher than 5-10% of the kinetic energy. The available kinetic energy is the relative energy between the two colliding shells, so the greater the relative velocity, the greater the available energy.

Suppose that the two shells had Lorenz factors $\Gamma \sim 2\gamma$, and the second one was emitted with a time delay $\Delta T \sim R_0/c$. They will collide at a radius (the *internal shock radius*):

$$R_I = 2\frac{\alpha_\Gamma^2}{\alpha_\Gamma^2 - 1}\gamma^2 c\Delta T = 2.6 \times 10^{13}\ \Gamma_2^2 R_{0,9}\ \text{cm} \tag{2.23}$$

where $\alpha_\Gamma = \Gamma/\gamma = 2$ has been used to derive the numerical estimate. Note that, for typical values, the internal shock radius is larger than the transparency radius given by eq. 2.10, i.e. the shell is already Thomson thin.

2.3 Models for precursor emission

Many GRBs show a multiepisodic emission behavior, i.e. emission preceding or following the main event. In the literature this property, observed in 10-20% of the bursts, has been often referred as “precursor” or “postcursor” emission. The definition of “precursor” is somewhat subjective, as the same pulse may be identified as part of the main emission or not according to the criterion used to define what a pulse is. Similar issues characterize the definition of “postcursors”. The easiest definition might refer to precursor as something that comes before the main emission episode. In turn, the main emission being identified as the pulse(s) with the largest flux. Adopting the same, “loose” definition, a postcursor is some flux which follows the main event.

One common feature of the definition of precursors and postcursors is the fact that they should be separated from what is considered the main GRB episode, even if also

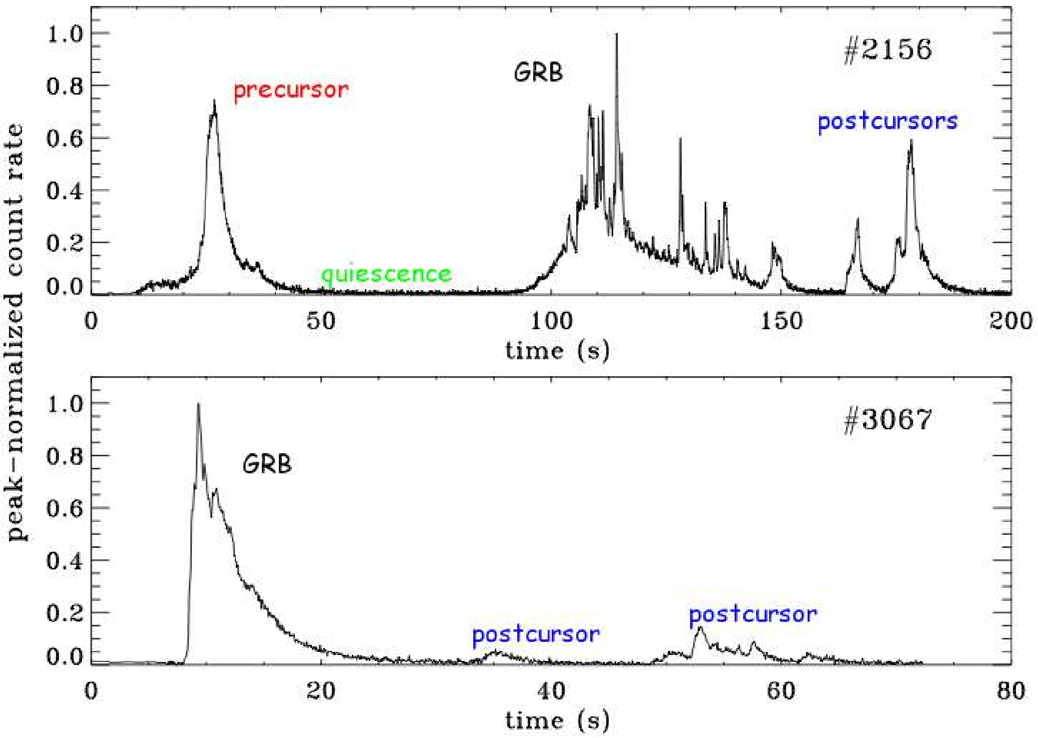

Figure 2.3 Light curves of two γ-ray bursts observed by BATSE (at energies > 20 keV) that contain periods of emission and quiescence. *Top:* GRB 930201 show a "precursor" and a complex light curve after $\sim$ 50 s of quiescence. *Bottom:* GRB 940708 light curve shows a main event followed by two "postcursors". Time is in the observer reference frame.

the definition of separation (i.e. quiescence) is somewhat arbitrary. In any case, in both cases of precursors and postcursors a quiescent phase (no emission above background) is present in the GRB light curve. Fig. 2.3 show two examples of bursts showing precursors and postcursors. We highlighted what we might call "precursor", "postcursor", and quiescence in red, blue, and green, respectively.

The interpretation of the quiescent phase is all but trivial, and several theoretical models have been proposed. None the less, there are at least two fundamental observational constraints (see e.g. Koshut et al., 1995; Lazzati, 2005; Burlon et al., 2008), that all the model have to account for:

- the duration of "precursors" and "postcursors" has to be of the same order of the duration of the main GRB,
- the quiescent phase can last from seconds to hundreds of seconds (in a few cases).

The spectral characterization is controversial as both a thermal (Murakami et al., 1991) and non-thermal (see Lazzati, 2005) behavior has been claimed for precursor activity. Moreover, postcursors have been poorly studied as a separated phenomenon. In this section we will review these observational evidences in more detail.

From a general theoretical point of view any model should explain precursors and postcursors and their common property, i.e. the quiescent phase which separates them from the main emission episode(s). Indeed, assuming that both precursors and the main event of a γ-ray burst are due to the same central engine, the quiescent phase can be explained in two ways: (i) the central engine stops its activity for the time corresponding to the quiescent phase; (ii) the central engine is always active but its emission is somewhat modulated in high and low phases. In the latter case, when the emission becomes comparable to the background noise, we see separated phases of emission in the light curves. Observationally it is hard to distinguish between these two possibilities.

In section 2.3.1 we invoke the standard fireball evolution with a discussion on the effect that arises as a natural consequence of the physics of the expanding fireball. In section 2.3.2 we describe another model which deals with the propagation of the fireball far away from the central engine: a modulation in the Lorentz factor of the shells, that might account for the quiescent phases. Both these models can be reported as part of the "fireball precursor" family. If precursors and postcursors were demonstrated to be nothing but isolated pulses within the complex light curve of GRBs, than what remains to be explained is how the central engine can produce long quiescent phases. A possibility (discussed in §2.2) is an *ad hoc* modulation of the energy emission in the internal shocks, according to some function.

In section 2.3.3 we discuss disk fragmentation, proposed to account for flare activity in GRBs. The common feature is that precursors and main events are due to extraction of energy from the same compact object. However, any model successful in interpreting the nature of precursors/postcursors as due to the activity of the central engine should also support the fact that the same engine is active (in some cases) for thousands of seconds.

Alternatively, precursors and postcursors can be thought to have a different origin than the main GRB emission, which, in the standard model is ascribed to internal shocks. For instance, the pulses preceding the main event can be thought to be produced by the break out of the jet from the stellar envelope. We discuss some of these possibilities in sections 2.3.4 and 2.3.5.

Finally, in section 2.3.6, we discuss "two-step engine" models in which the precursor is formed when the progenitor initially forms a neutron star (some differences arise when we consider different properties of the NS, like angular momentum and magnetic field). The main GRB is then formed when the NS shrinks to form a black hole. In addition we discuss also some alternative possibilities which have not been proposed so far.

Notes on central engines Independently of the way the energy is extracted, i.e. from accretion, from the magnetic field, or from transition phases, in this section we overview the main differences of the proposed models in producing precursors/postcursors and quiescent phases. We can identify the following

1. The most widely adopted GRB central engine model invokes a central black hole and a surrounding torus. In this system there are three energy sources: the gravitational binding energy of the torus, the spin energy of the black hole, and the magnetic energy. The extraction of energy from this system produces the observed prompt and afterglow emission of GRBs;
2. Another type of GRB central engine is a millisecond magnetar. In this case the sources of energy is the spin of the pulsar and the magnetic field. In this case, there could be in principle two energy components, a prompt one powering the prompt GRB (via neutrino emission or via dissipation of the toroidal field) and another long-term one via spin-down luminosity. The second component could explain long-lived central engines;
3. An even more exotic central engine mechanism involves the phase transition from normal neutron matter to strange quark matter, but there is no evidence yet about the existence of such a state of matter.

2.3.1 Fireball transparency

The rapid injection of a huge amount of energy in a small volume generates a plasma composed of photons and pairs, with small baryonic content. GRBs are cosmic sources, so their energy is huge. Moreover, variability in the light curves of GRBs suggested that the release of energy has to occur in a volume of a few Schwarzschild radii, in order not to violate causality. The fireball is initially optically thick and photons cannot escape. Moreover, the huge internal energy density results in an acceleration of the material inside the fireball to relativistic speed, until equipartition is reached between the internal energy of the fireball and the kinetic energy of the expanding material. When the fireball reaches equipartition, is enters into the “coasting” phase, i.e. expands with constant velocity.

We recall that the transparency radius (i.e. the distance at which transition from optically thick to thin regime takes place and photons leak out freely) is:

$$R_\tau = \left(\frac{M\sigma_T}{4\pi m_p}\right)^{1/2} \simeq 2.4 \times 10^{13}\ E_{51}^{1/2}\Gamma_2^{-1/2}\ \mathrm{cm},$$

The coasting radius (i.e. when acceleration phase ends and constant speed is reached) is:

$$R_c = \Gamma R_{in} \simeq 10^{11}\ \Gamma_2 R_{in,9}\ \mathrm{cm}.$$

where R_{in} is the initial radius of the fireball. For typical values $R_\tau > R_c$. The transition between the thick to thin regime is crucial for the evolution of the fireball and for the observational evidences.

In fact, if transparency is reached before coasting ($R_\tau < R_c$), i.e. when the fireball is still accelerating, only part of the energy has been converted into the fireball bulk motion. We than expect, in analogy to the "pure fireball" example, a strong black body emission corresponding to the prompt phase and no (or very weak) afterglow emission. Most of the energy should be converted into radiation at the same time. Therefore, one fireball can produce only one single pulse.

If transparency is reached after coasting ($R_\tau > R_c$), most of the internal energy of the fireball has been transformed into bulk kinetic energy. In this case we expect a weak pulse with a black body spectrum (see e.g. Daigne and Mochkovitch, 2002, for a detailed calculation). Such weak thermal signals preceding the main emission has been identified in the literature as precursor emission, but it has not been seen, apart from a few cases (Murakami et al., 1991). In this scenario, subsequent internal and external shocks can produce the main event and the afterglow, respectively, where most of the initial energy is reprocessed into radiation.

2.3.2 Modulation of Γ

Ramirez-Ruiz et al. (2001) tested different possibilities for GRBs central engines to explain dormant periods. Although the presence of quiescent time intervals in some very complicated time profiles of long GRBs had been regarded as an indication of the turning-off of the central engine, an alternative explanation could be found within the internal/external shock model, by requiring a modulation of the Lorentz factor of the emitted shells.

In Ramirez-Ruiz and Merloni (2001) a quantitative proportionality relation is shown between the duration of an emission episode and the quiescent time elapsed since the previous episode. However, note that the tight correlations require tuning of the parameters also in the simplest, modulated outflow.

Consider that the first collisions between the shells remove the initial random differences among the Lorentz factors of the shells. If the mean Lorentz factor $\bar{\Gamma}$ remains steady for the entire burst duration, than the efficiency steadily decreases during the outflow expansion. If $\bar{\Gamma}$ is modulated on a time-scale much smaller than the overall duration of the wind, dynamically efficient collisions at large radii are still possible. In Ramirez-Ruiz et al. (2001) both scenarios (switch-off of the engine and modulation of Γ) were numerically tested:

1. **Central engine switch-off**. As the time of arrival of the pulses at the detector closely reflects the activity at the central engine (Kobayashi et al., 1997), it is not surprising to find a quiescent time interval in the γ-ray light curve with a duration comparable to the quiet emission period at the central engine. This is generally the case whenever the central engine turns off for a long enough time and the internal shocks develop well inside the radius where the external shock occur (Fenimore, 1999). The presence of a quiet emission period in the central engine would divide the relativistic outflow into two well-separated thick shells, each of them composed of many concentric inner shells moving at different (relativistic) speeds.

2. **Central engine continuous injection**. There are at least two mechanisms which might lead to a period of quiescence in the observed light curve without postulating any quiet phase in the central engine. One possibility is that the central engine ejects consecutive shells moving with Lorentz factors that are essentially constant over a period $\Delta t_{\Gamma=const}$. In this steady outflow scenario, the requirement is that the difference in Γs, of consecutive shells, was small enough for the shells not to collide until the deceleration radius. A second possibility is that the Lorentz factors of the emitted shells decrease monotonically during a certain interval.

   In the former case, it can be shown (Ramirez-Ruiz et al., 2001) that if the constant Lorentz factor during $\Delta t_{\Gamma=const}$, Γ_{const}, is lower that the average Γ_{ave} speed of the shells before and after $\Delta t_{\Gamma=const}$, quiescent time interval can be produced. However, in the latter case the temporal profiles characterized by precursor activity would require a sine-like modulation of the bulk Lorentz factor of the emitted shells.

The two scenarios reflect in an observationally detectable feature of the afterglows. γ-ray bursts with longer quiescent times should have more prominent afterglows, but such a correlation has not been observed yet. If the central engine switches-off for a certain period, a collision is likely to occur between the outer shells (which, after the internal shocks have been taken place, are left with an energy E_{out}), and the inner ones (with energy E_{in}). The overall effect of the collision is, at a fixed frequency, to increase the flux by a factor $\sim (1 + E_{in}/E_{out})^{1.4}$ (Kumar and Piran, 2000). This generates a rebrightening in the light curve of the afterglow, whose location depend on the dynamical parameters of the two shells and the external medium density (Kumar and Piran, 2000).

2.3.3 Ring-shaped or fragmented disks

By noticing the similarity in the flaring activity (i.e. from $\sim 10^1$ to 10^4 s after the main event) of long and short γ-ray bursts, Perna et al. (2006) proposed the following. Unless the similarities among the late emission in GRBs with different class of progenitors are coincidental, the flares have a common origin in the disk rapidly accreting onto a black hole. Since an accretion disk (or torus) is thought to be formed both in long and short GRBs, then X-ray flares that are seen in both classes, could originate in the accretion disk.

We already pointed out, in the previous section, that within the internal shock scenario, the variability in the light curve of a GRB reflects the variability in the inner engine (Kobayashi et al., 1997). Assuming that the central engine can be active for such long time intervals, the flares directly reflect the activity of the central black hole.

There are two principal observational evidences in flaring activity. First, the duration of the flares (within each burst) is positively correlated with the time the flares occurs (O'Brien et al., 2006; Cusumano et al., 2006; Godet et al., 2006). Second, the peak luminosity of a flare is negatively correlated with its arrival time: the later a flare, the lower the luminosity. This second issue is particularly evident for GRB 050904

(Watson et al., 2006). Moreover, the total fluence of the flares also tends to decrease with the arrival time.

Let us assume that the ultimate source of power is black hole accretion. Whether the accreting material is provided by the envelope of a collapsing star as in the collapsar model (MacFadyen and Woosley, 1999) or by the debris of a tidally disrupted companion in binary merger scenarios (Eichler et al., 1989), the outcome is a disk accreting at very high rates.

To produce the typical luminosity observed in GRBs the accretion rate has to be roughly $\dot{M} \sim 1 M_{\odot}$ s^{-1}. At these accretion rates it has been shown (Popham et al., 1999; Narayan et al., 2001; Di Matteo et al., 2002) that the accretion disk is advection-dominated because it cannot cool efficiently. When the accreting material is exhausted, the accretion rate and consequently the engine power drops rapidly. The flares might be due to the reenergization by blobs of material that make their way from a range of initial distances, toward the accreting black hole. The two correlations we recalled in the previous paragraph can be understood in this scenario. The overall emission of a γ-ray burst, starting from the "precursor" might be due to the same mechanism.

Disk properties and timescales The properties of the GRB disk are highly dependent on the mass accretion rate; for a given accretion rate they further depend on the radial location within the disk (Narayan et al., 2001; Di Matteo et al., 2002) and on the composition which affects the opacity. A typical timescale for accretion can be found, once the disk properties are known. i.e. the viscous time:

$$t_{visc}(R) = \frac{R^2 \Omega_k}{\alpha c_s^2} \rightarrow t_{visc} \propto R^{3/2}, \tag{2.24}$$

that sets the typical duration of the accretion phase for a ring of material initially at a distance R. $\Omega_k = \sqrt{GM/R}$ is the Keplerian velocity of the gas in the disk (orbiting a body of mass M); c_s is the sound speed of the accreting material; α is a parameter characterizing the strength of viscosity (Shakura and Sunyaev, 1973). When advection dominates, for $\dot{M} \gtrsim 1 M_{\odot}$ s^{-1}, then the disk scale height $H = c_s/\Omega_k$ is $\sim R$ and the viscous time can be approximated as

$$t_{visc} \sim \frac{1}{\alpha \Omega_k} \sim 5 \times 10^{-4} \left(\frac{\alpha}{0.1}\right)^{-1} \left(\frac{M}{3M_{\odot}}\right) \left(\frac{R}{R_s}\right)^{3/2} \text{ s}, \tag{2.25}$$

where R_s is the Schwarzschild radius. At a distance $r = R/R_s \sim 1000$ the accretion time is $\sim 15(\frac{\alpha}{0.1})^{-1}(\frac{M}{3M_{\odot}})$ s. The viscous time scales are evidently too short to account for the largest durations of GRBs. However, at large radii (late times), the accretion rate is smaller, the fraction of advected energy is smaller, so the disk cools more efficiently, implying $H < R$. This increases t_0 of a factor $(H/R)^{-2}$. If we assume that later time flares arise from disks which are not substantially advection-dominated, then accretion time of 10^4 s from material at $r > 1000$ is not unreasonable.

Depending on the conditions, the accretion timescales from material originally in the outer parts of the disk can vary between ~ 10 to 10^4 s, with the longer timescales deriving from the outermost rings of material.

Continuous disk To explain the delays between different pulses, and the quiescent phases, a possible solution is that the disk develops a ring-like structure, but remains continuous in the azimuthal direction. Then the arrival time of a ring of material initially at a distance R is $\sim t_0(R)$. Once this ring begins to accrete onto the black hole, the duration of the main accretion phase is also $\sim t_0$. After a time $t \sim t_0$ the flux should drop rapidly. The positive correlation between duration of a pulse and its arrival time is then explained. Moreover, if we assume the mass of the rings to be roughly constant (equal mass translates in equal energy from accretion), also the negative correlation between luminosity and arrival time is evident.

Fragmented disk Alternatively it is possible that the disk, in its outer regions, does not remain a continuous fluid, but rather fragments into bound "blobs" of material. This does not alter the generic behavior discussed above on timescales. In particular, if most of the mass at large radii is bound up in fragments, then the timescales for those objects to be dragged onto the black hole via viscous effects is lenghted by a factor of the order of $M_{frag}/M_{disk} > 1$, where M_{disk} is the exterior disk mass (Syer and Clarke, 1995). This could in principle permit even longer timescales for any give radius. The initial mass of a fragment is $\sim \Sigma(2H)^2$ where Σ is the surface density. However such fragments will merge rapidly until their tidal influence on the disk manages to open a gap. This occurs at a mass (Takeuchi et al. (1996)):

$$M_{frag} \simeq (H/R)^2 \alpha^{1/2} M \tag{2.26}$$

where M is the mass of the black hole.

Note that the total energy output of flares in short GRBs is lower than in long GRBs, but the peak luminosities are comparable (Gehrels et al., 2005). This might suggest that while the total mass accreted by the disk is lower in the merger progenitor scenario, the accretion rates during the prompt phase are comparable, and can range from 1/10 $M_\odot$ s^{-1} to some $M_\odot$ s^{-1}.

Several classes of known disk instabilities can lead to flux variations:

- Thermal instabilities might occur when the logarithmic derivative of the heating rate, with respect to the temperature, is higher than the cooling one. However, this seems to be the less promising explanation (Perna et al., 2006).

- Intrinsic instability either due to MHD turbulence or with shock instabilities associated with the photo-disintegration of α nuclei. This kind of instability is more likely to explain the variability in the prompt phase.

- Gravitational instability might be a better, although speculative possibility, especially if it results in fragmentation of the disk. The gravitational stability of a disk is governed by the Toomre parameter:

  $$Q_{\mathrm{T}} = \frac{c_s k}{\pi G \Sigma}, \tag{2.27}$$

  where k is the epicyclic frequency. If $Q_{\mathrm{T}} < 1$ the disk is gravitationally stable. Narayan et al. (2001) and Di Matteo et al. (2002) found that a gravitationally unstable region $Q_{\mathrm{T}} \sim 1$ is possible for $R \gtrsim 100\ R_s$ if the accretion rate is $\dot{M} \gtrsim 3M_{\odot}$ s^{-1}. this translates in a reasonable requirement, although strong, on the specific angular momentum of the in-falling matter.

Once the disk becomes unstable, two behaviors are possible. First, the disk may develop a spiral structure. Second, the disk may fragment in bound blobs. The latter possibility is driven by the physics of the disk, as it becomes inevitable if the cooling time is less that a critical value $\approx 3\Omega_k^{-}1$.

More recently, Wang and Mészáros (2007) and Janiuk et al. (2007) recalled that precursors and long gaps might be the results of the thermal-viscous instabilities in the opaque inner regions of the disk. The instabilities, if accompanied by disk fragmentation, may lead to the several episodic accretion events and several rebrightenings of the central engine.

Eventually, it is yet under debate whether disk fragmentation can cause precursors, but it is for sure a non-negligible possibility.

2.3.4 Jet shock breakout

In the collapsar progenitor scenario, the prompt emission is caused by relativistic jets expelled along the rotation axis of a collapsing stellar core. Theoretical models for precursors have been proposed, relating it to the breakout of the main GRB jet. We refer to these models in the following, as the "progenitor precursor" family, according to the location of the emission producing the precursor. A cartoon of the jet erupting from the star is shown in Fig. 2.4.

As suggested by Ramirez-Ruiz et al. (2002), Waxman and Mészáros (2003), and Wang and Mészáros (2007), when the jet is making its way out of the stellar mantle, a bow shock runs ahead and a strong thermal precursor is produced as this shock breaks out (but see Nakar and Sari, 2011). In this model, as usual, the main GRB is produced when the internal shock occurs at some radius R_{γ}, the delay time between the precursor and the main burst being of the order of $\Delta t \sim 10$ s. The spectrum is suggested to be thermal, i.e. produced by the non-relativistic head of the jet which emerges from the stellar surface and by the heated material of the star. A non-thermal component could arise during shock breakout, due to repeated Compton scattering of shocked breakout thermal photons by the relativistic ejecta driving the shock.

As the jet advances through the star, it drives a bow (forward) shock ahead of itself into the star, while the ram pressure of the shocked gas ahead of the jet drives a reverse

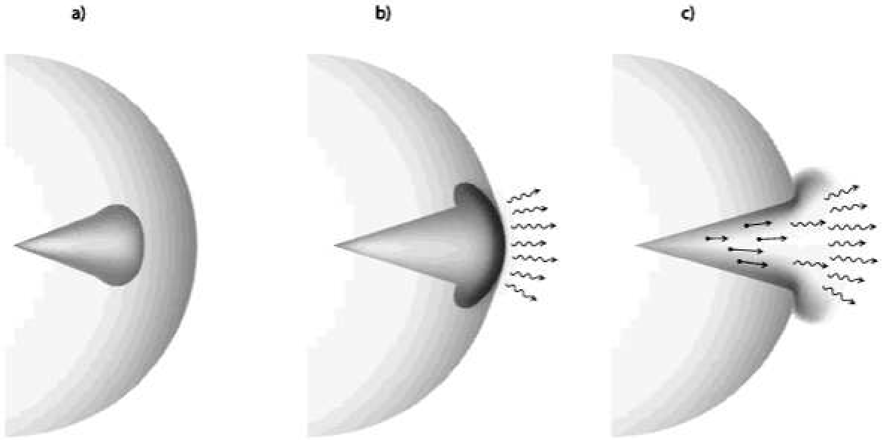

Figure 2.4 Diagram illustrating the propagation of the jet through the stellar mantle. The jet is initially unable to push the material at a velocity comparable to its own, and is decelerated. As the jet propagates a bow shock runs ahead of it (a). The shock heats the material and makes it expand sideways. The thermal precursor is produced when the shock breaks out the surface (also allowing the cocoon material to escape) (b-c). The fireball escapes the stellar envelope and finds the soft photons on its way out (c). Picture taken from Ramirez-Ruiz et al. (2002).

shock into the head of the jet, which slows the jet down to sub-relativistic velocity. Thus we can identify three distinct regions:

1. the thin layer of shocked stellar gas in front of the contact discontinuity between the jet and the stellar gas. It moves outward with velocity v_h (we use the label $_h$ for the head of the jet, $_j$ for the jet itself);
2. behind the contact discontinuity there is a shocked jet region where the relativistic velocity of the jet, $\Gamma_j >> 1$, is slowed down to $\sim v_h$ by the reverse shock;
3. the unshocked, ultra-relativistic jet, whose bulk Lorentz factor behaves as if it were a free jet. In the latter, at lower radii, the gradual conversion of internal energy into kinetic energy, results in $\Gamma_j = \Gamma_0(r\theta_j/r_0\theta_0)$, where Γ_0 is the initial Lorentz factor at the injection radius r_0, and θ_j is the jet opening angle at a radius r.

In this scenario the "precursor" is produced by the bow shock emission or the cocoon emission when the jet head breaks out of the stellar surface. After this the progressively unshocked material emerges, that is part of the freely expanding jet. As $\Gamma \propto \theta^{-1}$, an observer located off-axis, with respect to the direction of the emerging jet, will see the initial cocoon or bow shock emission, but **not** the subsequent one. The observer at larger viewing angle would see a dark phase (quiescence).

Nevertheless, this model for quiescence cannot account for large quiescent time intervals. One might thinck that the dark phase can last as the longest observed quiescence, i.e. $\sim$ 570 s, requiring that the shocked jet material moves with low enough velocity.

However, when the head of the jet uncorks the stellar mantle, the pressure in front of the jet decreases immediately, and a rarefaction wave propagates back into the shocked jet material at the speed of sound. The speed of sound, c_s, is independent from the jet head velocity $v_h \ll c$, and in a shocked jet plasma is $c_s = c/\sqrt{3}$.

The rarefaction wave quickly reaches the reverse shock which was propagating backward, the pressure of the shocked jet material also drops and can no longer decelerate the fast unshocked jet. If we assume that the rarefaction wave reaches the reverse shock well below the stellar surface, than the width of the shocked jet is $\Delta \lesssim R_\star$. The time to reach the reverse shock is then (Wang and Mészáros, 2007):

$$t_1 = \Delta/c_s \lesssim R_\star/c_s = 6\ R_{\star,11}\ \mathrm{s}. \tag{2.28}$$

The unshocked jet then takes a time:

$$t_2 \simeq R_\star/c = 3\ R_{\star,11}\ \mathrm{s}, \tag{2.29}$$

to reach the stellar surface. Supposing that the internal shocks occur at a radius R_γ, there is an additional time delay of the GRB relative to the precursor emission:

$$t_3 \simeq R_\gamma/2\Gamma^2 c = 0.03\ R_{\gamma,13}\Gamma_2^{-2}\ \mathrm{s}. \tag{2.30}$$

Therefore, the **total** gap period between the precursor and the main burst is of the order of: $T_{gap} = t_1 + t_2 + t_3 \simeq 12 R_{\star,11}$ s, which is indeed too short to account for the largest delays.

After the rarefaction wave has reached the first reverse shock, a new system of forward and reverse shocks forms, and the shocked, rarefied, jet plasma is re-accelerated to a relativistic velocity (Wang and Mészáros, 2007) equal to:

$$\Gamma_{h2} = \Gamma_{h1}[4\Gamma_{h1}(1 + c_s t/\Delta)^3]^{1/4}, \tag{2.31}$$

where Γ_{h1} is the Lorentz factor of the shocked jet before the rarefaction wave propagated back (see also Waxman and Mészáros (2003)). Even for sub-relativistic velocities, i.e. $\Gamma_{h1} \simeq 1$, the rarefied shock jet is accelerated to a relativistic velocity $\Gamma_{h2} \gtrsim 2$ after a time given by eq. 2.28.

It has been shown (Waxman and Mészáros, 2003) that this system leads to the formation of a series of progressively shorter, harder, thermal pulses in the X-ray band, with the peak of the spectrum (in a νF_ν plot) varying a factor of ~10 according to the chemical composition of the material of the star. These pulses are caused by successive cycles of shock and rarefaction waves reaching the inner and outer boundaries of the shocked material. The Lorentz factor of the shocked plasma increases with each succeeding and increasingly relativistic shock that goes through it. A small fraction of material might be accelerated inside the star to larger velocities, up to a limit of $\Gamma \sim 10$ (Waxman and Mészáros, 2003).

The expansion and acceleration of the main bulk of the material between the forward and the reverse shock lead to a decrease of the scattering optical depth, and photon diffusion times. As a result, the successive shocks are predicted to have increasingly higher bolometric fluences, shorter durations, and higher peak photon energies. After a few shocks and when the jet goes through the outer layers of the stellar envelope with $\rho \sim 10^{-5} - 10^{-7}$ g cm^{-3}, the material will have reached Lorentz factors comparable to the "standard" GRB values ~ 100, leading to an additional non-thermal component in the very end pulses of the precursor.

It's worthy to point out that when the first slow head of the jet emerges, the channel opened behind it undergoes the effect of the transverse pressure given by the unshocked material of the star and by the cocoon. In fact, while the jet finds its way out of the star, propagating through its envelope, the shocked material is pushed sideways from the jet direction, forming a high-pressure, hot plasma cocoon which flows out behind the head of the jet. Immediately after, the stellar material re-expands closing the channel at the speed of sound. So typically in a time ($\sim \theta_j r/v_\perp$) comparable to the breakout time, the channel closes again, before the subsequent jets starts to propagate. The free-fall time of the material, along the rotational axis is:

$$t_{ff} = 3000[\rho/(1 \text{ g cm}^{-3})] \text{ s} \rightarrow t_{ff} > T_{gap} \tag{2.32}$$

where the density of the stellar material can range from 1 to 500 g cm^{-3} for He and C/O core material, respectively. Therefore it is not unreasonable that the channel (aside from re-closing) remains the same during the time that the jet takes to propagate.

2.3.5 Jet with widening θ

In the jet breakout scenario presented in the previous section (see also Fig. 2.4), Lazzati and Begelman (2005) showed that the jet is likely decollimated soon after it escapes the stellar surface. The prediction of the authors is that the angle of the jet, θ_j evolves exponentially with time. Initially the breakout of the jet produces a very narrow jet (collimation is provided by the cocoon transverse pressure on the channel), which widens in time. An observer positioned at θ_{obs} should not see the first emission, but only the thermal emission from the cocoon that follows the breakout. Later on when $\theta_j \sim \theta_{obs}$ the main GRB becomes visible. The onset of the GRB is thus dependent upon the viewing angle.

We can draw two predictions in the "widening-angle" scenario, assuming a constant luminosity engine, and constant efficiency of γ-ray production:

1. the brightness of a GRB should tend to decrease with time since the photon flux is proportional to the energy per solid angle. If the angle evolves, the flux should track the same behavior;
2. consider an observer at $\theta_{obs} > \theta_{j,br}$, where $\theta_{j,br}$ is the jet opening angle at the time of breakout. Initially the observer lies outside the beaming cone and does

not detect the GRB. But if quasi-isotropic emission marks the breakout (Ramirez-Ruiz et al. (2002)), such emission would not be followed immediately by γ-rays for observers lying outside of $\theta_{j,br}$. This delay may explain the unusually long delays between precursors and main emission detected in several GRBs.

2.3.6 Transition NS-BH

The above described difficulty in interpreting long gaps through a single jet breakout makes it necessary to explore a new alternative. This section is focused on what might be called a "two-step" model for the production of GRBs. If the origin of precursor is controversial, what is even more puzzling is the extremely long quiescent phases often observed in GRBs with precursor activity (e.g. hundreds of seconds in GRB 041219A, GRB 050820A and GRB 060124). The common topic of the section is that the precursor emission is due to the transition from the progenitor star to a NS or the activity of a highly magnetized NS. In both cases only subsequently a transition NS→BH produces the main GRB event.

Fallback collapsar scenario. Here we review a model (Wang and Mészáros, 2007) where the gap is related to the central engine activity, and the precursor is produced by an initial weak jet launched before the main jet. The ~ 100 s long gap is reminiscent of the natural timescales calculated numerically in the fallback collapsar (type II collapsar) model (MacFadyen et al., 2001), where the fallback disk forms minutes to hours after the initial core collapse. In this scenario, the collapse of the iron core initially forms a proto-neutron star and launches a supernova shock. However, this shock lacks sufficient energy to eject all the matter outside the neutron star, especially for more massive helium cores. If the explosion energy is lower than $\sim 10^{51}$ erg, as the supernova shock decelerates while it travels outward, some of the expanding material can decelerate below the escape velocity and falls back.

During the initial collapse, it is possible that a weak jet with an energy of a few times 10^{50} erg, is produced as a result of MHD processes in the collapsed core, or through propeller effects associated with a proto-neutron star (e.g. Wheeler et al., 2000). If such a jet is weak enough so as not to immediately disrupt the star (as the binding energy of a star is $E_{bind} = (GM^2)/R \simeq 2 \times 10^{53} (M/M_{\odot})^2$ erg), a fallback accretion disk can form in the core on a fallback timescale. Accretion of the fallback disk can launch a stronger jet producing the main burst. Such initial weak jets may be responsible for precursors with non-thermal spectra, through internal dissipation mechanisms such as internal shocks or reconnection, after they exit the stellar progenitor. The non-thermal spectra are consistent with those observed from most recent GRB precursors (e.g. Lazzati, 2005; Cenko et al., 2006; Romano et al., 2006; Page et al., 2007).

Immediately after the core collapse, a proto-neutron star (PNS) forms with a radius of ~ 50 km and mass $M \sim 1.4\ M_{\odot}$. For a reasonable angular momentum of the progenitor core of $j \simeq 10^{16}$ cm^{-2} s^{-1}, the rotation energy of the proto-neutron star is:

$$E_{rot,PNS} \simeq \frac{1}{2} I_{PNS} \Omega^2 \simeq 2 \times 10^{51} \left(\frac{\Omega}{400\text{s}^{-1}} \right)^2 \left(\frac{R_{PNS}}{50\text{km}} \right)^2 \text{erg} \tag{2.33}$$

Over a cooling time $\sim 5 - 10$ s, the hot proto-neutron star deleptonizes by neutrino emission and contracts to form the final neutron star. The principal reactions are:

$$\begin{array}{lll} e^+ + e^- & \rightarrow & \nu_i + \bar{\nu_i} \\ n + n & \rightarrow & n + n + \nu_i + \bar{\nu_i} \\ p + e^- & \rightarrow & n + \nu_e \\ n + e^+ & \rightarrow & p + \bar{\nu_e} \\ n & \rightarrow & p + e^- + \bar{\nu_e} \end{array}$$

If a fraction, e.g. $\sim 10\%$, of the rotation energy is tapped by some MHD process and converted into a relativistic outflow, this outflow will have the right energy and timescale for a GRB precursor.

After a time ~ 100 s following the initial collapse, enough gas has fallen back for the neutron star to collapse to a black hole. The energy that can be released, supplied by accretion is then $E \simeq \eta \Delta M c^2 \sim 1.8 \times 10^{53} \eta_{-1} (M/M_{\odot})$ erg, which is the typical energy of long GRBs. In the fallback collapsar scenario, the accretion rate depends on the initial supernova shock energy. For a weak SN explosion with an energy $\lesssim 0.5 \times 10^{51}$ erg, the accretion rate is about $\sim 0.01 M_{\odot}$s^{-1} (see MacFadyen et al., 2001). With the above accretion rate, the neutron star will collapse to a black hole on a timescale of the order of $30 - 100$ seconds. After the black hole forms, gas that continues to fall in with sufficient angular momentum will settle into a disk, which can power a main jet. This ~ 100 s accumulation timescale of the accretion material may be responsible for the long time delay of inactivity seen in some bursts with precursors.

Magnetar supramassive NS. This example is similar to the previous one, although it should be considered at least tentative. We wonder if the "precursor" emission is due to the spin-down luminosity from a NS. The main difference is that we assume that the newly born NS is a magnetar, i.e. it's magnetic field is a factor of 10^3 higher, i.e. of the order of 10^{15} gauss. In the *oblique rotator* model, a standard NS rotates at a frequency Ω and possesses a magnetic dipole moment $\mathbf{m}$ oriented at an angle α to the rotation axis. Such a configuration has a time-varying dipole moment, and so radiates energy with rate $\dot{E} = -2|\ddot{\mathbf{m}}|^2/(3c^3)$, which corresponds to a luminosity (Shapiro and Teukolsky, 1983):

$$\begin{aligned} L_{s-d} &= \frac{B^2 R^6 \Omega^4 sin^4 \alpha}{6c^3} \\ &= 3 \times 10^{49}\ B_{15}^2\ R_{15}^6\ \Omega_4^4\ sin^4\alpha \text{ erg s}^{-1} \end{aligned} \tag{2.34}$$

where R_{15} is in units of 15 km. We can thus account for precursor's energy up to a few times 10^{50} erg, as the typical precursor duration is ~ 10 s. Note that radiation is emitted at frequency Ω. But we foresee that such a huge amount of energy, radiated in a small volume by a rotating magnetar, generates a fireball like in the standard scenario for GRBs. Consequently, expansion of the fireball and shocks at $R_\gamma \sim 10^{13}$ cm might produce emission similar to the GRB main prompt emission.

Equation 2.34 has an important consequence: the energy is supplied by the rotational energy of the NS, and deriving eq. 2.33:

$$\dot{E} = I\Omega\dot{\Omega}. \tag{2.35}$$

Since $\dot{E} < 0$, the NS slows down and emits lower energy as t^{-2} (under the assumption that the magnetic field is frozen at the initial value). However, when E_{rot} has been radiated completely the NS has slowed down its spin and does not radiate. In this scenario the main GRB emission via accretion of the fallback material follows the initial spin-down-ignited precursor. A major objection of this scenario is that of requiring a large B field. Indeed, this may prevent accretion through the "propeller effect", i.e. the large pressure due to the magnetic field should stop and eject material, instead of accreting it. No subsequent main emission would than be produced.

To account for a subsequent main GRB emission, via accretion, we require the magnetar to be also "supramassive". In this case, the transition from the NS to the BH is a consequence of spin-down alone, as the initial mass of the NS was over the critical limit which prevents gravitational collapse (Vietri and Stella, 1998), and was supported by rapid rotation. The time scale for the collapse is the one needed to halve the angular momentum of the neutron star:

$$t_{collapse} = 315 \left(\frac{j}{0.6}\right) \left(\frac{M}{3M_\odot}\right)^2 \; B_{15}^2 \; R_{15}^6 \; \Omega_4^{-4} \text{ s}, \tag{2.36}$$

where j is given in units of the critical angular momentum of a black hole of the same mass $J_c = GM^2/c$. Not all the mass of the NS feeds immediately the black hole. Part of it forms an equatorial torus whose accretion provides the energy for the main GRB emission. The accretion takes place in a viscous time (eq. 2.25) which indeed is very short. None the less, eq. 2.34 showed that a supramassive magnetar can provide enough energy via spin-down to power a "precursor", in a timescale comparable to the long quiescent time intervals observed in all GRBs. Long dark phases during accretion are though a fundamental problem for all models, so far.

2.4 Open issues in GRB studies

The observational progress led by the Swift detections and prompt follow up in the X-ray and optical band have forced the GRB scientific community to revise and re-discuss many of the aspects of the standard model. In particular there are a series of issues and open problems which still need to be explained, which we list here in random order for future reference.

- GRB classifications and progenitor systems: the current paradigm of short-hard vs long-soft GRBs, which is based on the bimodal duration distribution, seems to be challenged by the recent discovery of a possible third "hybrid" category of short spikes followed by a long smooth tail (dubbed "short bursts with extended emission"). Present speculations are aimed at understanding if this classification scheme is correct and if it is highlighting intrinsically different progenitors.

- Long GRB types: it remains to be explained if XRF and XRR bursts form a distinct class or if they are the extension to low energies and luminosities of the so-called "classical" GRBs. In the former scenario, several possibilities have been proposed (e.g. off-axis bursts, highly baryon loaded fireballs) that need to be tested.

- Soft/long low luminosity GRBs: the recent discovery of extremely long and soft bursts (like 060218 and 080109) which can be detected if at low redshifts, opened the possibility to observe, for the first time, the interaction of the burst jet with the stellar envelope (thought to originate an intense thermal emission in the soft X-ray band).

- GRB central engine: a general question, which is common also to other jetted astrophysical sources like powerful AGN, is the source of the collimation of the GRB jets. Moreover, if late time flares are interpreted as due to the late time central engine activity, it remains to be explained how can it work for thousands of seconds (is it fall-back?). If instead the central engine is able to inject energy steadily for so long time, can this explain the flat phase observed in several X-ray afterglows? Another important issue consists in understanding the role of MHD processes in the early phases of the burst emission. In particular we refer the reader to the exceptional case of GRB 110328A also known as Swift J1644+57 (Burrows et al., 2011; Levan et al., 2011; Krolik and Piran, 2011; Zauderer et al., 2011).

- Composition of the GRB outflow: the long lasting debate is if GRB outflows are matter dominated or Poynting-flux dominated. What is the evidence for/against either possibility? Possibly clear detection of thermal components in the prompt or early afterglow phases would rule out the latter model. Moreover, polarization measurements of the prompt and afterglow emission could help to distinguish between these two scenarios. However, the GRB outflow should be at least hybrid.

- GRB prompt emission mechanism and site: are prompt gamma-rays produced in internal shocks, at the photosphere, or in magnetic reconnection regions? Is the emission site "closer-in" (near photosphere) or "further-out" (near deceleration radius)? Is the thermal component important in the spectrum? (It is noted that a thermal component may be also required to fit some of the X-ray flare spectra. What is the non-thermal mechanism: synchrotron or Comptonization? Related questions would be what powers high energy emission (leptonic vs. hadronic) and whether GRBs are emitters of cosmic rays and high energy neutrinos.

- Properties and origins of the afterglows: What are the origins of the distinct afterglow components (especially the shallow decay component)? How much can the external shock model explain? What is the role of the central engine and the internal dissipation regions? What is the nature of temporal breaks, especially the chromatic ones? Swift observations seem to suggest what we call "afterglows" actually include both the traditional external component and some other components unrelated to the external shocks. X-ray flares are a good example of a distinct (late internal dissipation) origin. Even some smoothly decaying components may be also related to the central engine or the internal dissipation regions. The most puzzling question is the nature of the afterglow temporal breaks, especially those that are not achromatic. Extensive data mining and sorting are indeed needed to understand the breaks.
- Properties of GRB shocks: are the electrons accelerated to a power law distribution? Is the electron power law index (i.e. the slope of the electron distribution driven by a shock) universal? What defines the shock microphysics parameters? Are there correlations between these parameters? Do microphysics parameters evolve with time (see Filgas 2011 and Filgas et al. 2011)? Numerical simulations and analytical studies have started to answer the fundamental questions about particle acceleration and magnetic field generation but still the connection with the data has to be established.

Chapter 3

Time resolved spectral behavior of bright BATSE precursors[1]

Abstract

Gamma Ray Bursts (GRBs) are sometimes preceded by dimmer emission episodes, called “precursors”, whose nature is still a puzzle: they could either have the same origin as the main emission episode or they could be due to another mechanism. We investigate if precursors have some spectral distinctive feature with respect to the main GRB episodes.To this aim we compare the spectral evolution of the precursor with that of the main GRB event. We also study if and how the spectral parameters, and in particular the peak of the νF_ν spectrum of time resolved spectra, correlates with the flux. This allows us to test if the spectra of the precursor and of the main event belong to the same correlation (if any). We searched GRBs with precursor activity in the complete sample of 2704 bursts detected by BATSE finding that 12% of GRBs have one or more precursors. Among these we considered the bursts with time resolved spectral analysis performed by Kaneko et al. 2006, selecting those having at least two time resolved spectra for the precursor. We find that precursors and main events have very similar spectral properties. The spectral evolution within precursors has similar trends as the spectral evolution observed in the subsequent peaks. Also the typical spectral parameters of the precursors are similar to those of the main GRB events. Moreover, in several cases we find that within the precursors the peak energy of the spectrum is correlated with the flux similarly to what happens in the main GRB event. This strongly favors models in which the precursor is due to the same fireball physics of the main emission episodes.

---

[1] This Chapter appeared Burlon et al. (2009)

3.1 Introduction

How does a GRB behave before the onset of the main emission is a debated issue. The so–called “precursor” activity has been observationally addressed by e.g. Koshut et al. (1995) [hereafter K95], Lazzati (2005) [L05] and Burlon et al. (2008) [B08].

K95 searched in the BATSE sample for precursors defined as pulses with a peak intensity lower than that of the main GRB and separated from it by a quiescent phase at least as long as the duration of the main event. They found precursors in ∼3% out of a sample of GRBs detected by BATSE up to 1994 May. Their duration appeared weakly correlated with those of the main GRBs and on average shorter than that of the burst. The spectral properties of these precursors showed no systematic difference with respect to those of the main GRB event, being both softer and harder. However, the comparison of the spectral properties of the precursors and of the main event were based on the hardness ratio which is only a proxy of the real shape of burst spectra.

L05 searched for precursors as weak events *preceding* the BATSE trigger. He found, within a sample of 133 bright GRBs, that ∼20% showed precursor activity. These precursors were on average extremely dimmer than the main GRB event, and their durations are weakly correlated with that of the main event. In contrast with the results of K95, the precursors studied by L05 were softer than the main event. Also in this analysis, however, the spectral characterization of the precursors were based on the fluence hardness ratio. However, given the typically extreme low fluence of most of the precursors found by L05, a better spectral characterization (e.g. through model fits of a high resolution BATSE spectrum) was almost impossible. A difference is how the precursor–to–burst separation is measured: K95 consider the time difference between the peak of the precursor and that of the main event, while L05 measure the precursor–to–main event separation from the end of the precursor to the start of the GRB.

B08 searched for precursors in the sample of 105 *Swift* GRBs with measured redshifts. In ∼15% of the sample a precursor was found. The definition of precursors adopted in B08 is similar to that used by K95. The main difference, however, is that B08 did not require that the precursor precedes the main event by an amount of time comparable to the duration of the main event. The novelty of B08 was to search and study precursors found in a sample of bursts with known redshifts. This allowed, for the first time, to characterize the precursor energetics and to study how they compare with the main event energetics, also as a function of the rest–frame time separation between the precursors and the main events. The results of B08 suggest that precursors’ spectra are consistent with those of the main event. Moreover, regardless of the rest frame duration of the quiescence (i.e. the time interval separating the precursor and the burst), precursors carry a significant fraction of the total energy (≈30%) of the main event (see Fig. 1 therein). The conclusions of B08 point to a common origin for both precursor and main event. Namely, they are nothing but two episodes of the same emission process.

Theoretical models for precursors can be separated into three classes: the “fireball precursor” models (Li, 2007; Lyutikov and Blandford, 2003; Mészáros and Rees, 2000; Daigne and Mochkovitch, 2002; Ruffini et al., 2001); the “progenitor precursor” models

(Ramirez-Ruiz et al., 2002; Lazzati and Begelman, 2005) and the "two step engine" model (Wang and Mészáros, 2007 [W07], Lipunova et al., 2009 [L09]). In the first class the precursor is associated to the initially trapped fireball radiation being released when transparency is reached. In the second class, based on the collapsar scenario, the precursor is identified with the interaction of a weakly relativistic jet with the stellar envelope. A strong terminal shock breaking out of the envelope is expected to produce transient emission. In both classes of models the precursors emission is predicted to be thermal, characterized by a black–body spectrum. As for the third class in W07 the progenitor collapse leads to the formation of a neutron star whose emission would be responsible for the precursor, while the star shrinks; subsequent accretion onto the neutron star causes its collapse onto a black hole, originating the GRB prompt. Conversely, in L09 the precursor is produced when a collapsing "spinar" halts at the centrifugal barrier, whereas the main emission is due to a spin–down mechanism. Thus, in L09 accretion is not invoked in either steps.

One of the main limitations of K95 and L05 analyses is the poor spectral characterization of precursors. They used the hardness ratio HR, i.e. the ratio of the counts (or fluences reported in the BATSE catalogue) measured over broad energy channels. However, it is well established that the broad band spectra of GRBs can be fitted by empirical models (e.g. Band et al. 1993) composed by low and high spectral power–laws with different slopes. The HR is only a proxy of the real spectral properties of GRB spectra (e.g. Ghirlanda et al., 2009) , in particular for GRBs with vastly different $E_{\rm peak}$. The other main limitation of these studies, based on the BATSE GRB catalogue, is the lack of redshifts. Indeed, this motivated the study of B08 of *Swift* GRBs with precursors of known redshifts. Nonetheless, the spectral analysis of B08 of *Swift*-BAT spectra was limited by the narrow spectral range (15–150keV): most *Swift* spectra of precursors could be fitted by a single power–law (i.e. the peak energy of the νF_ν spectrum is unknown) and in all cases no time resolved spectral analysis of the precursor could be performed.

The latter point is particularly important: the information carried by the strong spectral evolution of GRB spectra (e.g. Ryde, 2005; Ghirlanda et al., 2002, Kaneko et al., 2006 [K06]) is completely averaged out when time integrated spectra are considered (integrated over the duration of the burst or over the duration of single emission episodes, like the precursor and the main event in B08). An interesting feature found by time resolved analysis of GRB spectra is that there could be a positive trend between the spectral peak energy $E_{\rm peak}$ and the flux P within single emission episodes of GRBs (Liang et al., 2004) [L04]. Interestingly, this trend appears similar (Firmani et al., 2009) [F09] to that found between the rest frame GRB peak energies and their isotropic equivalent luminosities, when considering different GRBs with measured z (i.e. so called "Yonetoku" correlation, Yonetoku et al., 2004).

For these reasons we consider, in this paper, a still unanswered question: how does the spectrum of the precursor evolve and how does it compare with the evolution of the associated main event? In order to answer this question we compare the time evolution of the spectral parameters of precursors and main events. We also want to test if a possible correlation between the peak energy and the flux, i.e. $E^{\rm obs}_{\rm peak}$–P within the precursors exists. If this correlation is due to the physics of the emission process or to that of the central engine is still to be understood, but if the precursors and the main event do follow a similar correlation, this would be another piece of the puzzle (in addition to the results of B08) suggesting that precursors are nothing else than the first emission episodes of the GRB. To this aims spectral data with high time and spectral resolution are necessary. BATSE provides the best data for this purpose.

The paper is organized as follows: in Sec. 2 we describe the sample selection and global properties; in Sec. 3 we present the spectral comparison between the precursor and the main event within single GRBs and we draw our conclusions in Sec. 4.

3.2 The sample

The Compton Gamma Ray Observatory satellite (*CGRO*) had on board the Burst Alert and Transient Source Experiment (BATSE, Fishman et al., 1982), which provided the largest sample of GRBs, detected during the 9 yr lifetime. By applying different precursor definitions, K95 and L05 searched for BATSE bursts showing a precursor activity. A common feature of these studies is that a precursor is a peak separated (i.e. preceding) by a time interval and with a lower count rate with respect to the main GRB event.

The definition of a precursor is somewhat subjective and can easily bias the sample. L05, by excluding precursors that triggered BATSE, selected the faintest precursors. K95 instead is missing precursors which can be closer than the duration of the rest of the burst. For these reasons, consistently with the definition adopted in B08, we adopted a definition of “precursor” as any peak with a peak flux smaller than the main prompt that follows it and that is separated from the main event by a quiescent period (namely, a time interval during which the background subtracted light curve is consistent with zero). We didn’t assume *a priori* that precursors can occur only in long GRBs (i.e. duration of the main emission episode be > 2 sec in the observer’s frame), albeit in B08 we found no short burst with a precursor. We adopted this “loose” definition in order to check, a posteriori, if distinguishing characteristics emerge in the analysis. This definition is subject to find more easily precursors events of the type of K95 in the BATSE sample. Since K95 limited the search to half of the BATSE sample (considering events between 910405 and 940529) and due to the slightly different precursor definition, we searched for precursors in the complete BATSE sample.

The final BATSE GRB sample[2] contains 2704 GRBs. We found 2121 GRBs out of 2704 total triggers for which there was a 64 ms binned light curve[3] available. We inspected the background subtracted light curve of each GRB and found 264 GRBs (12.5%) with a precursor. The majority (191) of GRBs showed one precursor, 48 showed double precursors, 19 showed three precursors, 5 showed four precursors and in only one case we found five precursors, according to our definition.

---

[2] http://heasarc.gsfc.nasa.gov/docs/cgro/batse/BATSE_Ctlg/basic.html

[3] http://[...]/batse/batseburst/sixtyfour_ms/index.html

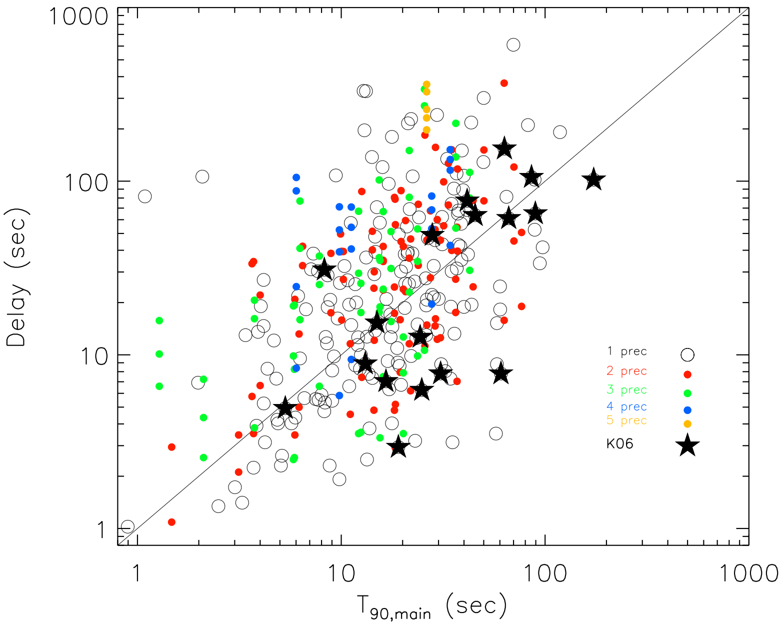

Figure 3.1 Delay (precursors to main event) vs T90 of the main prompt emission for the 264 GRBs with precursors found in the BATSE sample. Black empty circles are GRBs with single precursors (191 cases), while filled dots show GRBs with multiple precursors (color code as in the legend). Black filled stars represent the 18 precursors with at least two spectra in K06. The solid line represents equality.

3.3 Sample properties

From the 64 ms BATSE light curves we calculated the duration of the precursor and main emission event for each of the 264 GRBs with precursors. The duration was defined as in the BATSE GRB catalogue, i.e. T90. This corresponds to an integral measure, being the time interval containing the 90% (from 5% to 95%) of the counts inside each peak considered, either precursor or main event.

We define the time delay between the precursor and the main event as the difference between the beginning of the main event and the end time of the precursor. The mean durations of precursors and main emission episodes are ∼15 s and ∼24 s respectively. The mean duration of the delays is ∼50 s.

In Fig. 3.1 we show the delays of the precursors versus the duration T90 of the main GRB for the 264 GRB with precursors. The probability of a chance correlation among the duration of the GRBs with a single precursor (open circles and filled star symbols in Fig.3.1) and the corresponding delay is 3.53×10^{-14}. An even lower chance probability is found including also GRBs with multiple precursors.

Since we do not know the redshift of these GRBs, we cannot exclude that the correlation is at least in part the result of the common redshift dependence of both the delay and the T90. Moreover, Fig. 3.1 shows no apparent difference between GRBs with

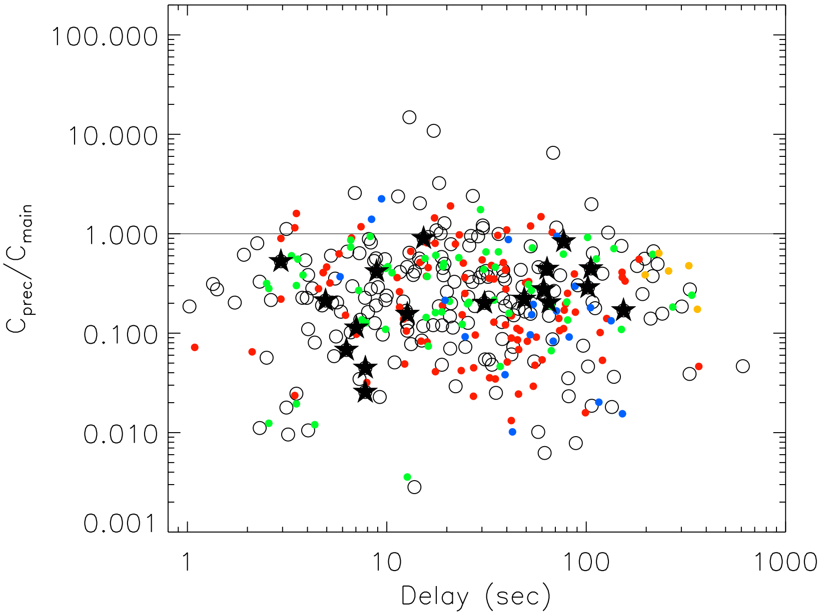

Figure 3.2 Ratio of precursor to main event counts versus delay times. Symbols and color codes are as in Fig. 3.1.

single or multiple precursors. This result is somewhat different from that reported by Ramirez-Ruiz and Merloni (2001). By investigating the temporal properties of multi–peaked GRBs (but note that they put no particular emphasis on precursors) they found a strong one–to–one correlation (4σ consistency) between the duration of a peak and the duration of the quiescence time interval before it.

In Fig. 3.2 we show the ratio of the total counts (integrated over T90) of each precursor with respect to the counts in the corresponding main GRB plotted as a function of the delay time. In most cases the precursor total counts are a fraction (of the order 10–20%) of the counts of the main GRB. Also in this case we do not find any difference between single precursors and multiple ones. Not surprisingly, a handful of GRBs show a precursor stronger than the main emission. In these cases, typically the precursor has a duration much larger than that of the main which over-compesates its lower peak flux, thus giving a higher integral count number for the precursor with respect to the main event.

Fig. 3.3 shows the total counts of the precursors with respect to the total counts in the main GRBs. In this plane different selection cuts are evident. The selection criterion for defining precursors in this work is evident as the lack of precursors to the left of the equality line (solid).

It is apparent from Fig. 3.2 and Fig. 3.3 that neither the delay times of the precursors with respect to the onset of the main event, nor the integrated counts of the peaks seem to show a specific clustering. Therefore, we can rule out the existence of a sub-class of “real” precursors among the complete sample, given the selection method.

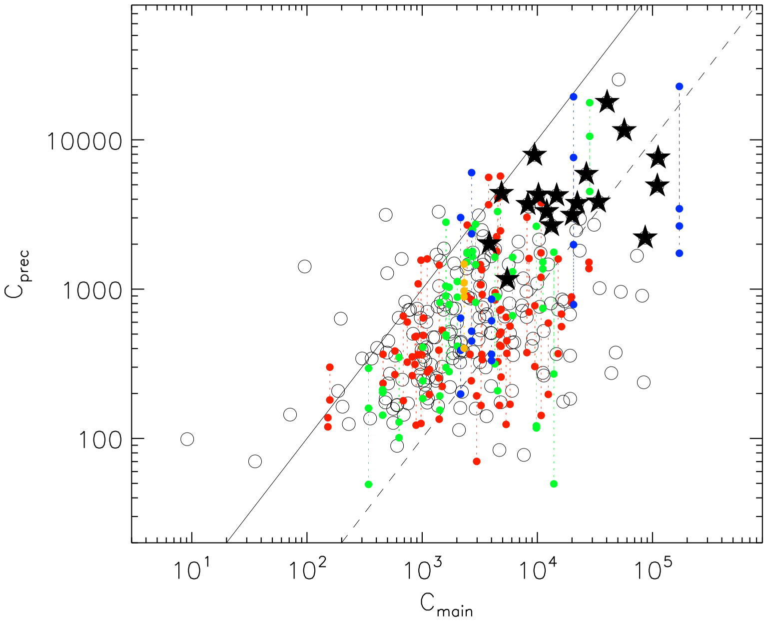

Figure 3.3 Total counts of the precursor versus the total counts of main event. Symbols and color codes are as in Fig. 3.1. The solid line represents equality, while the dashed line corresponds to precursors dimmer than main events by a factor 10.

3.4 Spectral evolution

In order to study the spectral evolution of the precursors and compare it with that of the main event, we rely on the time resolved spectral catalogue of Kaneko et al. (2006). K06 analyzed the spectra of selected bright BATSE GRBs. These were selected to have a peak photon flux (on the 256 ms time scale and integrated in the 50–300 keV) greater than 10 photons cm^{-2} s^{-1} or a total energy fluence greater than 2.0×10^{-5} erg cm^{-2} in the energy range ∼20–2000 keV. This mixed criterion ensured K06 to have a minimum number of time resolved spectra distributed within the duration of each GRB so to study the features of its spectral evolution with sufficient details. This led to a sample of 350 GRB.

For most GRBs the high energy resolution data of the LAD detectors were analyzed. These data consists of ∼ 128 energy channels distributed between ∼ 30 keV and 2 MeV accumulated during the burst with a minimum time resolution of 128 ms. In some cases also lower energy resolution data (MER) were analyzed. K06 fitted both the time integrated spectra and the time resolved spectra with 5 different spectral models:

a simple power–law (PWR), the Band model (Band et al., 1993) (BAND), a Band model with fixed high energy power law component β (BETA), a power–law with an exponential cutoff at high energies (COMP), or a smoothly broken power–law (SBPL). The spectra within a single GRB were accumulated in time according to a minimum S/N ratio (required to be larger than 45 in each time resolved spectrum, integrated over the energy range 30 and 2000 keV). In the final catalogue of K06 the best fit parameters for all the fitted models are given for all the time resolved spectra within a single burst. Through this large data set, it is possible to construct the time evolution of the spectral parameters of the bursts.

We cross–checked the sample of K06 with the 264 GRB with precursors that we have found in the BATSE catalogue. We found 51 GRBs with precursors with time resolved analysis reported in the K06 sample. However, since our aim is to characterize how the spectrum of the precursor evolves in time, we restricted this sample to those GRBs with at least 2 time resolved spectra analyzed by K06 in the time interval of the precursor. This condition reduces the sample to 18 GRBs. All these have a single precursor in their light curve (except for trigger #6472, that has two precursors). In Figs. 3.1, 3.2, and 3.3 these 18 events are shown (star symbols): they correspond to the bright end of the distribution of count fluence of the precursors.

For these 18 GRBs with time resolved spectral analysis reported in K06 we show (panel (a) of Fig. 3.4, and left part of figures 3.8 to 3.24) the light curve in counts (and in physical units as obtained by the spectral analysis) and the time evolution of the best fit parameters. It has been shown that when analyzing time resolved BATSE spectra, especially for S/N $\lesssim$ 80 (e.g. K06), the best fit model is often a cutoff power–law. This might be due to the difficulty of constraining the best fit parameter of the BAND model (i.e. the high energy spectral index of the power–law) when the fluence of the spectrum is low (as systematically expected in time resolved spectra with respect to time integrated ones). For this reason we decided to plot for all the 18 GRBs the spectral results given by K06 of the fit with the COMP model. In some cases this is not the best fit model of the time resolved spectra but for the aims of the present analysis, i.e. the *relative* comparison of the spectral evolution of precursors with respect to that of main bursts, any systematic effect due to the fit of the spectra with the COMP model is not affecting our conclusions. We show in Fig. 3.4 that both the photon spectral index and $E^{\rm obs}_{\rm peak}$ follow a strong soft–to–hard evolution in the rising part of the precursor, and vice-versa in the descending part. In the main emission event both spectral parameters show a general hard–to–soft trend, but inside each peak they *both* follow the same trend shown inside the single peak of the precursor and moreover they track the flux.

The latter consideration is shown in panel (b) of Fig. 3.4 (see for comparison the lower panel of the right side of figures 3.8 to 3.24) where a correlation between the peak energy $E^{\rm obs}_{\rm peak}$ and the flux P is apparent. Note however that GRB 930201 is the case with best statistics and hence does not necessarily stand for a general behavior. We connected (dashed line) the evolution of the spectral parameters only inside the precursor. The color code is as in panel (a): namely, the first (last) spectrum is the black (red) one. It has been recently pointed out (e.g. Borgonovo and Ryde 2001,

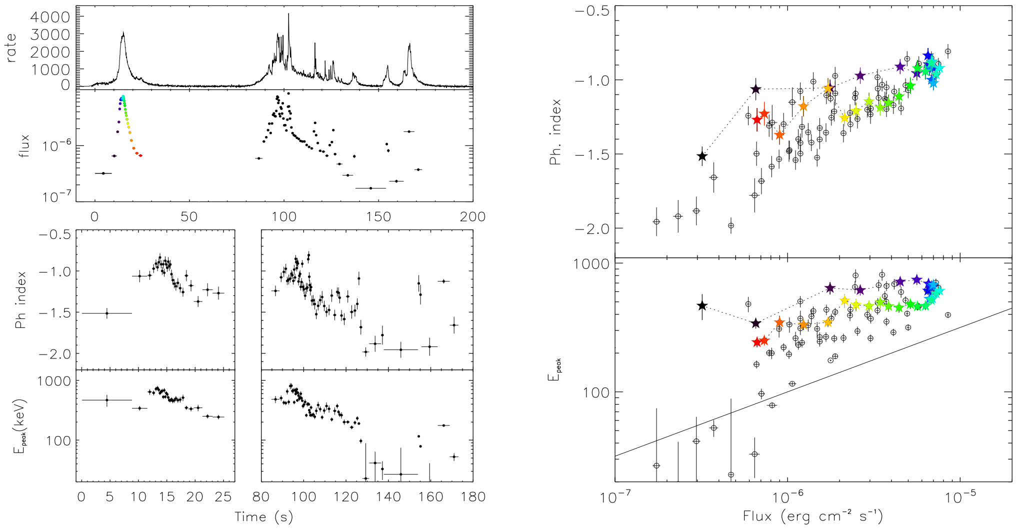

(a) The top panel shows the complete light–curve in units of count–rate and just below is the same light curve in physical units (erg cm^{-2}s^{-1}) binned into time intervals corresponding to the time resolved spectra extracted and analyzed by K06. The mid panels show the evolution of the spectral parameters of the COMP model, i.e. the low energy photon spectral index α and the peak energy of the νFν spectrum ($E_{\rm peak}$). These correspond to the zoom in the time interval of the precursor and of the main event (color symbols corresponding to the precursor).

(b) Panels show α (*top*) and $E^{\rm obs}_{\rm peak}$ (*bottom*) versus the flux. The spectral parameters of the precursor are shown with filled stars and joined by a dashed line. The first spectrum is the black one. The spectral parameters of the main emission episode are shown with empty circles.

Figure 3.4 GRB 930201 (trigger #2156)

Liang et al. 2004, and more recently by Firmani et al. 2009 for *Swift* GRBs), that when considering the spectral evolution of long GRBs there is a trend between the evolution of the flux P and the peak energy $E^{\rm obs}_{\rm peak}$ i.e. approximately $P \propto {\rm E}^{\gamma}_{\rm peak,obs}$. In particular Firmani et al. (2009) show that 84% of the K06 sample have $\gamma \sim 2$ at the 3σ level. In addition, the correlation is not biased systematically by the value of P, though its uncertainty increases with decreasing flux. We can fiducially extrapolate this evidence to precursors, keeping open the question of identifying the hidden physical mechanism that determines the value of γ.

Intriguingly, this is similar to the correlation between the peak luminosity and the peak energy (time integrated over the duration of the burst) in GRBs with measured redshifts (so called “Yonetoku” correlation). A similar result was reached by Liang et al. (2004) based on the spectral evolution of the brightest BATSE GRBs but for which no redshift was measured. Again, when studying the correlation between the luminosity and the peak energy within the few GRBs detected by BATSE and with known z, Firmani et al. (2009) finds that the correlation is present. The existence of a correlation within a single GRB similar to the Yonetoku correlation could be indicative of a physical origin for the quadratic link between the flux and the peak energy.

We can test if and how such a correlation holds in the GRBs with precursors that we have considered and/or if the $E_{\rm peak}^{\rm obs}$ and P of the precursor are consistent with the correlation defined by the prompt.

If this correlation is due to the physics of the emission process or to that of the central engine is still to be understood, but if the precursors and the main event do follow a similar correlation, this would be another piece of the puzzle suggesting that precursors are nothing else than the first emission episodes of the GRB.

3.5 Discussion

Figs. 3.5 shows the photon spectral indices α versus the peak energy $E_{\rm peak}^{\rm obs}$ for all 51 GRBs with precursor present in K06, while Fig. 3.6 shows for the same bursts how α and $E_{\rm peak}^{\rm obs}$ behave with the flux P. Different symbols (and colors, in the electronic edition) marks the precursor and the main event points. Filled symbols correspond to the 18 GRBs with at least two spectra for the precursors. Red triangles mark the remaining precursors in K06 with just one spectrum. Empty black dots correspond to the spectral parameters of the main events.

Fig. 3.5 shows that on average precursors and main GRB emission episodes span the same parameter space, while Fig. 3.6 shows that they follow similar correlations with the flux.

The distributions of the low energy photon indices α of the precursors and the main events are roughly consistent (the Kolmogorov-Smirnov KS null hypothesis probability is $\simeq 10^{-2}$). Fitting the two distributions (see Fig. 3.7, upper panel) with gaussian profiles we find $\langle\alpha_{\rm prec}\rangle = -1.03 \pm 0.27$ and $\langle\alpha_{\rm main}\rangle = -0.94 \pm 0.34$.

Three (#5486, #6472, #7343) of the 18 GRBs studied here present extremely hard spectra. One of them, i.e. GRB 960605 (#5486, see right side of Fig. 3.9), could even be consistent with a black–body spectrum at the very beginning of the precursor. These few cases populate the upper part of Figs. 3.5 and 3.6 (upper panel). We have re-extracted the LAD data for this burst and reanalyzed them. We confirm the findings of K06. The finding of a precursor with a spectrum consistent with a black–body should not be taken as a proof of a radical difference with the main event, since it has been already pointed out (e.g. Ghirlanda et al., 2003)) that a non–negligible fraction of GRB ($\sim$5%) start their emission with a black body spectrum.

Comparing the distributions of $\log(E_{\rm peak}^{\rm obs})$ we find that they are somewhat different (K–S null hypothesis probability $\sim 10^{-4}$). Fitting again with gaussian profiles the two distributions in Fig. 3.7 (lower panel) we find the mean value and 1σ scatter for precursors: $\log(E_{\rm peak}^{\rm obs}) = 2.49 \pm 0.35$ to be compared to $\log(E_{\rm peak}^{\rm obs}) = 2.60 \pm 0.24$ for the main emission events. The distribution of $E_{\rm peak}^{\rm obs}$ for the precursors is slightly softer than

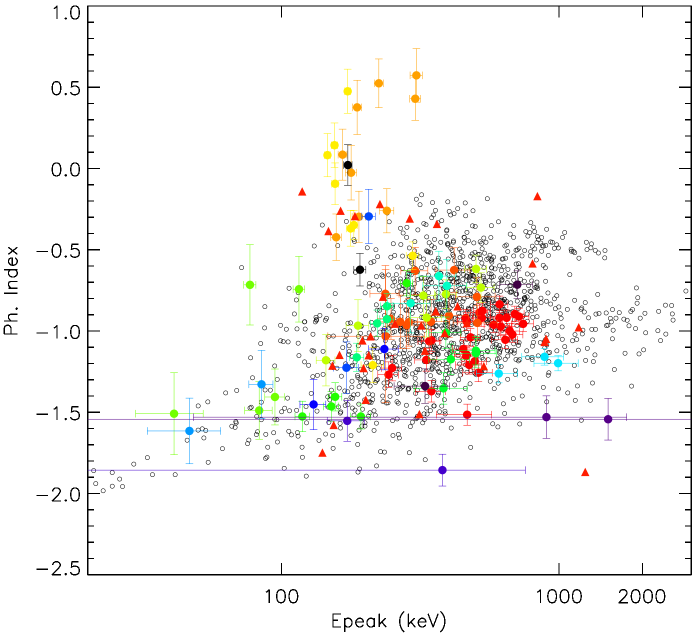

Figure 3.5 Photon spectral indices α versus the peak energy $E^{\rm obs}_{\rm peak}$ for 51 GRBs with precursor. Spectral parameters correspond to the time bins of the time resolved spectra extracted and analyzed by K06. The 18 bursts belonging to our sample are shown with filled dots (different colors represent different GRBs). We added also 33 precursors with a single spectrum data point (red triangles). Spectral parameters of the main emission episode are shown in black empty circles.

the one of the main prompt emission. This result is not surprising when looking at the bottom panel of Fig. 3.6: the peak energy of precursors seem to follow the trend (when $E^{\rm obs}_{\rm peak}$ is plotted with respect to flux) drawn by the GRB main emission, but at the lower left end of the track.

In the 7 precursors with more time resolved spectra (#2156, #7688, #5486, #6472, #3481, #3241, #1676), $E^{\rm obs}_{\rm peak}$ shows a strong evolution but nonetheless is always consistent with the correlation drawn by the main event (as shown in Fig. 3.4–b and lower panels in the right side of Figs. 3.8, 3.9, 3.10, 3.11, 3.12, 3.13). Note that these similar trends in the evolution of $E^{\rm obs}_{\rm peak}$ do not depend upon the delay, as these vary among ∼9 s (for #1676) and ∼75 s (for #7688). Note that at odds with B08, this consideration is based only on observed time intervals, because the redshift z is unknown for all GRBs in this work. Two of them, namely #2156 and #1676, also show consistent evolution in α between the precursor and the main event (see upper panels of Figs. 3.4–b and 3.13, right side). The other 5 GRBs (of this group of 7) show an evolution in α which is different in the precursor and in the main event: in two cases (#5486 and #6472) α starts extremely hard and evolves to softer values (see upper panel of Figs. 3.9 and 3.10, right sides). In the last three cases (#3481, #3241 and #7688) either the photon spectral index evolves in a different way with respect to the one of the main emission

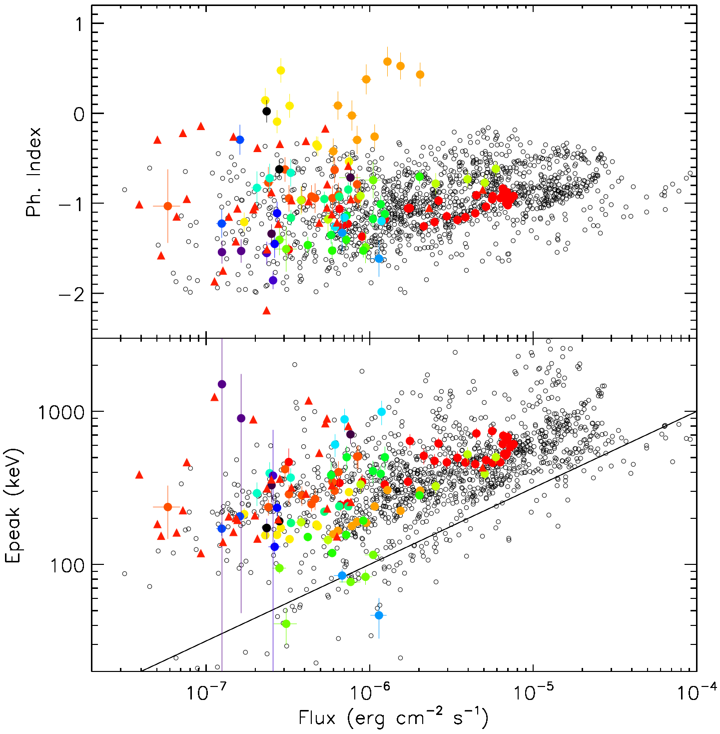

Figure 3.6 The photon spectral index α (*top*) and $E^{\rm obs}_{\rm peak}$ (*bottom*) versus the flux P in erg cm^{-2}s^{-1}. The solid line in the bottom panel corresponds to $P \propto \mathrm{E}^2_{\rm peak,obs}$. Color code and symbols as in Fig. 3.5.

episode (as in Figs. 3.12 and 3.8, upper panels on the right side), or it lies in a different region of the parameter space (see upper right panel of Fig. 3.11).

The remaining 11 GRBs of our sample have more coarsely sampled precursor spectra. The trend of $E^{\rm obs}_{\rm peak}$ of the precursor is consistent with that of the main event in 8 cases. In #3253, #6454, #3057, #4368, #1157, #6629, #3301, #7343 (see upper right panels of Figs. 3.15, 3.16, 3.17, 3.18, 3.20, 3.21, 3.23, 3.24) the peak energy in the spectra of precursors follow the same correlation with the flux drawn by the main emission. Notwithstanding, the number of spectra extracted by K06 in the precursor varies between five and two, thus preventing any more confident claim. Among these 8 GRBs, in the latter 3 the photon spectral indices α of the precursors do not track the trend drawn by the main emission event (see upper right panels of Figs. 3.21, 3.23, and 3.24), being always softer (with the exception of the onset of the precursor in #7343, which has $\alpha \simeq 0$). In the former badly sampled 5 GRBs, also α is consistent with the trend described by the spectra of the main impulse. Note that also in these 8 cases the delay does not represent a distinguishing feature, as it can vary from 7 s (e.g. #3253)

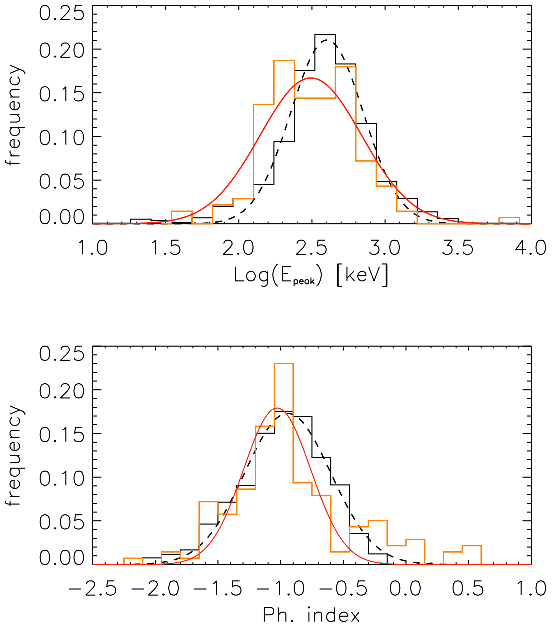

Figure 3.7 Normalized distribution of $E_{\rm peak}^{\rm obs}$ (*top*) and of the spectral photon indices α (*bottom*) of precursors and main emission episodes. Precursor distribution and gaussian fit are shown in colored filled line, main emission episode in black dashed line.

up to > 100 s (#3663).

The last three GRBs, namely #3663, #2700, and #3448 present hardly distinguishable spectral characteristics (i.e., both α and $E_{\rm peak}^{\rm obs}$). This is due either to the extremely low number of spectra extracted in the precursor, or in the main impulse, or both at the same time (see Figs. 3.14, 3.19, 3.22). In our opinion this prevents any further claim.

3.6 Conclusion

In this work we presented, for the first time, a time resolved spectral analysis of bright precursors based on spectral parameters, namely the photon spectral indices α and the observed peak energy $E_{\rm peak}^{\rm obs}$. This was done by using High Energy Resolution spectra extracted by K06 in a sample of 350 bright GRBs out of the complete sample of 2704 confirmed GRBs observed by the BATSE instrument. Of the 51 bursts with precursor present in K06, we selected a sample of 18 GRBs having at least two time resolved spectra of the precursor.

The comparison with the main emission episode has three outcomes. The first is that the photon spectral indices of precursors and main events are consistent, while the peak energies of the precursors are mildly softer (see Fig. 3.7). Secondly, both α and $E_{\rm peak}^{\rm obs}$ do show an evolution (extreme in a handful of cases) that defines a relation between the flux P and the spectral parameters (note that the $P - E^{\gamma}_{\rm peak,obs}$ correlation was recently reported (e.g. F09) regardless the presence of precursors). Finally we showed that delays do not represent a distinguishing feature in the trend of α or $E^{\rm obs}_{\rm peak}$.

We found one GRB (out of 18) in which the onset of the emission of the precursor is consistent with black–body emission (i.e., #5486 – see Fig. 3.9). This was expected, since Ghirlanda et al. (2003) showed that 5% of BATSE GRBs show extremely hard emission at the onset of the first impulse.

Moreover, comparing the integrated counts in the peaks of precursors with respect to the ones of the main impulses, we confirmed the results of B08 (see Fig. 3.3). Indeed precursors carry a significant fraction of the energy of the main emission episode, regardless the duration of the time interval of quiescence.

3.7 Outlook

Our results, in addition to B08, point strongly to the conclusion that the onset of emission of GRBs (called precursor), even if separated from the main emission episode by hundreds of seconds (in the observers frame), is indistinguishable from that of the main event. Moreover the delay remains a puzzling issue. This suggests that we should reconsider the idea of what a precursor is. Since our result is partially in contrast with L05 we cannot rule out the possibility that "real precursors" belong to another class of very dim pulses of different origin. Nonetheless, both kind of precursors can show very long delays, thus tackling any theoretical model for GRB prompt emission.

We identify at least three distinct lines of research that can be followed, as for the study of precursors:

1. Our work has been deemed interesting in particular by the LIGO collaboration, as for the use of precursor emission in short GRBs in connection with the emission of *gravitational waves* (see citations to Burlon et al. 2008 and Burlon et al. 2009 and references therein).

2. In Ghirlanda et al. (2011a) we showed that also short GRBs can display precursor emission, whose time resolved analysis is similar to the one of the main event. This has been possible uniquely due to the exceptional brightness of these events, which are among the 14 brightest ever observed by the *Fermi* satellite. An interesting possibility is to check in the whole GBM sample, once that it will have recorded several thousands of events, whether precursor emission is statistically less present in the BGO (higher energy detectors) than in the NaI (lower energy detectors) with respect to the main emission to which they are associated. This would not be a complete surprise, since already in this chapter we showed that the peak energy $E^{\rm obs}_{\rm peak}$ of precursors seems to be smaller than the one of the main emission. This would be another consequence of precursors following the spectral-energy correlations we mentioned, and of their selection criterium: a smaller peak flux corresponds to a smaller peak energy.

3. In Gruber et al. (2011b) we studied the extremely long GRB 091024, which was actually a composition of two precursors plus the standard main emission. The unusual characteristic, besides the duration, was an optical bump at a time of the burst where no $\gamma-$rays were detected. At the time of this work however, just partial and scarcely-sampled photometry of the afterglow was publicly available. This did not allow us to make strong claims beyond the standard scenario, therefore we interpreted the optical hump as a reverse shock, already seen in a handful of other GRBs. Another -more exotic- interpretation, could be that, since we argue that precursors are generated by normal fireballs, the hump was nothing by the onset of the afterglow of the first precursor.

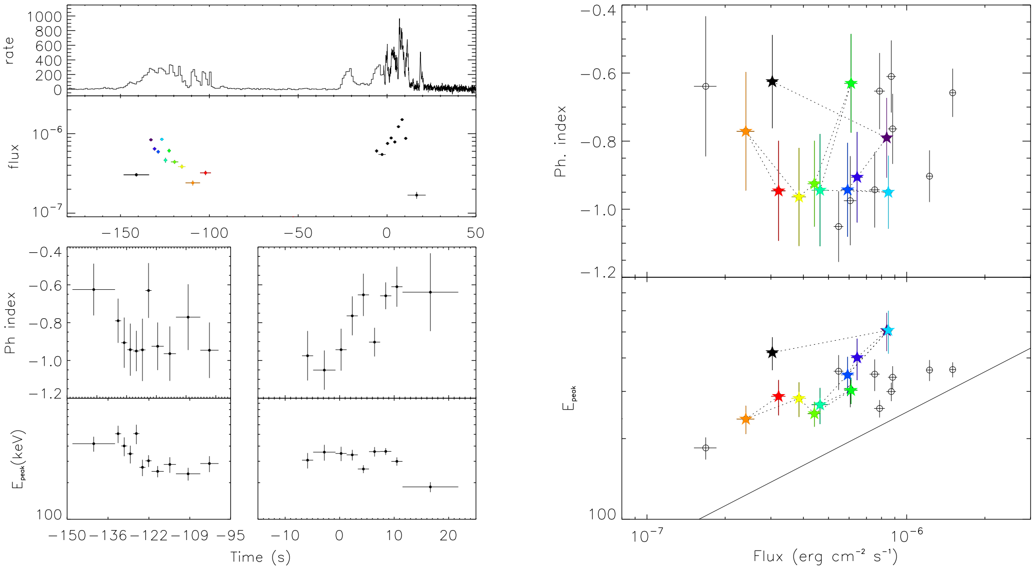

Figure 3.8 Trigger #7688. Color code and description as in Fig. 3.4

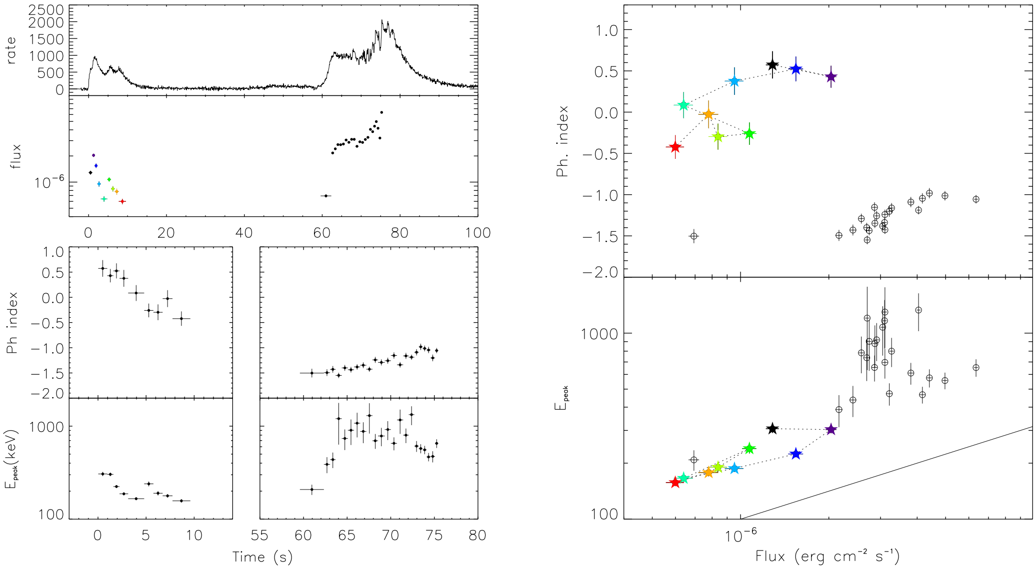

Figure 3.9 Trigger #5486. Color code and description as in Fig. 3.4

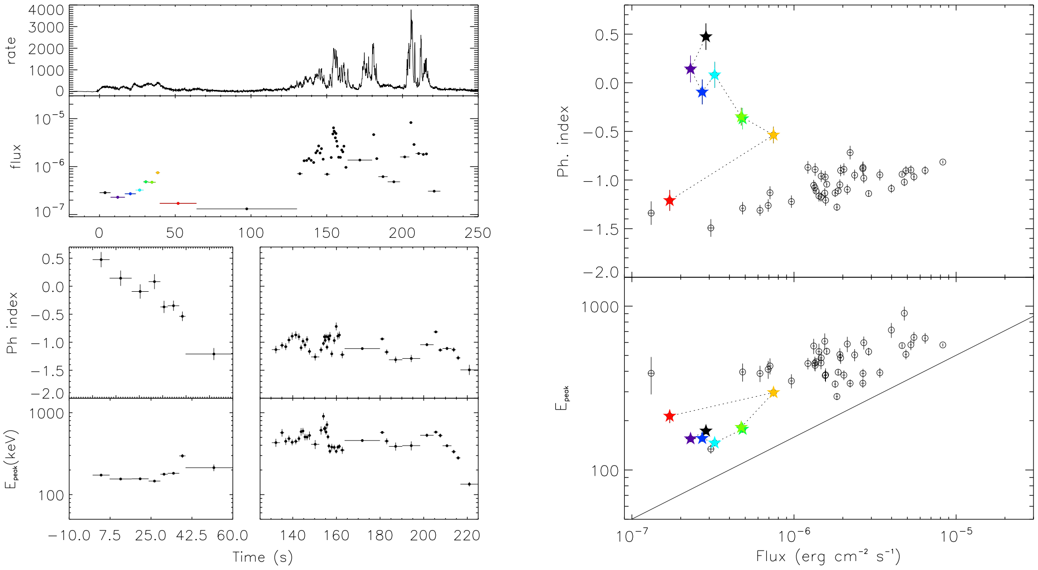

Figure 3.10 Trigger #6472. Color code and description as in Fig. 3.4

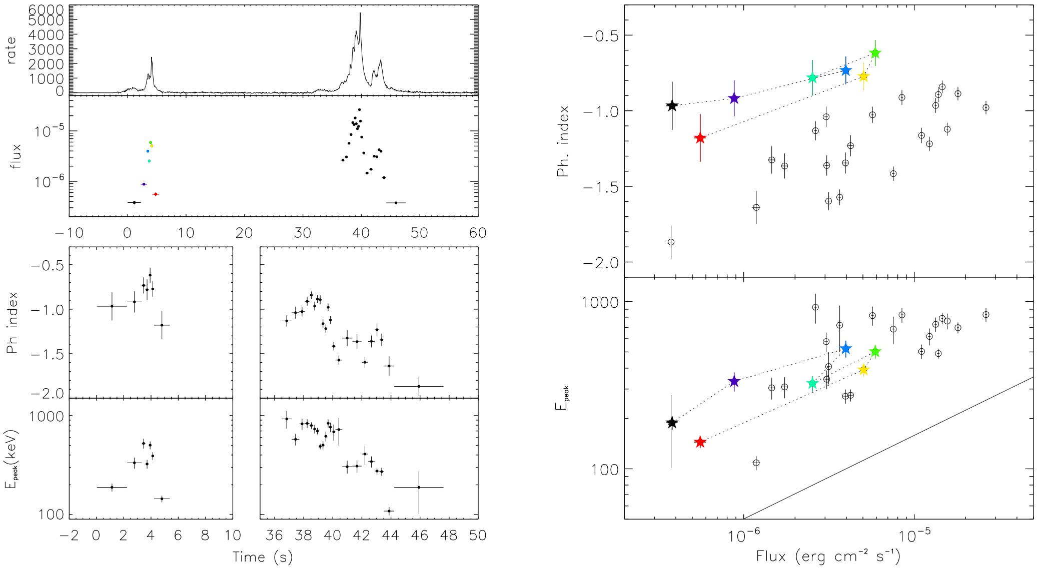

Figure 3.11 Trigger #3481. Color code and description as in Fig. 3.4–a

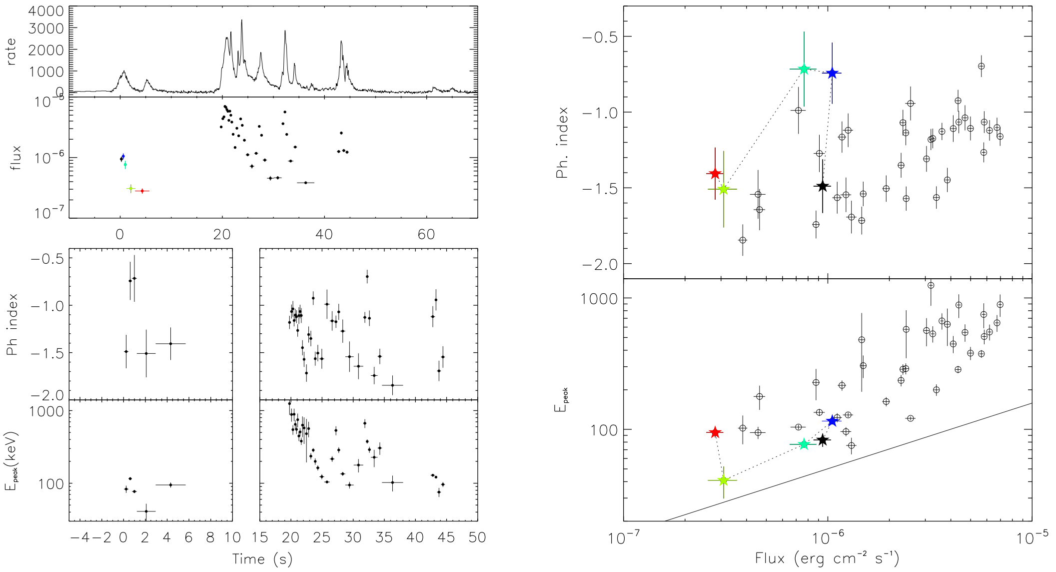

Figure 3.12 Trigger #3241. Color code and description as in Fig. 3.4

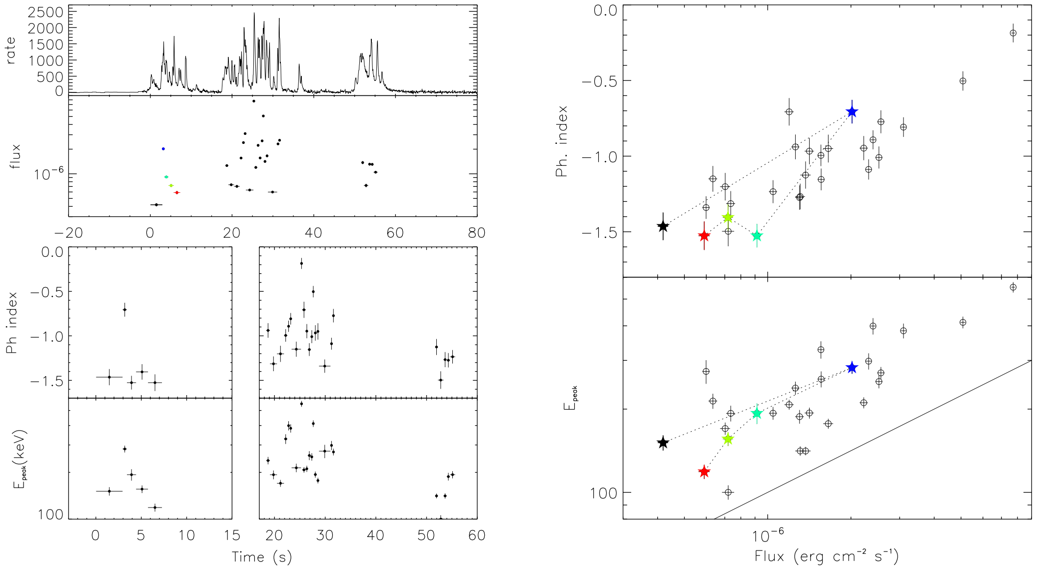

Figure 3.13 Trigger #1676. Color code and description as in Fig. 3.4

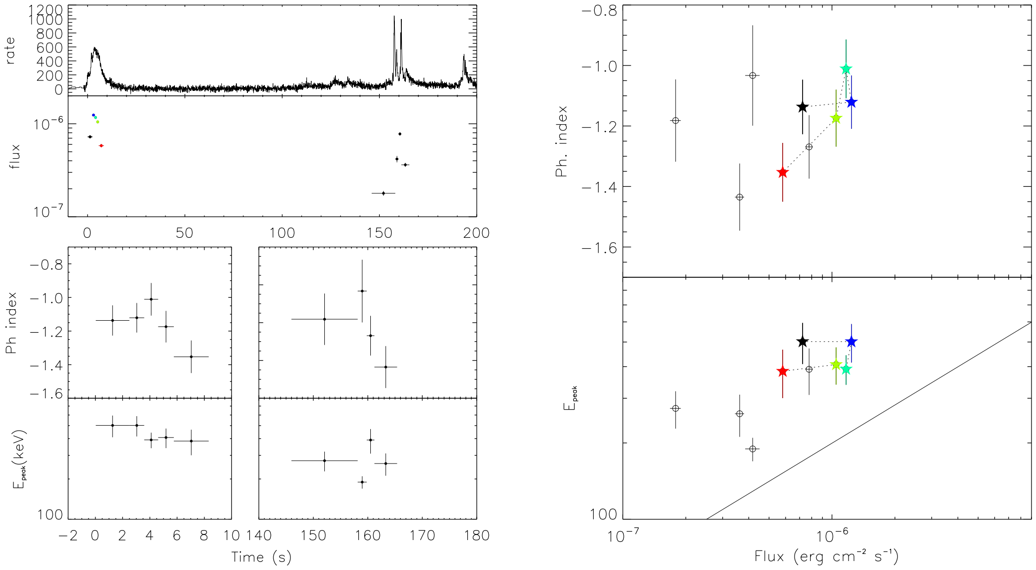

Figure 3.14 Trigger #3663. Color code and description as in Fig. 3.4

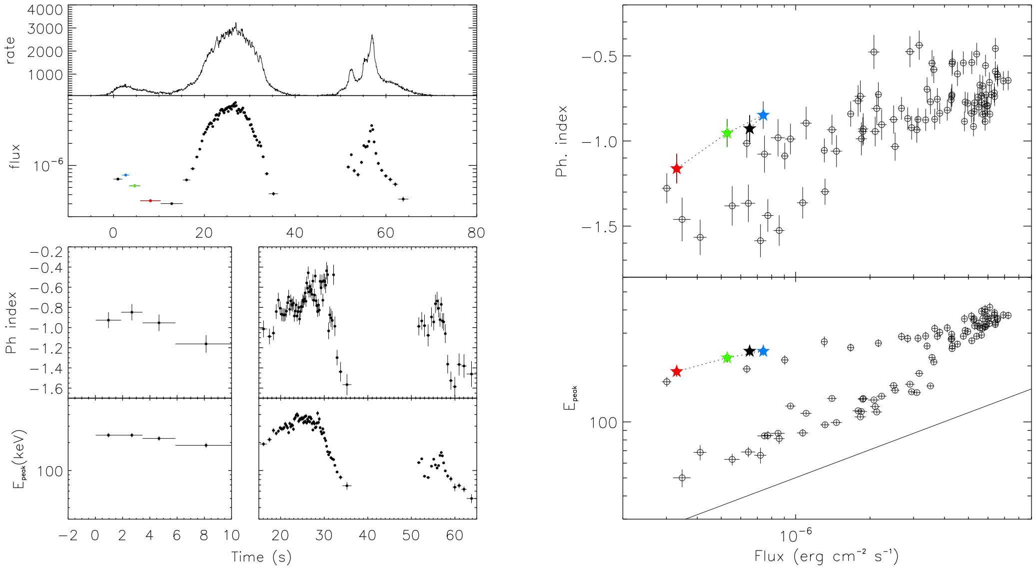

Figure 3.15 Trigger #3253. Color code and description as in Fig. 3.4

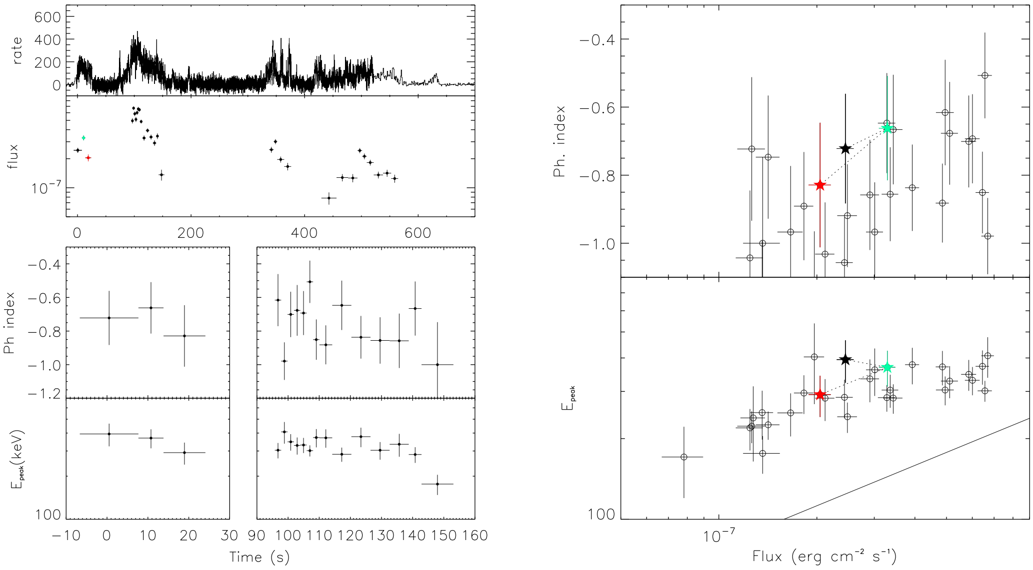

Figure 3.16 Trigger #6454. Color code and description as in Fig. 3.4

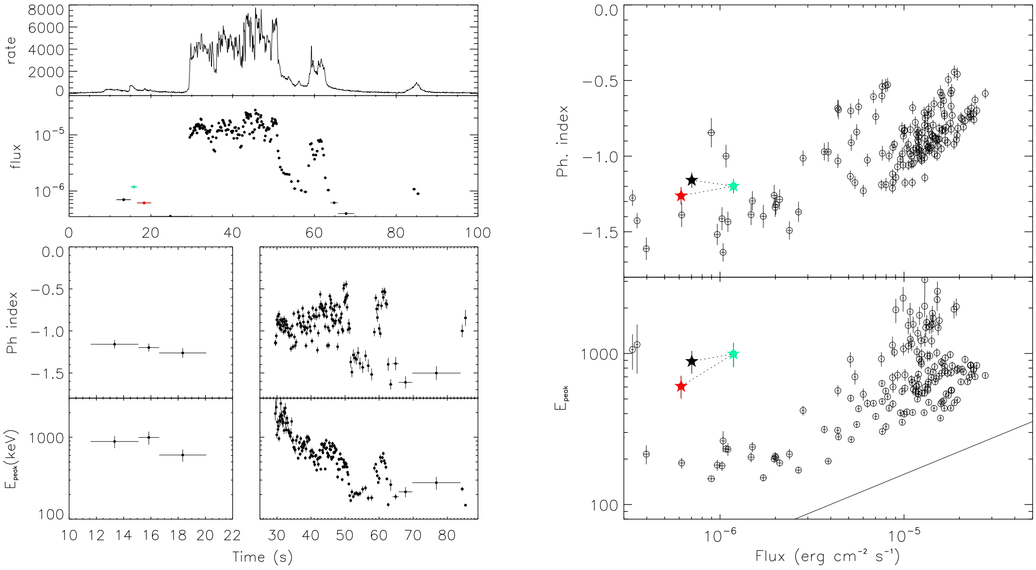

Figure 3.17 Trigger #3057. Color code and description as in Fig. 3.4

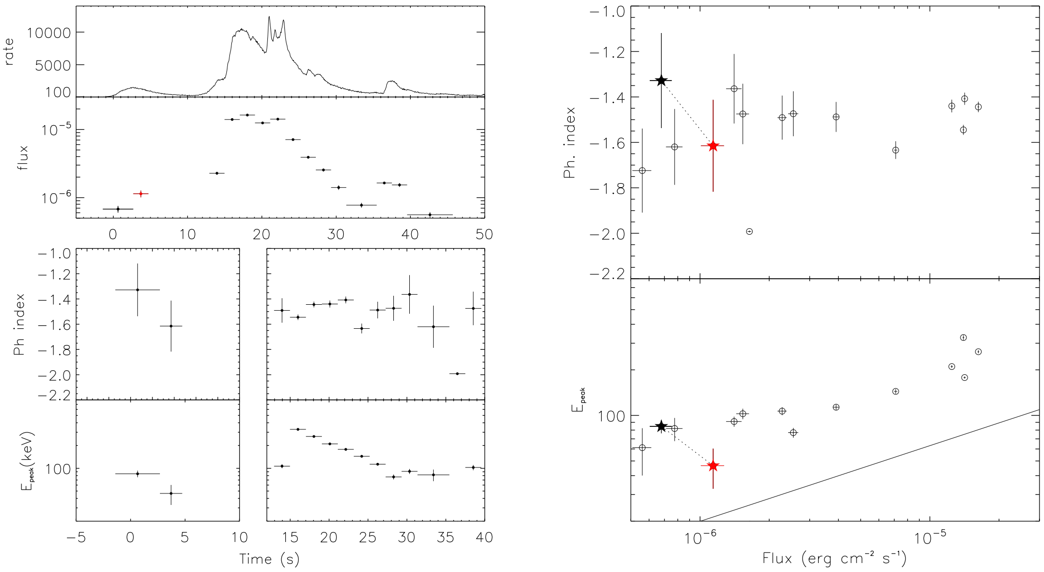

Figure 3.18 Trigger #4368. Color code and description as in Fig. 3.4

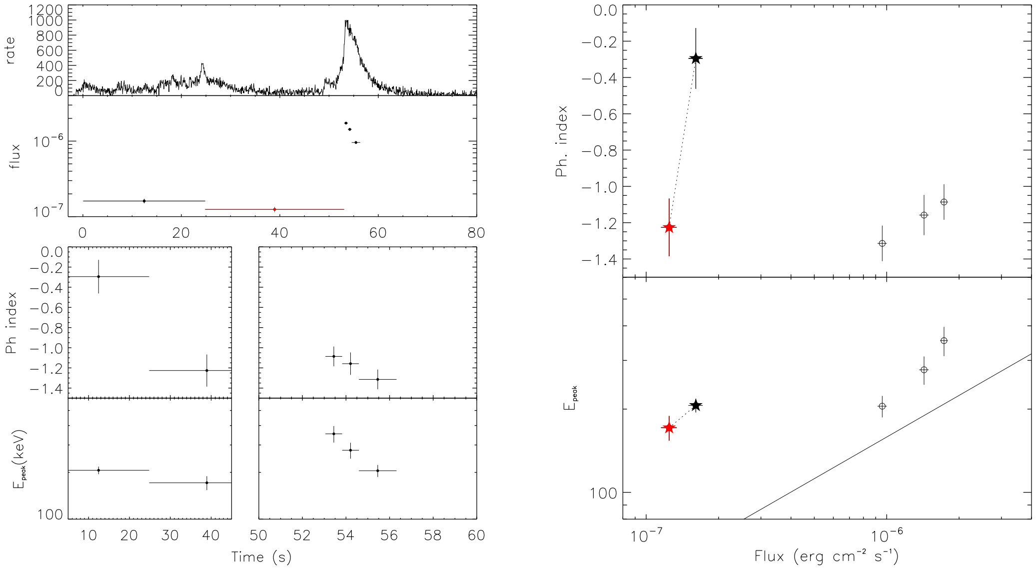

Figure 3.19 Trigger #2700. Color code and description as in Fig. 3.4

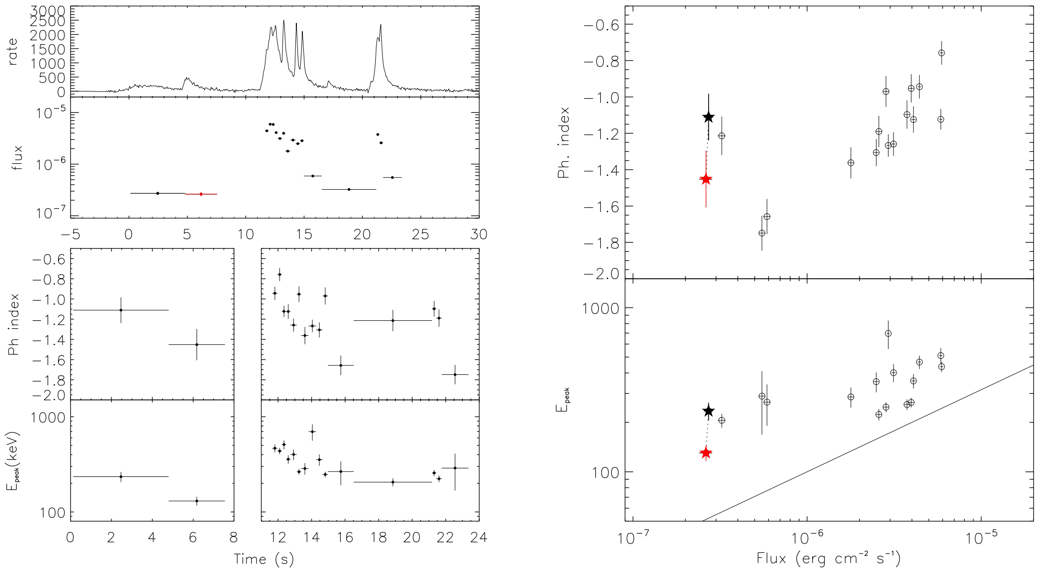

Figure 3.20 Trigger #1157. Color code and description as in Fig. 3.4

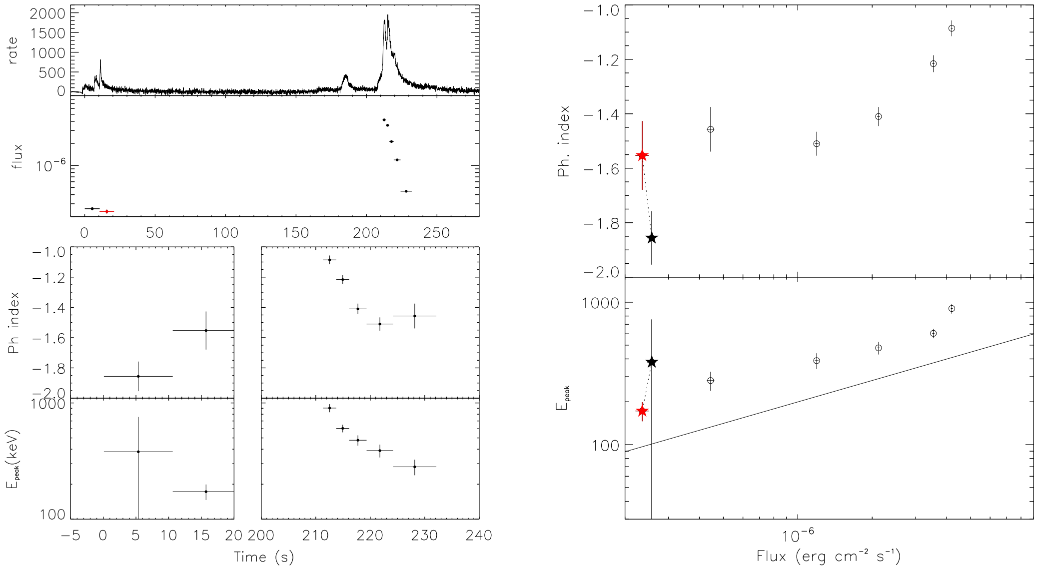

Figure 3.21 Trigger #6629. Color code and description as in Fig. 3.4

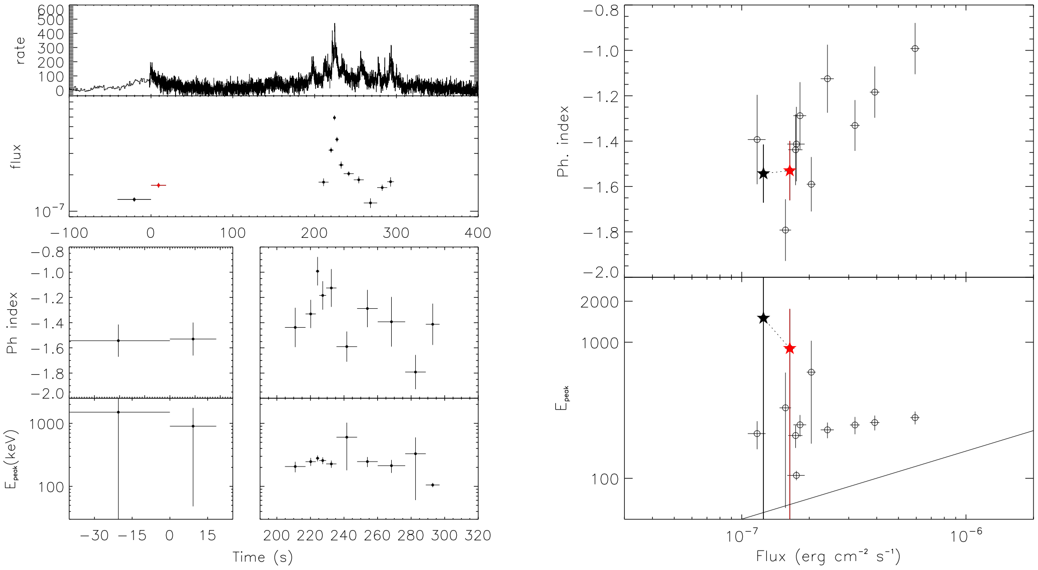

Figure 3.22 Trigger #3448. Color code and description as in Fig. 3.4

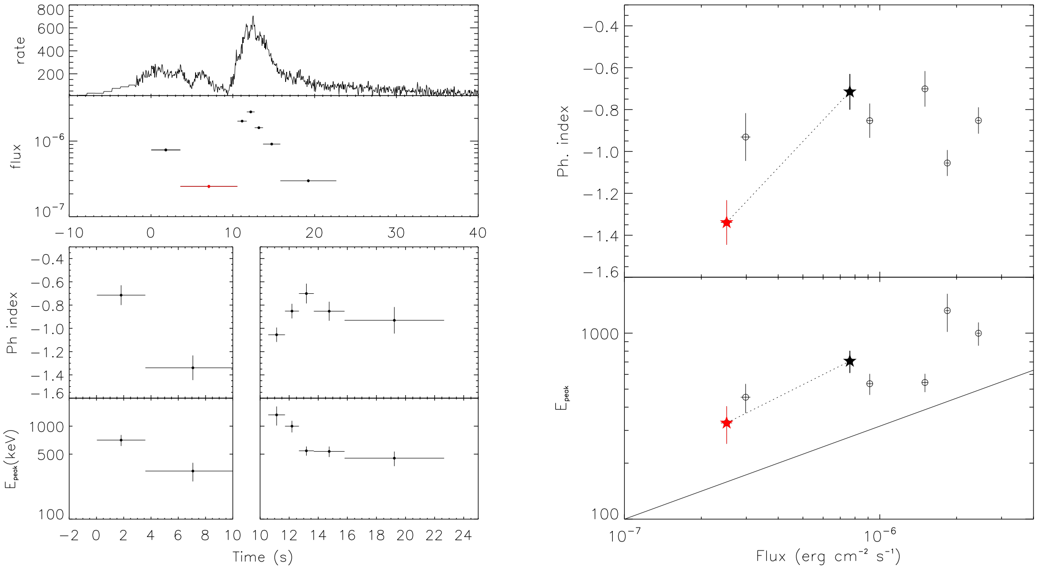

Figure 3.23 Trigger #3301. Color code and description as in Fig. 3.4

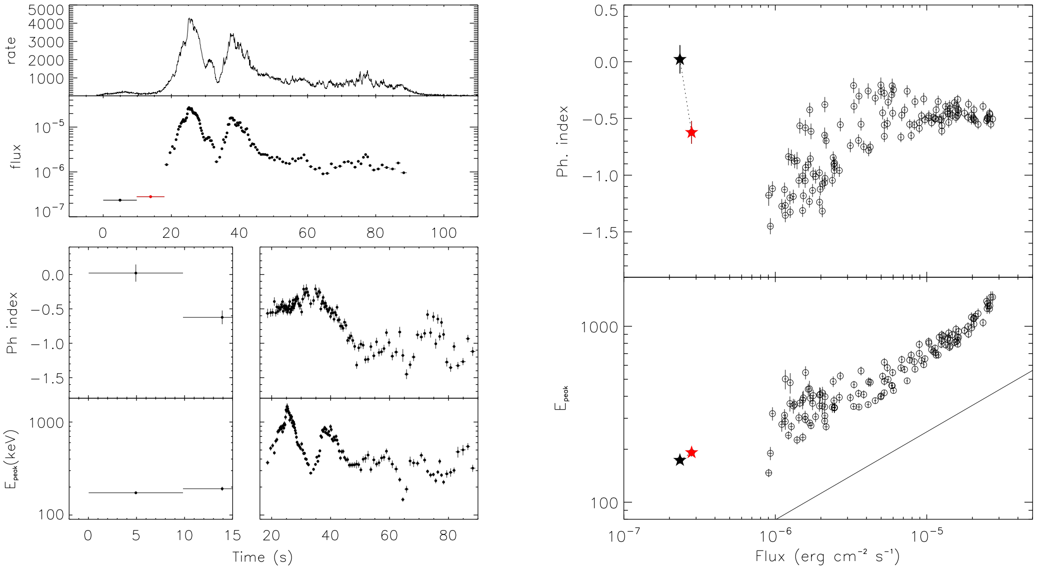

Figure 3.24 Trigger #7343. Color code and description as in Fig. 3.4

Chapter 4

Active Galactic Nuclei: an introduction

In the current paradigm all galaxies host a Super Massive Black Holes (SMBH) of mass $M \sim 10^6 - 10^9 M_{\odot}$ at their center. Observationally we note that the great majority ($\sim 99\%$) of the galaxies do not show core activity. Hence we infer that the BH of these galaxies are quiescent, meaning that they are not accreting material (or if they do, it is in a very inefficient fashion, either in the accretion mechanism itself or in the conversion of accretion energy in detectable radiation). The remaining $\sim 1\%$ that show activity are called Active Galactic Nuclei (AGN), and show an immense variety of properties. One in ten of these active galaxies develop also two counter-pointing jets which make them powerful Radio and γ-ray emitters (when the jets are pointing to us, these AGN are referred to as Blazars).

Disk Accretion: the Shakura and Sunyaev (1973) paradigm The most successful description of disk accretion is found in the pioneering paper by Shakura and Sunyaev (1973), which set the ground for efficient accretion on black holes of all scales, from stellar-sized ones to SMBH like the one powering AGNs. The description the authors display in that paper starts from the acknowledgement that since some angular momentum is present, the accretion flow naturally take from in a disk-shaped structure.

Large amounts of gas from the galactic environment can be funneled right into the potential well, releasing a fraction η of the gravitational energy of the material accreted in a given time span ($\dot{m}$), via heating through a certain viscosity parameter of the fluid up to temperatures of 10^5 K. It is just by effective removal of angular momentum that the gas can spiral closer in, be heated at higher temperatures, and shine at the luminosities required by the large distances (once that the community realized that AGN shine at whole distances, from the local universe to the early hundreds of million years after the Big Bang).

This produces a radiative luminosity $L = \eta \dot{m} c^2$, which is emitted mostly at optical-UV frequencies (in some cases up to soft X-rays) and manifests as the so-called "Big Blue Bump" (Shields, 1978), which can be modeled by a -multi black body- temperature profile (Shakura and Sunyaev, 1973) in the form given by e.g. Frank et al. (2002):

$$T^4 = \frac{3R_s L_{disk}}{16\pi\eta\sigma_{MB}R^3}\left[1-\left(\frac{3R_S}{R}\right)^{1/2}\right] \tag{4.1}$$

where σ_{MB} is the Maxwell-Boltzmann constant, and R_S is the Schwarzschild radius. Note that the bulk of emission of an AGN accreting at a fraction of its Eddington luminosity[1] will take place at $\sim 5R_s$, i.e. close the innermost stable orbit of a Schwarzschild (non-rotating) black hole, where the temperature is at maximum, and the frequency scaling of the peak in a $\nu F\nu$ representation is

$$T_{max} \propto (L_{disk}/L_{Edd})^{1/4} \times M_{BH}^{-1/4} \tag{4.2}$$

Hence more massive black holes have a bump emerging at softer energies.

The central BH is thought to be surrounded by a distribution of photo-ionized clouds of gas at distances 0.1-1 pc, that orbit at high speeds thus producing strong-broad emission lines (hence the name of this region -BLR- after the presence of Broad Lines). In the current picture at somewhat larger distances (1-10 pc) a dusty cold torus partially absorbs the emission of the BLR and of the central BH, and re-radiates it in the IR region of the spectrum, emerging as a IR bump (Elvis et al., 1994). The nature of the torus (homogeneous or clumpy) is still a matter of debate, and will be discussed more in detail in the following chapter. We recall also that clouds at even larger distances ($\sim 100\,\mathrm{pc}$) will orbit at smaller velocities and produce less prominent lines. This distant region is commonly referred to as Narrow Line Region (NLR). Noteworthy was the discovery of tight relations that link the mass of the BH and the mass of the hosting galaxy, or the velocity dispersion (or the luminosity) of the surrounding stellar bulge (Kormendy and Richstone, 1995; Magorrian et al., 1998; Ferrarese et al., 2001; Tremaine et al., 2002; Marconi and Hunt, 2003). These relations point towards a feedback mechanisms that couples the various components. Indeed the accretion power produced by the growth of the BH is 100-1000 times bigger than the binding energy $E_{bind} = GM_{Gal}^2/R_{Gal}$ of the galaxy, so some form of feedback is at least quantitatively possible. Nonetheless, the form this feedback takes is still a matter of debate since both energy (e.g. Silk and Rees, 1998) and momentum (e.g. Fabian, 1999) deposition can be invoked. As recalled by e.g. Fabian et al. (2009) winds, jets, and radiation pressure might all play a role, although in different phases of the accretion history.

As mentioned, the standard disk accretion theory dates back to Shakura and Sunyaev (1973), and it is beyond the scope of this chapter to recall some or many of the characteristics of this process. We will rather focus on the specific characteristics of how the X-ray and hard X-ray radiation is thought to be produced, with an insight into absorption and Compton scatter. We will also discuss briefly the importance of the discovery of a coupling of the properties of the BH, namely its mass, and the efficiency at which it is accreting, with the properties of the galaxy or the galactic bulge.

---

[1] The Eddington luminosity is defined as $L_{Edd} \equiv 4\pi GcMm_p/\sigma_T$, G and c being the gravitational constant and the speed of light, M and m_p the mass of the black hole and of the proton, σ_T the Thompson cross section.

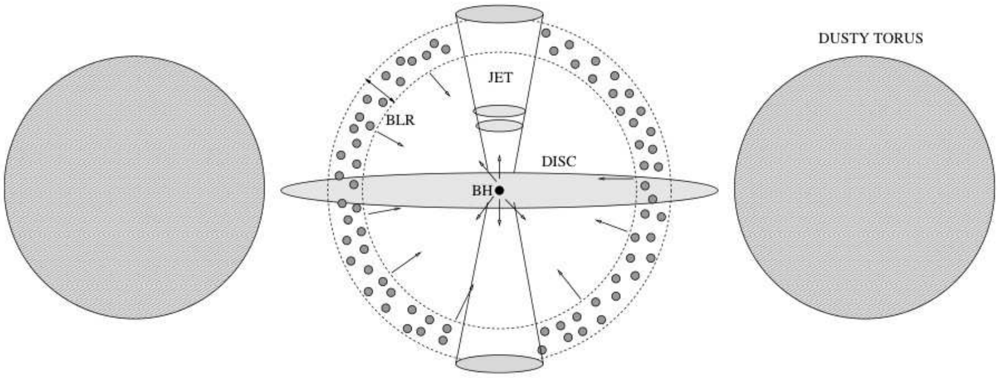

Figure 4.1 Schematic picture of the central region of an AGN. The central BH is surrounded by infalling gas from the accretion disk. Photoionized gas in the clumpy Broad Line Region (BLR) is located at 0.1-1 pc from the BH, and is responsible for intense broad line emission. At larger distances (1-10 pc) a dusty torus here depicted homogeneous -but maybe clumpy as well in nature- obscures both the disk and the BLR for observers located at large angles. Jets are also shown, even if their presence is not always required, and the NLR is not shown. This picture has been taken from publicly available notes by F. Tavecchio named "Gamma-ray emission of AGNs: a sketch".

Advection-Dominated Accretion: the Narayan and Yi (1994) solution The Shakura-solution we mentioned in the previous paragraph is not the only one available. A viscous rotating accretion flow in which most of the dissipated energy is stored rather then radiated is known as an Advection-Dominated Accretion Flow (ADAF, Narayan and Yi 1994), was proposed more than 20 years later. The ADAFs are characterized by gas that cannot cool efficiently and display a whole independent class of solutions for the flow. We summarize the main characteristics:

- the sound speed of the gas is nearly the Keplerian speed, which means that the temperature of the gas is nearly *virial*, i.e. the gas is "hot";
- the vertical thickness of the flow is comparable to the distance from the center, i.e. the flow is quasi-spherical and the *radial* velocity is much larger than the disk scenario;
- the so-called "Bernoulli parameter" is positive, i.e. the system can easily develop outflows of gas or winds;
- the luminosity is proportional to $L \propto \dot{m}^2$, and is much less than the one associated with "standard" accretion. Moreover, since the gas is hotter, the spectrum of ADAFs are harder than the thin-disk ones.

Already in the seminal paper on ADAFs, the authors suggested that this type of accretion, albeit mathematically valid for all $\dot{m}$, were more likely to occur at very low accretion rates, when the infalling material would not cool sufficiently to collapse to a thin standard-disk. Almost 20 years after , ADAF has become a fundamental description of quiescent-like BH like the one hosted at the center of our own Milky Way, as well as for interpreting a subclass of blazars known as BL Lacs.

4.1 A unified view of AGN

In the largely accepted model that unifies Seyfert galaxies (i.e. local AGN hosted usually by spiral galaxies, with moderate luminosities $\sim 10^{43}\,\mathrm{erg\,s^{-1}}$), the difference between different subclasses is assumed to be the inclination angle of observation with respect to the normal to the disk and the torus (Lawrence and Elvis, 1982; Antonucci, 1993; Urry and Padovani, 1995). The characteristics at the 0th order are that

- the presence or absence of the BLR is merely a matter of line-of-sight obscuration (i.e. is always present, sometimes not detectable);
- the obscuring torus is a physically separated entity, homogeneous in nature, optically and geometrically thick;
- the optical classification of AGN depends on the angular size of the torus;
- the optically obscured (or Sy2) AGN show absorbed X-ray spectra;
- the Sy1, unobscured AGN show simple power-law continuum (whose origin is as described in §4.4)

and these proved to be correct in most of the cases, even if they fail to explain some observational evidence. The failures of an unified view of AGN will be discussed as for our X-ray analysis is concerned in the following chapter. Here we recall some of the observations that *support* the idea of line-of-sight inclination being the main discriminating parameter: the presence of broad lines in the polarized light of Sy2 galaxies, which is explained as being due to the scattering towards the observer of the hidden Sy1 nucleus by warm material outside the torus (Miller and Antonucci, 1983; Antonucci and Miller, 1985); the anisotropic continuum emission seen through the ionization cones (e.g. Pogge, 1988; Wilson and Tsvetanov, 1994); the large -on average- X-ray column densities of Sy2 galaxies (first discussed extensively in Nandra and Pounds, 1994).

A large fraction of the AGN in the local universe show spectra which are obscured in the X-ray band by large amount of gas and dust, i.e. absorption that can take place very close in the BLR as well as much further out in the torus. This prevents us from looking directly at the black hole for energies smaller than a certain limit that depends upon the amount of intrinsic absorption. In addition, Compton scatter adds to photoelectric absorption. The bound-free cross section σ_{bf} for photons with energies in excess of $\gtrsim 10\,\mathrm{keV}$, is linked to the Compton cross section σ_C via the single scattering albedo $\lambda(E)$ (using the notation of Magdziarz and Zdziarski, 1995):

$$\lambda(E) \equiv \frac{\sigma_C(E)}{\sigma_C(E) + \sigma_{bf}(E)} \qquad (4.3)$$

which is almost unity in that energy range. The process of reflection of X-rays is in fact of paramount importance in high energy diagnostics of AGN, and is connected to several aspects like spectral hardening, reverberation of the primary continuum (Zoghbi et al., 2011), energy dependent variability studies (see the discussion in Ghisellini et al., 1994), and the contribution to the peak of the Cosmic X-ray Background (CXB) for population synthesis studies (Gilli et al., 2007; Treister et al., 2009). Note that, as we will detail in the following sections, the albedo *decreases* with photon energies in the soft-γ regime (photon energies $\gtrsim 50\,\mathrm{keV}$) due to the effect of a reduced scattering cross section, the preferred forward scattering, and the faster energy loss. According to Magdziarz and Zdziarski (1995) this results in a *softening* of the total (i.e. incident plus reflected) spectrum with respect to the incident component alone.

Compton-thick absorbers In the most extreme cases the obscuring material has a column density as high as the Thomson cross-section, hence the source is referred to as “Compton thick” (CT). This happens for $\mathrm{N_H} \gtrsim \sigma_T^{-1} \simeq 1.5 \times 10^{24}\,\mathrm{cm}^{-2}$. However, it should be pointed out that recently Draper and Ballantyne (2010) claimed that there might well be two distinct classes of Compton-thick objects. One is indeed associated to the predicted stage of black hole paroxystic growth and increased star formation, as envisaged by (e.g. Fabian, 1999). Black holes in this stage are expected to be accreting close to the Eddington limit, as a result of a merger event that has provided the black hole (and possibly the pair of BH, until coalescence) with large amounts of gas in a short time scale. On the other hand, their model requires also a distinct population of CT sources with $\lambda_{Edd} \equiv L/L_{edd} \lesssim 0.01$, which would contribute as well to the CXB. The puzzling state-of-the-art observational evidence is that also local CT objects can well display very high λ_{Edd}.

There are indications that (but see the review by e.g. Comastri, 2004) at least some torii are thick to Compton scatter. One of the first attempts to model the contribution of an obscuring torus to a Sy1-like AGN, taking into account scattering into the line of sight of primary photons that would otherwise escape detection, was carried on by Ghisellini et al. (1994), while very recent modeling that take into account a full relativistic treatment are by Yaqoob et al. (2010) and Brightman and Nandra (2011).

Note that if the torus is Compton-thick, obscured AGN should be dimmer also at hard X-rays, because a significant fraction of high energy photons are down-scattered, and can eventually be absorbed or emerge at lower energies. At the same time this implies a *bias* of past and present hard X-ray missions in detecting the most absorbed objects, as well as in the computation of their intrinsic (i.e. de-absorbed) luminosities. At the highest energies, the progressive decline of the Klein-Nishina (see the following section) cross-section implies that a larger fraction of photons pass the torus unscattered. So the flux received by an observer and the shape of the spectrum is a function of the optical depth of the torus (see fig. 4.2). A typical diagnostic of the presence of CT obscuring matter is provided by the intensity of the iron line, which is expected to be produced both by transmission through and reflection by the disk/torus complex. As far as the transmitted continuum is concerned, the line equivalent width (EW) increases

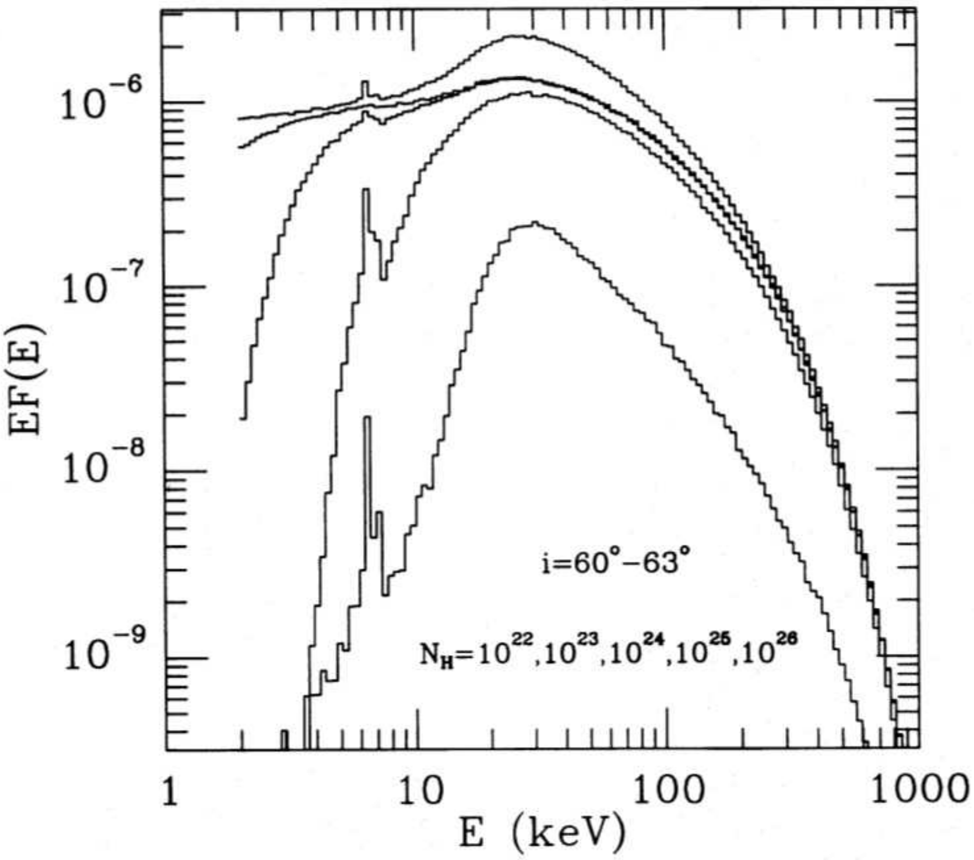

Figure 4.2 Simulated spectra of an AGN with progressively (from top to bottom) higher column densities, and inclination with respect to the observer of $\sim 60°$. The assumed torus half-opening angle is assumed to be 30°, and the incident primary continuum was modeled by a power-law with a cut-off at high energies kT$\sim$ 100 keV. This picture has been taken from Ghisellini et al. (1994).

for progressively larger columns, since the continuum is damped by absorption, up to EW$\sim$ 1 keV (Lightman and White, 1988). The signature of CT matter is also present on the so-called "Compton hump" peaking at $\sim$ 30 keV which is produced by significant absorption and Compton down-scatter at the low and high end, respectively. This looks like a flat (steep) power-law in a low (high) energy band. So it is mandatory to consider the band-pass of the instrument we use when we draw conclusions based on a pure power-law fit. The 'smoking gun' is also in this case the iron EW$\sim$ 1 keV.

We would like to point out that there is increasing evidence of a mismatch between the optical and X-ray classification (for instance in Chapter 5 we will refer as to absorption purely base on the X-ray analysis). This suggests that any classification one may encounter has to be used with a pinch of salt, specifying the band in which this classification is made. In fig. 4.3 (right panel) we show the sum of the contribution if reflection from cold and thick matter subtending 2π sr to a typical intrinsic power-law spectrum with an exponential cut-off at 300 keV. This is pictured together with the shape of the CXB as observed by many different observatories, and fitted by the model presented in Gilli et al. (2007).

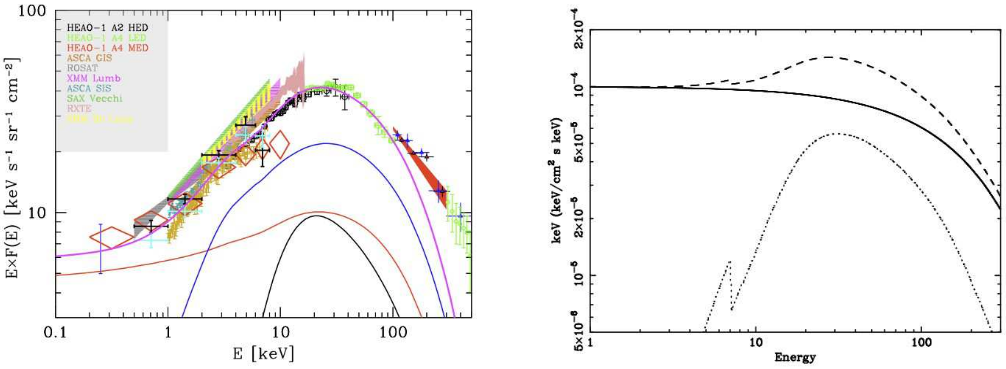

Figure 4.3 *Left panel*: the spectrum of the CXB as seen by different X-ray observatories. The relative contribution of absorbed (blue), unabsorbed (red), and CT (black) AGN are shown. *Right panel*: a cut-off power-law with $\Gamma = 2$ and $E_c = 300\,\text{keV}$ is shown (solid line), together with a component reflected by cold thick matter subtending 2π sr (dotted line), and the combination of the two (long-dashed line).

4.2 The Cosmic X-ray Background

The amount of obscuring gas in AGN, and the distribution of of column density with redshift z and luminosity are key ingredients in the understanding of the CXB (sometimes referred to as simply XRB). Setti and Woltjer (1989) and later Madau et al. (1994), Comastri et al. (1995), up to the more recent works by Gilli et al. (2007) and Treister et al. (2009), there is little doubt in associating the CXB to the integrated emission of unobscured, obscured, and Compton-thick AGN (see also fig. 4.3, left panel). Albeit a description of population synthesis models is way beyond the scope of this section, it might be useful for the reader to focus on the main features (Comastri, 2004) of these models:

- assume a template for the “canonical”, unobscured AGN
- add to the template the N_H distribution in order to model the right fraction of absorbed AGN
- fold all the spectra with an evolving X-ray luminosity function with best fit parameters determined from soft X-ray surveys

By varying the N_H distribution until a good fit to the XRB is determined, source counts[2] in different energy bands, and redshift distributions at different limiting fluxes are obtained. Notwithstanding the discrepancies among different measurements at the

---

[2] A useful tool is public available at http://www.oabo.inaf.it/~gilli

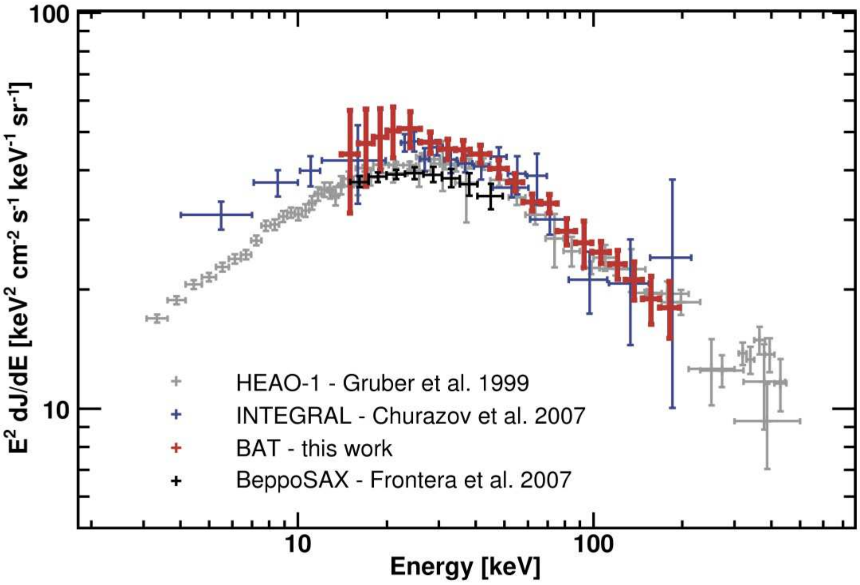

Figure 4.4 The CXB as seen by hard X-ray observatories. The picture is taken from Ajello et al. (2008b).

peak of the spectrum, observations agree within 10%. Fig. 4.4 shows a compilation of CXB observations by hard X-ray telescopes. As pointed out in Ajello et al. (2008b) and Ajello (2007) it is clear that the scatter in CXB intensities does not depend solely on the adopted spectra for the Crab Nebula. Some of the measurements might still be affected by systematic uncertainty in the instrumental response used. To our knowledge, BAT is the only instrument for which a dedicated instrumental response has been derived and tested for the analysis of the CXB, while in general all observatories are designed and calibrated for the study of point-like sources. Therefore, the reliability of the XRB measurement depends on the discrimination of that component among others that contribute as well at the overall "background" (i.e. total flux minus point-like sources). This in turn translates into a similar inaccuracy in the determination of the fraction of CT sources, which is still of the order of 10%.

The prediction of Gilli et al. (2007) are in agreement with other authors (Hasinger et al., 2005; La Franca et al., 2005; Ueda et al., 2003), finding that the obscured to unobscured AGN ratio is *luminosity dependent* and decreases from 4 to 1, whereas the number of CT sources is predicted to be as high the the obscured Compton-thin ones. The dependence of the luminosity functions with absorption, and the ratio of obscured AGN with luminosity is discussed thoroughly in chapter 5.

4.3 Radiative processes

We introduce with a recap on the most fundamental radiative processes, the discussion in the following session on two scenarios, with a focus on thermal Comptonization and we refer the reader to Pozdnyakov et al. (1983) and Rybicki and Lightman (1979) for a complete description. A more detailed description of this section can be found in publicly available notes by G. Ghisellini under the name "Beaming, Synchrotron, and Inverse Compton", from which the pictures are taken. We take four 'steps' to get to the final description, and we start with a brief recap on *direct* Compton scatter, the Klein-Nishina regime, inverse Compton, and eventually the Comptonization produced by a population of electrons with a thermal energy distribution (like a "hot corona" above an accretion disk that pumps radiation upwards).

4.3.1 Direct Compton scatter

Scattering is the simplest interaction between photons and free electrons. When the electron is at rest and the energy of the incoming photon (as seen by the electron) is small compared to $m_e c^2$, the process is known as *Thompson scatter.* When $h\nu \gtrsim m_e c^2$ a quantum treatment is required and the regime is known as Klein-Nishina. If we consider the scattering process as a collision between an electron and a photon, and we apply the conservation rules for energy and momentum, then we get:

$$x_1 = \frac{x}{1 + x(1 - cos\,\theta)} \tag{4.4}$$

being x and x_1 the energy of the photon before and after the scattering measured in units of the rest mass of the electron, respectively. The angle between the incoming and outgoing photon is θ. Note that for $x \ll 1$ the scattered energy is $x_1 \simeq x$, i.e. we are in the classical Thomson regime because the electron does not recoil.

4.3.2 The Klein-Nishina regime

We start from the Thomson cross section:

$$\left(\frac{d\sigma}{d\Omega}\right)_{unpol} = \frac{1}{2} r_0^2 (1 + cos^2\,\theta) \tag{4.5}$$

which integrated over all angles gives the known value $\sigma_T = (8/3)\pi r_0^2 = 6.65 \times 10^{-25}\,\mathrm{cm}^2$ (r_0 being the classical electron radius) which is the classical limit of the more general Klein-Nishina cross section:

$$\frac{d\sigma_{KN}}{d\Omega} = \frac{3}{16\pi}\sigma_T \left(\frac{x_1}{x}\right)^2 \left(\frac{x}{x_1} + \frac{x_1}{x} - sin^2\,\theta\right) \tag{4.6}$$

which can be simplified by inserting equation 4.5 and integrating over all angles to get the total KN cross section:

$$\sigma_{KN} = \frac{3}{4}\sigma_T \left\{ \frac{1+x}{x^3}\left[\frac{2x(1+x)}{1+2x} - \ln(1+2x)\right] + \frac{1}{2x}\ln(1+2x) - \frac{1+3x}{(1+2x)^2} \right\} \tag{4.7}$$

which can be seen, normalized to the Thomson cross section, in fig.4.5. This was discussed in the previous sections, as far as the torus of AGN becoming more transparent for high energy radiation.

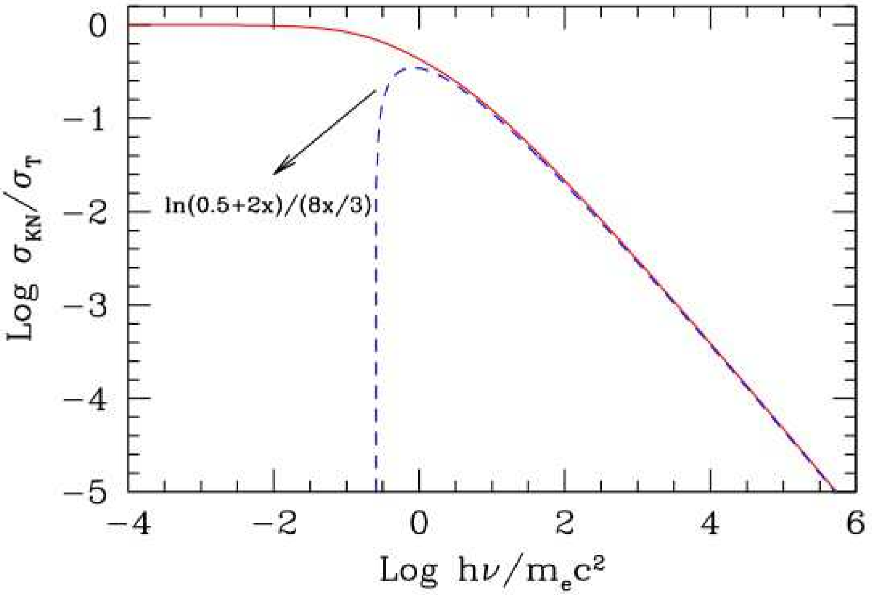

Figure 4.5 The total Klein-Nishina cross section as a function of energy. The dashed line is the limit for $x \gg 1$.

4.3.3 Inverse Compton scatter

Let's now imagine that the electron responsible for the scattering in not at rest, but rather has an energy greater than the typical photon energy: in this case there can be a net transfer from the former to the latter. We recall just a few useful formulae, like the energy gain after a single scattering event given by (in the lab frame):

$$x_1 = x\frac{1 - \beta cos\,\psi}{1 - \beta cos\,\psi_1} \tag{4.8}$$

where we used the same notation adopted before, and ψ (or ψ_1) is the angle between the photon direction and electron velocity before (after) the encounter. This applies to a single photon-electron event, but for an isotropic distribution of photons, in the limit $\gamma \gg 1$, the energy photon energy after scattering is:

$$\langle x_1 \rangle = \frac{4}{3}\gamma^2 x \tag{4.9}$$

where γ is the Lorentz factor of the moving electron.

Now, if we consider a population of electrons, with a non-thermal energy distribution in the form $N(\gamma) = N(E)(dE/d\gamma) = K\gamma^{-p}$ in the range $[\gamma_{min}; \gamma_{max}]$, this -as in the case of synchrotron radiation- will produce an energy spectrum whose slope is linked to p via $\alpha = (p-1)/2$. The similarity is not a chance coincidence, since both synchrotron and IC scatter spectra of each particles are peaked at a typical frequency, γ^2 times the starting one.

4.3.4 Thermal Comptonization: thin vs. thick cases

Finally, let's consider the process of *multiple* scattering of a photon due to a population of electrons with a *thermal* energy distribution. The final form of the spectrum is the superposition of many spectra, and the details of the particle distribution will be lost (i.e. it is not required that is a perfect Maxwellian, it just needs to be peaked) in the final shape. The parameter measuring the importance of the inverse Compton process, and the multiple scatterings is known as *Comptonization parameter* defined as:

$$y = [\text{average}\,\#\,\text{of scatterings}] \times [\text{average fractional energy gain for event}]$$

If $y > 1$ the Comptonized spectrum has more energy than the one of the seed photons, at the expense of the thermal energy of the electrons.

Given the Thomson scattering optical depth $\tau_T = \sigma_T n R$, where R is the size of the source and n the electron density, the average number of scattering a photon will experience before leaving the source is τ_T^2. The average gain per scattering is non-trivial to compute, and depends on whether we are dealing with the relativistic Maxwellian, rather then the non-relativistic case. In short anyway, we know from equation 4.9 that the problem reduces to compute the average $\langle\gamma^2\rangle$ factor. If we define $\Theta \equiv kT/m_e c^2$, than the fractional gain $\Delta x/x$ per scattering is $16\Theta^2$ in the relativistic case, and $4\Theta - x$ in the non-relativistic one. Therefore we can re-write the Comptonization parameter as:

$$y = \max(\tau_T, \tau_T^2) \times [16\Theta^2 + 4\Theta - x] \tag{4.10}$$

Thin case In this case $\tau_T < 1$, a fraction $e^{-\tau_T}$ of the seed photons escape without doing any scattering, while a fraction $1 - e^{-\tau_T} \to \tau$ undergoes at least one scattering. This fractions can be worked out for each scattering order (producing the vertical shift of the spectrum in figure 4.6), while the amplification (producing the horizontal shift) at each scattering is given by

$$A \equiv \frac{x_1}{x} = 16\Theta^2 + 4\Theta + 1 \sim \frac{y}{\tau_T} \tag{4.11}$$

neglecting the downscattering factor $-x$. It is trivial therefore to see (fig. 4.6) that the energy spectral index α is produced by the sum of all the scatterings, each of which produces an enhancement $\log(A)$ in the abscissa, and a decrease $-\log(\tau_T)$ in the ordinates, leading to:

$$\alpha = -\frac{\log(\tau_T)}{\log A} \sim -\frac{\log(\tau_T)}{\log y - \log(\tau_T)} \tag{4.12}$$

leading to the spectral behaviors described in table 4.1.

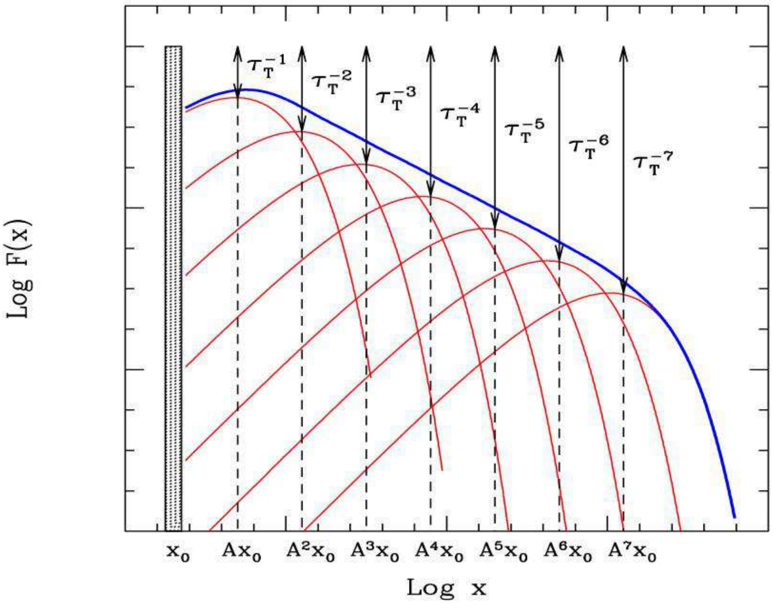

Figure 4.6 Multiple Compton scattering in the thin-case scenario ($\tau_T < 1$). A fraction τ_T of the photons of the previous scattering undergoes another scattering event, and the frequency is enhanced by a factor A, until the frequency $x = h\nu/m_e c^2$ equals the electron temperature Θ. Further scatterings make the distribution evolve only in the 'vertical' direction, producing the cutoff.

Table 4.1 Thin case: Comptonization parameter and energy spectral index

Compt. par. y	Spectral index α	
~ 1	~ 1	flat in $\nu F \nu$
> 1	< 1	flat/hard spectrum
< 1	> 1	steep/soft spectrum

Mildly-thick case In this case $\tau_T \gtrsim 1$, one needs to solve the Kompaneets equation (Rybicki and Lightman, 1979). The result is always a power-law with spectral index

$$\alpha = -\frac{3}{2} + \sqrt{\frac{9}{4} + \frac{4}{y}} \tag{4.13}$$

Extremely thick case This is also referred to as "saturation" (i.e. $\tau_T \gg 1$), the interactions between photons and matter is maximally efficient. Hence they go to equilibrium, sharing the same temperature. The resulting spectrum has a Wien shape, and the intensity $I(x)$ has the typical frequency dependence:

$$I(x) \propto x^3 e^{-x/\Theta} \tag{4.14}$$

which is *harder* than a black-body at low frequencies.

“Quasi-saturation” case Finally, when $\tau_T > 1$, and $y > 1$ we have to imagine a source with large τ_T, and soft photons all around. In this case, only the photons which are produced close to the surface where $\tau_T = 1$ are able to freely leave to infinity without incurring in a single scattering event. The remaining fraction $(1 - 1/\tau_T)$, i.e. almost all the photons, remain inside. This is true for each scattering: a small fraction escapes, a dominant fraction undergoes another scattering. This effect translates into an accumulation of photons at the classical frequency $x = 3\Theta$, which produces the Wien bump. It’s important to note that the slope of the spectrum below the bump is always $\alpha = 0$ (see fig. 4.7, left panel), since at any scattering only a *fixed* amount of photons leave the source. In this sense the spectral index is “saturated” in a part of the spectrum, and the slope is independent of the value of τ_T or the temperature of the electrons. By changing τ_T the flux in the x^0 portion of the spectrum changes in the opposite direction, and the Wien bump shifts at lower frequencies (i.e. dominates earlier, until reaching the case discussed above $\tau_T \gg 1$).

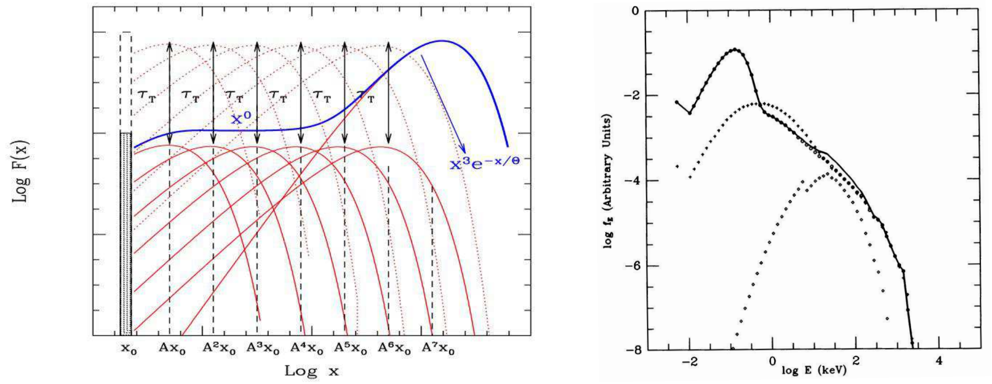

Figure 4.7 *Left panel*: multiple Compton scattering in the “quasi-saturated” scenario ($\tau_T > 1$, $y > 1$). Nearly all photons are scattered, only a fraction $1/\tau_T$ escapes. therefore the number of photons escaping at each scattering order is the same. In the flat part $F(x) \propto x^0$, but when the photon frequency is $\sim \Theta$, radiation and electrons are in equilibrium and the Wien bump is formed. *Right panel*: the solid line represents the Monte Carlo simulation of the two-phase emitted spectrum in Haardt and Maraschi (1991). The downscattered component is shown (crosses) along with the reflected one (diamonds). The parameters of the simulation are $\tau = 0.1$ and $\Theta = 0.51$. The soft photons source is a black-body of temperature $kT = 50\,\mathrm{eV}$, which is clearly emerging in the upper left part of the plot.

4.4 The X-ray emission in AGN

As discussed in the previous sections, the X-ray continuum of AGN is modeled with a cut-off power-law, which is then folded with absorption and Compton scatter processes. Scattering, bound-free transitions, atomic excitations play all a role in determining the final shape of each AGN, and contributing to the spread of the observed properties. As already noted by Pounds et al. (1990), the complex spectra can be described as a intrinsic power-law of slope $\alpha \sim 0.9$ (in a $F(\nu) \propto \nu^{-\alpha}$, i.e. related to the photon spectral index via $\Gamma = \alpha + 1$) which undergoes the recalled physical processes.

In this section we discuss the most relevant radiative process for the primary emission of AGN, in the two most successful scenarios: the standard "corona scenario" (Haardt and Maraschi, 1991) in which a distribution of hot electrons sandwiches the accretion disk, up-scattering the soft thermal photons of the Big Blue Bump to high energies (note that inverse Compton had been discussed by e.g. Zdziarski, 1985 and Zdziarski et al., 1990); the other scenario, known as "aborted-jet scenario" (Ghisellini et al., 2004), posits that all AGN are able to produce jets at some level, but the ones that have jets unable to escape the gravitational potential of the BH will collapse onto the newly formed ones, in a mechanism similar to the internal shocks for GRBs.

4.4.1 The corona scenario

We show in fig. 4.7 (right panel) the result of the pioneering work by Haardt and Maraschi (1991), to account for the primary emission of AGN. As we have explained in the previous discussion, scattering is well able to play a fundamental role in the broad-band X-ray emission of AGN, and this result matches nicely with the observed values of the spectral indices. We have also seen that in some cases the expected value of the spectral index is independent from other parameters, making it a rather universal characteristic. The importance of Compton scatter had been invoked already by Pozdnyakov et al. (1983) or Zdziarski (1985) (and see references therein as a result of a large discussion in the '70 about this topic), but a "two-phase" treatment was first proposed by Sunyaev and Titarchuk (1989) (analytically) and Haardt and Maraschi (1991) (numerically).

By two-phase we mean that the authors reconsidered *thermal Comptonization* as the basic mechanisms for producing the X-ray continuum in a new framework of the inner region of emission. The key ingredient is to assume that a fraction of the gravitational energy of the accreted material is released in a geometrically/optically thin, hot layer that "sandwiches" the cold standard accretion disk, i.e. a "corona". The two phases can coexist if there is a mechanism that transports and dissipates part of the binding energy outside the cool phase (the disk). A situation of this kind had been already discussed by models that invoked accretion plus magnetic viscosity, and dissipation through buoyancy and/or reconnection above the disk. Regardless the details of how energy is transferred from the disk to the corona, in order to keep the electrons "hot", the main step forward in this work was to consider the coupling of the two phases: the soft photons feed the corona, while the Comptonized photons heat the thick phase. The resulting spectrum (see fig. 4.7, right panel)is the result of the superposition of three spectral component:

1. a black-body from the cold-thick phase, i.e. the disk;
2. a cut-off power-law from Comptonization in the hot-thin layer;
3. a reflected component by the disk.

The findings of that work, was that if energy dissipation occurred mainly in the hot phase, the three components of typical Seyfert galaxies' X-ray spectra could be understood. The shape of the power-law component and its small dispersion were accounted for; the strength of the reflection bump and of the Fe line were explained due to the 2π coverage of the hot phase and the asymmetry of the Comptonized flux[3]. If the requirement on the covering factor of the disk is released, some black-body photons can emerge freely, and in turn translating in a softer spectrum.

4.4.2 The aborted-jet scenario

At odds with the more conventional "corona" scenario, Ghisellini et al. (2004) proposed that the ultimate source of energy is the rotation of the black hole. As a matter of fact, there is a general trend in the community in thinking of AGN within the dichotomy radio-quiet and radio-loud (but see the recent work by Broderick and Fender, 2011). The Seyfert galaxies we have dealt with in this section, and that are the subject of chap. 5 were generally thought to be associated with slowly rotating BH, while distant radio-emitting quasars were thought to be generated by highly spinning, highly efficient BH. On the other hand, we are quite confident that at least some of the close, radio-quiet objects are hosting BH spinning at high speed (e.g. starting from the well studied case of MGC-6-30-15, Tanaka et al., 1995), and that emission takes place very close in the accretion system, i.e. at a few Schwarzschild radii, which typically are needed to be just above the disk, in order to account for the reflected component. Note also that the definition of radio-quiet tends to be misleading, being commonly associated to "radio-silent". In fact, this has been shown to be a wrong statement, since probably all AGN are able to produce radio emission at some level. The origin of relativistic electrons that can emit via synchrotron radiation can be debated, since it could originate in a jet or in other (less collimated) forms of outflows. In general though, the idea that some radio emission is always present, has been supported by VLBI imaging (Ulvestad, 2003) and by the coupling of X-ray and radio emission (Panessa et al., 2007), which are consistent with the presence of small jets at the sub-pc scale in Seyfert galaxies.

Ghisellini et al. (2004) argue that all black holes are able to produce some kind of collimated outflow/jet, but only in the minority of the cases ($\sim 1/10$th, i.e. the classic radio-loud family) the jets are successfully launched and accelerated to relativistic speeds. In the majority of cases the jet is "aborted", yet it is responsible for weak radio emission. The novelty of their work is to assume that these jet are sub-relativistic *and* that most of emitting electrons are thermal, with sub-relativistic temperatures.

Being unable to escape the gravitational potential of the BH, the shells of emitted material are bound to re-collapse onto the central source, but they clash with the subsequent shell in a framework which is reminiscent of the one ("internal shocks") discussed in 2.2.3. The kinetic energy of each shell is dissipated, and under the assumption

---

[3] Note that if one places a relativistic electron above an infinitely extended disk which emits radiation, the ratio of Compton flux downward over upward is seven, independently on any parameters, provided that the electron is in the vicinity of the disk.

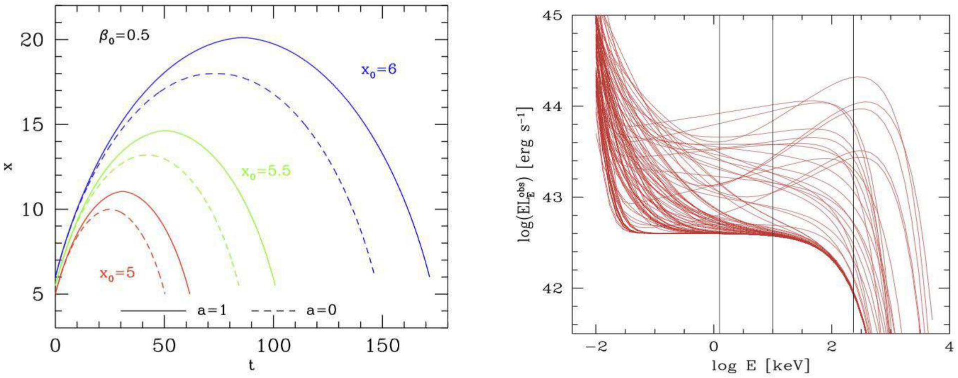

Figure 4.8 *Left panel*: trajectories of test particles launched along the spin axis of a maximally ($a = 1$, solid line) and Schwarzschild (dashed line) BH for different initial radii. The initial velocity is the same for all $\beta_0 = 0.5$. Note that times are measured in units of the initial light crossing time, and distances in units of gravitational radii. *Right panel*: adapted from Ghisellini et al. (2004), time dependent spectra emitted by a $10^8\ M_\odot$ black hole. Vertical lines mark the 1, 10, and 200 keV bands.

of equipartition among protons, electrons, and magnetic field, this can be radiated away via inverse Compton, once temperatures and optical depths are calculated.

In fig. 4.8 we show some of the quantitative results of their simulations: in the left panel we show the trajectories of test particles which are ejected along the rotation axis of a maximally rotating Kerr black hole, with the same initial speed but with different launching distances. In the right panel, some examples of time dependent spectra are shown. These are based on the basis of thermal Comptonization, with a given temperature of the seed photons (in this case 5 eV). The vertical lines in the plot show the observing windows of the typical focussing X-ray telescope (1-10 keV) and the limit of the *Swift*–BAT intrument (200 keV).

Note that this model is not completely alternative to the “corona scenario”, since both can well be at work. The authors argue that also a steadier component in the X-ray band is required to account for the observe spectral indices, but it is certainly an intriguing possibility that deserves to be discussed.

Chapter 5

Three-years *Swift*/BAT survey of AGN: reconciling theory and observations?[1]

Abstract

It is well accepted that unabsorbed as well as absorbed AGN are needed to explain the nature and the shape of the Cosmic X-ray background, even if the fraction of highly absorbed objects (dubbed Compton-thick sources) substantially still escapes detection. We derive and analyze the absorption distribution using a complete sample of AGN detected by *Swift*–BAT in the first three years of the survey. The fraction of Compton-thick AGN represents only 4.6% of the total AGN population detected by *Swift*–BAT. However, we show that once corrected for the bias against the detection of very absorbed sources the real intrinsic fraction of Compton-thick AGN is 20^{+9}_{-6} %. We proved for the first time (also in the BAT band) that the anti-correlation of the fraction of absorbed AGN and luminosity it tightly connected to the different behavior of the luminosity functions (XLFs) of absorbed and unabsorbed AGN. This points towards a difference between the two subsamples of objects with absorbed AGN being, on average, intrinsically less luminous than unobscured ones. Moreover the XLFs show that the fraction of obscured AGN might also decrease at very low luminosity. This can be successfully interpreted in the framework of a disk cloud outflow scenario as the disappearance of the obscuring region below a critical luminosity. Our results are discussed in the framework of population synthesis models and the origin of the Cosmic X-ray Background.

5.1 Introduction

It is well known that absorbed active galactic nuclei (AGN) are needed to explain the shape of the Cosmic X-ray background (CXB) spectrum (e.g. Gilli et al., 2007;

---

[1] This chapter appeared in Burlon et al. (2011)

Treister et al., 2009). A large fraction of them is indeed detected in the shallow and deep < 10 keV X-ray surveys (see e.g. Brandt and Hasinger, 2005). Nonetheless, a large fraction of Compton-thick ($N_H \geq 1.5 \times 10^{24}$ H-atoms cm^{-2}, for a review see Comastri, 2004) AGN still escapes detection. Because of their large absorbing column density, these sources contribute a ∼10–25% fraction of the CXB emission (Gilli et al., 2007; Treister et al., 2009, respectively) at 30 keV, but at the same time are expected to be fairly numerous representing up to ∼ 30 % of the entire AGN population (Risaliti et al., 1999; Worsley et al., 2005) . The advent of sensitive all-sky surveys above 15 keV (e.g. *Swift*–BAT and INTEGRAL) opened the possibility to detect these objects. Indeed, it is above 10–15 keV that part of the primary continuum emission pierces through the veil of Compton-thick material, making it easier for these objects to be detected. Despite this fact, the early results from the *Swift* and INTEGRAL surveys showed that the fraction of Compton-thick AGN is merely a 5–10% of the total AGN population (see Ajello, 2009, and references therein). Thus it might be that the fraction of Compton-thick AGN is intrinsically smaller than previously determined. Nevertheless, it should be taken into account that even above > 15 keV, instruments are biased against the detection of $\log N_H > 24$ sources. Indeed as shown in e.g. Ghisellini et al. (1994), Ajello (2009), 50% of the source flux (between 15-55 keV) is lost if $\log N_H > 24.5$. The fact that three of the closest AGN ever detected (i.e. NGC 1068, Circinus galaxy and NGC 4945) are absorbed by $N_H \geq 10^{24}$ atoms cm^{-2} suggests that indeed this is the likely explanation.

In this work, we present and discuss the results of the most complete - until now - survey of AGN in the local Universe (z<0.1) using data from the *Swift*–BAT telescope. We performed a detailed spectral study of the three years sample of Seyfert-like objects by combining the hard X-ray information with the soft X-ray observations realized by different missions in the recent past. To this aim we extracted *Swift*–BAT spectra and spectra in the 0.3–10 keV band using archival *XMM–Newton* and *Swift*–XRT data. In a handful of cases we requested and obtained target-of-opportunity (ToO) observations with *Swift* for objects without previous coverage at soft X-rays. The use of X-ray data in the 0.3–195 keV band allows us to constrain robustly all the source parameters (including the absorbing column density).

This paper is organized as follows. In §2 we present the sample and discuss how the joint spectral analysis was performed. The general properties of the 15–195 keV continuum of AGN, the stacked analysis for the absorbed, unabsorbed, and Compton-thick spectra are presented in §3. §4 presents the observed N_H distribution. We then evaluate, for the BAT survey, the bias against the detection of the most obscured AGN and estimate -for the first time- the intrinsic absorption distribution. §5 presents the anti-correlation between the fraction of absorbed AGN (relative to the whole population) and luminosity, while the luminosity functions of AGN are derived in §6. The results of these analyses are discussed in §7 while §8 summarizes our findings. In this work we use a standard cosmology ($H_0 = 70$, $q_0 = 0$, and $\Omega_\Lambda = 0.73$).

5.2 The *Swift*–BAT sample and data analysis

5.2.1 The sample

The Burst Alert Telescope (BAT; Barthelmy et al., 2005) onboard the *Swift* satellite (Gehrels et al., 2004), represents a major improvement in sensitivity for imaging of the hard X-ray sky. BAT is a coded mask telescope with a wide field of view (FOV, 120°×90° partially coded) aperture, sensitive in the 15–200 keV domain. Thanks to its wide FOV and its pointing strategy, BAT monitors continuously up to 80% of the sky every day achieving, after several years of the survey, deep exposure in the entire sky. Results of the BAT survey (Markwardt et al., 2005; Ajello et al., 2008a; Tueller et al., 2010) show that BAT reaches a sensitivity of ∼1 mCrab[2] in 1 Ms of exposure. Being the BAT survey not a flux-limited survey, but rather a significance-limited one, it is important to address how the survey flux limit changes over the sky area. This is often referred to as sky coverage, that is the distribution of the surveyed area as a function of limiting flux. Its knowledge is very important when performing population studies as the ones described in the next sections. The reader is referred to Ajello et al. (2008a) for how to derive the sky coverage as a function of the minimum detectable flux F_{min}. This is defined as the sum of the area covered to fluxes $f_i < F_{min}$:

$$\Omega(< F_{min}) = \sum_{i}^{N} A_i \ , f_i < F_{min} \tag{5.1}$$

where N is the number of image pixels and A_i is the area associated to each of them. A visual representation of the sky coverage is reported in figure 5.1 which shows clearly the good sensitivity of BAT. The survey, in our analysis (15–55 keV), reaches a limiting sensitivity of ∼0.6 mCrab (7.3×10^{-12} erg cm^{-2} s^{-1}). We *ex post* checked that cutting the sample at 50 % of the complete sky coverage (i.e. at 1.1×10^{-11} erg cm^{-2} s^{-1}) does not affect significantly the findings of this work, since the 35 objects below this limit do not populate a particular N_H range.

The sample used in this work is the collection of non-blazar AGN detected by BAT during the first three years, more precisely between March 2005 and March 2008. This sample is part of the one used in Ajello et al. (2009a) which comprises all sources detected by BAT at high ($|b|>15°$) Galactic latitude and with a signal-to-noise ratio (S/N) exceeding 5 σ. All the 199 sources which are identified as non-blazar AGN (e.g. Seyferts) constitute the sample used in this work and are reported (along with their properties) in the table at the end of the paper. Note that the main sample, from which the sub-sample of AGN is derived, comprises 307 objects of which only 7 are as of today without identification. The incompleteness or the parent population is thus 2.3 %. We note that in our sample 19 objects are classified as 'Galaxies' or 'Liners'. We believe these are normal AGN (e.g. Seyfert galaxies) for which an accurate optical classification is not yet available in the literature. This is based on the fact that the average redshift, luminosity and absorbing column density are respectively 0.03, $4.5{\times}10^{43}$erg s^{-1} and

---

[2] 1 mCrab in the 15–55 keV band corresponds to $1.27{\times}10^{-11}$ erg cm^{-2} s^{-1}

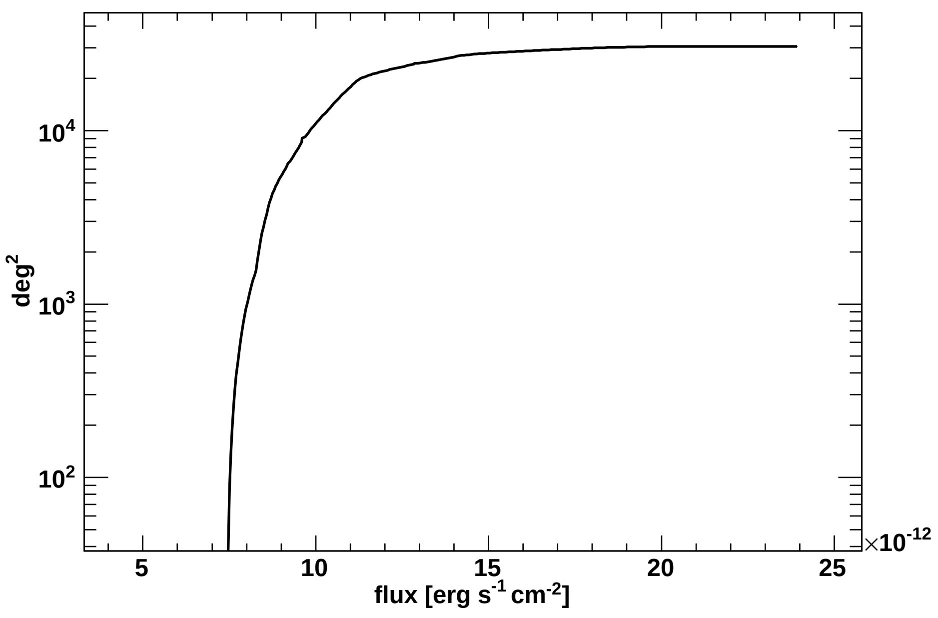

Figure 5.1 Surveyed area as a function of limiting flux for the BAT survey used in this work.

10^{23} cm^{-2}. These values are in good agreement with the ones derived from the rest of the sample giving confidence to our hypothesis that these objects are AGN.

5.2.2 Extraction of *Swift*–BAT spectra

For each source in our sample we extracted a 15–195 keV spectrum following the method described in Ajello et al. (2008c). Here we recall the main steps: the details can be found in the aforementioned paper. For a given source, we extract a 12 channel spectrum from each observation where the source is in the field of view. These spectra are corrected for residual background contamination and for vignetting; the per-pointing spectra are then (weighted) averaged to produce the final source spectrum. Thus, the final spectrum represents the average source emission over the time-span considered here (three years). Moreover the reader is referred to Ajello et al. (2009b) for a discussion about the accuracy of the spectra extracted with this method.

5.2.3 Extraction of the soft X-ray spectra

The goal of the present work is to obtain a reliable estimate of the intrinsic absorbing column density for the BAT AGN. 102 objects (out of the 199 AGN in our sample) have a reliable estimate of the absorbing column density present in the literature. The large majority (86) of these N_H measurements comes from earlier results of the *Swift* survey

(Tueller et al., 2008; Winter et al., 2008, 2009a,b) while for the rest (16) we used single-source publications (see the table at the end of the paper for details).

For all the objects without a N_H measurement we used the available follow-up observations performed by two observatories (i.e. *Swift*–XRT and *XMM–Newton* in 83 and 12 cases, respectively). XRT was used preferentially, while *XMM–Newton* was used in a handful of cases (i.e. when the detection significance by *Swift*–XRT was too low to constrain the spectral parameters and/or the N_H). Only in 2 cases we could not find any XRT or XMM follow up (i.e. 1H 2107-097) or the available soft X-ray pointing was not deep enough to extract a spectrum of the source (i.e. [VV2003c] J014214.0+011615).

For the filtering and spectra extraction we used `xrtproducts` only on Photon Counting Level 2 event files (grades 0–12) and the standard ftools of *Headas v6.6.3* software, and *SAS v9.0.0* for *Swift*–XRT and *XMM–Newton* observations respectively. We used *Xspec v*12.4.0*ad* (Arnaud, 1996) to perform, for each AGN, joint spectral fits between the 15–195 keV and the 0.3–10 keV data. Normally the spectra of sources detected (in the 0.3–10 keV band) with sufficient S/N were re-binned as to have a minimum of 20 counts/bin. In a handful of cases spectra were re-binned as to have 10 counts/bin, and consequently Cash in place of χ^2 statistics was adopted.

During the spectral fitting stage we took into account, regardless of the spectral model used (i) the local Galactic absorption (Kalberla et al., 2005) and (ii) a normalization factor to account for the different inter-calibration of the two instruments and for a possible variation of the source between the observation epochs. Small differences in the computed value of N_H might be present when comparing observations taken at different times. The case of NGC 7582 is discussed in §4.2, but in general we warn that variations of the column densities are expected (see e.g. Risaliti et al., 2002, 2009; Bianchi et al., 2009a, and references therein).

5.3 General properties

We discuss in the following the general properties of the sample, focussing on the hard X-ray continuum emission. The joint analysis is considered in this section only to the aim of splitting the parent population in un-absorbed and absorbed sources. Fig. 5.2 shows the luminosity-redshift plane for all the AGN in the BAT sample. The $k-$corrected L_X luminosities (not corrected for absorption, but see §3.2 and §4.2) were computed according to:

$$L_X \;=\; 4\pi d_{\rm L}^2 \frac{F_X}{(1+z)^{2-\Gamma_X}} \tag{5.2}$$

where F_X is the X-ray flux in the 15–55 keV energy range as listed in the table at the end of the paper (see Ajello et al., 2008b, for details about the flux determination), and Γ_X is the photon spectral index. Throughout this work, absorbed sources are those with an absorbing column density (N_H) larger than (or equal to) 10^{22} atoms cm^{-2}. It is apparent from Fig. 5.2 that obscured AGN populate more densely the low-luminosity/low-redshift part of the graph with respect to the high-luminosity/high-redshift part. A Kolmogorov-Smirnov (KS) test between the redshifts of the two populations of AGN (absorbed and

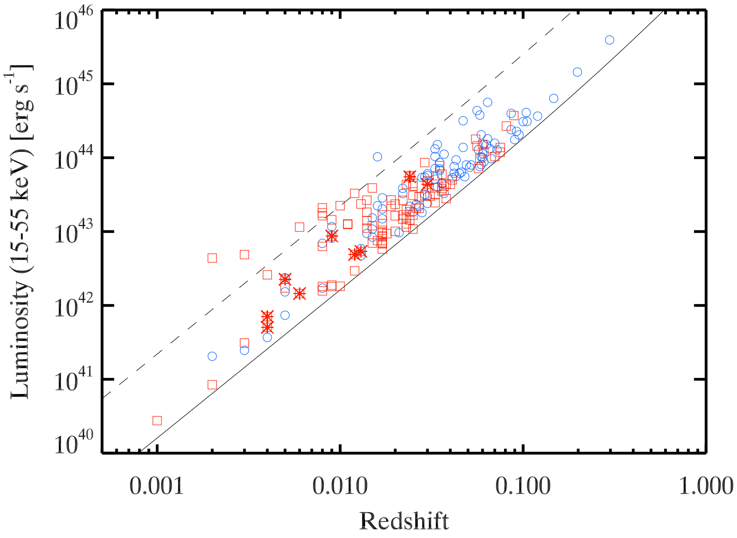

Figure 5.2 Luminosity-redshift plane for unabsorbed sources (blue circles) and for absorbed sources (red squares). The solid line represents the limiting sensitivity of the *Swift*–BAT survey for a source with photon index equal to 1.9, while the dashed line represents the sensitivity of the survey at a brighter flux, i.e. 10^{-10} erg cm^{-2} s^{-1}.

unabsorbed) shows that the probability that both classes are drawn from the same parent population is $\sim 1.4 \times 10^{-3}$.

The lines reported in Fig. 5.2 represent the current limiting flux of the BAT survey ($\sim 7.3 \times 10^{-12}$ erg cm^{-2} s^{-1}, solid line) and a much brighter flux of 10^{-10} erg cm^{-2} s^{-1} (dashed line). In the shallower case it is apparent that sources detected are preferentially absorbed with $\log N_H$ larger than 22.

5.3.1 Analysis of the 15-195 keV continuum

We performed a simple power-law fit to the BAT spectra in the 15–195 keV band to derive a measurement of the photon index. These values are reported in the last table with the corresponding 90% uncertainties. The distribution of photon indices of all the BAT AGN is compatible with a Gaussian distribution with a mean of 1.95±0.02 and a sigma of 0.27±0.02. We analyzed separately the distribution of photon indices of obscured and unobscured sources respectively. These are reported in Fig. 5.3. We find that the two distributions appear to be different with the one of obscured sources showing a mean of 1.92±0.02 and a sigma of 0.25±0.02 while the one of unobscured AGN displays a mean of 2.07±0.03 and a sigma of 0.27±0.03. This is also confirmed by the Kolmogorov-Smirnov test which yields a probability of 3×10^{-3} that the two distributions are drawn from the same parent population. The CT sources are not the main drivers of the distribution of absorbed sources. Indeed eliminating the 9 most

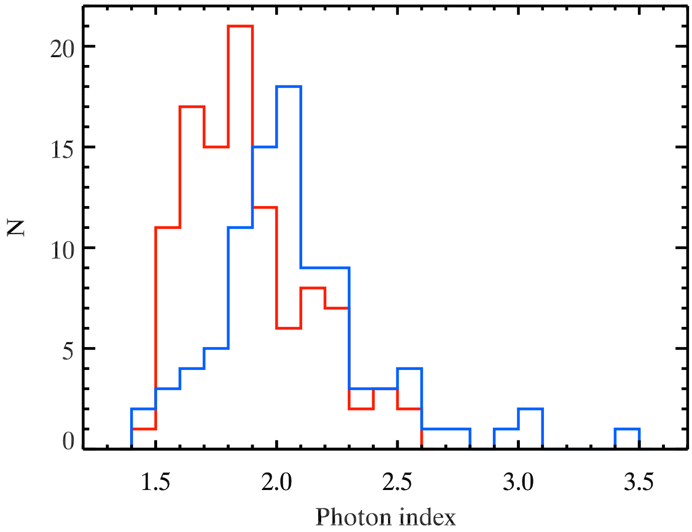

Figure 5.3 Photon indices distribution of absorbed AGN (logN_H ≥22, red line) and unabsorbed AGN (logN_H <22, blue line). The photon indices used are the ones derived in the BAT band only (i.e. 15–195 keV band) and reported in the table at the end of the paper.

absorbed sources from the sample does not in turn introduce an appreciable difference in the distribution. The KS test returns a null probability of $\sim 1 \times 10^{-3}$ in this case. Thus, there is an indication, albeit marginal, that absorbed sources display, on average, a harder power-law continuum than unobscured ones.

According to Hopkins et al. (2009) radiatively inefficient accretion flows (RIAFs) make the intrinsic X-ray spectrum of an AGN harder. This may cause to incorrectly classify, at energies below <10 keV, an AGN as obscured if only simple estimators (e.g. hardness ratios) are used. This is not however the case for the present work, because: 1) BAT is able to sample the intrinsic power-law spectral index independently of the level of absorption, 2) all sources have sufficient signal-to-noise ratio to correctly derive the absorption level using *XMM–Newton* or *Swift*–XRT data in conjunction with BAT ones. Thus, while RIAFs might certainly affect the intrinsic shape of the 15-195 keV continua, we believe that the differences observed here are ascribed to orientation effects (as shown already in Ajello et al., 2008c). As it can be seen in Fig. 5.4 we show the scatter plot of photon indices versus the absorbing column density and indeed there is a weak indication of a correlation between the two parameters (the Spearman's rank is -0.27, and null hypothesis probability $P \sim 1.2 \times 10^{-4}$). The low, negative rank correlation coefficient and the P value indicate that a chance correlation can be excluded at more than the $\gtrsim 3\sigma$ level. However if the sources with unconstrained $\mathrm{N_H}$ are excluded from the sample the correlation is not statistically significant any longer ($P = 1.3 \times 10^{-3}$). A mild correlation is anyway expected, because of the contribution of the higher reflection component of type 1 AGN, in the low energy channel of the BAT. The "softening"

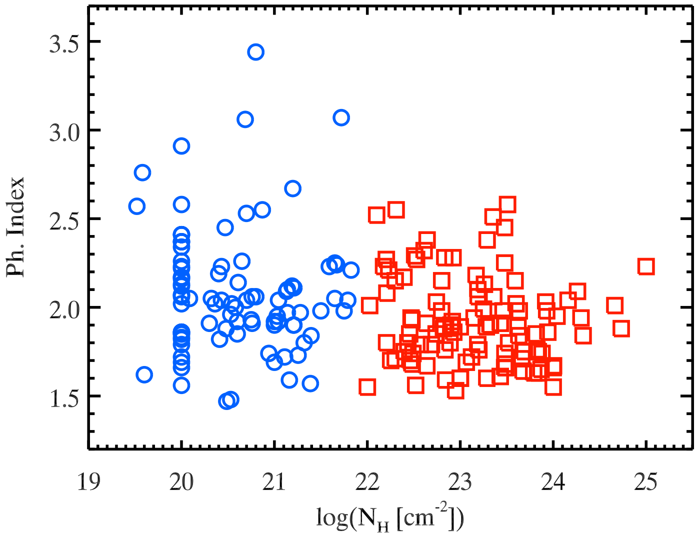

Figure 5.4 Photon spectral index as obtained from fitting with a simple power-law the BAT spectrum alone, versus the N_H found from the combined spectra in the 0.3–195 keV energy range. Different color/symbol identify absorbed and unabsorbed sources.

effect that is introduced when fitting with a simple power-law is further discussed in the following section.

We note that three AGN (i.e. Mrk 766, IRAS 05480+5927, Mrk 739) show a very soft BAT spectrum (e.g. photon index >3). For Mrk 766 we analyzed XRT and BAT data jointly and found out that the intrinsic power-law seems to be ∼2.0 and that indeed a large reflection component is required (the data show also the presence of a soft excess). The large reflection component is what makes (very likely) the BAT spectrum softer. The BAT spectrum of IRAS 05480+5927 is quite noisy and very soft. Nonetheless by a joint fit with XRT the photon index is constrained to be ∼1.8. A cutoff-powerlaw is statistically (ftest probability $> 3\sigma$) better but in turn requires the cutoff energy to be at 18 keV (in the 12–30 keV range, 3σ contours). As for Mrk 739, a joint fit with XRT gives a slope of 1.7. We note that again a cutoff-powerlaw is statistically preferred with a cutoff energy of $\sim$ 50 keV. Our results are unaffected by the change of these three BAT-soft spectra to the flatter value reported for the joint analysis.

Stacked spectra analysis – In order to investigate the global spectral properties of AGN we performed a stacking analysis of the AGN in the BAT sample. The stacked spectrum of several sources is produced performing the weighted average of all the spectra. The weight is chosen to be the inverse of the variance of a given bin and it is exactly the same procedure used to extract the spectra of each individual source. The same stacking technique has been already applied with success to both the study of Seyfert galaxies and galaxy clusters detected by BAT (Ajello et al., 2008b, 2009b). This stacking technique is appropriate for the stacking of background-subtracted spectra

Table 5.1 Best-fit parameters for the stacked spectra. Errors are 90 % CL and parameters without an error were kept fixed during the fitting stage. The columns report the value of the photon index (Γ), normalization of the reflection component R, the cut-off energy E_c and the absorption.

SAMPLE	# Obj	Γ	R	E_c (keV)	$N_{\rm H}$ (10^{22} cm^{-2})	χ^2/dof
All	199	$1.78^{+0.25}_{-0.39}$	< 4.50	> 80	–	5.2/8
All	199	$1.80^{+0.08}_{-0.08}$	$1.00^{+0.48}_{-0.36}$	300	–	5.2/9
Absorbed[1]	96	$1.74^{+0.07}_{-0.07}$	$0.55^{+0.67}_{-0.35}$	300	–	3.3/9
Unabsorbed[1]	92	$1.71^{+0.10}_{-0.06}$	$1.23^{+1.12}_{-1.00}$	300	–	3.6/9
Compton-thick	9	1.80	–	88^{+35}_{-21}	265^{+171}_{-131}	9.6/9

[1] For absorbed and unabsorbed AGN we have assumed that the inclination angle between the normal to the disk/torus and the line of sight is 60 and 30 degrees respectively. The class of absorbed AGN includes all AGN which are absorbed but are not Compton-thick (e.g. $22 \leq \log N_{\rm H} \leq 24$). We did not include the 2 AGN for which $N_{\rm H}$ could not be calculated.

generated by coded masks telescopes. As already reported in Ajello et al. (2009b), this stacking technique allows to determine the average properties of a source population. The stacked spectrum of the 199 AGN is not compatible with a simple power law (χ^2/dof = 22.62/10). This is due to a substantial curvature of the spectrum around 30 keV (see Fig. 5.5). We found that an acceptable fit to the data ($\chi^2/dof = 5.2/8$) is achieved when using a PEXRAV model. In this case we find that the best fit parameter for the slope is $1.78^{+0.25}_{-0.39}$ (error are 90 % CL). Given the small dynamic range of the BAT spectrum (15–195 keV) is impossible to disentangle uniquely the reflection component and the cut-off energy. Indeed, our best fit shows that, at 90 % confidence, the normalization of the reflection component is consistent with zero while the cut-off energy is bound to be ≥ 80 keV. The parameters of this best fit are reported in Tab. 5.1. In order to avoid this degeneracy we fixed the cut-off energy at 300 keV (see Dadina, 2008, which reported an average cut-off of 300 keV for *BeppoSAX* sources). The best fit parameters (reported also in Tab. 5.1) for the photon index and the reflection are respectively $1.80^{+0.08}_{-0.08}$ and $1.00^{+0.48}_{-0.36}$, which are in good agreement with the findings of Nandra and Pounds (1994). The normalization of the reflection component is compatible with the presence of a reflecting medium which covers an angle of 2π at the nuclear source.

In addition we generated stacked spectra for unabsorbed ($\log N_{\rm H} < 22$), absorbed ($22 \leq \log N_{\rm H} \leq 24$) and Compton-thick ($\log N_{\rm H} > 24$) AGN. A simple power-law fit to the spectra of unabsorbed and absorbed AGN yields that the best-fit photon indices are 2.13±0.06 and 2.00±0.06 respectively. This is found to be in agreement with what derived from the analysis of the photon index of the two distributions: i.e. on average unabsorbed AGN have steeper spectra than absorbed ones. The indices derived from the stacking analysis are slightly steeper than the average ones derived from the photon index distribution because the stacked spectra show a significant curvature which makes the simple power-law fit not the most accurate one (e.g. reduced $\chi^2 \geq 2.0$). We thus decided to fit the stacked spectra with a PEXRAV model. Also in the stacked spectra

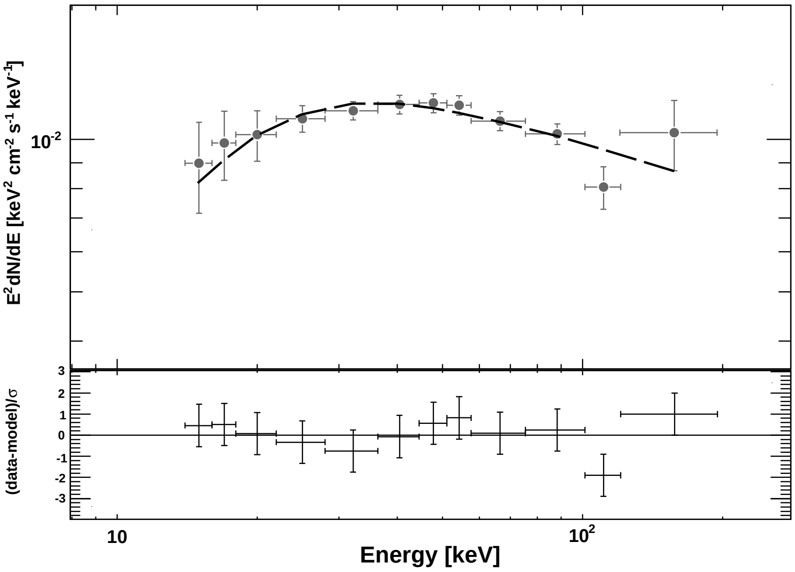

Figure 5.5 Stacked spectrum of the 199 Swift AGN. The dashed line is the best-fit PEXRAV model. Note the substantial curvature of the spectrum around ∼30–40 keV.

of absorbed and unabsorbed AGN the cut-off energy and the reflection component cannot be determined uniquely. We thus fixed the cut-off energy to 300 keV. A fit to the stacked spectrum of absorbed sources yields a photon index of $1.74^{+0.07}_{-0.07}$, and a reflection component of $R=0.55^{+0.67}_{-0.35}$.

The fit to the stacked spectrum of unobscured sources yields a photon index of $1.71^{+0.10}_{-0.06}$ and a reflection component of $R=1.23^{+1.12}_{-1.00}$. The uncertainties are large, however these results (which are reported in Tab. 5.1) seem consistent with the unified model which predicts a larger reflection component for unobscured sources (for a discussion see e.g. Ajello et al., 2008a, and references therein). In addition, our findings agree with the modeling of obscured sources in Gilli et al. (2007), where the reflection efficiency for high inclination angles (expected for obscured AGN in the unified picture) is lower (0.88 rather than 1.3) than the one assumed for unobscured ones.

The 15–195 keV Spectrum of Compton-thick AGN

Finally we also investigate, for the first time, the average spectrum of Compton-thick AGN. Our first goal is to determine an empirical model which describes the 15-200 keV emission of Compton-thick AGN reasonably well and then later to interpret the features of the spectrum. Thus, we started fitting the stacked spectrum of the 9 Compton-thick AGN with a simple power-law model. The best-fit photon index is 2.04±0.09, but because of the spectral curvature this model represents a poor description of the data (χ^2/dof=42.1/10). The fit improves (χ^2/dof=16.1/9) if we use an absorbed power-law model. In this case the best-fit photon index and absorbing column density are

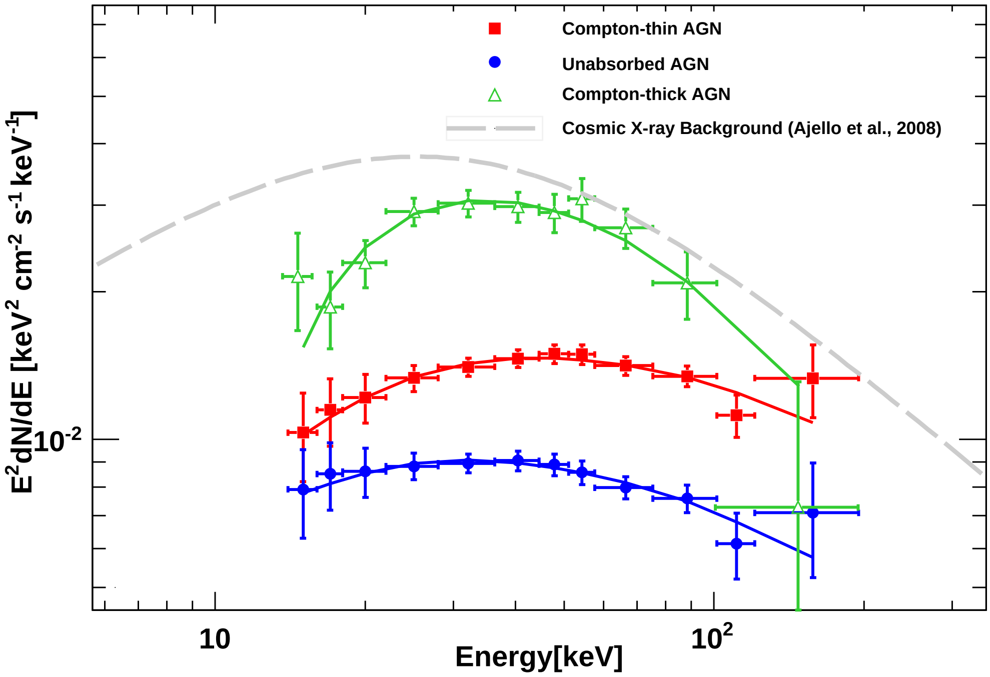

Figure 5.6 Stacked spectra of obscured AGN (22 $\leq$logN$_{\rm H}$ $\leq$ 24), unabsorbed AGN (logN$_H$ $<$ 22) and Compton-thick AGN (logN$_{\rm H}$ $>$ 24) compared to the Cosmic X-ray background (CXB) as measured by Ajello et al. (2008b). Note that both the CXB spectrum and the spectrum of Compton-thick AGN have been rescaled arbitrarily.

respectively $2.48^{+0.21}_{-0.18}$ and $N_H = 4.7^{+2.4}_{-1.9} \times 10^{24}\,\rm cm^{-2}$. As a last step we tried to fit the stacked spectrum with an absorbed cut-off power-law model. We fixed the photon index of the power law to 1.8 to avoid degeneracy among the parameters. This model provides a good representation of the BAT data (χ^2/dof=9.7/9). The column density is consistent with being Compton-thick ($\rm N_H = 289^{+163}_{-131} \times 10^{22}$ atoms cm^{-2}) and the cut-off energy is 82^{+39}_{-19} keV. The results of this fit are summarized in Tab. 5.1. However, we caution the reader this model (zphabs in *Xspec*) takes into account only photoelectric absorption and it is used only as a functional form to show that the average continuum of Compton-thick AGN is indeed very curved. Fig. 5.6 shows the average spectra of unabsorbed, absorbed and Compton-thick AGN and compares it to the general shape of the Cosmic X-ray Background (Ajello et al., 2008b).

The peak of the stacked spectrum of Compton-thick AGN (at z$\approx$0) is at almost twice the energy of the peak of the CXB (see Fig. 5.6), testifying that if Compton-thick AGN are responsible for part of the emission at the peak of the CXB then the bulk of the population should be at z$\approx$ 1. This seems to be in agreement with the prediction of population synthesis models (e.g. Gilli et al., 2007; Treister et al., 2009).

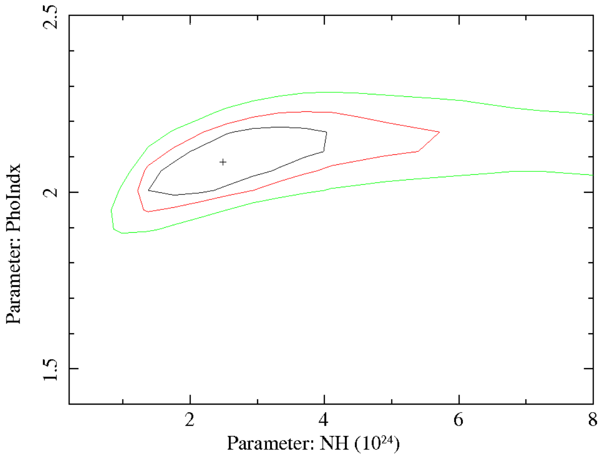

Figure 5.7 Confidence contours (1, 2, and $3\,\sigma$) for the photon index and the absorbing column density of the MYTorus model fitted simultaneously to all the 9 Compton-thick AGN spectra.

We also adopt a different strategy to check the results of the analysis of the stacked spectrum of the Compton-thick AGN. Instead of producing a stacked spectrum, we performed a simultaneous fit to the 9 spectra. In doing this we use the same baseline model for all the spectra (e.g. a power law or an absorbed power law) with a free normalization constant as to take into account the different source fluxes. As a first test, we tried as before a fit with a simple power-law model. This fit yields a photon index of 1.94±0.07 (in reasonable agreement with what found before) and a χ^2/dof=148.1/98. We then tried fitting with an absorbed power-law model. The improvement in the fit, with respect to the previous one, is very large (e.g. χ^2/dof =118.6/97) and the F-test confirms that the probability of obtaining such improvement by chance is $\sim 4 \times 10^{-6}$. The best-fit photon index is $2.29^{+0.15}_{-0.14}$ and the column density is $2.4^{+1.0}_{-0.8} \times 10^{24}\,\mathrm{cm}^{-2}$. A fit with a cut-off absorbed power law model (with the photon index set to 1.8 as before) produces a slight improvement (e.g. $\chi^2 = dof$=113.1/97) yielding an absorbing column density of $1.8^{+0.8}_{-0.3} \times 10^{24}\,\mathrm{cm}^{-2}$ and cut-off energy of 128^{+63}_{-34} keV. Within the statistical uncertainties, the results of this new analysis appear to be consistent with the results of the analysis of the stacked spectrum.

Our next step was then to fit the stacked spectrum of Compton-thick AGN with a more physical model. In this case we adopted an improved version of the model of Yaqoob (1997) which fully treats relativistic Compton scattering, i.e. the MYTorus model by Murphy and Yaqoob (2009) and Yaqoob et al. (2010)[3]. This model provides tables for the attenuation of the continuum emission (transmitted through the torus) and the scattered component computed via Monte Carlo simulations (a similar model can be also found in Matt et al., 1999). In principle both the transmitted and the scattered components should be fitted to the spectrum to ensure self-consistency of the model. In practice, because of the many model parameters and the limited energy bandpass

---

[3] The model is available at www.mytorus.com

of BAT, a fit with both components was not successful (e.g. $\chi^2/dof > 3$). However in this first exercise the normalization of the scattered component was a factor > 10 larger then the transmitted one. We then tried to fit the two components separately to understand whether one component is dominating over the other one. The best fit using the transmitted components yields a χ^2/dof=20.6/9 and is still thus a fairly poor fit. Instead we achieved a good fit (χ^2/dof=11.3/9) using the scattered component alone and an orientation of the torus (with respect our line of sight) of 60 degrees. The best-fit photon index is $2.17^{+0.10}_{-0.11}$ while the absorbing column density is $N_H = 3.7^{+2.1}_{-1.9} \times 10^{24}\, cm^{-2}$. We also attempt a simultaneous fit with the MYTorus model to all the 9 Compton-thick AGN spectra, leaving the normalization of each spectrum to be a free parameter of the fit. Again it appears that the scattered component is dominating over the transmitted one. Indeed we achieve a good fit to the data using the scattered component alone (e.g. χ^2 =111.1/97) and an inclination of the torus of ∼60 degrees. The best fit photon index is 2.08±0.10 and the absorbing column density is $2.5^{+1.8}_{-1.2} \times 10^{24}$ cm^{-2}. Fig. 5.7 shows the confidence contours of these two parameters. If we remove the most obscured AGN from the fit (i.e. NGC 1068) the index and N_H become respectively 2.05±0.10 and $2.7^{+2.2}_{-1.3} \times 10^{24}$ cm^{-2} showing that our results are not driven by just one particular source.

From the best fit using the MYTorus model (either to stacked spectrum or the simultaneous fit) we derive that only ∼30 % of the intrinsic nuclear flux is observed in the 15–155 keV band. Finally, we note that the results presented in this section do not change if we remove the two brightest objects in the CT sample, nor if we remove the most absorbed source (e.g. NGC 1068, see above) from the sample. Nevertheless, given the paucity of CT AGN in our sample and the fact that they span one dex in absorbing column density, the results of this section must be taken with care as they might turn out not to be representative of the entire population of CT AGN.

5.3.2 Luminosity distribution and spectral properties

Luminosities of the Compton-thin AGN have been calculated through Eq. 5.2, therefore without taking absorption into consideration. We also tested whether the modeling of absorption introduced a bias in the distributions, even in the hard band sampled by BAT. To this aim we fitted all the sources with $\log N_{\rm H} > 23.5$ taking Compton scatter into consideration (i.e. we used `cabs*zwabs*pow` in *Xspec*) and compared the resulting de-absorbed flux distribution with the one tabulated at the end of the paper. The `cabs` model has nonetheless some caveats that should be stated clearly: it assumes a constant Compton cross section equal to the Thomson one, so that it fails in describing the spectral hardening of the transmitted component due to the decay with energy of the Klein-Nishina cross section. Therefore is typically used for spectra in the 2–10 keV energy band. Moreover, it does not take into account scattering from material out of the line-of-sight. The KS null probability (0.6) shows that indeed no appreciable difference is introduced by using a simple model for Compton-thin sources. As for the 9 Compton-thick objects, the fluxes have been de-absorbed as described in detail in

§5.4.2. Fig. 5.8 shows the distribution of luminosity in the energy range 15–55 keV for the complete sample of AGN along with the distributions for the absorbed and unabsorbed AGN. The median values of the two subclasses read a logarithmic value of 43.2 and 43.8, respectively. A Kolmogorov-Smirnov test between these two populations reads a null hypothesis probability of 6.6×10^{-5}, if we neglect those producing the peak at $\log N_H=20$ in Fig. 5.11. The distance between the two populations is exacerbated when taking into account all the sources with $\log N_H=20$, since the KS probability drops to $\sim 10^{-9}$. Hence already by comparing the luminosity distributions there is evidence that the two populations are unlikely belonging to the same parent population, and this difference is independent from the modeling of absorption. This behavior is further discussed in detail in §5.6, where the X-ray luminosity functions of the two AGN classes are derived.

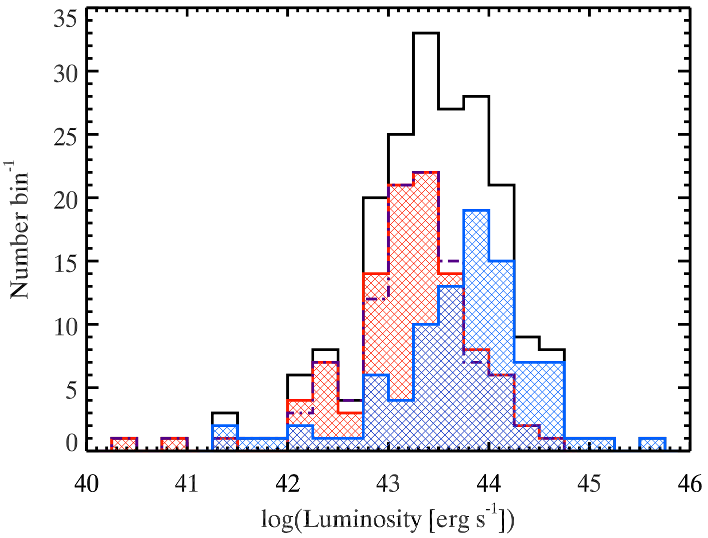

Figure 5.8 Luminosity distribution in the 15–55 keV energy range for the complete catalogue (grey) and for the absorbed sources (i.e. $\log N_H \geq 22$, red). We also show (blue) the distribution for the sources with $\log N_H < 22$. The purple line shows the luminosity distribution of the absorbed sources without correction for absorption.

Photon index vs. Luminosity – In general, a correlation between the photon index and the accretion rate (expressed as the ratio of the bolometric luminosity and the Eddington luminosity) has been confirmed in numerous studies (see Ishibashi and Courvoisier, 2010, and references therein). The general interpretation is that higher accretion rates lead to an increase in the photon density above the disk. This implies in general a more efficient cooling, and consequently steeper spectra (see chapter 4). In this section we test whether the hard X-ray power law index is correlated with the luminosity in the BAT range, even if we are aware that the hard X-ray luminosity alone is an inaccurate proxy of the accretion rate. As it can be seen in Fig. 5.9 there is no indication that luminosity and photon index are correlated, confirmed by the Spearman's rank coefficient and null hypothesis probability respectively equal to 0.19 and ~0.01. This might be produced by the fact that the objects in our sample have a broad distribution of black hole masses (and Eddington ratios). Winter et al. (2009a) recently showed the absence (in the local BAT-selected AGN sample) on average, of this correlation between the 2–10 keV de-absorbed luminosities and Γ, as well as between a proxy of the Eddington ratio and the spectral index. The correlation between the 2–10 keV photon index and the luminosity was found not to be significant in many papers (Reeves and Turner, 2000; Bianchi et al., 2009a), and the significance is generally low also in the works where it is claimed as real (Dai et al., 2004; Saez et al., 2008). It is worth noting that Winter et al. (2008) reported a positive correlation between the photon index and the 2–10 keV flux of individual sources, i.e. at high fluxes the sources tend to show steeper spectra. Interestingly, *Swift*–BAT beamed AGN (Fig. 2 in Ghisellini et al., 2010a; Ajello et al., 2009a) do show a rather remarkable relation between the 15–55 keV luminosity and the spectral index. This relation is even stronger when looking at samples selected in the *Fermi*/LAT energy range. Nonetheless, the reason of the absence of this correlation in the objects of our sample is beyond the aims of this work.

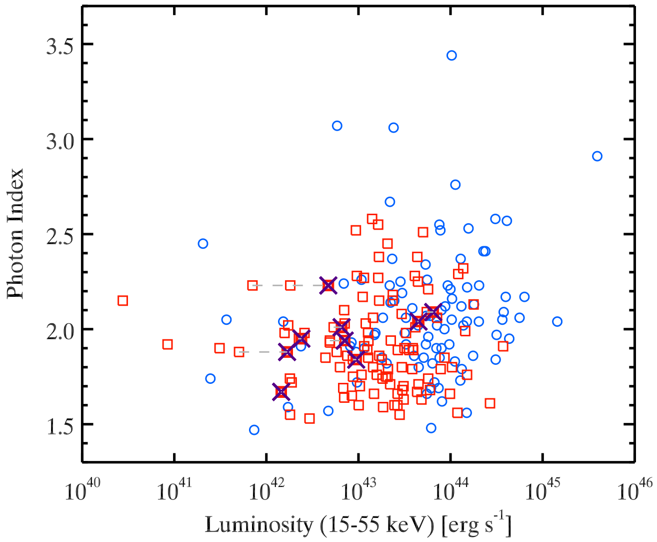

Figure 5.9 Photon spectral index resulting from the simple power law fit as a function of the BAT luminosity in the 15–55 keV range. The unabsorbed sources are shown with blue circles, while the absorbed sources are shown in red squares. The 9 Compton-thick sources are highlighted with crosses, and their de-absorbed luminosity is connected to the absorbed one by horizontal lines.

Hard X-ray flux versus Absorbing column density – Fig. 5.10 shows the distribution of the sources in the flux–N_H plane. The absence of objects under $\sim 7 \times 10^{-12}$ erg cm^{-2} s^{-1} (which is represented by the horizontal line) reflects the sensitivity of *Swift*–BAT in the energy range we selected. Indeed we see no correlation between these two parameters (Spearman's rank coefficient 0.04, and null hypothesis probability $P = 0.64$). Note that the absence of sources at small N_H and high fluxes, i.e. the top left region of the plot, reflects the tendency of the more luminous sources (which are intrinsically less numerous) of being unabsorbed. Indeed we showed in Fig. 5.2 that at a higher flux the sources are typically absorbed by columns in excess of 10^{22}. This explains the handful bright objects, i.e. with $F_X > 10^{-10}$ erg cm^{-2} s^{-1}, in the range 22 $<\log N_H<$ 23. We discuss in further detail the nine Compton-thick objects in §5.4.2.

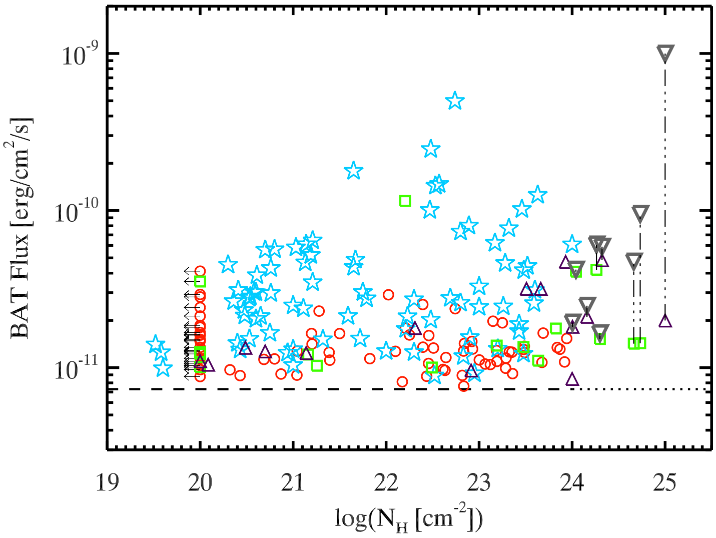

Figure 5.10 Scatter plot of the 15–55 keV fluxes of the sources *vs*. column density. Blue stars and purple triangles represent respectively the AGN already present in Tueller et al. (2008) and other references (see last table). Sources treated separately in this work are shown as red dots (follow up by *Swift*–XRT) and green squares (follow up by *XMM–Newton*). The horizontal dashed line represents the sensitivity limit of the 3-year survey (note that we draw a dotted line in the CT regime, where also BAT is biased, as discussed in § 5.4.2). Absorbed and un-absorbed fluxes (connected by vertical dash-dotted lines) are drawn for the 9 Compton-thick sources.

5.4 Absorption in the local Universe

5.4.1 Observed N_H distribution

We derived the photoelectric absorption by the combined fit of the BAT spectra (averaged over 3 yrs.) and the available follow up observations in the 0.3–10 keV energy range (e.g. *XMM–Newton* or XRT). As described in § 5.2.3 we adopted the value reported in the literature for ∼ 50% of the sample, and the specific reference is reported in the table at the end of the paper. The absorption distribution is reported in Fig. 5.11. For 33 AGN (out of 197) the absorbing column density we measured was found to be consistent with (or smaller than) the Galactic absorption in the direction of the source. When we could not constrain the absorption or when its value was consistent with the Galactic one, we put the value $\log N_H=20$, which in turn produced the high peak in the distribution in the bin $20<\log N_H<20.5$. Note that there are a handful of cases taken from the literature in which the column density is found to be lower than 10^{20} cm^{-2}.

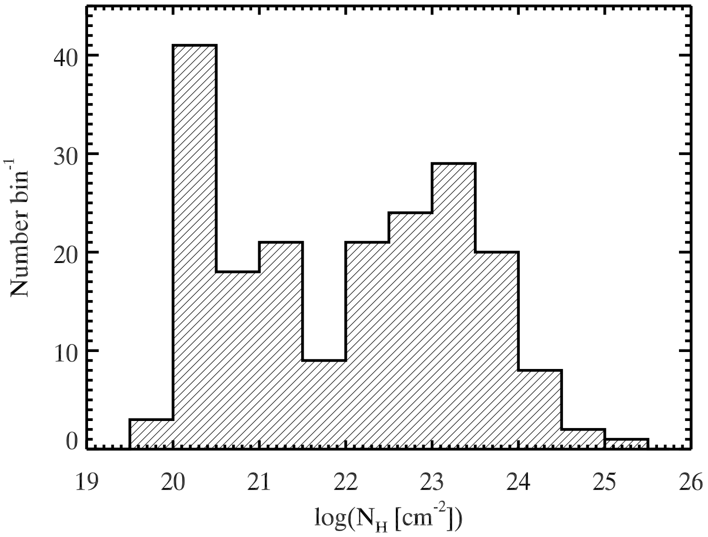

Figure 5.11 Observed column density distribution. The peak at $\log N_H = 20$ is produced by the sources for which absorption was negligible (of the same order of the galactic one).

When considering the whole AGN population we find that 53±4% ($1\,\sigma$ statistical error) are absorbed by column densities $\geq 10^{22}$ cm^{-2}. We find that the number of objects whose N_H is greater then 10^{24} cm^{-2} is 9/197. Thus the fraction of highly absorbed sources, know as Compton-thick AGN is $4.6^{+2.1}_{-1.5}$% ($1\,\sigma$ statistical error), all already known in the literature as extremely absorbed sources. These objects are highlighted in the table at the end of the paper. The fraction of Compton-thick sources at $\sim 10^{-11}$ erg cm^{-2} s^{-1} was predicted by population synthesis models to be, at the typical fluxes sampled by BAT in the range 7–15 % (see Comastri et al., 2009; Treister et al., 2009, and references therein).

An updated compilation of the most recent survey results in the hard X-ray band (e.g. above 10 keV) is reported in Tab. 5.2. It is clear that most, if not all, of these results indicate a lack of Compton-thick AGN if compared to the ~30 % fraction found by Risaliti et al. (1999).

5.4.2 The BAT bias and the intrinsic N_H distribution

BAT is the least biased X-ray instrument, particularly when comparing it to 2–10 keV telescopes, for the detection of obscured objects. Nonetheless, even in the >

Table 5.2 Observed fraction of absorbed and Compton-thick AGN, relative to the whole population for different X-ray surveys.

Reference	# Obj	Completeness	% Absorbed	% C-thick	Band (keV)	Instrument
Markwardt et al., 2005	54	95 %	~ 64%	~10%	15–200	*Swift*–BAT
Beckmann et al., 2006	36[a]	100 %	~ 64%	~ 10%	20–40	INTEGRAL
Bassani et al., 2006	56[b]	77 %	~ 65%	~ 14%	20–100	INTEGRAL
Sazonov et al., 2007	91	93 %	~ 50%	~ 10-15%	17–60	INTEGRAL
Ajello et al., 2008a	24	100 %	~ 55%	<20 %	14–170	*Swift*–BAT
Tueller et al., 2008	103	100 %	~ 50%	~ 5%	14–195	*Swift*–BAT
Paltani et al., 2008	34[c]	100 %	~ 60%	<24 %	20–60	INTEGRAL
Della Ceca et al., 2008	62	97 %	~ 57%	0	4.5–7.5	*XMM–Newton*
Malizia et al., 2009	79[d]	100 %	~ 43%	7%	20–40	INTEGRAL
Beckmann et al., 2009	135[e]	~ 97 %	~ 44%	~4 %	18–60	INTEGRAL
Our work	197	100 %	~ 53%	$4.6^{+2.1}_{-1.5}$ %	15–195	*Swift*–BAT

[a] The complete sample is 42 AGN, 36 of which are Seyfert galaxies.

[b] The complete sample is 62 AGN, 6 of which are Blazars and 14 are unindentified.

[c] Since the Paltani et al. sample may contain a fraction of spurious sources, we restricted their sample to a limiting significance of $6\,\sigma$. Above this threshold all sources are identified (see Tab. 2 in Paltani et al., 2008).

[d] There are 88 objects reported to be at significance $> 5.2\sigma$. 79 of those are Seyfert galaxies, the remaining being Blazars.

[e] The complete sample comprises 187 objects with $> 3\sigma$ significance in the 18–60 keV energy band. According to the authors (see Sect 4.1 in Beckmann et al., 2009) there are 135 Seyfert galaxies with measured absorption. Only 7/187 sources are listed generically as AGN without information on redshift.

10 keV band a relevant fraction of the source flux might be lost if the source is Compton-thick. In order to show this effect we computed the ratio between the observed and the intrinsic nuclear flux of an AGN for increasing column densities. In this exercise, we took both photoelectric absorption and Compton scattering into account using MYTorus. The nuclear, intrinsic, emission has been modeled as a power law with a photon index of 1.9. The results are shown in Fig. 5.12. From this plot it is apparent that the BAT survey is unbiased up to $\log N_H \approx 24$ and then becomes biased against the detection of Compton-thick objects. Furthermore, the absorption bias affects much more severely the 2-10 keV band already for $\log N_H \geq 23$ (see same Fig. 5.12).

We also performed joint spectral fits of *XMM–Newton* and *Swift*–BAT data for all the Compton-thick objects in our sample to determine the fraction of the intrinsic flux which is seen in the 15-55 keV band. The results of the spectral analysis are summarized in Tab. 5.3 and in Fig. 5.12. Only for SWIFT J0601.9-8636, NGC 5728, CGCG 420-015, and NGC 1068 we used the values available in the literature. Indeed, *XMM–Newton* data are not available for SWIFT J0601.9-8636 and NGC 5728, so we used the values derived with Suzaku by Ueda et al. (2007) and Comastri et al. (2010), respectively. NGC 7582 was largely discussed in Piconcelli et al. (2007) and Bianchi et al. (2009b), as for the variations of a factor ~ 2 in the thicker absorber. We used the *XMM–Newton* observation taken in 2005, and therefore tagged this object as Compton-Thick. Variations of the thick absorber can in principle take place for other sources as well,

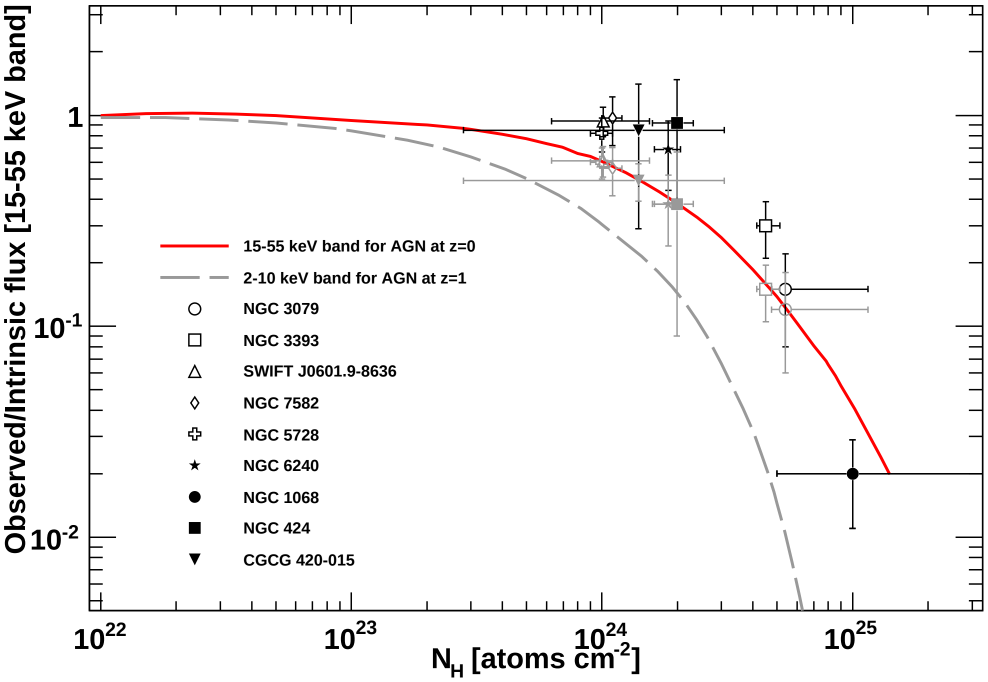

Figure 5.12 Ratio of observed to intrinsic nuclear flux for an AGN, with a power-law spectrum with index of 1.9, as a function of the column density of the torus as seen edge-on. The red solid line shows the ratio for the 15-55 keV band for an AGN in the local Universe (e.g. the typical case for the BAT survey). The dashed line shows the ratio for the 2-10 keV band for an AGN at redshift $\sim$ 1, i.e. the typical redshift for AGN detected in the *XMM–Newton*/Chandra surveys (see e.g. Akylas et al., 2006). Note that the BAT survey is unbiased (e.g. ratio $\approx$1) for logN_H $\leq$23.5. The black data points show the ratio of observed to intrinsic flux estimated for the BAT Compton-thick AGN taking into account only photoelectric absorption. The gray data points show the ratio also when Compton scattering is fully taken into account.

altering the fraction of CT objects according to the observation used for the analysis. The Compton-thick nature of CGCG 420-015 (aka IRAS 04507+0358) was discovered by Severgnini et al. (2011). It was known to be a highly absorbed Sy2 galaxy, but with the use of deep (100 ks) Suzaku observations, in addition to the ones available, the authors found N_H to be $\sim 1.3 - 1.5 \times 10^{24}$ cm^{-2}, with minor variations according to the model used to fit the combined spectra. NGC 1068 is a complex object which has been analyzed in detail in the past. According to Matt et al. (2004), the nuclear emission is completely suppressed and the source is seen only in reflected light. The column density is probably in excess of 10^{25} atoms cm^{-2} (Matt et al., 2004) and the reflection component is of the order of a *few* % of the nuclear flux (Iwasawa et al., 1997). For these reasons the position on the plot of NGC 1068 should be considered tentative. Fig. 5.12 also shows the difference in the observed-to-intrinsic flux ratio when also Compton scattering is taken into account (using the MYTorus model). Note however that modeling with MYTorus contains an implicit assumption, i.e. that the scattering material has a toroidal geometry with given parameters (half-opening angle of 60°, corresponding to a covering factor of $\Delta\Omega/4\pi = 0.5$). The line-of-sight of the observer is a fixed parameter of the fit.

It is interesting to note that there is relatively good agreement between the model line and the observations of single Compton-thick objects detected in the *Swift*–BAT survey. In Fig. 5.10 we showed the fluxes of the 9 Compton-thick AGN, before and after the correction for the missed flux, connected by dash-dotted lines. The horizontal line representing the limiting flux of the survey was turned into a dotted line to visually indicate the increasing bias in the CT regime.

Table 5.3 Ratio of the observed flux with respect to the nuclear (unabsorbed) flux in the 15–55 keV band for the 9 Compton-thick objects in the sample. Errors are quoted at 90 % CL. Four sources were fitted using *XMM–Newton* and *Swift*–BAT. For the remaining objects we used values from the literature.

Source	F_{obs}/F_{nucl}	Error	N_H (10^{24} cm^{-2})	N_H error (10^{24} cm^{-2})
NGC 3079	0.15	0.07	5.40	(-0.65,6.10)
NGC 3393	0.30	0.10	4.50	(-0.36,0.62)
SWIFT J0601.9-8636 [a]	0.94	0.15	1.01	(-0.38,0.54)
NGC7582	0.97	0.25	1.10	(-0.05,0.05)
NGC 5728 [b]	0.82	0.15	1.0	(-0.1,0.1)
NGC 6240	0.69	0.25	1.83	(-0.23,0.22)
NGC 1068 [c]	0.02	0.01	>10	(-5, >10)
NGC 424	0.92	0.56	1.99	(-0.40,0.32)
CGCG 420-015 [d]	0.85	∼0.20	1.46	(-0.11,0.07)

[a] Ueda et al. (2007) [b] Comastri et al. (2010) [c] Matt et al. (2004) and Iwasawa et al. (1997) [d] Severgnini et al. (2011)

Essentially the absorption bias limits the detection of Compton-thick objects only to those with bright (intrinsic) fluxes and in the very local Universe. Indeed three of the most famous Compton-thick objects (NGC 1068, NGC 4945 and the Circinus galaxy) are also among the closest known AGN. Thus the distribution reported in Fig. 5.11 compares sources detected at different limiting *intrinsic* fluxes. It is possible to correct for this effect by taking into account the selection effect due to the large column density. The *intrinsic* absorption distribution can be expressed as:

$$\frac{dN}{dLogN_{\rm H}} = \int_{S_{min}}^{S_{max}} \frac{dN}{dS}(N_{\rm H})\, dS, \tag{5.3}$$

where the $dN/d\mathrm{Log}N_{\rm H}$ is in unit of sr^{-1} per logarithmic bin of $N_{\rm H}$, S is the observed source flux, and $dN/dS(N_{\rm H})$ is the log$N$–log$S$ of sources in a given log$N_{\rm H}$ bin. The minimum *observed* flux (S_{min}) of integration should be set so that the limiting *intrinsic* flux is the same for all the bins. In this way the absorption distribution derived is representative of the density of sources at the same limiting intrinsic flux.

The relationship between observed and intrinsic flux can be expressed as $S^{obs} = K(N_{\rm H})\ S^{intr}$ where $K(N_{\rm H})$ is the ratio plotted in Fig. 5.12. Thus S_{min} can be set to $10^{-11} \times K(N_{\rm H})$ to produce a uniform absorption distribution for sources with an intrinsic flux greater than 10^{-11} erg cm^{-2} s^{-1}. Eq. 5.3 can thus be rewritten as:

$$\frac{dN}{dLogN_{\rm H}} = \frac{A(N_H)}{1-\alpha}\left[S_{max}^{1-\alpha} - (10^{-11}K(N_{\rm H}))^{1-\alpha}\right] \quad , \tag{5.4}$$

where $A(N_{\rm H})$ and α are the normalization and the index of the *log* N–*log* S in a given $\log N_{\rm H}$ bin. Here we assumed that the source count distribution can be approximated with a power-law function (e.g. $dN/dS = AS^{-\alpha}$). This assumption is well justified by the fact that the source count distribution of the entire BAT sample is well represented by a single power law (e.g. see Ajello et al., 2009a) and that the source count distribution of AGN shows a break at much lower fluxes (e.g. Cappelluti et al., 2007). In order to derive the intrinsic absorption distribution we used 0.25 dex $\log N_{\rm H}$ bins. For each bin, a source count distribution has been constructed and a power law has been fitted to it employing a Maximum Likelihood algorithm. This power law was then used to estimate the density of objects (per steradian) in a given $\log N_{\rm H}$ bin (i.e. Eq. 5.4). All the power-law indices were found to be compatible with a Euclidean index (i.e. 2.5 for a differential distribution). The index α has been fixed to 2.5 for all those bins with less than 5 objects. We checked that fixing the index to 2.5 for all bins or allowing it to vary does not change the results presented here. For each $\log N_{\rm H}$ bin the error on the density of sources is derived from the Poisson error on the number of sources present in that bin to preserve the original counting statistics.

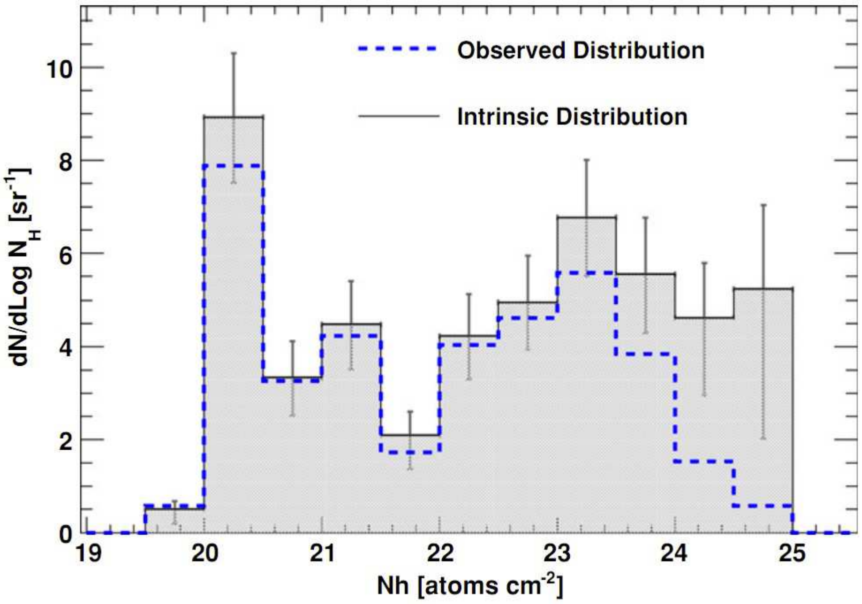

Figure 5.13 Intrinsic absorption distribution compared to the observed one (dashed line). Errors bars are derived from counting statistics in each bin.

The intrinsic absorption distribution is shown in Fig. 5.13. From this we derive that the *intrinsic* fraction of Compton-thick sources (logN_H >24) is 20^{+9}_{-6} %, where the error is only statistical. It is apparent that the observed distribution starts to deviate from the observed one only for logN_H ≥23.5. We also derive that the *intrinsic* fraction of absorbed sources is 65±4 %. A systematic error in estimating the *intrinsic* fraction of Compton-thick sources might arise from both the power-law indices fitted in Eq. 5.4 and from the $K(N_{\rm H})$ correction factor (e.g. the curve plotted in Fig. 5.12). Fixing all the α parameters to 2.5 or allowing all of them to vary changes the above fraction of about 1 %. Thus the exact shape of the log$N$–log$S$ in each log$N_{\rm H}$ bin does not contribute a large systematic error.

On the other hand, the knowledge of the fraction of transmitted flux (e.g. $K(N_{\rm H})$ and Fig. 5.12) plays a major role in the derivation of the density of Compton-thick AGN. The angle at which our line-of-sight intersects the torus and the power-law index of the intrinsic AGN spectrum can modify the fraction of Compton-thick AGN. Playing with these different parameters we derive that the systematic uncertainty on the fraction of Compton-thick AGN is ∼5 %.

Also Malizia et al. (2009), using INTEGRAL, showed that the fraction of Compton-thick AGN is likely larger than the observed ∼5 %. Instead of correcting for the missing population, they adopt a redshift cut (z≤0.015) which would ensure, according to the authors, to have a complete sample. In their sample of 25 AGN, they found 6 Compton-thick AGN, thus the fraction of Compton-thick AGN is 24^{+11}_{-9} % of the total population in agreement with our estimate.

As visible from Fig. 5.12, there is also a slight overestimate (although compatible within 1 σ with the observed density) of the intrinsic density of objects with Log$N_H \approx$ 20. This is due to the fact that a few objects in that bin have actually a lower column density that could not be effectively constrained in the 0.3–10 keV energy band. For all those objects the Log$N_H \sim$ 20 can be considered an upper limit to the true absorbing column density. Because of this, the source count distribution in the Log$N_H \approx$ 20 bin tends to overestimate the true intrinsic density. However, as seen in the Fig. 5.12 this effect is small.

5.5 Anti-correlation of Absorption and Luminosity

According to the AGN unified model (Antonucci, 1993; Urry and Padovani, 1995) all the different properties of AGN can be ascribed solely to orientation effect. Thus one should not observe variations of any other property with e.g. luminosity, accretion rate and redshift. However, already 30 years ago, Lawrence and Elvis (1982) reported the discovery of the anti-correlation of the fraction ($F_{\%}$) of obscured AGN (relative to the whole population) and luminosity. More recently different authors addressed the same issues with contradicting results. For example some studies (e.g. Treister and Urry, 2006; La Franca et al., 2005; Della Ceca et al., 2008; Winter et al., 2009a; Brusa et al., 2010) suggest that $F_{\%}$ decreases with X-ray luminosity, while Dwelly and Page (2006) point to $F_{\%}$ being independent of L_X. Also Sazonov and Revnivtsev (2004), Sazonov et al. (2007), and Beckmann et al. (2009) pointed out that an anti-correlation of the fraction of absorbed sources and X-ray luminosity seems to exist.

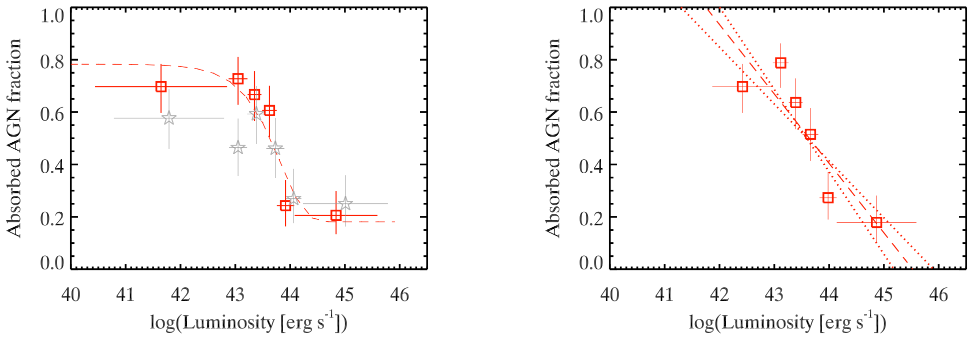

(a) The red dashed line represent the fit with Eq. 5.5. Grey stars represent, for comparison, data from Beckmann et al. (2009). Luminosities measured by INTEGRAL have been converted into the 15–55 keV energy range.

(b) Same as (a) but with a cut in luminosity, as discussed in the text. The dashed (dotted) line represents a linear fit to the data (1σ uncertainties).

Figure 5.14 Fraction of the obscured (i.e. $N_H \geq 10^{22}$ cm^{-2}) AGN as a function of 15–55 keV luminosity (red squares). The data have been grouped such as to have an equal number of sources per luminosity bin. Errors on fraction of absorbed AGN have been computed using Binomial statistics (see Gehrels, 1986) and are drawn at 1 σ level.

Fig. 5.14 shows how the fraction of obscured AGN (those with $\log N_H \geq 22$) changes as a function of X-ray luminosity (in the 15–55 keV band) in our survey. The width of each bin has been chosen so that the number of object per bin is constant (~ 33). The errors on the number of absorbed sources and the total number of sources per bin have been propagated with the recipes for Binomial statistics (see Gehrels, 1986, in particular Tab. 6). Binomial statistics apply specifically when dealing with ratios of small numbers. The data are correlated, as the Spearman's rank correlation coefficient is r_s = -0.94. The probability of a chance correlation (4.8×10^{-3}) shows that the correlation is true at the 2.9σ confidence level.

We also show for comparison the INTEGRAL results of Beckmann et al. (2009), by converting the INTEGRAL 20–100 keV luminosities into 15–55 keV luminosities and selecting only non-blazar sources with z<0.3. The two data-sets are in reasonable agreement although the lower fraction of absorbed AGN in the INTEGRAL sample (with respect to the BAT sample) might be ascribed to completeness issues of the former.

In the BAT sample, the absorbed AGN fraction displays a flattening in the low luminosity regime, and the correlation becomes clearly non-linear ($\chi^2/dof \gtrsim 3.5$). Thus, we tried to fit the fraction of absorbed AGN with the empirical function proposed by Gilli et al. (2007) of the form:

$$F_{\%}(L_X) = R_{low}e^{(-L_X/L_C)} + R_{high}[1 - e^{(-L_X/L_C)}] \tag{5.5}$$

where R_{low} is the low luminosity asymptotic behavior, R_{high} the high luminosity one, and L_C is a "critical" luminosity at which the drop occurs. We fitted this function to the data: the best fit values for R_{low}, R_{high}, and $\log(\mathrm{L}_C)$ are respectively 0.8, 0.2, and 43.7. This fit yields a $\chi^2/dof = 1.3$ which shows that this fit is better than a simple linear relation between the obscured AGN fraction and (the logarithm of) luminosity. This result will be discussed in details in in § 5.6.

In the literature (e.g. Hasinger, 2008; Della Ceca et al., 2008) the minimum luminosity considered for an AGN in the 2–10 keV energy range, was typically greater than 10^{42} erg s^{-1}. Since the low luminosity tail of our distribution (see Fig. 5.8) extends to $\sim 2.8 \times 10^{40}$ erg s^{-1} we checked, for the sake of completeness, if by introducing a cut at 10^{42} erg s^{-1}, changed our findings. When transforming the 2–10 keV luminosity of 10^{42} erg s^{-1} to the 15–55 keV band, we find that only 7 sources fall below this limiting luminosity. The level of correlation of the data remains unchanged, while instead the χ^2/dof value for a linear fit, decreases to ~ 1.8. These results are shown in Fig. 5.14 (b). It is still apparent that the linear fit (which shows a slope of -0.26 ± 0.05) is not a good representation of the data since the first bin and the last two show a flattening of the fraction of absorbed AGN. Finally, it is worth considering that (i) the contribution from the stellar population hardly extends above $\sim 10^{41}$ erg s^{-1} (Ranalli et al., 2003; Norman et al., 2004), and (ii) in the 15–55 keV band this contribution is expected to decrease to even a lower fraction of the "bolometric" luminosity (see e.g. Voss and Ajello, 2010).

5.6 Luminosity Functions of AGN

We estimate the X-ray luminosity function (XLF) of AGN using the $1/V_{MAX}$ method (equivalent in our formalism to the $1/V_a$ method). In this framework the XLF can be expressed as:

$$\Phi(L_X, z) = \frac{dN}{dL_X} = \frac{1}{\Delta\ L_X} \sum_{i=1}^{N} \frac{1}{V_{MAX,i}} \tag{5.6}$$

where $V_{MAX,i}$ is the maximum comoving volume associated with the i_{th} source. This is defined as:

$$V = \int_{z=0}^{z=z_{MAX}} \frac{dV}{dz}\ \Omega(L_i, z) dz, \tag{5.7}$$

where dV/dz is the comoving volume element per unit redshift and unit solid angle (see e.g. Hogg, 1999), z_{MAX} is the maximum redshift after which the sources would not be detected anymore in the BAT survey and $\Omega(L_i, z)$ is the sky coverage of the survey. The XLF of the two different classes of AGN, obscured and unobscured, is reported in Fig. 5.15.

We made a Maximum Likelihood fit to the two different datasets using a broken power-law of the form (see e.g. Ueda et al., 2003; Hasinger et al., 2005):

$$\Phi(L_X, z = 0) = \frac{dN}{dL_X} = \frac{A}{ln(10)L_X} \left[\left(\frac{L_X}{L_*}\right)^{\gamma_1} + \left(\frac{L_X}{L_*}\right)^{\gamma_2} \right]^{-1} \tag{5.8}$$

The ML estimator can be expressed as:

$$\mathcal{L} = -2 \sum_i \ln \frac{\Phi(L_{X,i}, z_i) V(L_{X,i}, z_i)}{\int \Phi(L_X, z) V(L_X, z) dL_X} \ . \tag{5.9}$$

Table 5.4 Best-fit parameters of X-ray Luminosity Functions in the 15-55 keV band

SAMPLE	# Objects	Norm.[1]	L*[2]	γ_1	γ_2
ALL	199	1.53e-5	$0.53^{+0.15}_{-0.15}$	$0.74^{+0.07}_{-0.08}$	$2.60^{+0.19}_{-0.20}$
ABSORBED	105	2.59e-5	$0.26^{+0.08}_{-0.07}$	$0.58^{+0.12}_{-0.13}$	$2.75^{+0.34}_{-0.30}$
ABSORBED[3]	99	3.93e-5	$0.26^{+0.14}_{-0.09}$	$0.51^{+0.28}_{-0.34}$	$2.63^{+0.38}_{-0.31}$
UNABSORBED	92	1.90e-6	$1.34^{+0.48}_{-0.38}$	$0.80^{+0.11}_{-0.12}$	$2.88^{+0.37}_{-0.31}$

[1] Normalization of the XLF expressed in units of $\mathrm{erg}^{-1}\,\mathrm{s}\,\mathrm{Mpc}^{-3}$.

[2] In units of 10^{44} erg s^{-1}.

[3] *Intrinsic* XLF of absorbed AGN. The luminosity of the absorbed AGN with $\mathrm{LogN}_H \geq 23.5$ have been de-absorbed with the method described in § 5.4.2.

The best-fit parameters are obtained by minimizing $\mathcal{L}$. Their 1 σ error are computed by varying the parameter of interest, while the others are allowed to float, until an increment of $\Delta\mathcal{L}$=1 is achieved. This gives an estimate of the 68 % confidence region for the parameter of interest (Avni, 1976). The likelihood function does not depend on the normalization A since it cancels out in Eq. 5.9. Once the slope α is determined, the normalization is derived as the value which reproduces the number of observed sources. An estimate of its statistical error is given by the Poisson error on the number of sources used to build the XLF.

The results of the ML fits to the XLFs of whole population of AGN and obscured and unobscured subclasses are summarized in Tab. 5.4. We focussed mainly on the difference between the two subsamples of absorbed and unabsorbed AGN, but we used the total XLF in Fig. 5.17 in order to account for the obscuration-luminosity relation. It is apparent that the XLFs of the two classes of objects are not the same. In particular the 'break' luminosity L^* is different at ~2.8 σ level, with absorbed AGN having on average lower luminosity than unabsorbed ones. Also Della Ceca et al. (2008), analyzing a small sample of XMM-Newton AGN, found different XLFs for obscured and unobscured sources. However, in their case they cannot allow (presumably due to the low number of sources) L* to be a free parameter of the fit. In our case, this can be done and there is evidence (albeit marginal) that the typical luminosity of absorbed and unabsorbed AGN is different. The difference between the luminosity functions of absorbed and unabsorbed objects is however not a surprise. Indeed it is expected in view of the anti-correlation of the absorption fraction and luminosity (e.g. Fig. 5.14). The two luminosity function are equal at a luminosity of $4{\times}10^{43}$ erg s^{-1}. This is exactly the luminosity at which the fraction of absorbed objects is 0.5 (see Fig. 5.14). For the very first time this trend is clearly seen in the luminosity function of absorbed and unabsorbed objects (as derived from the same energy band).

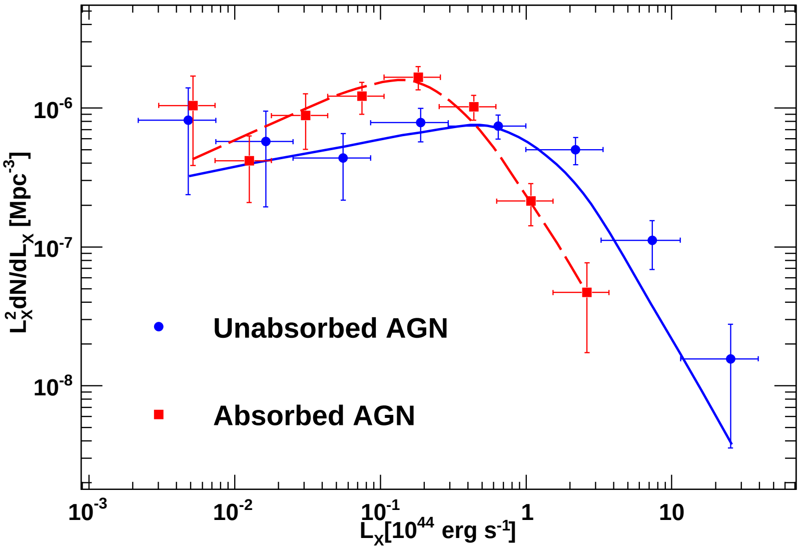

Figure 5.15 Luminosity function of absorbed (logN$_H$ $\geq$22, squares) and unabsorbed AGN (logN$_H$ <22, circles) with the respective best-fit models (solid and dashed lines). The luminosity functions have been multiplied by L_X^2 to highlight the different positions of the break luminosities.

We tested if this 'trend' of the break luminosity holds for smaller subsamples, namely if the very most absorbed sources show a significantly smaller value of L^*. This exercise needs of course a sufficient number of sources per subsample, in order to constrain the parameters of the fit with the broken power law. Therefore we divided the parent population into four bins of absorption containing $\sim$ 50 sources each. For each of the subsamples we computed the best fit values of the XLF as described before. In Fig. 5.16 we showed the break luminosity (in units of 10^{44} erg cm^2 s^{-1}) versus N$_{\rm H}$. This exercise confirms, albeit with a statistical significant uncertainty, that absorbed AGN appear to be intrinsically less luminous than unabsorbed AGN. We also performed an additional test in order to exclude that this finding is partially driven by the bias against the detection of the most absorbed AGN. We computed the *intrinsic* XLF of absorbed AGN by de-absorbing the AGN luminosities using the model described in §5.4.2. As clearly seen from Fig. 5.13, this correction is negligible for all AGN with LogN$_{\rm H}\leq$23.5, modest for all those with 23.5 <LogN$_{\rm H}\leq$24 and relevant for AGN with LogN$_{\rm H}\geq$24. It has to be noted that the *intrinsic* XLF of absorbed AGN suffers from incompleteness at the lowest luminosities. Indeed, because of the effect of large absorption, sources with an intrinsic luminosity large enough to be detected by BAT might be pushed below the BAT sensitivity. In order to avoid this problem we cut the sample at the minimum de-absorbed luminosity for which the $K(N_H)$ correction (discussed in §5.4.2) was less than 1. This minimum, de-absorbed, luminosity is 2×10^{42} erg s^{-1} and we consider the BAT sample to be complete above it. The parameters of the *intrinsic* XLF of absorbed AGN are reported in Tab. 5.4. It is clear that the *intrinsic* XLF of absorbed AGN is

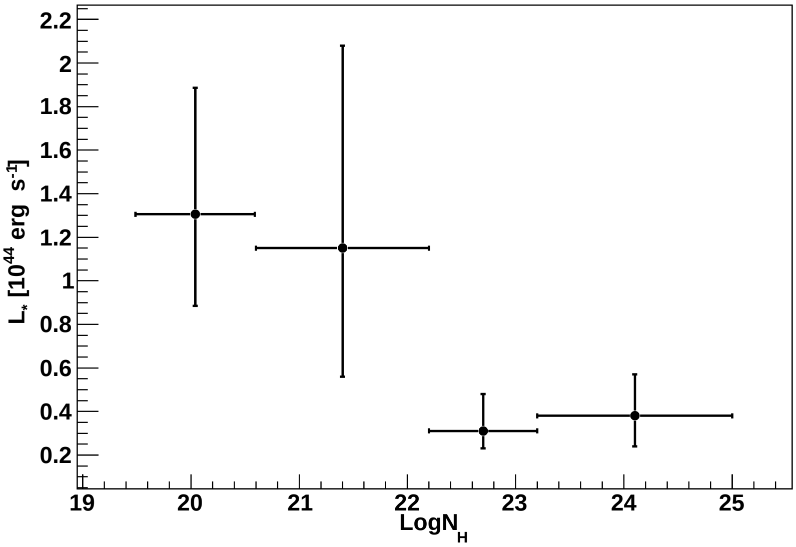

Figure 5.16 Break luminosity (L^*, as in Eq. 5.8) in units of 10^{44} erg cm^2 s^{-1}, versus column density. The sample was divided into four equally populated subsamples of ~50 sources. Errors are quoted at $1\,\sigma$ level.

found to be in very good agreement with the XLF of absorbed AGN. This is because the bias against the detection of absorbed AGN is relevant only for LogN$_{\rm H}\geq$ 24 and above this threshold the BAT sample contains very few objects.

Finally, we test whether the anti-correlation of the fraction of obscured AGN and luminosity (found in the previous section) can be reproduced by the two different XLFs for absorbed and unabsorbed AGN. To this extent we divide the XLF of absorbed AGN by the XLF of the entire sample. We computed the $1\,\sigma$ error on this function via bootstrap with replacement employing 1000 bootstrapped samples. In order not to suffer from biases derived from the detection of Compton-thick AGN and also to avoid the need of correcting for them, we also excluded all objects with LogN_H $\geq$24. As shown in the previous sections the BAT sample can be considered complete for all AGN with LogN_H $\leq$24. The results of our analysis are shown in Fig. 5.17 along with the observed anti-correlation of the obscured AGN fraction and luminosity. The agreement within errors is clear at all luminosities and the decreasing trend in the absorbed fraction at low luminosity does not depend on the presence or the absence of Compton-thick AGN. The trend of the fraction of obscured AGN and luminosity can be perfectly reproduced by the analysis of the XLFs of the absorbed and unabsorbed AGN. In turn, this difference can be ascribed to the fact that on average obscured AGN appear to be less luminous. Even more interestingly, the ratio of XLFs predicts (in agreement with the observations) that the fraction of obscured sources decreases at low luminosities (i.e. $L_X < 10^{42}$ erg s^{-1}). However, we caution the reader that, due to the lack of sources, the obscured AGN fraction is, at low-luminosities, compatible within $3\,\sigma$ with a constant fraction of

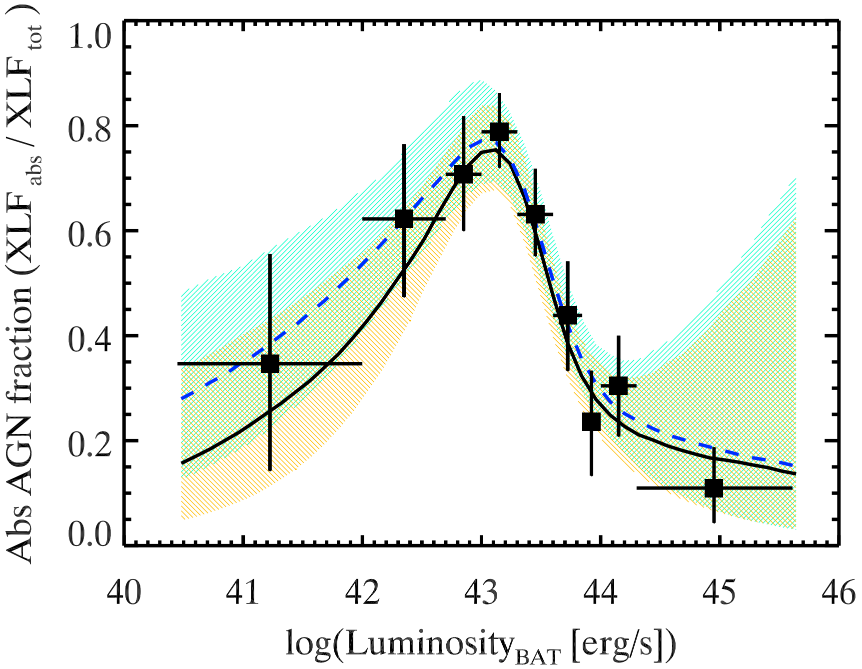

Figure 5.17 Fraction of the absorbed AGN versus luminosity in the 15–55 keV energy range. The lines are obtained by dividing the XLF of obscured AGN by the XLF of the whole population. The dashed (solid) line represents the whole sample (with a cut at 2×10^{42} erg s^{-1}). The shaded bands represent the $1\,\sigma$ uncertainty computed with a bootstrap analysis, blue for the whole sample and yellow for the sample with the cut in luminosity. The points are those used in Fig. 5.14 (the 9 CT objects have been excluded) with a different binning.

$\sim 80\,\%$.

5.7 Discussion

5.7.1 Compton-thick AGN and the Cosmic X-ray Background

It is well understood that the shape and the intensity of the CXB cannot be reproduced successfully if Compton-thick AGN ($\log N_H \geq 24$) are not invoked. They are required to produce $\sim$10 % of the CXB intensity at $\sim$ 30 keV (Gilli et al., 2007; Treister et al., 2009). However, since the extreme absorption makes these objects faint at X-rays, Compton-thick AGN have to be numerous (e.g. $\sim$30 % of the whole AGN population) in order to fulfill the above requirement. Despite this general belief, all searches of Compton-thick AGN have so far highlighted a lack of Compton-thick AGN (see Tab. 5.2). This work, which uses the largest AGN sample collected so far above 15 keV, shows that the *detected* fraction of Compton-thick AGN is only $4.6^{+2.1}_{-1.5}\,\%$. At the fluxes currently sampled by *Swift*–BAT population synthesis models predict this fraction to be either ∼16% if one adopts the Gilli et al. (2007) or ∼8% the Treister et al. (2009) model. Thus our measurement appears to be substantially lower than both predictions, but compatible within $\sim 2\,\sigma$ with what reported by Treister et al. (2009).

However, one must take into account that even X-rays with energies larger than 15 keV are absorbed if the source is mildly Compton-thick. Fig. 5.12 shows how dramatic this effect is. Indeed, if the source has $\log N_H \approx 24$ then only ∼50 % of the intrinsic, nuclear, flux is visible above 15 keV. This fraction becomes much lower (e.g. a few %) if the source has $\log N_H \approx 25$. Thus the extreme low number of Compton-thick AGN detected in shallow surveys at hard X-rays is due to fact that only the population of *intrinsically* bright objects is being sampled. As such these objects are rare. For the first time, we use the knowledge of how X-rays are absorbed through a Compton-thick medium to determine the *intrinsic* absorption distribution. We find that Compton-thick AGN are $20^{+9}_{-6}\,\%$ (statistical error) of the whole AGN population. Our result shows beyond doubt that Compton-thick sources are indeed *intrinsically* numerous, but due to the large absorption, very difficult to detect.

The average spectrum of all Compton-thick AGN detected by BAT is, in the 15-195 keV band, compatible with a very curved spectrum peaking around 40–50 keV (see Fig. 5.5). Since the peak of the CXB is located at ∼ 25 keV (Ajello et al., 2008b), this implies that the bulk of the Compton-thick AGN must be located at $z \approx 1$ in order to explain the missing fraction of the CXB. We employed the MYTorus model, that fully treats photoelectric absorption and relativistic Compton-scattering in a toroidal geometry, to fit the BAT spectra of the Compton-thick AGN. We derived that in the BAT band the spectrum of Compton-thick AGN is very likely dominated by the scattered component. The photon index is compatible with 2.0 while the absorbing column density is constrained to be Compton-thick using BAT data alone. We also found out that on average only ∼30 % of the intrinsic nuclear flux is visible in the BAT band.

Summarizing we find that Compton-thick AGN: 1) are *intrinsically* as numerous as required by the AGN unified model , and 2) have a spectral shape which 'fits' the one required to explain the shape and the peak of the CXB. However, the predictions of population synthesis models (Gilli et al., 2007; Treister et al., 2009) in terms of *observed* Compton-thick AGN are between a factor of 2 to 3 larger than what is currently observed by BAT.

5.7.2 A receding torus or a Clumpy torus model ?

It is generally accepted that all kinds of AGN are different manifestations of the same engine (i.e. the accreting super-massive black hole), seen under different line of sights. Thus, in the unified picture, obscuration depends solely on orientation effects. This hypothesis breaks down when showing that the fraction of obscured sources (relative to the whole population) decreases with luminosity. This result has been reported several times in the past, but it has been confirmed now by BAT (with a sample a factor ∼2 greater than the one presented in Tueller et al. 2008).

Our results, like the previous claims of this anti-correlation, are inconsistent with the simplest prediction of the unified model, for which $F_{\%}$ should not depend on L_X. Already Lawrence (1991) tried to overcome this contradiction by proposing a *receding torus model.* In this model, the inner radius is set by the dust sublimation radius which increases with source luminosity. This model predicts that the fraction of obscured sources scales with luminosity as $F_{\%} \propto L^{-0.5}$.

Behavior at high luminosities In basic terms the inner radius is set from the following:

$$R_d \simeq 0.4 \left(\frac{L}{10^{45}\mathrm{erg\ s^{-1}}}\right)^{0.5} \left(\frac{1500\ \mathrm{K}}{T_{sub}}\right)^{2.6} \mathrm{pc} \tag{5.10}$$

where L is the bolometric luminosity and T_{sub} is the sublimation temperature of the dust. Given the angular dependence of $F_{\%}$ (i.e. the angle at which a smooth torus becomes transparent to radiation), a constant H/R implies $F_{\%} \propto L^{-0.5}$. While attractive, this simple idea fails to reproduce correctly the dependence of the obscured fraction with luminosity, in particular when looking just at the hard X-ray portion of the spectral energy distribution. Indeed, in this work we showed that $F_{\%} \propto L_X^{-0.26\pm0.05}$ for $\mathrm{L}_X \geq 10^{42}$ erg s^{-1}.

Nonetheless, one has to consider that (i) the torus is likely clumpy, (ii) H/R is a function of luminosity (Simpson, 2005), and (iii) that even if the dusty components of the torus do absorb optical, UV, and X-ray photons, X-ray obscuration can take place also in the -dust free- inner region, in the proximity ($<$ 0.1pc) of the AGN. This has been largely discussed in Risaliti et al. (2002, 2007). Recently (see Hönig and Beckert, 2007; Nenkova et al., 2008) $F_{\%}$ was interpreted in the framework of a *radiation-limited clumpy dust torus* in which $F_{\%} \propto L^{-0.25}$, which is much closer to our findings. In this scenario, the obscuration–luminosity relation is recovered in terms of probability that the photons intercept a sufficient number of clouds in the line of sight. In addition, the work of Hasinger (2008) shows similar results in the 2–10 keV energy band, even if just proxies of $\mathrm{N_H}$ are used. Finally, Maiolino et al. (2007) interpreted those early results by comparing them to a similar relation between the fraction of obscured AGN and the O[III] luminosity (as well as other bands, but see their detailed description). According to the authors this was a signature of the variation of the covering factor of the AGN dust with luminosity. The variation of the covering factor of the torus is -in general- also associated with the "Iwasawa-Taniguchi" (IT) effect (Iwasawa and Taniguchi, 1993), i.e. the anti-correlation of the EW of FeKα and X-ray luminosity. Bianchi et al. (2009a) discussed the agreement among the findings of Dadina (2008) in the 20-100 keV regime, and their updated *XMM–Newton* sample. If the anti-correlation of $F_{\%}$ and luminosity is interpreted as the variation of the covering factor of the torus, then this can be in turn compared to the IT effect. From the results of Della Ceca et al. (2008), they found a slope of $\simeq 0.22$, in very good agreement with the IT effect, with the slope ($\simeq 0.18$) presented in Maiolino et al. (2007), and eventually with our findings ($\simeq 0.26$). Although these similarities are intriguing, they certainly deserve a profound investigation. This is even more compelling when considering that the methods differ and in principle sample different materials.

Behavior at low luminosities In the low luminosity regime (i.e. below 10^{42} erg s^{-1}), the behavior of the torus is likely more complex than what reported above. Different authors (e.g. Elitzur and Shlosman, 2006; Elitzur and Ho, 2009) showed that below a bolometric luminosity of $\sim 10^{42}$ erg s^{-1} the torus obscuration region disappears. This results under the assumption that the clouds are generated by a disk-wind outflow, rather then accreted from the galaxy (Krolik and Begelman, 1988). In the framework proposed by Elitzur and Shlosman (2006) and Elitzur and Ho (2009) the cloud mass outflow $\dot{M}_{cl}$ is proportional to the mass accretion rate, which is related to the bolometric luminosity via $\dot{M}_{acc} = 0.02 L_{45}/\eta M_{\odot}$ yr^{-1}, η being the accretion efficiency. The ratio $\dot{M}_{cl}/\dot{M}_{acc}$ increases at progressively lower luminosities but since it cannot exceed unity, there is a limiting luminosity at which the system cannot sustain the cloud outflow any longer.

At low luminosities we then expect absorption of X-rays to be less effective, due to the lack of obscuration in the torus. We should then observe a decrease in the fraction of obscured AGN at low luminosity. For the first time, and thanks to BAT, we are able to inspect the behavior of $F_{\%}$ at low luminosities. Indeed, Fig. 5.17 shows[4] that the fraction of obscured AGN decreases at low luminosities as one would expect if the torus obscuring region would cease to exist. There are no other evidences (perhaps beside this one, but see van der Wolk et al., 2010) which shows that the torus disappears at low luminosities[5], but there are ample evidences that at least the broad line region (BLR) disappears at low luminosities. This happens for two known class of objects: 1) BL Lac sources and 2) low-luminosity type-2 AGN.

BL Lacs are a class of (low-luminosity) blazars characterized by the absence of emission lines in their optical spectrum. Their broad-band spectrum is normally well understood in terms of the Synchrotron-Self Compton model (Maraschi et al., 1992) where the electrons responsible for the synchrotron emission are up-scattering (via inverse Compton) the same synchrotron radiation to high energy. The main difference with the more luminous flat spectrum radio quasars is that in these latter ones an additional high-energy component (refereed to as 'external Compton' component) is normally detected. In the external Compton model photons from the BLR and/or the disk are up-scattered to high energy by the electrons in the jet. It is believed that the absence of lines and of this external components is caused, in BL Lac objects, by the lack of the BLR, and a lower radiation field density. Moreover, BL Lacs are characterized by low Eddington ratios (e.g. $\lambda_{Edd} \simeq 0.01$). Around this Eddington ratio, the accretion process experiences a transition from an optically thick, geometrically thin

---

[4] We caution the reader that within 3σ the behavior of $F_{\%}$ at low luminosity is still compatible with a constant value of 0.8.

[5] During the compilation of this work, Brightman and Nandra (2011) published a very similar result, based on the same interpretation, on a completely independent sample of AGN

disk ($\lambda_{Edd} > 0.01$) to a radiatively inefficient geometrically thick disk (Narayan and Yi, 1994; Ghisellini et al., 2009). Therefore in blazars with low Eddington ratios, the electrons in the jet find a medium starved of external radiation, weak or no lines are produced, and the AGN is classified as BL Lac.

Another evidence for the absence of BLR at low luminosities is produced by low-luminosity type-2 AGN. These AGN, are sometimes referred to as 'true' type-2 AGN because when observed in polarized light they do not show broad lines (Ho, 2008) and hence lack a BLR. How the "local" changes in the accretion regime affect the environment at the BLR and the torus region is non-trivial and debated (according to Nicastro (2000) and Nicastro et al. (2003), the main driver for the disappearance of the BLR appears to be the accretion rate), nonetheless in this framework we find a convincing interpretation of our findings. The clumpy torus, and the BLR progressively disappear, resulting in a less efficient X-ray obscuration. Therefore we should expect $F_{\%}$ to flatten or even to invert its dependence on the luminosity at progressively low Eddington ratios. With future X-ray missions like *NuSTAR* (Harrison et al., 2005), and *NHXM* (Pareschi et al., 2009) it will be possible to sample with better statistics the population of the low-luminosity AGN and to investigate the behavior of the BLR and the torus in greater detail.

5.8 Summary and conclusion

We addressed the study of a complete, flux limited, sample of local AGN collected by the *Swift*–BAT instrument in the first three years of survey. The sources are listed in Tab. 5.5, along with their properties. The aim of this work is to characterize the AGN population from two fundamental observables such as the hard X-ray (15–55 keV) luminosity and absorption. To this aim we jointly fitted the BAT spectra with the available follow up in the 0.3–10 keV domain. In the following we briefly review the main findings. We remind the reader that AGN are defined 'absorbed' if the column density for photoelectric absorption exceeds 10^{22} atoms cm^{-2}.

- Performing a stacked analysis of the complete 199 AGN sample, a simple power law model was shown not to account for the continuum emission. In addition we performed the stacked analysis of the different subsamples of sources: unabsorbed, absorbed, and -for the first time- Compton-thick one. The average spectrum of CT sources was found to be dominated (in the BAT band) by the scattered component and its photon index was found to be compatible with ∼2.0. According to our results, only ∼30 % of the source intrinsic flux is visible in the 15–55 keV band.

- We showed that absorbed AGN are characterized by slightly harder spectra (1.91) with respect to the unabsorbed ones (2.00). Nonetheless the distributions are quite broad, resulting in a Kolmogorov-Smirnov probability of 3.5×10^{-3} of belonging to the same parent population.

- We computed the observed N_H distribution, which shows that the observed fraction absorbed sources is 54±4%, with columns peaking at 10^{23} cm^{-2}. The observed fraction of Compton-thick objects is $4.6^{+2.1}_{-1.5}$%, a factor 2 to 3 lower than what predicted from population synthesis models at the fluxes of the BAT survey.

- We estimated the bias of the BAT instrument against the detection of the Compton-thick AGN. We consequently derived the *intrinsic* $\mathrm{N_H}$ distribution by integrating the logN-logS in bins of $\log\mathrm{N_H}$ setting the minimum observed flux of integration so that the limiting intrinsic flux was the same for all the bins. Therefore we showed that even if the CT objects are only a minor fraction of the observed sample, their contribution rises to 20^{+9}_{-6} % in the intrinsic AGN population.
- The relation between the observed fraction of obscured AGN and the hard X-ray luminosity ($F_{\%}$), was found to have different behaviors according to the luminosity regime considered. For luminosities greater then 10^{42} erg s^{-1} we found a monotonic decline with a slope of -0.26±0.05. At smaller luminosities, albeit affected by poor statistics, we found a flattening of $F_{\%}$ which we interpreted as the manifest disappearance of the obscuring region. In a disk–cloud outflow scenario, this is indeed expected to happen under a critical luminosity, which is of the same order of the luminosity at which we observe the flattening.
- We showed that the obscuration–luminosity relation can be explained by the different X-ray Luminosity Functions of the obscured and unobscured subsamples. This in turn means that absorbed AGN are intrinsically less luminous. This result, if the mass distribution is narrow, points towards a trend in the Eddington ratios in which objects accreting at lower values (thus having smaller effects on their environments) are more absorbed. Obscuring clouds would be able to come closer to the nuclear region without being affected, and bury the AGN.

A key test to improve our findings will be the calculation of the BH masses for the sample. By means of the two physical quantities (i.e. λ_{Edd} and mass) we begin to test in the next chapter whether it is possible to find a sequence relating absorption, Eddington ratio, and mass of the black hole. Some information can already be found in Middleton et al. (2008) and Beckmann et al. (2009). They found that for two different samples of AGN selected in the local Universe, the mean Eddington ratio is in the 0.01-0.06 range. Cappelluti et al. (2010) also showed that, on average, the BAT AGN used in this work have an Eddington ratio of 0.01. Moreover, Middleton et al. (2008) and Beckmann et al. (2009) found that on average unobscured AGN have larger Eddington ratios with respect to obscured ones. This would be consistent with the presence of a trend in λ_{Edd} for non-jetted AGN. The obscured objects could be accreting at lower Eddington ratios and with flatter spectra; the unobscured ones, with steeper spectra, could be accreting slightly more efficiently. By means of this analysis it would be also possible to relate our findings to a physical consistent picture, in the framework of merger driven AGN activity.

Indeed, merging of gas-rich galaxies provides an efficient way to funnel large amount of gas and dust to the central black hole and triggers AGN activity (e.g. Kauffmann and

Haehnelt, 2000; Wyithe and Loeb, 2003; Croton et al., 2006). Noteworthy a very recent work by Koss et al. (2010) determined that a considerable fraction (i.e. $\sim$24 %) of the hosts of the BAT AGN have a close companion within 30 kpc and are experiencing a major merging event. This fraction is extremely relevant when compared -as done by the authors of that paper- to a control sample of local (i.e. $z < 0.1$) optically selected narrow-line AGN, where the fraction of interacting companions is ~ 1 %. We counted how many objects of the sample of merging AGN of Koss et al. (2010) are obscured. We found that $\geq$63 % are obscured AGN[6] with an average column density of $\log N_{\rm H} \approx 23.4$. Nonetheless, contradicting results emerge in the literature when one wants to compare the fractions of AGN hosting galaxies that display signs of merging (see e.g. the opposite conclusions between Cisternas et al. 2010 and Silverman et al. 2011).

A limitation to this simple picture is that in case of a merging event and of a large gas quantity being funneled towards the center, the black hole is expected to accrete with high Eddington ratios (e.g. Di Matteo et al., 2005; Hopkins et al., 2006). According to Fabian (1999) a SMBH accreting at Eddington luminosities should clear the environment from any Compton-thin (e.g. $\log N_H < 24$) column density and therefore transit to a less obscured phase. If the very first phase of the gas-rich merger event is the creation of a Compton-thick AGN, then we would expect it to display large Eddington ratios. However, two of the most famous Compton-thick AGN (Circinus and NGC 4945) display an Eddington ratio far from unity (i.e. $\leq 10^{-2}$, see Gültekin et al., 2009), proving that this argument still escapes a conclusive explanation. The largest hard X-ray selected samples of AGN in the local Universe may shed some light on the physical interpretation of the feedback of black holes on their surroundings.

---

[6] For comparison, we remind that in our sample the fraction of obscured sources is $\sim$50 %.

Table 5.5. *Swift* sample of AGN.

SWIFT NAME	R.A. (J2000)	DEC (J2000)	Flux [15-55 keV] (10^{-11} cgs)	S/N	ID	Type‡	redshift	Ph. Index (BAT only)	log(N_H)	Reference
J0006.4+2009	1.600	20.152	1.16±0.20	5.8	Mrk 335	Sy1	0.03	$2.38^{+0.50}_{-0.42}$	22.6	(2)
J0038.6+2336	9.650	23.600	1.10±0.21	5.3	Mrk 344	Sy	0.02	$2.06^{+0.46}_{-0.41}$	23.2	(2)
J0042.7-2332	10.680	-23.548	2.44±0.21	11.7	NGC 235A	Sy2	0.02	$1.60^{+0.20}_{-0.19}$	23.0	(1)
J0048.7+3157	12.188	31.962	7.71±0.20	37.8	Mrk 348	Sy2	0.02	$1.90^{+0.08}_{-0.07}$	23.3	(1)
J0051.9+1726	12.998	17.447	1.81±0.21	8.6	QSO B0049+171	Sy1	0.06	$2.13^{+0.28}_{-0.25}$	20.0	(2)
J0059.9+3149	14.997	31.831	1.66±0.21	8.0	SWIFT J0059.4+3150	Sy1.2	0.01	$1.93^{+0.35}_{-0.32}$	21.0	(1)
J0101.0-4748	15.274	-47.800	0.97±0.18	5.6	2MASX J01003469-4748303	GALAXY	0.08	$2.32^{+0.44}_{-0.38}$	22.6	(2)
J0108.8+1321	17.201	13.351	1.78±0.22	8.2	4C 13.07	Sy2	0.06	$1.76^{+0.34}_{-0.27}$	23.8	(3)
J0111.4-3805	17.867	-38.086	1.52±0.18	8.3	**NGC 424**	Sy2	0.01	$1.94^{+0.28}_{-0.27}$	24.3	(4)
J0113.8-1450	18.453	-14.850	1.24±0.21	5.8	Mrk 1152	Sy1	0.05	$2.10^{+0.38}_{-0.34}$	21.1	(5)
J0114.3-5524	18.600	-55.400	0.92±0.17	5.3	SWIFT J0114.4-5522	Sy2	0.01	$1.53^{+0.33}_{-0.38}$	22.9	(1)
J0123.8-5847	20.952	-58.785	2.65±0.17	15.3	Fairall 9	Sy1	0.05	$2.02^{+0.15}_{-0.15}$	20.4	(1)
J0123.8-3504	20.974	-35.067	2.72±0.18	14.7	NGC 526A	Sy1.5	0.02	$1.71^{+0.14}_{-0.14}$	22.3	(1)
J0127.9-1850	22.000	-18.847	1.27±0.20	6.2	MCG-03-04-072	Sy1	0.04	$2.26^{+0.54}_{-0.44}$	20.0	(2)
J0134.0-3629	23.506	-36.486	2.36±0.18	13.0	NGC 612	Sy2	0.03	$1.63^{+0.17}_{-0.15}$	23.7	(6)
J0138.6-4000	24.674	-40.008	3.17±0.18	18.0	ESO 297-018	Sy2	0.03	$1.71^{+0.11}_{-0.11}$	23.8	(7)
J0142.6+0118	25.652	1.300	1.28±0.22	5.7	[VV2003c] J014214.0+011615	Sy1	0.05	$2.52^{+1.10}_{-0.57}$	…	
J0152.9-0326	28.250	-3.448	1.47±0.22	6.6	IGR J01528-0326	Sy2	0.02	$2.28^{+0.48}_{-0.41}$	22.9	(2)
J0201.2-0649	30.320	-6.821	4.17±0.22	19.3	NGC 788	Sy2	0.01	$1.74^{+0.11}_{-0.11}$	23.5	(1)
J0206.5-0016	31.631	-0.270	1.53±0.22	6.9	MRK 1018	Sy1.5	0.04	$1.48^{+0.40}_{-0.39}$	20.5	(1)
J0215.0-0044	33.751	-0.749	1.30±0.22	5.9	Mrk 590	Sy1.2	0.03	$2.23^{+0.54}_{-0.47}$	20.4	(1)
J0226.0-6315	36.500	-63.250	0.91±0.18	5.2	FAIRALL 0926	Sy1	0.06	$2.55^{+0.57}_{-0.47}$	20.9	(2)
J0226.8-2819	36.703	-28.324	1.14±0.18	6.4	2MASX J02262568-2820588	Sy1	0.06	$2.21^{+0.59}_{-0.49}$	21.8	(2)
J0228.4+3118	37.120	31.316	4.38±0.23	19.4	NGC 931	Sy1.5	0.02	$2.25^{+0.22}_{-0.16}$	21.6	(1)
J0232.0-3639	38.020	-36.662	1.09±0.17	6.4	IC 1816	Sy2	0.02	$2.03^{+0.38}_{-0.34}$	23.9	(2)
J0234.4+3229	38.612	32.489	1.60±0.23	7.1	NGC 973	Sy2	0.02	$1.70^{+0.41}_{-0.33}$	22.5	(2)
J0234.8-0847	38.702	-8.794	2.13±0.21	10.2	NGC 985	Sy1	0.04	$2.23^{+0.26}_{-0.24}$	21.6	(1)
J0235.6-2935	38.900	-29.600	0.99±0.18	5.6	ESO 0416-G0002	Sy1.9	0.06	$1.62^{+0.45}_{-0.35}$	19.6	(1)
J0238.5-5213	39.647	-52.220	1.31±0.17	7.6	ESO 198-024	Sy1	0.05	$1.69^{+0.26}_{-0.25}$	21.0	(1)
J0239.0-4043	39.767	-40.732	0.97±0.17	5.8	2MASX J02384897-4038377	Sy1	0.06	$2.12^{+0.61}_{-0.52}$	20.0	(2)
J0241.5-0813	40.381	-8.220	1.34±0.21	6.4	NGC 1052	Sy2	0.01	$1.47^{+0.38}_{-0.38}$	20.5	(8)
J0242.9-0000	40.732	-0.012	2.00±0.22	8.9	**NGC 1068**	Sy2	0.004	$2.23^{+0.33}_{-0.30}$	>25	(4)
J0249.3+2627	42.349	26.451	1.25±0.23	5.5	IRAS 02461+2618	Sy2	0.06	$1.66^{+0.39}_{-0.38}$	23.5	(2)
J0252.8-0830	43.200	-8.500	1.06±0.21	5.0	MCG-02-08-014	Sy2	0.02	$1.69^{+0.54}_{-0.40}$	23.1	(2)
J0255.4-0010	43.873	-0.170	4.48±0.22	20.1	NGC 1142	Sy2	0.03	$1.85^{+0.12}_{-0.11}$	23.4	(9)

Table 5.5 (continued)

SWIFT NAME	R.A. (J2000)	DEC (J2000)	Flux [15-55 keV] (10^{-11} cgs)	S/N	ID	Type‡	redshift	Ph. Index (BAT only)	log(N_H)	Reference
J0256.4-3212	44.117	-32.208	1.31 ± 0.17	7.7	ESO 417-6	Sy2	0.02	$1.86^{+0.25}_{-0.24}$	22.9	(2)
J0311.6-2045	47.919	-20.760	1.27 ± 0.18	6.9	2MASX J03111883-2046184	Sy1	0.07	$1.79^{+0.43}_{-0.34}$	20.0	(2)
J0325.1+3409	51.296	34.152	1.61 ± 0.24	6.8	2MASX J03244119+3410459	Sy1	0.06	$1.56^{+0.42}_{-0.30}$	20.0	(2)
J0333.5+3716	53.397	37.278	1.63 ± 0.24	6.8	IGR J03334+3718	Sy1	0.06	$2.37^{+0.53}_{-0.44}$	20.0	(2)
J0333.7-3608	53.433	-36.141	3.12 ± 0.17	18.9	NGC 1365	Sy1.8	0.01	$2.02^{+0.25}_{-0.24}$	23.6	(1)
J0342.2-2114	55.554	-21.244	2.15 ± 0.18	11.8	SWIFT J0342.0-2115	Sy1	0.01	$1.88^{+0.20}_{-0.19}$	20.5	(1)
J0347.3-3029	56.850	-30.500	0.89 ± 0.17	5.3	RBS 0741	Sy1	0.10	$2.04^{+0.48}_{-0.43}$	20.4	(2)
J0350.7-5022	57.679	-50.377	1.29 ± 0.17	7.5	SWIFT J0350.1-5019	Sy2	0.04	$1.79^{+0.39}_{-0.29}$	23.2	(2)
J0357.0-4039	59.268	-40.666	0.89 ± 0.17	5.4	2MASX J03565655-4041453	Sy1.9	0.07	$1.56^{+0.35}_{-0.34}$	22.5	(1)
J0402.5-1804	60.639	-18.077	1.35 ± 0.19	7.0	ESO 549- G049	Sy2	0.03	$1.75^{+0.50}_{-0.38}$	22.4	(2)
J0407.5+0342	61.883	3.717	1.90 ± 0.25	7.6	3C 105	Sy2	0.09	$1.91^{+0.30}_{-0.28}$	23.4	(1)
J0415.2-0753	63.800	-7.900	1.31 ± 0.23	5.6	LEDA 14727	Sy1	0.04	$2.25^{+0.44}_{-0.39}$	23.5	(2)
J0426.4-5712	66.603	-57.201	1.40 ± 0.17	8.2	1H 0419-577	Sy1	0.10	$2.57^{+0.56}_{-0.33}$	19.5	(1)
J0433.4+0521	68.355	5.365	5.21 ± 0.26	19.8	3C-120	Sy1	0.03	$2.12^{+0.13}_{-0.12}$	21.2	(1)
J0438.5-1049	69.633	-10.830	1.48 ± 0.23	6.4	MCG-02-12-050	Sy1	0.04	$2.02^{+0.61}_{-0.53}$	20.0	(2)
J0444.7-2812	71.199	-28.200	1.07 ± 0.18	5.9	2MASX J04450628-2820284	Sy2	0.15	$2.17^{+0.88}_{-0.66}$	20.0	(2)
J0451.8-5807	72.966	-58.133	0.88 ± 0.17	5.2	RBS 0594	Sy1	0.09	$1.86^{+0.42}_{-0.38}$	20.0	(2)
J0453.5+0403	73.380	4.060	2.11 ± 0.28	7.6	**CGCG 420-015**	Sy2	0.03	$2.04^{+0.36}_{-0.33}$	∼24.2	(4)
J0455.3-7528	73.841	-75.477	1.27 ± 0.18	6.9	ESO 33-2	Sy2	0.02	$2.52^{+0.49}_{-0.41}$	22.1	(2)
J0505.9-2351	76.497	-23.854	2.78 ± 0.20	13.9	XSS J05054-2348	Sy2	0.04	$1.79^{+0.18}_{-0.17}$	22.7	(1)
J0516.2-0009	79.071	-0.161	4.11 ± 0.28	14.5	QSO B0513-002	Sy1	0.03	$2.16^{+0.17}_{-0.16}$	20.0	(2)
J0519.7-3240	79.930	-32.676	2.38 ± 0.19	12.9	SWIFT J0519.5-3140	Sy2	0.04	$1.72^{+0.18}_{-0.14}$	21.1	(1)
J0519.8-4546	79.963	-45.774	2.49 ± 0.17	14.9	Pictor-A	Sy1	0.04	$1.90^{+0.17}_{-0.17}$	21.0	(1)
J0524.2-1212	81.050	-12.200	1.42 ± 0.25	5.6	LEDA 17233	Sy1	0.05	$1.90^{+0.36}_{-0.33}$	21.2	(2)
J0552.3-0727	88.090	-7.457	14.75 ± 0.29	51.7	NGC 2110	Sy2	0.01	$1.79^{+0.00}_{-0.00}$	22.6	(1)
J0552.3+5929	88.100	59.500	1.14 ± 0.21	5.3	IRAS 05480+5927	Sy1	0.06	$3.44^{+1.00}_{-0.73}$	21.1	(2)
J0558.1-3820	89.549	-38.347	2.12 ± 0.18	11.6	EXO 055620-3820.2	Sy1	0.03	$2.21^{+0.23}_{-0.21}$	22.2	(1)
J0602.9-8633	90.749	-86.555	1.82 ± 0.22	8.4	**SWIFT J0601.9-8636**	Sy2	0.01	$1.67^{+0.24}_{-0.37}$	∼24	(4)
J0603.1+6523	90.799	65.399	1.38 ± 0.20	6.8	UGC 3386	GALAXY	0.02	$2.10^{+0.36}_{-0.33}$	23.2	(3)
J0615.8+7101	93.967	71.021	6.08 ± 0.20	30.8	Mrk 3	Sy2	0.01	$1.66^{+0.01}_{-0.01}$	24.0	(1)
J0623.9-3214	95.994	-32.248	1.53 ± 0.20	7.5	ESO 426-G 002	Sy2	0.02	$1.86^{+0.38}_{-0.35}$	23.9	(2)
J0624.1-6059	96.028	-60.998	1.25 ± 0.17	7.4	SWIFT J2141.0+1603	Sy2	0.04	$2.51^{+0.42}_{-0.36}$	23.4	(2)
J0640.7-4324	100.200	-43.400	0.92 ± 0.18	5.2	2MASX J06400609-4327591	Sy2	0.06	$2.06^{+0.44}_{-0.39}$	23.4	(2)
J0652.1+7425	103.044	74.425	3.29 ± 0.19	17.1	Mrk 6	Sy1.5	0.02	$1.89^{+0.13}_{-0.13}$	23.0	(1)
J0656.1+3959	104.027	39.986	2.29 ± 0.26	8.7	UGC 3601	Sy1	0.02	$1.97^{+0.29}_{-0.27}$	21.3	(2)

Table 5.5 (continued)

SWIFT NAME	R.A. (J2000)	DEC (J2000)	Flux [15-55 keV] (10^{-11} cgs)	S/N	ID	Type‡	redshift	Ph. Index (BAT only)	$\log(N_H)$	Reference
J0718.0+4405	109.517	44.084	1.67±0.24	7.1	2MASX J07180060+4405271	Sy1	0.06	$2.22^{+0.41}_{-0.35}$	20.0	(2)
J0742.5+4947	115.644	49.793	2.98±0.21	14.4	Mrk 79	Sy1.2	0.02	$2.06^{+0.17}_{-0.16}$	20.8	(1)
J0800.1+2322	120.032	23.370	1.62±0.24	6.6	SDSS J0759.87+232448.3	GALAXY	0.03	$1.70^{+0.31}_{-0.30}$	22.3	(2)
J0800.3+2638	120.099	26.648	1.79±0.24	7.5	IC 486	Sy1	0.03	$1.80^{+0.30}_{-0.28}$	22.2	(2)
J0804.2+0506	121.050	5.101	3.18±0.25	12.6	UGC 4203	Sy2	0.01	$2.58^{+0.60}_{-0.48}$	23.5	(10)
J0811.1+7602	122.798	76.049	1.15±0.19	6.2	PG 0804+761	Sy1	0.10	$2.58^{+0.60}_{-0.48}$	20.0	(2)
J0814.4+0423	123.600	4.400	1.26±0.24	5.2	CGCG 031-072	Sy1	0.03	$1.90^{+0.49}_{-0.42}$	23.3	(2)
J0823.2-0456	125.800	-4.947	1.35±0.23	6.0	SWIFT J0823.4-0457	Sy2	0.02	$1.66^{+0.38}_{-0.37}$	23.5	(3)
J0832.8+3706	128.200	37.100	1.03±0.20	5.2	RBS 707	Sy1.2	0.09	$2.41^{+0.63}_{-0.52}$	20.0	(2)
J0839.8-1214	129.950	-12.248	1.28±0.21	6.1	3C 206	Sy1	0.20	$2.04^{+0.34}_{-0.31}$	21.0	(2)
J0904.9+5537	136.250	55.632	1.04±0.17	6.0	SWIFT J0904.3+5538	Sy1.5	0.04	$1.92^{+0.42}_{-0.39}$	21.0	(1)
J0911.5+4528	137.898	45.471	1.23±0.18	7.0	SWIFT J0911.2+4533	Sy2	0.03	$2.45^{+0.54}_{-0.44}$	23.5	(1)
J0918.4+1618	139.615	16.316	1.65±0.21	8.0	Mrk 704	Sy1.5	0.03	$1.98^{+0.26}_{-0.24}$	21.5	(2)
J0921.0-0803	140.257	-8.067	2.59±0.20	12.9	SWIFT J0920.8-0805	Sy2	0.02	$2.15^{+0.21}_{-0.19}$	22.8	(1)
J0923.8+2256	140.962	22.936	2.05±0.20	10.5	MCG +04-22-042	Sy1.2	0.03	$1.85^{+0.23}_{-0.21}$	20.6	(1)
J0925.2+5217	141.316	52.285	3.03±0.17	18.1	Mrk 110	Sy1	0.04	$2.00^{+0.14}_{-0.13}$	20.6	(1)
J0945.8-1419	146.468	-14.332	1.28±0.21	6.1	NGC 2992	Sy2	0.01	$1.55^{+0.34}_{-0.33}$	22.0	(1)
J0947.7-3056	146.939	-30.948	11.50±0.22	51.5	ESO 434-40	Sy2	0.01	$2.27^{+0.01}_{-0.01}$	22.2	(3)
J0959.6-2250	149.916	-22.834	4.44±0.22	19.8	NGC 3081	Sy2	0.01	$1.80^{+0.13}_{-0.12}$	23.5	(1)
J1001.8+5542	150.453	55.700	1.43±0.16	8.8	**NGC 3079**	Sy2	0.004	$1.88^{+0.26}_{-0.25}$	24.7	(4)
J1006.0-2306	151.500	-23.100	1.25±0.23	5.5	ESO 499-G 041	Sy1	0.01	$1.57^{+0.60}_{-0.62}$	21.4	(2)
J1021.7-0327	155.450	-3.450	1.35±0.22	6.3	MCG+00-27-002	Sy1	0.04	$2.34^{+0.54}_{-0.44}$	20.0	(2)
J1023.5+1951	155.888	19.864	7.35±0.20	36.8	NGC 3227	Sy1.5	0.004	$1.98^{+0.01}_{-0.01}$	22.8	(1)
J1031.8-3451	157.975	-34.860	4.71±0.26	18.4	NGC 3281	Sy2	0.01	$1.98^{+0.17}_{-0.16}$	23.9	(6)
J1031.9-1417	157.996	-14.300	2.13±0.23	9.3	H 1029-140	Sy1	0.09	$2.17^{+0.32}_{-0.29}$	20.0	(2)
J1044.0+7023	161.003	70.400	0.99±0.17	5.9	MCG+12-10-067	Sy2	0.03	$1.60^{+0.37}_{-0.35}$	23.3	(2)
J1046.5+2556	161.649	25.950	1.12±0.19	5.9	UGC 05881	GALAXY	0.02	$1.60^{+0.38}_{-0.36}$	23.0	(2)
J1048.5-2512	162.149	-25.200	1.42±0.27	5.3	**NGC 3393**	Sy2	0.01	$2.01^{+0.43}_{-0.37}$	24.7	(4)
J1049.3+2256	162.350	22.950	1.57±0.20	8.0	SWIFT J1049.4+2258	Sy2	0.03	$1.89^{+0.24}_{-0.23}$	23.3	(2)
J1106.6+7234	166.654	72.571	6.45±0.17	38.0	NGC 3516	Sy1.5	0.01	$1.90^{+0.01}_{-0.01}$	21.2	(1)
J1115.9+5426	168.999	54.450	0.88±0.15	5.7	SDSS J111519.98+542316.6	Sy2	0.07	$1.80^{+0.57}_{-0.42}$	22.4	(2)
J1125.4+5421	171.352	54.351	0.97±0.15	6.3	ARP 151	Sy1	0.02	$1.72^{+0.48}_{-0.37}$	20.0	(2)
J1127.5+1908	171.900	19.148	1.12±0.20	5.6	1RXS J112716.6+190914	Sy1	0.10	$1.84^{+0.62}_{-0.54}$	21.4	(2)
J1132.7+5259	173.188	52.988	1.01±0.15	6.6	UGC 6527	Sy1	0.03	$1.85^{+0.36}_{-0.34}$	20.0	(3)
J1136.5+2132	174.150	21.548	1.13±0.19	5.9	Mrk 739	Sy1	0.03	$3.06^{+0.64}_{-0.53}$	20.7	(2)

Table 5.5 (continued)

SWIFT NAME	R.A. (J2000)	DEC (J2000)	Flux [15-55 keV] (10^{-11} cgs)	S/N	ID	Type‡	redshift	Ph. Index (BAT only)	log(N_H)	Reference
J1139.0-3744	174.764	-37.741	10.07±0.27	37.9	NGC 3783	Sy1	0.01	$1.94^{+0.01}_{-0.01}$	22.5	(1)
J1139.1+5912	174.783	59.212	1.25±0.15	8.1	SBS 1136+594	Sy1.5	0.06	$2.76^{+0.46}_{-0.39}$	19.6	(1)
J1139.4+3156	174.869	31.935	1.00±0.17	5.8	NGC 3786	Sy1.8	0.01	$1.74^{+0.45}_{-0.34}$	22.5	(3)
J1144.7+7939	176.190	79.662	2.13±0.18	11.9	SWIFT J1143.7+7942	Sy1.2	0.02	$2.26^{+0.24}_{-0.23}$	20.6	(1)
J1145.3+5859	176.349	59.000	0.81±0.15	5.3	Ark 320	GALAXY	0.01	$2.23^{+0.74}_{-0.55}$	22.2	(2)
J1145.5-1825	176.393	-18.428	2.84±0.27	10.5	2MASX J11454045-1827149	Sy1	0.03	$2.02^{+0.22}_{-0.21}$	20.5	(1)
J1148.9+2938	177.230	29.634	1.06±0.18	6.1	MCG+05-28-032	LINER	0.02	$1.85^{+0.39}_{-0.35}$	22.5	(2)
J1158.0+5526	179.502	55.449	1.04±0.15	6.9	NGC 3998	Sy1	0.003	$2.05^{+0.40}_{-0.41}$	20.1	(8)
J1201.0+0647	180.250	6.800	1.18±0.21	5.6	SWIFT J1200.8+0650	Sy2	0.04	$1.89^{+0.33}_{-0.30}$	22.8	(1)
J1203.0+4432	180.773	44.534	2.33±0.15	15.1	NGC 4051	Sy1.5	0.002	$2.45^{+0.18}_{-0.17}$	20.5	(1)
J1204.5+2018	181.149	20.301	1.32±0.19	7.1	ARK 347	Sy2	0.02	$1.76^{+0.29}_{-0.23}$	23.2	(1)
J1206.2+5242	181.565	52.710	1.24±0.15	8.3	NGC 4102	LINER	0.003	$1.74^{+0.30}_{-0.28}$	20.9	(1)
J1209.1+4700	182.300	47.000	0.76±0.15	5.0	Mrk 198	Sy2	0.02	$1.76^{+0.47}_{-0.36}$	22.8	(2)
J1209.4+4341	182.370	43.686	1.56±0.15	10.1	NGC 4138	Sy1.9	0.003	$1.90^{+0.22}_{-0.21}$	22.9	(1)
J1210.5+3924	182.633	39.406	24.60±0.16	153.4	NGC 4151	Sy1.5	0.003	$1.93^{+0.01}_{-0.01}$	22.5	(1)
J1210.6+3819	182.667	38.333	0.96±0.16	6.0	LEDA 38759	Sy1	0.02	$1.91^{+0.35}_{-0.33}$	22.6	(2)
J1217.2+0711	184.300	7.200	1.21±0.20	5.9	NGC 4235	Sy1	0.01	$1.59^{+0.44}_{-0.44}$	21.2	(3)
J1218.3+2950	184.593	29.839	1.53±0.17	9.1	Mrk 766	Sy1.5	0.01	$3.07^{+0.42}_{-0.36}$	21.7	(1)
J1219.0+4715	184.750	47.252	0.96±0.15	6.3	NGC 4258	Sy1	0.001	$1.92^{+0.37}_{-0.34}$	22.9	(11)
J1222.0+7518	185.503	75.311	1.27±0.17	7.4	Mrk 205	Sy1	0.07	$2.53^{+0.42}_{-0.37}$	20.7	(12)
J1225.7+1239	186.447	12.665	12.58±0.19	65.6	NGC 4388	Sy2	0.01	$1.84^{+0.01}_{-0.01}$	23.6	(1)
J1225.8+3330	186.466	33.513	1.25±0.16	7.7	NGC 4395	Sy1	0.001	$2.15^{+0.27}_{-0.25}$	22.3	(1)
J1235.6-3955	188.902	-39.919	10.21±0.26	39.4	NGC 4507	Sy2	0.01	$1.98^{+0.19}_{-0.14}$	23.5	(1)
J1238.8-2718	189.723	-27.308	4.39±0.28	15.9	ESO 506-027	Sy2	0.02	$1.74^{+0.13}_{-0.13}$	23.6	(9)
J1239.0-1611	189.769	-16.196	2.02±0.26	7.7	XSS J12389-1614	Sy2	0.04	$1.68^{+0.28}_{-0.22}$	22.5	(1)
J1239.5-0520	189.898	-5.341	4.52±0.23	19.8	NGC 4593	Sy1	0.01	$1.91^{+0.11}_{-0.11}$	20.3	(1)
J1246.6+5434	191.661	54.575	1.34±0.15	9.0	NGC 4686	LINER	0.02	$1.75^{+0.25}_{-0.20}$	23.8	(2)
J1302.8+1624	195.700	16.400	0.90±0.17	5.1	Mrk 0783	Sy1.2	0.07	$1.92^{+0.43}_{-0.41}$	21.0	(2)
J1306.7-4024	196.698	-40.415	2.37±0.27	8.9	ESO 323-077	Sy1.2	0.02	$2.03^{+0.27}_{-0.25}$	22.7	(2)
J1309.1+1137	197.279	11.632	2.19±0.18	12.0	SWIFT J1309.2+1139	Sy2	0.03	$1.63^{+0.15}_{-0.15}$	23.4	(13)
J1315.4+4424	198.852	44.404	1.28±0.15	8.4	IGR J13149+4422	Sy	0.04	$2.28^{+0.31}_{-0.28}$	22.8	(2)
J1322.3-1642	200.591	-16.716	2.57±0.27	9.5	MCG -03-34-064	Sy1.8	0.02	$2.15^{+0.30}_{-0.28}$	23.6	(1)
J1325.4-4301	201.366	-43.017	49.77±0.26	187.6	Cen A	Sy2	0.002	$1.85^{+0.00}_{-0.00}$	22.7	(1)
J1334.8-2323	203.700	-23.400	1.49±0.29	5.1	ESO 509-38	Sy2	0.03	$2.37^{+0.69}_{-0.54}$	20.0	(2)
J1335.7-3418	203.944	-34.302	4.86±0.29	16.6	MCG -06-30-015	Sy1.2	0.01	$2.24^{+0.17}_{-0.17}$	21.7	(1)

Table 5.5 (continued)

SWIFT NAME	R.A. (J2000)	DEC (J2000)	Flux [15-55 keV] (10^{-11} cgs)	S/N	ID	Type‡	redshift	Ph. Index (BAT only)	log(N_H)	Reference
J1338.1+0433	204.547	4.552	3.63±0.20	17.9	NGC 5252	Sy2	0.02	$1.67^{+0.12}_{-0.12}$	22.64	(13)
J1341.4+3022	205.356	30.369	1.15±0.16	7.2	Mrk 268	Sy2	0.04	$2.38^{+0.35}_{-0.30}$	23.3	(2)
J1349.5-3018	207.390	-30.304	17.87±0.31	58.2	IC 4329A	Sy1	0.02	$2.05^{+0.00}_{-0.00}$	21.6	(1)
J1353.2+6919	208.305	69.327	2.78±0.17	16.7	Mrk 279	Sy1.5	0.03	$1.96^{+0.15}_{-0.15}$	20.5	(1)
J1356.1+3835	209.033	38.583	1.22±0.16	7.7	Mrk 464	Sy1	0.05	$1.69^{+0.30}_{-0.29}$	20.0	(3)
J1408.4-3024	212.100	-30.400	1.65±0.32	5.1	PGC 050427	Sy1	0.02	$2.67^{+0.65}_{-0.52}$	21.2	(2)
J1413.5-0312	213.375	-3.201	14.38±0.24	59.0	NGC 5506	Sy1.9	0.01	$2.27^{+0.11}_{-0.14}$	22.5	(1)
J1418.2+2507	214.568	25.133	3.12±0.17	18.2	NGC 5548	Sy1.5	0.02	$1.82^{+0.12}_{-0.12}$	20.4	(1)
J1419.5-2639	214.893	-26.663	3.49±0.34	10.4	ESO 511-G030	Sy1	0.02	$2.11^{+0.22}_{-0.20}$	21.2	(1)
J1421.6+4750	215.420	47.838	1.03±0.16	6.4	QSO B1419+480	Sy1	0.07	$1.73^{+0.35}_{-0.27}$	21.3	(3)
J1424.3+2435	216.100	24.600	0.89±0.17	5.1	NGC 5610	GALAXY	0.02	$1.88^{+0.46}_{-0.42}$	22.8	(2)
J1429.6+0117	217.400	1.300	1.26±0.23	5.4	QSO B1426+015	Sy1	0.09	$2.41^{+0.74}_{-0.59}$	20.0	(3)
J1436.5+5847	219.149	58.798	1.37±0.16	8.3	QSO J1436+5847	Sy1	0.03	$1.68^{+0.27}_{-0.22}$	23.5	(2)
J1441.2+5330	220.300	53.500	0.85±0.16	5.1	Mrk 477	Sy2	0.04	$1.47^{+0.88}_{-0.46}$	24.0	(14)
J1442.6-1713	220.664	-17.223	4.83±0.34	14.4	**NGC 5728**	Sy2	0.01	$1.84^{+0.14}_{-0.14}$	24.3	(4)
J1453.1+2556	223.282	25.936	1.29±0.18	7.0	RX J1453.1+2554	Sy1	0.05	$1.82^{+0.26}_{-0.25}$	20.0	(2)
J1504.2+1025	226.073	10.417	1.51±0.22	6.8	Mrk 841	Sy1	0.04	$1.80^{+0.38}_{-0.36}$	21.3	(1)
J1515.4+4201	228.868	42.033	1.05±0.18	5.9	NGC 5899	Sy2	0.01	$1.72^{+0.56}_{-0.51}$	23.1	(2)
J1536.2+5753	234.061	57.890	1.43±0.18	7.9	Mrk 290	Sy1	0.03	$2.19^{+0.39}_{-0.34}$	20.4	(1)
J1548.4-1344	237.106	-13.749	2.91±0.39	7.4	NGC 5995	Sy2	0.03	$2.01^{+0.26}_{-0.24}$	22.0	(2)
J1554.8+3242	238.700	32.700	1.04±0.20	5.2	2MASX J15541741+3238381	Sy1	0.05	$1.66^{+0.76}_{-0.52}$	20.0	(2)
J1628.3+5147	247.082	51.793	2.45±0.20	12.4	SWIFT J1628.1+5145	Sy1.9	0.05	$2.13^{+0.19}_{-0.18}$	23.3	(1)
J1653.2+0224	253.319	2.404	4.20±0.35	12.1	**NGC 6240**	Sy2	0.02	$2.09^{+0.18}_{-0.17}$	24.3	(4)
J1822.1+6421	275.541	64.361	1.10±0.21	5.3	QSO B1821+643	Sy1	0.30	$2.91^{+0.97}_{-0.65}$	20.0	(15)
J1824.2-5620	276.057	-56.348	1.98±0.29	6.9	IC 4709	Sy2	0.02	$1.94^{+0.28}_{-0.26}$	23.1	(2)
J1835.1+3240	278.791	32.683	4.67±0.21	22.0	3C 382	Sy1	0.06	$2.09^{+0.11}_{-0.10}$	21.1	(1)
J1837.1-5922	279.284	-59.368	1.79±0.28	6.3	FAIRALL 49	Sy2	0.02	$2.55^{+0.43}_{-0.37}$	22.3	(14)
J1838.6-6523	279.658	-65.394	6.23±0.28	22.4	ESO 103-035	Sy2	0.01	$2.18^{+0.12}_{-0.12}$	23.2	(1)
J1842.4+7946	280.616	79.771	5.82±0.19	29.9	3C 390.3	Sy1	0.06	$1.95^{+0.07}_{-0.07}$	21.0	(1)
J1845.1-6223	281.297	-62.399	2.52±0.28	9.0	ESO 140-43	Sy1	0.01	$2.17^{+0.27}_{-0.25}$	22.4	(2)
J1857.3-7827	284.341	-78.464	1.86±0.26	7.1	LEDA 140831	Sy1	0.04	$1.85^{+0.36}_{-0.34}$	20.0	(2)
J1921.2-5840	290.323	-58.677	3.54±0.28	12.6	ESO 141-55	Sy1	0.04	$1.83^{+0.19}_{-0.18}$	20.0	(3)
J1942.7-1018	295.680	-10.316	4.30±0.30	14.3	NGC 6814	Sy1	0.01	$1.91^{+0.15}_{-0.14}$	20.8	(1)
J2009.1-6103	302.289	-61.064	3.03±0.26	11.5	SWIFT J2009.0-6103	Sy1	0.01	$1.98^{+0.21}_{-0.20}$	21.8	(1)
J2044.1-1043	311.039	-10.731	5.62±0.29	19.7	Mrk 509	Sy1.2	0.03	$2.04^{+0.12}_{-0.11}$	20.7	(1)

Table 5.5 (continued)

SWIFT NAME	R.A. (J2000)	DEC (J2000)	Flux [15-55 keV] (10^{-11} cgs)	S/N	ID	Type[‡]	redshift	Ph. Index (BAT only)	log(N_H)	Reference
J2052.0-5703	313.017	-57.063	4.63±0.25	18.3	IC 5063	Sy2	0.01	$1.89^{+0.12}_{-0.12}$	23.3	(1)
J2109.1-0939	317.300	-9.652	1.58±0.27	5.9	1H 2107-097	Sy1	0.03	$2.15^{+0.40}_{-0.35}$	...	
J2132.1-3343	323.028	-33.727	2.92±0.27	10.7	CTS 109	Sy1	0.03	$2.07^{+0.22}_{-0.20}$	20.0	(2)
J2136.0-6223	324.006	-62.400	2.42±0.23	10.6	QSO J2136-6224	Sy1	0.06	$2.23^{+0.26}_{-0.24}$	20.0	(2)
J2138.8+3206	324.713	32.115	1.29±0.00	6.3	LEDA 67084	Sy1	0.03	$2.06^{+0.55}_{-0.48}$	20.0	(2)
J2200.7+1033	330.199	10.565	1.76±0.21	8.6	SWIFT J2200.9+1032	Sy1.9	0.03	$2.08^{+0.27}_{-0.25}$	22.2	(1)
J2202.1-3152	330.526	-31.878	8.01±0.25	31.8	NGC 7172	Sy2	0.01	$1.80^{+0.01}_{-0.01}$	22.9	(1)
J2204.5+0335	331.149	3.600	1.33±0.21	6.3	IRAS 22017+0319	Sy2	0.06	$2.29^{+0.48}_{-0.40}$	22.5	(2)
J2209.5-4709	332.387	-47.166	3.02±0.23	13.4	NGC 7213	Sy1.5	0.03	$1.92^{+0.17}_{-0.16}$	20.6	(1)
J2223.8-0207	335.962	-2.121	1.93±0.22	8.9	3C 445	Sy1	0.06	$1.99^{+0.24}_{-0.23}$	23.2	(2)
J2235.8-2603	338.966	-26.054	2.76±0.24	11.6	NGC 7314	Sy1.9	0.005	$2.04^{+0.20}_{-0.18}$	21.8	(1)
J2236.1+3357	339.040	33.952	1.66±0.19	8.8	Arp 319	Sy2	0.02	$1.75^{+0.27}_{-0.23}$	23.7	(2)
J2236.8-1235	339.223	-12.599	1.43±0.23	6.2	Mrk 915	Sy1	0.02	$1.59^{+0.33}_{-0.27}$	22.8	(2)
J2245.7+3941	341.449	39.695	1.71±0.18	9.2	3C 452	Sy2	0.08	$1.61^{+0.24}_{-0.19}$	23.4	(1)
J2254.1-1734	343.535	-17.578	5.67±0.23	24.7	MR 2251-178	Sy1	0.06	$2.06^{+0.13}_{-0.12}$	20.8	(1)
J2258.9+4053	344.749	40.899	1.31±0.18	7.2	UGC 12282	Sy1	0.02	$1.65^{+0.28}_{-0.22}$	23.9	(2)
J2259.5+2455	344.899	24.929	1.51±0.19	8.0	LEDA 70195	Sy1	0.03	$1.86^{+0.29}_{-0.28}$	20.0	(2)
J2303.2+0853	345.809	8.885	3.87±0.20	19.4	NGC 7469	Sy1.2	0.02	$2.14^{+0.12}_{-0.12}$	20.6	(1)
J2304.7-0841	346.194	-8.686	6.09±0.22	27.9	Mrk 926	Sy1.5	0.05	$1.97^{+0.01}_{-0.01}$	21.1	(1)
J2304.7+1217	346.200	12.300	1.11±0.20	5.6	NGC 7479	Sy2	0.01	$1.98^{+0.40}_{-0.37}$	23.6	(3)
J2318.4-4221	349.614	-42.360	4.09±0.20	20.7	**NGC 7582**	Sy2	0.01	$1.95^{+0.22}_{-0.24}$	24.1	(4)
J2319.0+0014	349.762	0.241	2.82±0.00	13.5	NGC 7603	Sy1	0.03	$2.07^{+0.18}_{-0.17}$	20.0	(2)
J2326.3+2154	351.600	21.900	0.97±0.19	5.1	RBS 2005	Sy1	0.12	$2.05^{+0.52}_{-0.47}$	20.3	(2)
J2342.0+3035	355.500	30.600	1.08±0.19	5.7	UGC 12741	Sy2	0.02	$1.64^{+0.33}_{-0.30}$	23.7	(2)

[‡] The optical classification comes mainly from Tueller et al. (2008), Winter et al. (2009a), Parisi et al. (2009), Cusumano et al. (2010), SIMBAD, and NED.

References. — (1) Tueller et al., 2008; (2) This work: follow up with XRT; (3) This work: follow up with XMM; (4) See Tab. 5.3 for a detailed analysis of the Compton-thick sources. (5) Shinozaki et al., 2006; (6) Winter et al., 2009a; (7) Ueda et al., 2007; (8) Georgantopoulos et al., 2005; (9) Winter et al., 2009b; (10) Matt et al., 2009; (11) Cappi et al., 2006; (12) Page et al., 2005; (13) Winter et al., 2008; (14) Shu et al., 2007; (15) Jiménez-Bailón et al., 2007.

Chapter 6

Three-year *Swift*–BAT survey: is there an accretion dichotomy? Current work and future prospects

We wish to discuss some of the directions we explored, in light of our findings detailed in Chap. 5. After a short introduction on the main ideas we suggested in the concluding section of Burlon et al. (2011) and the previous chapter, we present the Infrared (IR) sample we adopted, the method we tried to follow, and some results. We discuss our findings in light of the available literature, but we stress this can be considered part of the future prospects of this work.

6.1 Introduction

In the previous chapter we showed, among our results, that the obscuration-luminosity relation, i.e. the anti-correlation between the fraction of obscured AGNs and the luminosity in the 15-55 keV energy range, is in turn related to the difference of the intrinsic luminosity functions (XLF) of the obscured and unobscured populations. We showed that, apart from the very low luminosity regime, in which we argued that we are starting to see the disappearance of the obscuring region, the more efficient AGN in blowing away their obscuring material (or the ones which have developed a clumpy torus with Compton-thick clouds) are the most luminous ones.

We also wondered whether this empirical relation could be translated in a more physical relation among the mass of the black hole, it's absorbing column, and the efficiency of accretion expressed in Eddington units. We are not interested, in the first place, in a precise measurement of the *absolute* measure of the BH masses, but rather in the *relative* difference in the accretion efficiency between, e.g. absorbed and unabsorbed AGN. In order to get rid of the mass dependency of the relations among the observables, we express the luminosities in Eddington units: we can choose to start either the luminosities in the BAT energy band (for consistency with the rest of our work), or the 2–10 keV band typical of focussing X-ray missions (for comparison with e.g. Winter et al. 2009a), or the bolometric output, via some correction factor k.

The starting key ingredient is therefore a way to estimate the BH mass of AGN. As we discussed briefly in 4, there are several known correlations between the properties of the black hole and the bulge (Kormendy and Richstone, 1995; Magorrian et al., 1998; Ferrarese et al., 2001; Tremaine et al., 2002; Marconi and Hunt, 2003). In a recent work also based on a primary selection of the *Swift*–BAT AGN by Vasudevan et al. (2009), the authors stress that the most accurate measurements of BH masses via Reverberation Mapping are only available for 35 AGN. Following that work, we decided to employ the correlation $M_{BH} \propto L_{K,\,bulge}$, where $L_{K,\,bulge}$ is the luminosity of the bulge in the K-band (filter centered at $2.159\,\mu$m with a width of $0.262\,\mu$m). We decided to adopt the 2MASS catalog, which we describe in the following section. The method adopted for taking some corrections into consideration is explained in § 6.3.

6.2 The 2MASS Point Source Catalog

We adopt the correlation found by Marconi and Hunt (2003), therefore we use the IR luminosity in the K-band. The choice is driven by the fact that the 2MASS data were gathered with two ground-based telescopes (the Whipple Observatory in Arizona, USA, and the Cerro Tololo telescope at La Serena, Chile) which cover the whole sky. This allows us to find counterparts for $\sim 98\%$ of our X-ray selected sample (193/197 AGN). The choice of the K-band over the J and H bands[1] is driven by the smaller effect of Galactic reddening in that band (Vasudevan et al., 2009).

The 2MASS provides magnitudes in three different bands in two forms: the "extended source" catalog, and the "point source" catalog (PSC). We adopt the second because the seeing for the 2MASS is typically $\approx$2.6 arcsec (see Vasudevan et al., 2009, and references therein). For bulges of 0.5–1 kpc size this translates into the bulge being unresolved at distances of $z \sim 0.01$. Therefore for the great majority of our *Swift* sample the bulge is always unresolved. This means that by taking the PSC magnitude we are summing up the contribution of the nucleus and the bulge. In order to find the correct bulge luminosity, we therefore need to correct the magnitude given in the PSC as described in the following section.

A different approach could be used in the original paper by Marconi and Hunt (2003) who found the correlation we want to use, because the AGN they selected lied at closer distances. This translated into the possibility for them to decompose the images with the software `GALFIT`, to obtain a very accurate estimate of the bulge luminosity alone. Also Mushotzky et al. (2008) based their analysis of the bulge luminosity and their relation to the X-ray power of the BAT AGN subtracting the nuclear component from the extended source catalog, and then obtaining an estimate of the bulge luminosity.

---

[1] The 2MASS magnitudes are given in the Vega system.

6.3 Methods

By using the PSC we are aware that we are summing up the contribution from the bulge and the AGN. It is therefore important to decompose the contribution of the former, in order to use it for the BH mass estimate. The relative contribution of the nucleus and bulge for the total flux in the PSC catalogue can be estimated from the spectral energy distribution (SED) templates of Silva et al. (2004), which made use of a radiative transfer code for dust heating and confronted it to a sample of 33 Seyfert galaxies. They presented SED templates for the host galaxy by subtracting the nuclear template from the total photometry. Their host templates are provided for different levels of photo-electric absorption and divided into classes of X-ray luminosity (in the 2-10 keV band). Under the assumption that $L_{K,bulge}/L_{K,total} = L_{K,host}/L_{K,total}$, which also Vasudevan et al. (2009) deem reasonable given the choice of the K-band for the reason described in the previous section, we call $f_{bulge} = L_{K,bulge}/L_{K,total}$.

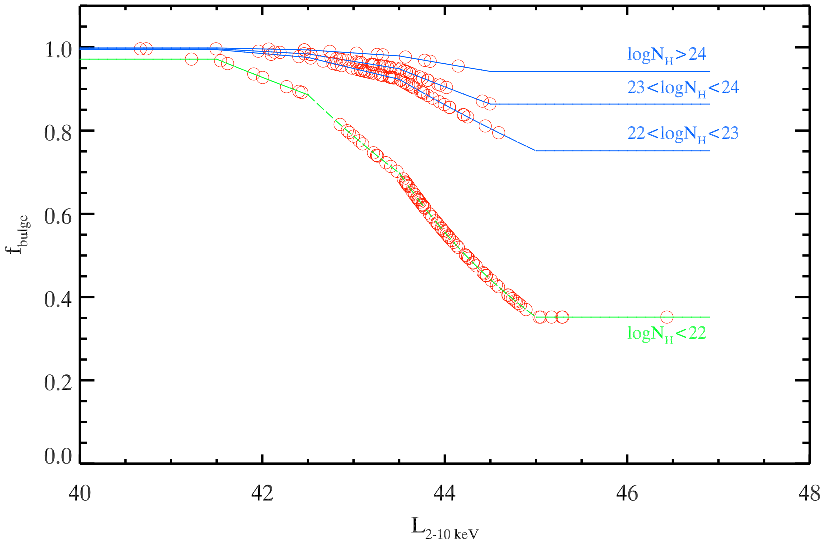

Figure 6.1 Bulge over total K-band luminosity vs. X-ray luminosity, for different levels of photo-electric absorption. The picture is adapted from Vasudevan et al. (2009), interpolating the templates of Silva et al. (2004), by courtesy of R. Vasudevan. The red circles represent the position of the *Swift*–BAT AGN.

In fig. 6.1 we show f_{bulge} vs. the X-ray luminosity, for different classes of absorption. The higher is absorption, the more the AGN contribution to the total flux becomes smaller (i.e. f_{bulge} becomes closer to one). We can then scale the PSC magnitudes via

$$M_{K,\,bulge} = M_{K,\,PSC} - 2.5 \times log[f_{bulge}(L_X)] \tag{6.1}$$

and knowing the absolute magnitude of the Sun in the Vega system $M_{K,\odot} = 3.28$ (Binney and Merrifield, 1998) we obtain the corresponding IR luminosities, in units of solar luminosities (we drop the suffix "bulge" for simplicity):

$$\frac{L_K}{L_{K,\odot}} = 10^{-0.4(M_K - M_{K,\odot})} \tag{6.2}$$

and finally using the correlation by Marconi and Hunt (2003):

$$log(M_{BH}) = 8.21(\pm 0.07) + 1.13(\pm 0.012) \times [log(L_K/L_{K,\odot}) - 10.9] \tag{6.3}$$

we have the masses of our AGN. The computation of the corresponding Eddington luminosities and Eddington ratios is straightforward, depending on whether we want to use the luminosities in a certain band, or we want to scale the BAT luminosities to the bolometric ones via some bolometric correction k as done e.g. in Fabian et al. (2009).

6.4 Discussion of the results

L/L_{Edd} (λ_{Edd}) distributions We show in figure 6.2 the distribution we obtain for λ_{Edd} dividing by the Eddington luminosity in (a) the BAT luminosities we adopted also in § 5, and in (b) a possible bolometric correction. The choice of the bolometric factor k in (b) is dictated by Fabian et al. (2009), where the authors adopt a value $k = 19$ for the "hard" sources (those with a photon index harder than 1.9) and $k = 55$ for the "soft" sources, exhibiting a photon index greater than 1.9. The colors adopted are the same ones we used in the previous chapter, namely red (X-ray absorbed AGN) and blue (unabsorbed AGN). It is apparent how the two populations do not differ at the 3σ level if we use just the BAT luminosity, but their distance becomes statistically significant at more than 5σ if we introduce the factor k. In order to compare our λ_{Edd} with Fabian

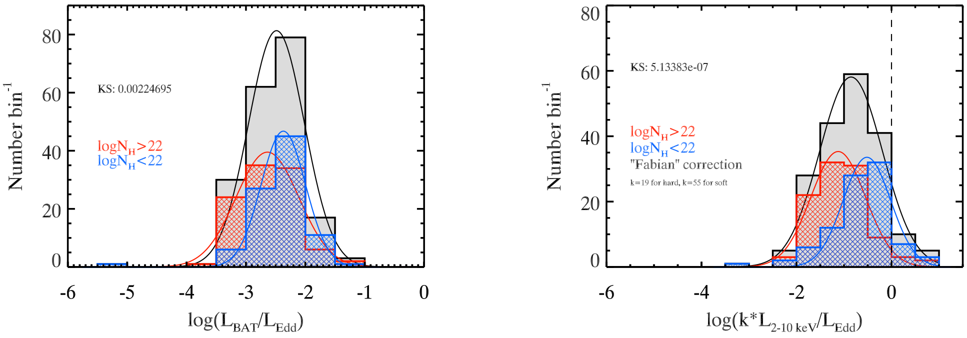

(a) L_{BAT}/L_{Edd} for the absorbed (red) and unabsorbed (blue) subsamples. No bolometric corrections are applied.

(b) Distribution of $k \times L_{2-10\,\mathrm{keV}}/L_{Edd}$ for the two subsamples (k is described in the text). The color code is as (a). The vertical dashed line represent $\lambda_{Edd} = 1$.

Figure 6.2 λ_{Edd} distributions using the BAT luminosities or adopting a bolometric correction.

et al. (2009) we adopt the very same k as in that paper (which is also based on BAT AGN), and we scaled the BAT luminosities to the 2–10 keV band.

Note that some AGN lie somewhat at super-Eddington values in case (b), and also that a handful of objects show extremely low λ_{Edd} in (a). This is due partially by unphysical values of the bulge magnitudes, that propagate throughout our analysis, resulting in extremely high/low mass estimates and therefore extreme λ_{Edd}. The mean values, the spread of the distributions (if fitted with gaussian profiles), and the KS-test null hypotheses probability are listed in table 6.1

Table 6.1 λ_{Edd} gaussian fit parameter distributions.

Measure	Mean unabs. (1σ)	Mean abs. (1σ)	KS
λ_{Edd}[a]	-0.51 (0.50)	-1.12 (0.57)	5.13×10^{-7}
λ_{Edd} w/o corr	-2.37 (0.37)	-2.64 (0.53)	2.25×10^{-3}
Mass	8.04	7.81	4.48×10^{-3}

[a] The applied bolometric correction is the one in Fabian et al. (2009).

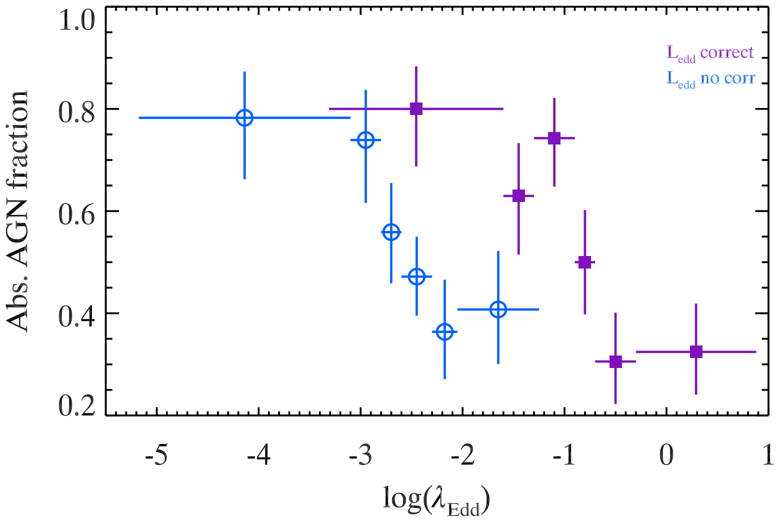

Figure 6.3 Relation between the X-ray absorbed AGN fraction versus λ_{Edd} in the case we adopt (or not) a bolometric correction, as discussed in the text.

Absorbed AGN fraction is a function of λ_{Edd} If we span the absorbed distributions in fig. 6.2 in the left-to-right direction, and we imagine to plot at each step the ratio of the absorbed over the total distribution, we obtain figure 6.3, where we substantially prove that independently from k, the absorbed AGN fraction is a function of their Eddington ratio. This is not completely unexpected since Winter et al. (2009a) showed that this relation indeed existed, even if their selection criterion was based on the optical classification of the AGN, rather than on the X-ray classification. Nonetheless, as we discussed in § 4 the optical and X-ray classification are comparable at least at the zeroth order. Our finding is also in agreement with the results of Middleton et al. (2008) and Beckmann et al. (2009), which showed how on average absorbed AGN show lower λ_{Edd}. We stress again that our goal was to understand whether a relative difference between the two subsamples existed, rather then their absolute values of black hole masses and therefore precise absolute estimates of λ_{Edd}.

On the relation between the spectral index and λ_{Edd} As we discussed in the previous chapter (in particular as for the discussion of fig. 5.9), a relation between the accretion rate and the spectral index is expected in view of the following idea: more efficient accretion systems should increase the photon density, which in turn translated in a more efficient cooling, and steeper spectra. When we compared the BAT luminosity with the spectral index we found no evidence of a correlation, and this is indeed still the case if we consider the λ_{Edd} without any correction (conversely we find a correlation of the spectral index with the corrected λ_{Edd}). Noteworthy Shemmer et al. (2006) report on this strong relation between these two parameters, but leaves the interpretation to a dubbed "thermostat behavior" of the corona: a more efficient AGN would result in a more efficient cooling.

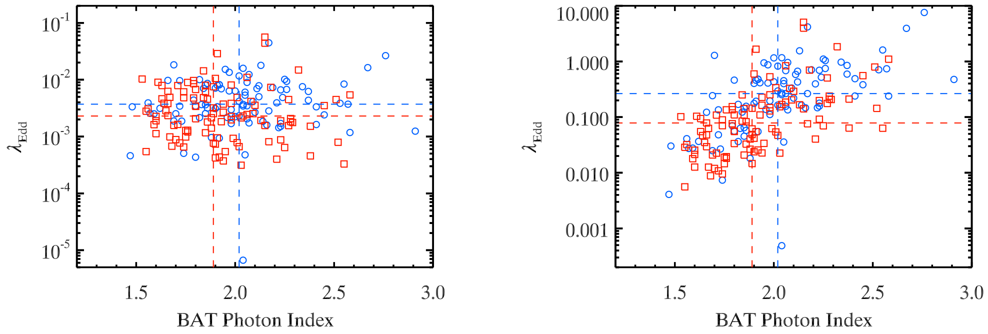

(a) L_{BAT}/L_{Edd} vs. the BAT photon index, with no bolometric corrections.

(b) Same as (a), but $k \times L_{2-10\,\mathrm{keV}}/L_{Edd}$ vs. BAT photon index is used.

Figure 6.4 Relation between the photon spectral index and λ_{Edd}. The colors are red for absorbed AGN and blue for unabsorbed ones. Dashed lines represent the median values for the corresponding samples.

In figure 6.4 we show the absence (in panel (a)) of a relation among the two parameters (slope of a linear fit is 0.09, with a correlation coefficient $r = 0.05$) if just L_{BAT}/L_{Edd} is used, while a positive linear correlation (in panel (b)) of slope 1.49 (and $r = 0.62$) is found when we use our bolometric correction, in analogy with the rest of this chapter. These results are independent on the level of absorption, which we plot with a color scale.

Stacking analysis using the information on λ_{Edd} As a final exercise for self-consistency, we checked whether by means of stacking analysis, we could find a trace of the results discussed in this section. If indeed the more efficient AGN (i.e. the ones accreting at higher λ_{Edd}) are also accompanied by a higher cooling, their stacked spectra should peak at somewhat lower temperatures, i.e. we would expect to find a cutoff at somewhat lower energies. Conversely, the AGN accreting worse should show higher temperatures. We show in fig. 6.5, the stacked spectra of half of our sample each, using the median L_{BAT}/L_{Edd} as a dividing line. It is quite evident how the two populations track each other.

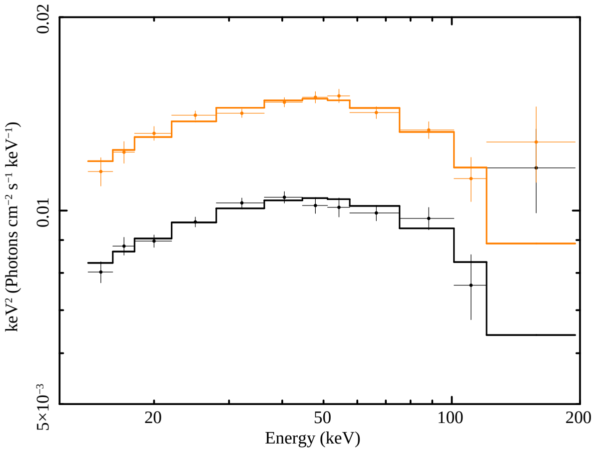

Figure 6.5 Stacked spectra in a $\nu F \nu$ representation for the two subsamples of AGN accreting more (black line) or less (orange line) than the median λ_{Edd}. The fit shown is a power-law with exponential cutoff.

If we account for the curvature in the spectra by fitting with a simple power-law with a cutoff (errors are quoted at 90%), we find it occurring at $E_c = 104 \pm 26$ for the AGN with $\lambda_{Edd} >$ median, and $E_c = 108 \pm 22$ for the AGN with $\lambda_{Edd} <$ median. The photon index is $\Gamma = 1.54 \pm 0.10$ and $\Gamma = 1.57 \pm 0.09$, respectively. Note that the hardness of the spectra is consistent within the errors, as well as the cutoff.

Finally, driven by the results of the stacking analysis in the previous chapter, we fitted also with a reflection component, in order to see (again for self-consistency), whether the AGN accreting better can be associated with the less absorbed ones (which on average showed higher reflection, as expected by population synthesis models, e.g. Gilli et al. 2007). We find that the reflection component of the best accreting AGN ($R = 0.57 \pm 0.26$) is also consistent within error when compared to the AGN accreting "worse" ($R = 0.66 \pm 0.25$).

We conclude that we cannot make any strong statement on the self-consistency or our interpretation, based on the quality of these spectra. The error on the cutoff energy, for instance, is $\sim 25\,\%$ so that even if there might have been an indication of the expected behavior, we would not be able to see it. The exercise is anyway interesting in nature, and will be one of the fundamental tests that the future generation telescopes like *NuSTAR* will be able to carry out.

6.5 Outlook

We wish to describe in the following two possible lines of research that can be pursued, based on our results, besides the improvements to this chapter that a more thorough analysis (or the next generation of telescopes) could bring:

- in the first place we think that a radio follow up study of the BAT selected sources would shed some light into the idea we have of radio-quiet objects. Referring to the discussion in § 4.4.2 we suggest that maybe all AGN, therefore also the ones included in this work, are able to produce a jet at some level. The definition of radio-quiet maybe should not be regarded as radio-silent, but rather radio-weak. We are aware that at the low levels of radio emission, the AGN component would probably be difficult to disentangle from other sources, e.g. Supernova remnants, stars, binaries.

- a second item that we deem interesting as a future work in this field is exactly on the other side of the spectrum with respect to the previous one, i.e. at hard $\gamma-$rays with the LAT instrument. Actually, exactly while compiling this final chapter there have been two independent works in the literature (which are still in pre-print form only, see Teng et al., 2011 and the work by The Fermi-LAT Collaboration, 2011) which develop our same idea. It is indeed interesting to look for a signature of emission at GeV energies in AGN hosted by Seyfert galaxies, in a way similar to what is found in Blazars, that are highly relativistic, jetted AGN, pointing in the direction of the Earth.

  From a theoretical point of view, there are at least three possibilities for these AGN to emit GeV radiation. In the first case (a "corona scenario") we do not get into the details of how the electrons in such a corona are kept hot. This can happen via some form of magnetic heating, but some non-thermal particle acceleration may as well be present. This could result in a radiation spectrum extending beyond the cutoff at few hundreds of keV, with an high energy tail up to GeV energies. In the second scenario, i.e. the "aborted-jet", or more generally for any form of jet interaction with the environment, GeV up to TeV photons are expected, in a similar way to Blazars. The difference is that the BAT AGN in our sample have mildly relativistic ejecta (if any) or even sub-relativistic, as discussed before. Note that the presence/absence of jets is also related to the first item of our proposed outlook. There is a third possibility, which we did not discussed so far, for the production of hundreds of MeV photons in the AGN we analyzed, or at least for those accreting at very low Eddington ratios. As we mentioned, ADAF accretion could take over in these cases (and actually does in Blazars. . .).

> A prediction of the most sophisticated ADAF models is a peak around 10^{23} Hz produced by the decay of pions, which in turn are produced by proton collisions. Therefore, the measurement of the shape and the normalization of the peak would give an insight on the temperature of the protons, the spin of the black hole, and the gas composition.

In general, we therefore envisage that the best outcomes from our sample, would be gained via a multi-wavelength follow-up, ranging between the two extremes of the electro-magnetic spectrum, from radio waves to GeV photons.

Bibliography

Abdo, A. A., Ackermann, M., Ajello, M., Asano, K., Atwood, W. B., Axelsson, M., Baldini, L., Ballet, J., Barbiellini, G., Baring, M. G., Bastieri, D., Bechtol, K., Bellazzini, R., Berenji, B., Bhat, P. N., Bissaldi, E., Blandford, R. D., Bloom, and others: 2009, *ApJL* **706**, L138

Ables, J. G.: 1968, Vol. 1, pp 172–+

Ajello, M.: 2007, *Ph.D. thesis*, MPE/TUM

Ajello, M.: 2009, *ArXiv e-prints 0902.3033*

Ajello, M., Costamante, L., Sambruna, R. M., Gehrels, N., Chiang, J., Rau, A., Escala, A., Greiner, J., Tueller, J., Wall, J. V., and Mushotzky, R. F.: 2009a, *ApJ* **699**, 603

Ajello, M., Greiner, J., Kanbach, G., Rau, A., Strong, A. W., and Kennea, J. A.: 2008a, *ApJ* **678**, 102

Ajello, M., Greiner, J., Sato, G., Willis, D. R., Kanbach, G., Strong, A. W., Diehl, R., Hasinger, G., Gehrels, N., Markwardt, C. B., and Tueller, J.: 2008b, *ApJ* **689**, 666

Ajello, M., Rau, A., Greiner, J., Kanbach, G., Salvato, M., Strong, A. W., Barthelmy, S. D., Gehrels, N., Markwardt, C. B., and Tueller, J.: 2008c, *ApJ* **673**, 96

Ajello, M., Rebusco, P., Cappelluti, N., Reimer, O., Böhringer, H., Greiner, J., Gehrels, N., Tueller, J., and Moretti, A.: 2009b, *ApJ* **690**, 367

Akylas, A., Georgantopoulos, I., Georgakakis, A., Kitsionas, S., and Hatziminaoglou, E.: 2006, *A&A* **459**, 693

Amati, L., Frontera, F., Tavani, M., in't Zand, J. J. M., Antonelli, A., Costa, E., Feroci, M., Guidorzi, C., Heise, J., Masetti, N., Montanari, E., Nicastro, L., Palazzi, E., Pian, E., Piro, L., and Soffitta, P.: 2002, *A&A* **390**, 81

Antonucci, R.: 1993, *ARA&A* **31**, 473

Antonucci, R. R. J. and Miller, J. S.: 1985, *ApJ* **297**, 621

Arnaud, K. A.: 1996, in G. H. Jacoby & J. Barnes (ed.), *Astronomical Data Analysis Software and Systems V*, Vol. 101 of *Astronomical Society of the Pacific Conference Series*, pp 17–+

Avni, Y.: 1976, *ApJ* **210**, 642

Band, D., Ford, L., Matteson, J., Lestrade, J. P., Teegarden, B., Schaefer, B., Cline, T., Briggs, M., Paciesas, W., and Pendleton, G.: 1992, *Experimental Astronomy* **2**, 307

Band, D., Matteson, J., Ford, L., Schaefer, B., Palmer, D., Teegarden, B., Cline, T., Briggs, M., Paciesas, W., Pendleton, G., Fishman, G., Kouveliotou, C., Meegan, C., Wilson, R., and Lestrade, P.: 1993, *ApJ* **413**, 281

Barthelmy, S. D., Barbier, L. M., Cummings, J. R., Fenimore, E. E., Gehrels, N., Hullinger, D., Krimm, H. A., Markwardt, C. B., Palmer, D. M., Parsons, A., Sato, G., Suzuki, M., Takahashi, T., Tashiro, M., and Tueller, J.: 2005, *Space Science Reviews* **120**, 143

Beckmann, V., Soldi, S., Ricci, C., Alfonso-Garzón, J., Courvoisier, T., Domingo, A., Gehrels, N., Lubiński, P., Mas-Hesse, J. M., and Zdziarski, A. A.: 2009, *A&A* **505**, 417

Bhat, P. N., Fishman, G. J., Meegan, C. A., Wilson, R. B., Brock, M. N., and Paciesas, W. S.: 1992, *Nature* **359**, 217

Bianchi, S., Bonilla, N. F., Guainazzi, M., Matt, G., and Ponti, G.: 2009a, *A&A* **501**, 915

Bianchi, S., Piconcelli, E., Chiaberge, M., Bailón, E. J., Matt, G., and Fiore, F.: 2009b, *ApJ* **695**, 781

Binney, J. and Merrifield, M.: 1998, *Galactic Astronomy*

Borgonovo, L. and Ryde, F.: 2001, *ApJ* **548**, 770

Brandt, W. N. and Hasinger, G.: 2005, *ARA&A* **43**, 827

Brightman, M. and Nandra, K.: 2011, *MNRAS* **413**, 1206

Broderick, J. W. and Fender, R. P.: 2011, *ArXiv e-prints 1105.3769*

Brusa, M., Civano, F., Comastri, A., Miyaji, T., Salvato, M., Zamorani, G., Cappelluti, N., Fiore, F., Hasinger, G., Mainieri, V., Merloni, A., Bongiorno, A., Capak, P., Elvis, M., Gilli, R., Hao, H., Jahnke, K., Koekemoer, A. M., Ilbert, O., and others: 2010, *ApJ* **716**, 348

Burlon, D., Ajello, M., Greiner, J., Comastri, A., Merloni, A., and Gehrels, N.: 2011, *ApJ* **728**, 58

Burlon, D., Ghirlanda, G., Ghisellini, G., Greiner, J., and Celotti, A.: 2009, *A&A* **505**, 569

Burlon, D., Ghirlanda, G., Ghisellini, G., Lazzati, D., Nava, L., Nardini, M., and Celotti, A.: 2008, *ApJL* **685**, L19

Burrows, D. N., Hill, J. E., Nousek, J. A., Wells, A. A., Short, A. D., Willingale, R., Citterio, O., Chincarini, G., and Tagliaferri, G.: 2000, in K. A. Flanagan & O. H. Siegmund (ed.), *Society of Photo-Optical Instrumentation Engineers (SPIE) Conference Series*, Vol. 4140 of *Presented at the Society of Photo-Optical Instrumentation Engineers (SPIE) Conference*, pp 64–75

Burrows, D. N., Kennea, J. A., Ghisellini, G., Mangano, V., Zhang, B., Page, K. L., Eracleous, M., Romano, P., Sakamoto, T., Falcone, A. D., Osborne, J. P., Campana, S., Beardmore, A. P., Breeveld, A. A., Chester, M. M., Corbet, R., Covino, S., Cummings, J. R., and others: 2011, *Nature* **476**, 421

Cappelluti, N., Ajello, M., Burlon, D., Krumpe, M., Miyaji, T., Bonoli, S., and Greiner, J.: 2010, *ApJL* **716**, L209

Cappelluti, N., Hasinger, G., Brusa, M., Comastri, A., Zamorani, G., Böhringer, H., Brunner, H., Civano, F., Finoguenov, A., Fiore, F., Gilli, R., Griffiths, R. E., Mainieri, V., Matute, I., Miyaji, T., and Silverman, J.: 2007, *ApJS* **172**, 341

Cappi, M., Panessa, F., Bassani, L., Dadina, M., Di Cocco, G., Comastri, A., della Ceca, R., Filippenko, A. V., Gianotti, F., Ho, L. C., Malaguti, G., Mulchaey, J. S., Palumbo, G. G. C., Piconcelli, E., Sargent, W. L. W., Stephen, J., Trifoglio, M., and Weaver, K. A.: 2006, *A&A* **446**, 459

Cenko, S. B., Kasliwal, M., Harrison, F. A., Pal'shin, V., Frail, D. A., Cameron, P. B., Berger, E., Fox, D. B., Gal-Yam, A., Kulkarni, S. R., Moon, D.-S., Nakar, E., Ofek, E. O., Penprase, B. E., Price, P. A., Sari, R., Schmidt, B. P., Soderberg, A. M., and others: 2006, *ApJ* **652**, 490

Cisternas, M., Jahnke, K., Inskip, K. J., and Inskip: 2010, in *IAU Symposium*, Vol. 267 of *IAU Symposium*, pp 326–326

Comastri, A.: 2004, in A. J. Barger (ed.), *Supermassive Black Holes in the Distant Universe*, Vol. 308 of *Astrophysics and Space Science Library*, pp 245–+

Comastri, A., Iwasawa, K., Gilli, R., Vignali, C., and Ranalli, P.: 2009, *ArXiv e-prints 0910.1025*

Comastri, A., Iwasawa, K., Gilli, R., Vignali, C., Ranalli, P., Matt, G., and Fiore, F.: 2010, *ApJ* **717**, 787

Comastri, A., Setti, G., Zamorani, G., and Hasinger, G.: 1995, *A&A* **296**, 1

Croton, D. J., Springel, V., White, S. D. M., De Lucia, G., Frenk, C. S., Gao, L., Jenkins, A., Kauffmann, G., Navarro, J. F., and Yoshida, N.: 2006, *MNRAS* **365**, 11

Cusumano, G., La Parola, V., Segreto, A., Ferrigno, C., Maselli, A., Sbarufatti, B., Romano, P., Chincarini, G., Giommi, P., Masetti, N., Moretti, A., Parisi, P., and Tagliaferri, G.: 2010, *A&A* **524**, A64+

Cusumano, G., Mangano, V., Chincarini, G., Panaitescu, A., Burrows, D. N., La Parola, V., Sakamoto, T., Campana, S., Mineo, T., Tagliaferri, G., Angelini, L., Barthelemy, S. D., Beardmore, A. P., Boyd, P. T., Cominsky, L. R., Gronwall, C., Fenimore, E. E., and others: 2006, *Nature* **440**, 164

Dadina, M.: 2008, *A&A* **485**, 417

Dai, X., Chartas, G., Eracleous, M., and Garmire, G. P.: 2004, *ApJ* **605**, 45

Daigne, F. and Mochkovitch, R.: 2002, *MNRAS* **336**, 1271

Della Ceca, R., Caccianiga, A., Severgnini, P., Maccacaro, T., Brunner, H., Carrera, F. J., Cocchia, F., Mateos, S., Page, M. J., and Tedds, J. A.: 2008, *A&A* **487**, 119

Di Matteo, T., Perna, R., and Narayan, R.: 2002, *ApJ* **579**, 706

Di Matteo, T., Springel, V., and Hernquist, L.: 2005, *Nature* **433**, 604

Dicke, R. H.: 1968, *ApJL* **153**, L101+

Draper, A. R. and Ballantyne, D. R.: 2010, *ApJL* **715**, L99

Dwelly, T. and Page, M. J.: 2006, *MNRAS* **372**, 1755

Eichler, D., Livio, M., Piran, T., and Schramm, D. N.: 1989, *Nature* **340**, 126

Elitzur, M. and Ho, L. C.: 2009, *ApJL* **701**, L91

Elitzur, M. and Shlosman, I.: 2006, *ApJL* **648**, L101

Elvis, M., Wilkes, B. J., McDowell, J. C., Green, R. F., Bechtold, J., Willner, S. P., Oey, M. S., Polomski, E., and Cutri, R.: 1994, *ApJS* **95**, 1

Fabian, A. C.: 1999, *MNRAS* **308**, L39

Fabian, A. C., Vasudevan, R. V., Mushotzky, R. F., Winter, L. M., and Reynolds, C. S.: 2009, *MNRAS* **394**, L89

Fenimore, E. E.: 1999, *ApJ* **518**, 375

Ferrarese, L., Pogge, R. W., Peterson, B. M., Merritt, D., Wandel, A., and Joseph, C. L.: 2001, *ApJL* **555**, L79

Filgas, R.: 2011, *Ph.D. thesis*, MPE/TUM

Filgas, R., Greiner, J., Schady, P., Kruehler, T., Updike, A. C., Klose, S., Nardini, M., Kann, D. A., Rossi, A., Sudilovsky, V., Afonso, P. M. J., Clemens, C., Elliott, J., Nicuesa Guelbenzu, A., Olivares Estay, F., and Rau, A.: 2011, *ArXiv e-prints*

Firmani, C., Cabrera, J. I., Avila-Reese, V., Ghisellini, G., Ghirlanda, G., Nava, L., and Bosnjak, Z.: 2009, *MNRAS* **393**, 1209

Firmani, C., Ghisellini, G., Avila-Reese, V., and Ghirlanda, G.: 2006, *MNRAS* **370**, 185

Fishman, G. J., Meegan, C. A., Parnell, T. A., and Wilson, R. B.: 1982, in R. E. Lingenfelter, H. S. Hudson, & D. M. Worrall (ed.), *Gamma Ray Transients and Related Astrophysical Phenomena*, Vol. 77 of *American Institute of Physics Conference Series*, pp 443–451

Frail, D. A., Kulkarni, S. R., Sari, R., Djorgovski, S. G., Bloom, J. S., Galama, T. J., Reichart, D. E., Berger, E., Harrison, F. A., Price, P. A., Yost, S. A., Diercks, A., Goodrich, R. W., and Chaffee, F.: 2001, *ApJL* **562**, L55

Frank, J., King, A., and Raine, D. J.: 2002, *Accretion Power in Astrophysics: Third Edition*

Gehrels, N.: 1986, *ApJ* **303**, 336

Gehrels, N., Chincarini, G., Giommi, P., Mason, K. O., Nousek, J. A., Wells, A. A., White, N. E., Barthelmy, S. D., Burrows, D. N., Cominsky, L. R., Hurley, K. C., Marshall, F. E., Mészáros, P., Roming, P. W. A., Angelini, L., Barbier, L. M., and others: 2004, *ApJ* **611**, 1005

Gehrels, N., Sarazin, C. L., O'Brien, P. T., Zhang, B., Barbier, L., Barthelmy, S. D., Blustin, A., Burrows, D. N., Cannizzo, J., Cummings, J. R., Goad, M., Holland, S. T., Hurkett, C. P., Kennea, J. A., Levan, A., Markwardt, C. B., Mason, K. O., Meszaros, P., and others: 2005, *Nature* **437**, 851

Georgantopoulos, I., Georgakakis, A., and Koulouridis, E.: 2005, *MNRAS* **360**, 782

Ghirlanda, G.: 2002, *Ph.D. thesis*, SISSA/ISAS

Ghirlanda, G., Celotti, A., and Ghisellini, G.: 2002, *A&A* **393**, 409

Ghirlanda, G., Celotti, A., and Ghisellini, G.: 2003, *A&A* **406**, 879

Ghirlanda, G., Ghisellini, G., and Firmani, C.: 2006, *New Journal of Physics* **8**, 123

Ghirlanda, G., Ghisellini, G., and Lazzati, D.: 2004, *ApJ* **616**, 331

Ghirlanda, G., Ghisellini, G., Nava, L., and Burlon, D.: 2011a, *MNRAS* **410**, L47

Ghirlanda, G., Nava, L., and Ghisellini, G.: 2010, *A&A* **511**, A43+

Ghirlanda, G., Nava, L., Ghisellini, G., Celotti, A., Burlon, D., Covino, S., and Melandri, A.: 2011b, *ArXiv e-prints 1107.4096*

Ghirlanda, G., Nava, L., Ghisellini, G., Celotti, A., and Firmani, C.: 2009, *A&A* **496**, 585

Ghirlanda, G., Nava, L., Ghisellini, G., and Firmani, C.: 2007, *A&A* **466**, 127

Ghisellini, G. and Celotti, A.: 1999, *A&AS* **138**, 527

Ghisellini, G., Della Ceca, R., Volonteri, M., Ghirlanda, G., Tavecchio, F., Foschini, L., Tagliaferri, G., Haardt, F., Pareschi, G., and Grindlay, J.: 2010a, *MNRAS* **405**, 387

Ghisellini, G., Ghirlanda, G., Nava, L., and Celotti, A.: 2010b, *MNRAS* **403**, 926

Ghisellini, G., Haardt, F., and Matt, G.: 1994, *MNRAS* **267**, 743

Ghisellini, G., Haardt, F., and Matt, G.: 2004, *A&A* **413**, 535

Ghisellini, G., Maraschi, L., and Tavecchio, F.: 2009, *MNRAS* **396**, L105

Gilli, R., Comastri, A., and Hasinger, G.: 2007, *A&A* **463**, 79

Godet, O., Page, K. L., Osborne, J. P., O'Brien, P. T., Burrows, D. N., Hill, J. E., Zhang, B., Beardmore, A. P., Angelini, L., Capalbi, M., Cummings, J., Gehrels, N., Goad, M. R., Kennea, J. A., Mangano, V., Moretti, A., and Morris, D. C.: 2006, *A&A* **452**, 819

Gruber, D., Greiner, J., von Kienlin, A., Rau, A., Briggs, M. S., Connaughton, V., Goldstein, A., van der Horst, A. J., Nardini, M., Bhat, P. N., Bissaldi, E., Burgess, J. M., Chaplin, V. L., Diehl, R., Fishman, G. J., Fitzpatrick, G., Foley, S., Gibby, M. H., and others: 2011a, *A&A* **531**, A20+

Gruber, D., Krühler, T., Foley, S., Nardini, M., Burlon, D., Rau, A., Bissaldi, E., von Kienlin, A., McBreen, S., Greiner, J., Bhat, P. N., Briggs, M. S., Burgess, J. M., Chaplin, V. L., Connaughton, V., Diehl, R., Fishman, G. J., Gibby, M. H., Giles, M. M., and others: 2011b, *A&A* **528**, A15+

Gültekin, K., Cackett, E. M., Miller, J. M., Di Matteo, T., Markoff, S., and Richstone, D. O.: 2009, *ApJ* **706**, 404

Haardt, F. and Maraschi, L.: 1991, *ApJL* **380**, L51

Harrison, F. A., Christensen, F. E., Craig, W., Hailey, C., Baumgartner, W., Chen, C. M. H., Chonko, J., Cook, W. R., Koglin, J., Madsen, K.-K., Pivavoroff, M., Boggs, S., and Smith, D.: 2005, *Experimental Astronomy* **20**, 131

Hasinger, G.: 2008, *A&A* **490**, 905

Hasinger, G., Miyaji, T., and Schmidt, M.: 2005, *A&A* **441**, 417

Ho, L. C.: 2008, *ARA&A* **46**, 475

Hogg, D. W.: 1999, *ArXiv e-prints 9905116*

Hönig, S. F. and Beckert, T.: 2007, *MNRAS* **380**, 1172

Hopkins, P. F., Hernquist, L., Cox, T. J., Di Matteo, T., Robertson, B., and Springel, V.: 2006, *ApJS* **163**, 1

Hopkins, P. F., Hickox, R., Quataert, E., and Hernquist, L.: 2009, *MNRAS* **398**, 333

Horack, J. M.: 1991, *Development of the Burst and Transient Source Experiment (BATSE)*

Hurley, K., Dingus, B. L., Mukherjee, R., Sreekumar, P., Kouveliotou, C., Meegan, C., Fishman, G. J., Band, D., Ford, L., Bertsch, D., Cline, T., Fichtel, C., Hartman, R., Hunter, S., Thompson, D. J., Kanbach, G., Mayer-Hasselwander, H., von Montigny, C., Sommer, M., and others: 1994, *Nature* **372**, 652

Ishibashi, W. and Courvoisier, T.: 2010, *A&A* **512**, A58+

Iwasawa, K., Fabian, A. C., and Matt, G.: 1997, *MNRAS* **289**, 443

Iwasawa, K. and Taniguchi, Y.: 1993, *ApJL* **413**, L15

Janiuk, A., Yuan, Y., Perna, R., and Di Matteo, T.: 2007, *ApJ* **664**, 1011

Jansen, F., Lumb, D., Altieri, B., Clavel, J., Ehle, M., Erd, C., Gabriel, C., Guainazzi, M., Gondoin, P., Much, R., Munoz, R., Santos, M., Schartel, N., Texier, D., and Vacanti, G.: 2001, *A&A* **365**, L1

Jansen, F. A.: 1999, *ESA Bulletin* **100**, 9

Jiménez-Bailón, E., Santos-Lleó, M., Piconcelli, E., Matt, G., Guainazzi, M., and Rodríguez-Pascual, P.: 2007, *A&A* **461**, 917

Kalberla, P. M. W., Burton, W. B., Hartmann, D., Arnal, E. M., Bajaja, E., Morras, R., and Pöppel, W. G. L.: 2005, *A&A* **440**, 775

Kaneko, Y., Preece, R. D., Briggs, M. S., Paciesas, W. S., Meegan, C. A., and Band, D. L.: 2006, *ApJS* **166**, 298

Kauffmann, G. and Haehnelt, M.: 2000, *MNRAS* **311**, 576

Kippen, R. M., Woods, P. M., Heise, J., in't Zand, J., Preece, R. D., and Briggs, M. S.: 2001, in E. Costa, F. Frontera, & J. Hjorth (ed.), *Gamma-ray Bursts in the Afterglow Era*, pp 22–+

Kobayashi, S., Piran, T., and Sari, R.: 1997, *ApJ* **490**, 92

Kommers, J. M., Lewin, W. H. G., Kouveliotou, C., van Paradijs, J., Pendleton, G. N., Meegan, C. A., and Fishman, G. J.: 2001, *ApJS* **134**, 385

Kormendy, J. and Richstone, D.: 1995, *ARA&A* **33**, 581

Koshut, T. M., Kouveliotou, C., Paciesas, W. S., van Paradijs, J., Pendleton, G. N., Briggs, M. S., Fishman, G. J., and Meegan, C. A.: 1995, *ApJ* **452**, 145

Koss, M., Mushotzky, R., Veilleux, S., and Winter, L.: 2010, *ApJL* **716**, L125

Krolik, J. H. and Begelman, M. C.: 1988, *ApJ* **329**, 702

Krolik, J. H. and Piran, T.: 2011, *ArXiv e-prints 1106.0923*

Kumar, P. and Piran, T.: 2000, *ApJ* **532**, 286

La Franca, F., Fiore, F., Comastri, A., Perola, G. C., Sacchi, N., Brusa, M., Cocchia, F., Feruglio, C., Matt, G., Vignali, C., Carangelo, N., Ciliegi, P., Lamastra, A., Maiolino, R., Mignoli, M., Molendi, S., and Puccetti, S.: 2005, *ApJ* **635**, 864

Lawrence, A.: 1991, *MNRAS* **252**, 586

Lawrence, A. and Elvis, M.: 1982, *ApJ* **256**, 410

Lazzati, D.: 2005, *MNRAS* **357**, 722

Lazzati, D. and Begelman, M. C.: 2005, *ApJ* **629**, 903

Lazzati, D., Ghisellini, G., and Celotti, A.: 1999, *MNRAS* **309**, L13

Lazzati, D., Ghisellini, G., Celotti, A., and Rees, M. J.: 2000, *ApJL* **529**, L17

Levan, A. J., Tanvir, N. R., Cenko, S. B., Perley, D. A., Wiersema, K., Bloom, J. S., Fruchter, A. S., Postigo, A. d. U., O'Brien, P. T., Butler, N., van der Horst, A. J., Leloudas, G., Morgan, A. N., Misra, K., Bower, G. C., Farihi, J., Tunnicliffe, R. L., and others: 2011, *Science* **333**, 199

Li, L.-X.: 2007, *MNRAS* **380**, 621

Liang, E. W., Dai, Z. G., and Wu, X. F.: 2004, *ApJL* **606**, L29

Lightman, A. P. and White, T. R.: 1988, *ApJ* **335**, 57

Lipunova, G. V., Gorbovskoy, E. S., Bogomazov, A. I., and Lipunov, V. M.: 2009, *MNRAS* **397**, 1695

Lyutikov, M. and Blandford, R.: 2003, *ArXiv e-prints 0312347*

MacFadyen, A. I. and Woosley, S. E.: 1999, *ApJ* **524**, 262

MacFadyen, A. I., Woosley, S. E., and Heger, A.: 2001, *ApJ* **550**, 410

Madau, P., Ghisellini, G., and Fabian, A. C.: 1994, *MNRAS* **270**, L17+

Magdziarz, P. and Zdziarski, A. A.: 1995, *MNRAS* **273**, 837

Magorrian, J., Tremaine, S., Richstone, D., Bender, R., Bower, G., Dressler, A., Faber, S. M., Gebhardt, K., Green, R., Grillmair, C., Kormendy, J., and Lauer, T.: 1998, *AJ* **115**, 2285

Maiolino, R., Shemmer, O., Imanishi, M., Netzer, H., Oliva, E., Lutz, D., and Sturm, E.: 2007, *A&A* **468**, 979

Malizia, A., Stephen, J. B., Bassani, L., Bird, A. J., Panessa, F., and Ubertini, P.: 2009, *MNRAS* **399**, 944

Maraschi, L., Ghisellini, G., and Celotti, A.: 1992, *ApJL* **397**, L5

Marconi, A. and Hunt, L. K.: 2003, *ApJL* **589**, L21

Markwardt, C. B., Tueller, J., Skinner, G. K., Gehrels, N., Barthelmy, S. D., and Mushotzky, R. F.: 2005, *ApJL* **633**, L77

Matt, G., Bianchi, S., Awaki, H., Comastri, A., Guainazzi, M., Iwasawa, K., Jimenez-Bailon, E., and Nicastro, F.: 2009, *A&A* **496**, 653

Matt, G., Bianchi, S., Guainazzi, M., and Molendi, S.: 2004, *A&A* **414**, 155

Matt, G., Pompilio, F., and La Franca, F.: 1999, *New Astronomy* **4**, 191

Meegan, C. A., Pendleton, G. N., Briggs, M. S., Kouveliotou, C., Koshut, T. M., Lestrade, J. P., Paciesas, W. S., McCollough, M. L., Brainerd, J. J., Horack, J. M., Hakkila, J., Henze, W., Preece, R. D., Mallozzi, R. S., and Fishman, G. J.: 1996, *ApJS* **106**, 65

Mészáros, P. and Rees, M. J.: 2000, *ApJ* **530**, 292

Middleton, M., Done, C., and Schurch, N.: 2008, *MNRAS* **383**, 1501

Miller, J. S. and Antonucci, R. R. J.: 1983, *ApJL* **271**, L7

Murakami, T., Inoue, H., Nishimura, J., van Paradijs, J., and Fenimore, E. E.: 1991, *Nature* **350**, 592

Murphy, K. D. and Yaqoob, T.: 2009, *MNRAS* **397**, 1549

Mushotzky, R. F., Winter, L. M., McIntosh, D. H., and Tueller, J.: 2008, *ApJL* **684**, L65

Nakar, E. and Sari, R.: 2011, *ArXiv e-prints 1106.2556*

Nandra, K. and Pounds, K. A.: 1994, *MNRAS* **268**, 405

Narayan, R., Piran, T., and Kumar, P.: 2001, *ApJ* **557**, 949

Narayan, R. and Yi, I.: 1994, *ApJL* **428**, L13

Nava, L., Ghirlanda, G., Ghisellini, G., and Celotti, A.: 2011, *MNRAS* pp 932–+

Nenkova, M., Sirocky, M. M., Nikutta, R., Ivezić, Ž., and Elitzur, M.: 2008, *ApJ* **685**, 160

Nicastro, F.: 2000, *ApJL* **530**, L65

Nicastro, F., Martocchia, A., and Matt, G.: 2003, *ApJL* **589**, L13

Norman, C., Ptak, A., Hornschemeier, A., Hasinger, G., Bergeron, J., Comastri, A., Giacconi, R., Gilli, R., Glazebrook, K., Heckman, T., Kewley, L., Ranalli, P., Rosati, P., Szokoly, G., Tozzi, P., Wang, J., Zheng, W., and Zirm, A.: 2004, *ApJ* **607**, 721

Norris, J. P., Marani, G. F., and Bonnell, J. T.: 2000, *ApJ* **534**, 248

O'Brien, P. T., Willingale, R., Osborne, J., Goad, M. R., Page, K. L., Vaughan, S., Rol, E., Beardmore, A., Godet, O., Hurkett, C. P., Wells, A., Zhang, B., Kobayashi, S., Burrows, D. N., Nousek, J. A., Kennea, J. A., Falcone, A., Grupe, D., Gehrels, N., and others: 2006, *ApJ* **647**, 1213

Page, K. L., Reeves, J. N., O'Brien, P. T., and Turner, M. J. L.: 2005, *MNRAS* **364**, 195

Page, K. L., Willingale, R., Osborne, J. P., Zhang, B., Godet, O., Marshall, F. E., Melandri, A., Norris, J. P., O'Brien, P. T., Pal'shin, V., Rol, E., Romano, P., Starling, R. L. C., Schady, P., Yost, S. A., Barthelmy, S. D., Beardmore, A. P., Cusumano, G., and others: 2007, *ApJ* **663**, 1125

Paltani, S., Walter, R., McHardy, I. M., Dwelly, T., Steiner, C., and Courvoisier, T. J.-L.: 2008, *A&A* **485**, 707

Panessa, F., Barcons, X., Bassani, L., Cappi, M., Carrera, F. J., Ho, L. C., and Pellegrini, S.: 2007, *A&A* **467**, 519

Pareschi, G., Tagliaferri, G., Attinà, P., Basso, S., Borghi, G., Citterio, O., Civitani, M., Cotroneo, V., Negri, B., Sironi, G., Spiga, D., Vernani, D., and Valsecchi, G.: 2009, in *Society of Photo-Optical Instrumentation Engineers (SPIE) Conference Series*, Vol. 7437 of *Society of Photo-Optical Instrumentation Engineers (SPIE) Conference Series*

Parisi, P., Masetti, N., Jiménez-Bailón, E., Chavushyan, V., Malizia, A., Landi, R., Molina, M., Fiocchi, M., Palazzi, E., Bassani, L., Bazzano, A., Bird, A. J., Dean, A. J., Galaz, G., Mason, E., Minniti, D., Morelli, L., Stephen, J. B., and Ubertini, P.: 2009, *A&A* **507**, 1345

Pendleton, G. N., Paciesas, W. S., Mallozzi, R. S., Koshut, T. M., Fishman, G. J., Meegan, C. A., Wilson, R. B., Horack, J. M., and Lestrade, J. P.: 1995, *Nuclear Instruments and Methods in Physics Research A* **364**, 567

Perna, R., Armitage, P. J., and Zhang, B.: 2006, *ApJL* **636**, L29

Piconcelli, E., Bianchi, S., Guainazzi, M., Fiore, F., and Chiaberge, M.: 2007, *A&A* **466**, 855

Piran, T.: 2004, *Reviews of Modern Physics* **76**, 1143

Pogge, R. W.: 1988, *ApJ* **328**, 519

Popham, R., Woosley, S. E., and Fryer, C.: 1999, *ApJ* **518**, 356

Pounds, K. A., Nandra, K., Stewart, G. C., George, I. M., and Fabian, A. C.: 1990, *Nature* **344**, 132

Pozdnyakov, L. A., Sobol, I. M., and Syunyaev, R. A.: 1983, *Astrophysics and Space Physics Reviews* **2**, 189

Preece, R. D., Briggs, M. S., Pendleton, G. N., Paciesas, W. S., Matteson, J. L., Band, D. L., Skelton, R. T., and Meegan, C. A.: 1996, *ApJ* **473**, 310

Ramirez-Ruiz, E., MacFadyen, A. I., and Lazzati, D.: 2002, *MNRAS* **331**, 197

Ramirez-Ruiz, E. and Merloni, A.: 2001, *MNRAS* **320**, L25

Ramirez-Ruiz, E., Merloni, A., and Rees, M. J.: 2001, *MNRAS* **324**, 1147

Ranalli, P., Comastri, A., and Setti, G.: 2003, *A&A* **399**, 39

Reeves, J. N. and Turner, M. J. L.: 2000, *MNRAS* **316**, 234

Reichart, D. E. and Stephens, A. W.: 2000, *ApJ* **537**, 904

Rhoads, J. E.: 1997, *ApJL* **487**, L1+

Risaliti, G., Elvis, M., Fabbiano, G., Baldi, A., Zezas, A., and Salvati, M.: 2007, *ApJL* **659**, L111

Risaliti, G., Elvis, M., and Nicastro, F.: 2002, *ApJ* **571**, 234

Risaliti, G., Maiolino, R., and Salvati, M.: 1999, *ApJ* **522**, 157

Risaliti, G., Salvati, M., Elvis, M., Fabbiano, G., Baldi, A., Bianchi, S., Braito, V., Guainazzi, M., Matt, G., Miniutti, G., Reeves, J., Soria, R., and Zezas, A.: 2009, *MNRAS* **393**, L1

Romano, P., Campana, S., Chincarini, G., Cummings, J., Cusumano, G., Holland, S. T., Mangano, V., Mineo, T., Page, K. L., Pal'Shin, V., Rol, E., Sakamoto, T., Zhang, B., Aptekar, R., Barbier, S., Barthelmy, S., Beardmore, A. P., Boyd, P., Burrows, D. N., and others: 2006, *A&A* **456**, 917

Ruffini, R., Bianco, C. L., Fraschetti, F., Xue, S.-S., and Chardonnet, P.: 2001, *ApJL* **555**, L113

Rybicki, G. B. and Lightman, A. P.: 1979, *Radiative processes in astrophysics*

Ryde, F.: 2005, *ApJL* **625**, L95

Saez, C., Chartas, G., Brandt, W. N., Lehmer, B. D., Bauer, F. E., Dai, X., and Garmire, G. P.: 2008, *AJ* **135**, 1505

Sakamoto, T., Barthelmy, S. D., Baumgartner, W. H., Cummings, J. R., Fenimore, E. E., Gehrels, N., Krimm, H. A., Markwardt, C. B., Palmer, D. M., Parsons, A. M., Sato, G., Stamatikos, M., Tueller, J., Ukwatta, T. N., and Zhang, B.: 2011, *ApJS* **195**, 2

Sazonov, S., Revnivtsev, M., Krivonos, R., Churazov, E., and Sunyaev, R.: 2007, *A&A* **462**, 57

Sazonov, S. Y. and Revnivtsev, M. G.: 2004, *A&A* **423**, 469

Setti, G. and Woltjer, L.: 1989, *A&A* **224**, L21

Severgnini, P., Caccianiga, A., Della Ceca, R., Braito, V., Vignali, C., La Parola, V., and Moretti, A.: 2011, *A&A* **525**, A38+

Shakura, N. I. and Sunyaev, R. A.: 1973, *A&A* **24**, 337

Shapiro, S. L. and Teukolsky, S. A.: 1983, *Black holes, white dwarfs, and neutron stars: The physics of compact objects*

Shemmer, O., Brandt, W. N., Netzer, H., Maiolino, R., and Kaspi, S.: 2006, *ApJL* **646**, L29

Shields, G. A.: 1978, *Nature* **272**, 706

Shinozaki, K., Miyaji, T., Ishisaki, Y., Ueda, Y., and Ogasaka, Y.: 2006, *AJ* **131**, 2843

Shu, X. W., Wang, J. X., Jiang, P., Fan, L. L., and Wang, T. G.: 2007, *ApJ* **657**, 167

Silk, J. and Rees, M. J.: 1998, *A&A* **331**, L1

Silva, L., Maiolino, R., and Granato, G. L.: 2004, *MNRAS* **355**, 973

Silverman, J. D., Kampczyk, P., Jahnke, K., Andrae, R., Lilly, S., Elvis, M., Civano, F., Mainieri, V., Vignali, C., Zamorani, G., Nair, P., Le Fevre, O., de Ravel, L., Bardelli, S., Bongiorno, A., Bolzonella, M., Brusa, M., Cappelluti, N., Cappi, A., and others: 2011, *ArXiv e-prints 1109.1292*

Simpson, C.: 2005, *MNRAS* **360**, 565

Sunyaev, R. A. and Titarchuk, L.: 1989, in J. Hunt & B. Battrick (ed.), *Two Topics in X-Ray Astronomy, Volume 1: X Ray Binaries. Volume 2: AGN and the X Ray Background*, Vol. 296 of *ESA Special Publication*, pp 627–631

Syer, D. and Clarke, C. J.: 1995, *MNRAS* **277**, 758

Takeuchi, T., Miyama, S. M., and Lin, D. N. C.: 1996, *ApJ* **460**, 832

Tanaka, Y., Nandra, K., Fabian, A. C., Inoue, H., Otani, C., Dotani, T., Hayashida, K., Iwasawa, K., Kii, T., Kunieda, H., Makino, F., and Matsuoka, M.: 1995, *Nature* **375**, 659

Teng, S. H., Mushotzky, R. F., Sambruna, R. M., Davis, D. S., and Reynolds, C. S.: 2011, *ArXiv e-prints 1109.2734*

The Fermi-LAT Collaboration: 2011, *ArXiv e-prints 1109.4678*

Treister, E. and Urry, C. M.: 2006, *ApJL* **652**, L79

Treister, E., Urry, C. M., and Virani, S.: 2009, *ApJ* **696**, 110

Tremaine, S., Gebhardt, K., Bender, R., Bower, G., Dressler, A., Faber, S. M., Filippenko, A. V., Green, R., Grillmair, C., Ho, L. C., Kormendy, J., Lauer, T. R., Magorrian, J., Pinkney, J., and Richstone, D.: 2002, *ApJ* **574**, 740

Tueller, J., Baumgartner, W. H., Markwardt, C. B., Skinner, G. K., Mushotzky, R. F., Ajello, M., Barthelmy, S., Beardmore, A., Brandt, W. N., Burrows, D., Chincarini, G., Campana, S., Cummings, J., Cusumano, G., Evans, P., Fenimore, E., Gehrels, N., Godet, O., and others: 2010, *ApJS* **186**, 378

Tueller, J., Mushotzky, R. F., Barthelmy, S., Cannizzo, J. K., Gehrels, N., Markwardt, C. B., Skinner, G. K., and Winter, L. M.: 2008, *ApJ* **681**, 113

Ueda, Y., Akiyama, M., Ohta, K., and Miyaji, T.: 2003, *ApJ* **598**, 886

Ueda, Y., Eguchi, S., Terashima, Y., Mushotzky, R., Tueller, J., Markwardt, C., Gehrels, N., Hashimoto, Y., and Potter, S.: 2007, *ApJL* **664**, L79

Ulvestad, J. S.: 2003, in J. A. Zensus, M. H. Cohen, & E. Ros (ed.), *Radio Astronomy at the Fringe*, Vol. 300 of *Astronomical Society of the Pacific Conference Series*, pp 97–+

Urry, C. M. and Padovani, P.: 1995, *PASP* **107**, 803

van der Wolk, G., Barthel, P. D., Peletier, R. F., and Pel, J. W.: 2010, *A&A* **511**, A64+

Vasudevan, R. V., Mushotzky, R. F., Winter, L. M., and Fabian, A. C.: 2009, *MNRAS* **399**, 1553

Vietri, M. and Stella, L.: 1998, *ApJL* **507**, L45

Voss, R. and Ajello, M.: 2010, *ApJ* **721**, 1843

Wang, X.-Y. and Mészáros, P.: 2007, *ApJ* **670**, 1247

Watson, D., Reeves, J. N., Hjorth, J., Fynbo, J. P. U., Jakobsson, P., Pedersen, K., Sollerman, J., Castro Cerón, J. M., McBreen, S., and Foley, S.: 2006, *ApJL* **637**, L69

Waxman, E. and Mészáros, P.: 2003, *ApJ* **584**, 390

Wheeler, J. C., Yi, I., Höflich, P., and Wang, L.: 2000, *ApJ* **537**, 810

Wilson, A. S. and Tsvetanov, Z. I.: 1994, *AJ* **107**, 1227

Winter, L. M., Mushotzky, R. F., Reynolds, C. S., and Tueller, J.: 2009a, *ApJ* **690**, 1322

Winter, L. M., Mushotzky, R. F., Terashima, Y., and Ueda, Y.: 2009b, *ApJ* **701**, 1644

Winter, L. M., Mushotzky, R. F., Tueller, J., and Markwardt, C.: 2008, *ApJ* **674**, 686

Worsley, M. A., Fabian, A. C., Bauer, F. E., Alexander, D. M., Hasinger, G., Mateos, S., Brunner, H., Brandt, W. N., and Schneider, D. P.: 2005, *MNRAS* **357**, 1281

Wyithe, J. S. B. and Loeb, A.: 2003, *ApJ* **595**, 614

Yaqoob, T.: 1997, *ApJ* **479**, 184

Yaqoob, T., Murphy, K. D., Miller, L., and Turner, T. J.: 2010, *MNRAS* **401**, 411

Yonetoku, D., Murakami, T., Nakamura, T., Yamazaki, R., Inoue, A. K., and Ioka, K.: 2004, *ApJ* **609**, 935

Zauderer, B. A., Berger, E., Soderberg, A. M., Loeb, A., Narayan, R., Frail, D. A., Petitpas, G. R., Brunthaler, A., Chornock, R., Carpenter, J. M., Pooley, G. G., Mooley, K., Kulkarni, S. R., Margutti, R., Fox, D. B., Nakar, E., Patel, N. A., and others: 2011, *Nature* **476**, 425

Zdziarski, A. A.: 1985, *ApJ* **289**, 514

Zdziarski, A. A., Ghisellini, G., George, I. M., Fabian, A. C., Svensson, R., and Done, C.: 1990, *ApJL* **363**, L1

Zoghbi, A., Uttley, P., and Fabian, A. C.: 2011, *MNRAS* **412**, 59

Acknowledgements

This thesis would not exist without the help and support of many people: this means that the credit of our scientific results is shared among many, while the imperfections should be ascribed to myself only. I will proceed in quite random order in these acknowledgements, hoping that nobody will be left out of them. I would like to thank Jochen, my supervisor here in MPE, for teaching me how to stand on my own legs, and for making me a more mature astronomer. I want to thank the never-ending support, teaching, discussions with Giancarlo and Gabriele, who have become more than just my old supervisors. They thought me the “way of the force” and I will always be grateful to them for being patient when I asked for one more explanation. I wish to extend lots of thanks to Marco who has been a patient supervisor and friend, for the opportunities he gave and the push he transmits. Finally Nico, Elena, and Eugenio share the responsibility of making me a more realistic scientist, and I thank them for this.

My parents, needless to say, deserve their own citation in these acknowledgements for their unconditioned support and for making me what I am. My brother Lorenzo also has a note of merit: despite being the small one, he has an inspiring nature (from time to time it’s opposite tough). I am happy to have run this race with lots of friends: Laura (I will truly miss you, you pest), Jacopo (freeze your ass in Montreal), Francesca, David (Zweinstein), Fra, Niki, Marcella and all the other IMPRS people. Thank you Mattia&Luisa (calcio alla viva il prete, verticalizzare), Lucia&Marco (soppa!fava!), Stefano&Irina (scacciteddi and privet drugu), Renzo&Katie, Silvia&Raul (hasta siempre), Marghi for her rakia, RoVert, Felicia, Victor, Lara, Marcolino and people that I am guilty to leave out in this line. Thanks Marcella and Andrea for having always left you office doors open to my visits.

A final thank-you goes to the person who was acknowledged already once at the end of a thesis. Thank you for being still so patient with me, for making me better day after day, and for being willing to share the rest of the adventure with me.

List of publications

Refereed

(10) Ghirlanda, G.; Nava, L.; Ghisellini, G.; Celotti, A.; **Burlon, D.**; Covino, S.; Melandri, A., 2011, submitted to MNRAS, arXiv: 1107.4096

(9) Nardini, M.; Greiner, J.; Krühler, T.; Filgas, R.; Klose, S.; Afonso, P.; Clemens, C.; Nicuesa Guelbenzu, A.; Olivares E., F.; Rau, A.; Rossi, A.; Updike, A.; Küpcü Yoldas, A.; Yoldas, A.; **Burlon, D.**; Elliott, J.; Kann, D. A., 2011, A&A, 531, 39

(8) Gruber, D., Krühler, T., Foley, S., Nardini, M. , **Burlon, D.**, Rau, A., Bissaldi, E., Kienlin, A. v., Greiner, J., Baht, P. N., Briggs, M. S., Connaughton, V., Kippen, R. M., Meegan, C., Paciesas, W. S., Preece, R., Wilson-Hodge, C., 2011, A&A, 528,15

(7) **Burlon, D.**, Ajello, M., Greiner, J., Comastri, A., Merloni, A., Gehrels, N., 2011, ApJ, 728, 58

(6) Ghirlanda, G., Ghisellini, G., Nava, L., **Burlon, D.**, 2011, MNRAS, 410, L47

(5) Cappelluti, N., Ajello, M., **Burlon, D.**, Krumpe, M., Miyaji, T., Bonoli, S., Greiner, J., 2010, ApJ, 716, 209

(4) Krühler, T., Greiner, J., Afonso, P., **Burlon, D.**, Clemens, C., Filgas, R., Kann, D. A., Klose, S., Küpcü Yoldas, A., McBreen, S., Olivares, F., Rau, A., Rossi, A., Schulze, S., Szokoly, G. P., Updike, A., Yoldas, A., 2009 A&A, 508, 593

(3) **Burlon, D.**, Ghirlanda, G., Ghisellini, G., Greiner, J., Celotti, A., 2009, A&A, 505, 569

(2) Ghisellini, G., Foschini, L., Volonteri, M., Ghirlanda, G., Haardt, F., **Burlon, D.**, Tavecchio, F., 2009, MNRAS, 399, L24

(1) **Burlon, D.**, Ghirlanda, G., Ghisellini, G., Lazzati, D., Nava, L., Nardini, M., and Celotti, A., 2008, ApJ, 685, L19

Non-refereed

(7) **Burlon, D.**, Ajello, M., Greiner, J., Comastri, A., Merloni, A., Gehrels, N., 2011, The X-ray Universe 2011, Presentations of the Conference held in Berlin, Germany, 27-30 June 2011, p.52

(6) Nardini, M.; Greiner, J.; Klose, S.; Krühler, T.; Filgas, R.; Schady, P.; Afonso, P.; Clemens, C.; Guelbenzu, A. Nicuesa; Olivares, F. E.; Updike, A.; Rossi, A.; Yoldas,

A. Küpcü; Yoldas, A.; **Burlon, D.**; Elliott, J.; Kann, D. A., 2011, GAMMA RAY BURSTS 2010. AIP Conference Proceedings, Volume 1358, pp. 150-153

(5) Gruber, D.; Krḧler, T.; Foley, S.; Nardini, M.; **Burlon, D.**, 2011, GAMMA RAY BURSTS 2010. AIP Conference Proceedings, Volume 1358, pp. 29-32

(4) Nardini, M.; Greiner, J.; Kruehler, T.; Filgas, R.; Klose, S.; Afonso, P.; Clemens, C.; Guelbenzu, A. N.; Olivares, E. F.; Rau, A.; Rossi, A.; Updike, A.; Kupcu Yoldas, A.; Yoldas, A.; **Burlon, D.**; Elliott, J.; Kann, D. A., 2011, yCat, 35319039N

(3) **Burlon, D.**, 2010, Active Galactic Nuclei 9: Black Holes and Revelations, Conference held 24-27 May, 2010 at Aula Magna dell'Universita di Ferrara., p.16, Bibliographic Code: 2010agn9.confE..16B

(2) Krühler, T., Greiner, J., Afonso, P., **Burlon, D.**, Clemens, C., Filgas, R., Kann, D. A., Klose, S., Küpcü Yoldas, A., McBreen, S., Olivares, F., Rau, A., Rossi, A., Schulze, S., Szokoly, G. P., Updike, A., Yoldas, A., 2009, yCat, 35080593K

(1) Nava, L., **Burlon, D.**, Ghirlanda, G., Ghisellini, G., Nardini, M., 2009, GRB Coordinates Network, Circular Service, 9235, 1